

Washington University in St. Louis

Washington University Open Scholarship

Arts & Sciences Electronic Theses and
Dissertations

Arts & Sciences

Spring 5-15-2023

Mechanisms and Consequences of Microtubule-Based Symmetry Breaking in Plant Roots

Natasha Anriel Bilkey

Follow this and additional works at: https://openscholarship.wustl.edu/art_sci_etds

Recommended Citation

Bilkey, Natasha Anriel, "Mechanisms and Consequences of Microtubule-Based Symmetry Breaking in Plant Roots" (2023). *Arts & Sciences Electronic Theses and Dissertations*. 2832.
https://openscholarship.wustl.edu/art_sci_etds/2832

This Dissertation is brought to you for free and open access by the Arts & Sciences at Washington University Open Scholarship. It has been accepted for inclusion in Arts & Sciences Electronic Theses and Dissertations by an authorized administrator of Washington University Open Scholarship. For more information, please contact digital@wumail.wustl.edu.

WASHINGTON UNIVERSITY IN ST. LOUIS

Division of Biology and Biomedical Sciences
Plant and Microbial Biosciences

Dissertation Examination Committee:

Ram Dixit, Chair

Marcus Foston

Elizabeth Haswell

Dmitri Nusinow

Christopher Topp

Mechanisms and Consequences of Microtubule-Based Symmetry Breaking in Plant Roots
by
Natasha Bilkey

A dissertation presented to
Washington University in St. Louis
in partial fulfillment of the
requirements for the degree
of Doctor of Philosophy

May 2023
St. Louis, Missouri

© 2023, Natasha Bilkey

Table of Contents

List of Figures	v
List of Tables	ix
List of Abbreviations	x
Acknowledgments.....	xii
Abstract of the Dissertation	xiv
Chapter 1: Introduction	1
1.1 Symmetry Breaking in Biology	1
1.1.1 Symmetry and Symmetry Breaking.....	1
1.1.2 The Cytoskeleton’s Role in Symmetry Breaking.....	3
1.2 Helical Growth in Plants	5
1.2.1 A Historical Perspective.....	5
1.2.2 The Purpose of Helical Growth	7
1.3 The Plant Root System.....	8
1.3.1 Root System Function and Development.....	8
1.3.2 Root Mechanobiology.....	10
1.3.3 Next-Generation Methods for Studying Roots	13
1.4 Cytoskeletal Control of Plant Directional Growth.....	15
1.4.1 Cortical Microtubule Cytoskeleton.....	15
1.4.2 Cell Wall Composition and Mechanics.....	16
1.5 Arabidopsis ‘Twisted’ Mutants.....	19
1.5.1 A Plethora of Twisted Mutants	19
1.5.2 Arabidopsis <i>spiral1</i> and <i>cmu1</i> Mutants.....	21
1.6 Outstanding Questions Regarding Twisted Plant Growth	24
1.7 Objectives and Significance of the Thesis	25
Chapter 2: Microtubule-generated anisotropy in the epidermis is required for maintaining anatomical symmetry in Arabidopsis roots.....	28
2.1 Abstract	28
2.2 Introduction	29
2.3 Materials and Methods.....	30

2.3.1	Plant Materials and Growth Conditions	30
2.3.2	Construction of Plasmids and Generation of Transgenic Plants	32
2.3.3	Image Acquisition and Analysis	33
2.4	Results	35
2.4.1	Epidermal Complementation of <i>spr1-3</i> and <i>cmu1</i> Rescues Straight Root Growth.....	35
2.4.2	Reduced Epidermal Cell Adhesion Suppresses Skewed Root Growth.....	40
2.4.3	Skewed Microtubules and Cell Morphology Precedes Cell File Twisting	42
2.4.4	Cell File Twisting and a Heterogeneous Mechanical Environment Promote Skewing	43
2.5	Discussion	44
2.6	Supplementary Information.....	46
Chapter 3: Twisted growth impairs Arabidopsis root mechanoresponse		50
3.1	Abstract	50
3.2	Introduction	51
3.3	Materials and Methods	53
3.3.1	Plant Growth Conditions.....	53
3.3.2	Agar Gradient Assay.....	53
3.4	Results	54
3.4.1	Root Skewing is Present at the Root System Level in the <i>spr1-3</i> Mutant	54
3.4.2	Stiffness of the Agar Medium Affects Organ-Level Root Growth in the <i>spr1-3</i> Mutant ...	56
3.4.3	ACC-induced Root Hair Production Straightens <i>spr1-3</i> Mutant Roots on 1% Agar.....	58
3.4.3	Root Hairs are Not necessary for Root Skewing in the <i>spr1</i> Mutant.....	60
3.5	Discussion	62
3.6	Supplementary Information.....	64
Chapter 4: Correlated mechanochemical maps of Arabidopsis primary cell walls using atomic force microscope-infrared spectroscopy		66
4.1	Abstract	66
4.2	Introduction	67
4.3	Materials and Methods	71
4.3.1	Sample Preparation	71
4.3.2	AFM-IR Measurement.....	71
4.3.3	NMF and Cross-Correlation with Phase Shift	72
4.4	Results and Discussion.....	72

4.4.1	AFM-IR Imaging of <i>A. thaliana</i> Epidermal Cell Walls.....	72
4.4.2	Determining the Spatial Variation in Primary Cell Wall Composition by AFM-IR.....	76
4.4.3	Deconvoluting AFM-IR Spectra for Mechanochemical Correlations	82
4.4.4	Correlating Cell Wall Composition and Stiffness.....	88
4.5	Supplementary Information.....	90
4.5.1	Supplementary Methods	90
4.5.2	Supplementary Figures and Tables	95
Chapter 5: Conclusions and Future Directions		104
5.1	The Epidermis Controls Root Directional Growth	105
5.2	Mechanisms of Twisted Root Growth and Consequences on the Root System	108
5.3	AFM-IR Can Be Used to Study Plant Cell Wall Mechanochemistry	114
References		117
Appendix I: Application of pan-sharpening algorithm for correlative multimodal imaging using AFM-IR.....		164
Appendix II: Structural insights into how the <i>Arabidopsis</i> SPIRAL2 protein targets and stabilizes microtubule minus ends		199

List of Figures

Figure 1.3.1: Arabidopsis root anatomy	8
Figure 1.3.2: Arabidopsis root waving during growth	12
Figure 1.5.1: <i>spirall</i> and <i>cmul</i> Arabidopsis twisted mutants exhibit opposing chirality.....	23
Figure 2.4.1: Expression of SPR1-GFP in the epidermis alone is sufficient to maintain root anatomical and growth symmetry	37
Figure 2.4.2: Expression of GFP-CMU1 in the epidermis alone is sufficient to maintain root anatomical and growth symmetry	38
Figure 2.4.3: Epidermal complementation of the <i>spr1-3</i> mutant restores the skewing and anisotropy of both epidermal and cortical cells to wild-type-like	39
Figure 2.4.4: Cell adhesion is required for twisted growth of <i>spr1-3</i> and <i>cmul</i> roots	41
Figure 2.4.5: Cortical microtubule and cell skewing precedes twisted growth in <i>spr1-3</i>	42
Figure 2.4.6: Root skewing requires a heterogenous environment	43
Figure 2.6.1: <i>spr1</i> and <i>cmul</i> roots skew with opposing chirality.	46
Figure 2.6.2: Epidermal complementation of the <i>spr1-3</i> mutant restores transverse microtubule orientation	47
Figure 2.6.3: Soil-grown <i>spr1-3</i> roots maintain skewed cell files	48
Figure 2.6.4: Biased root hair-agar interaction in <i>spr1</i> mutant does not contribute to skewed root growth	49
Figure 3.4.1: The spatial orientation of lateral roots in <i>spr1-3</i> affects root emergence and tip angles.....	55
Figure 3.4.2: <i>spr1-3</i> root skewing shifts from right- to left-handed on agar with increasing shear modulus.....	57
Figure 3.4.3: Hairy <i>spr1-3</i> roots induced by exogenous ACC treatment affect root mechanoreponse	59
Figure 3.4.4: Root hairs are not required for reorientation of <i>spr1-6</i> root skewing in response to increased shear modulus	61

Figure 3.6.1: LRs skew rightward in <i>spr1-3</i> seedlings	64
Figure 3.6.2: <i>spr1-3</i> roots flatten along plastic barriers during growth	64
Figure 3.6.3: Root skewing in <i>spr1-3</i> is unaffected by increasing osmotic stress	65
Figure 4.4.1: AFM-IR imaging of an epidermal cell wall in a PFA-fixed <i>A. thaliana</i> stem sample	75
Figure 4.4.2: AFM-IR data of PFA-fixed <i>A. thaliana</i> stem epidermal cell wall show similar absorption patterns to FTIR spectra of cell wall standards	80
Figure 4.4.3: Fixed wavenumber maps at 1075 cm ⁻¹ , 1525 cm ⁻¹ , and 1660 cm ⁻¹	81
Figure 4.4.4: NMF factor spectra represent carbohydrate-rich and protein-like regions in the epidermal cell wall	85
Figure 4.4.5: Higher relative presence of NMF Factor 1 positively correlates with cell wall stiffness	87
Figure 4.5.1: The epidermis and vasculature of PFA fixed stem sections maintain cell shape and tissue integrity	98
Figure 4.5.2: Pre-processing steps used for FTIR and AFM-IR spectra	99
Figure 4.5.3: PCA of AFM-IR spectra and FTIR spectra of the same carbohydrate standards show highly similar IR signatures	100
Figure 4.5.4: Lignin autofluorescence in Col-0 stem section	101
Figure 4.5.5: FTIR spectra of extracts from Arabidopsis seedling tissue	102
Figure 4.5.6: PCA shows chemical heterogeneity within the epidermal cell wall	102
Figure 4.5.7: Cophenetic coefficient of variation and residual sum of squares for NMF factors ranging from 2 to 6	103
Figure 4.5.8: Distribution maps of Factor 2 and Factor 3 representing their concentrations (absolute value) in each pixel	103
Figure 6.4.1: The general idea of the spectral pan-sharpening algorithm	171
Figure 6.4.2: Pan-sharpening applied to the simulated dataset using three NMF components at a downsampling rate of 16	174
Figure 6.4.3: Pan-sharpening applied to AFM-IR dataset with known ground truth	178

Figure 6.4.4: Pan-sharpening applied to AFM-IR dataset	179
Figure 6.4.5: Pan-sharpening for data fusion: the restored IR dataset from a biological object was separated into two components and correlated with the contact resonance	182
Figure 6.5.1: Simulated dataset which contains three distinct compounds with unique spectra	185
Figure 6.5.2: Component abundance maps after first NMF, interpolation and after second NMF for a simulated dataset	186
Figure 6.5.3: Cross correlation, SAM and RMSE as a function of the number of NMR components and downsample rate for a simulated dataset with noise	187
Figure 6.5.4: Quality assessment of the CNMF PS algorithm	188
Figure 6.5.5: Cross correlation, SAM and RMSE as a function of the number of NMR components and downsample rate for a simulated dataset without noise	189
Figure 6.5.6: Component abundance maps after first NMF, interpolation and after second NMF for a spectral PMMA/polystyrene+epoxy dataset with known ground truth	190
Figure 6.5.7: Cross correlation, SAM and RMSE as a function of the number of NMR components and downsample rate for a real AFM-IR dataset	189
Figure 6.5.8: Component abundance maps after first NMF, interpolation and after second NMF for a use-case PMMA/polystyrene+epoxy dataset	190
Figure 7.4.1: MT binding and minus-end localization of SPR2 fragments	210
Figure 7.4.2: Multimerization state of SPR2	212
Figure 7.4.3: Effect of SPR2 fragments on MT dynamics in vitro	214
Figure 7.4.4: SPR2 binds soluble tubulin dimers	216
Figure 7.4.5: SPR2 contains a bona fide TOG domain with a unique architecture	218
Figure 7.4.6: Phenotypes of <i>spr2-2</i> mutant expressing SPR2 fragments	222
Figure 7.4.7: Cortical MT dynamics and minus end localization of SPR2 fragments in hypocotyl epidermal cells	223
Figure 7.6.1: The SPR2 TOG domain structural core aligns well to the AlphaFold prediction model	230
Figure 7.6.2: The SPR2 TOG domain is highly conserved across plants	231

Figure 7.6.3: The SPR2 TOG domain face composed of intra-HEAT loops is highly conserved and basic	232
---	-----

List of Tables

Table 2.3.1: <i>Arabidopsis thaliana</i> lines used in Chapter 2	31
Table 2.3.2: Primers for amplifying cell layer-specific promoters from Col-0 genomic DNA ...	32
Table 3.3.1: <i>Arabidopsis thaliana</i> lines used in Chapter 3	53
Table 4.4.1: IR assignments of the average Arabidopsis AFM-IR spectrum compared to commercial	82
Table 4.4.2: IR assignments NMF factors	85
Table 4.5.1: IR assignments commercial standards	95
Table 4.5.2: The glycosyl composition analysis results of the three Arabidopsis cell wall reference extracts (Oxalate, 1 M KOH, and 4 M KOH), performed by the UGA CCRC	97
Table 4.5.3: Total carbohydrate and protein percentages of the three Arabidopsis cell wall reference extracts (Oxalate, 1 M KOH, and 4 M KOH)	98
Table 7.4.1: Dynamics of cortical microtubule plus and minus ends	225
Table 7.6.1: Crystallographic data processing and refinement statistics	232
Table 7.6.2: Oligonucleotides used in Appendix II	233

List of Abbreviations

AFM = Atomic Force Microscopy

Ca²⁺ = Calcium

Col-0 = Columbia-0

CSC = Cellulose Synthase Complex

GFP = Green Fluorescent Protein

IR = Infrared Spectroscopy

KOH = Potassium hydroxide

Ler-0 = Landsberg erecta

LR = Lateral root

MAP = Microtubule-Associated Protein

MS = Murashige and Skoog

MT = Microtubule

NMF = Non-negative Matrix Factorization

PCA = Principal Component Analysis

PFA = Paraformaldehyde

PGA = Polygalacturonic Acid

PI = Propidium Iodide

PR = Primary root

PS = Pan-Sharpening

RFP = Red Fluorescent Protein

RGI = Rhamnogalacturonic Acid I

RSA = Root System Architecture

+TIP = Microtubule Plus End-Localized Protein

-TIP = Microtubule Minus End-Localized Protein

Acknowledgments

I would like to thank my advisor, Ram Dixit, for your unwavering support in all aspects of my graduate school journey. You approach mentorship with kindness and open-mindedness, always considering the health of your trainees above all else. You continuously encouraged me to explore diverse training opportunities that were instrumental in my professional development. I cannot overstate how thankful I am that I chose your lab.

To all the members of the Dixit lab, old and new, thank you for being such wonderful people to work with. While our intellectual discussions helped steer my research, the collaborative and fun environment we built made coming to work each day worth it. I would like to especially thank Ryan Calcutt — I am very lucky to have a colleague become such a close friend. Thank you for being so thoughtful and supportive through everything. Don't worry, you will always be the funniest person in the lab.

To my colleagues in The Balsa Group — it has brought me immense joy to learn alongside you each day. I am so proud of our accomplishments and the positive impact we had on the St. Louis community. Thank you for helping me realize my passions and develop as a leader.

To Kiona Elliott, Erin Mattoon, and Kari Miller — our friendship has changed my life in more ways than I can count, and I am so grateful that graduate school brought us together. Thank you for the endless laughs and for always being there when I needed you. Together, we can do anything.

To Kelsey Dawson, Abby Horkan, and Erin Moriearty — it is impossible to summarize what our two decades of friendship mean to me. Thank you for never letting physical distance prevent us from supporting each other through everything.

To my parents and my sister — your love and support mean the world to me. Thank you for always trying to understand my research (or perhaps pretending to), supporting my passions, and never letting me forget how proud you are of me. Mom, our daily phone calls helped more than you know. And to all my extended family, thank you for always checking in and expressing how much you care. I am so lucky to have you all by my side.

Lastly, to my fiancé, Erik Nolan — you have been the most incredible teammate throughout every step of this journey. Thank you for being my cheerleader and for keeping me sane (or trying your best) when things got crazy. You (and Murphy) are my home, and I cannot imagine doing this without you.

This work was accomplished in collaboration with Dr. Marcus Foston (Washington University in St. Louis), Dr. Guy Genin (Washington University in St. Louis), and Dr. Charles T. Anderson (The Pennsylvania State University). This research was supported by the William H. Danforth Plant Sciences Fellowship and the Center for Engineering MechanoBiology, an NSF Science and Technology Center, under grant agreement CMMI: 15-48571.

Natasha Bilkey

Washington University in St. Louis

May 2023

ABSTRACT OF THE DISSERTATION

Mechanisms and Consequences of Microtubule-Based Symmetry Breaking in Plant Roots

by

Natasha Bilkey

Doctor of Philosophy in Biology and Biomedical Sciences

Plant and Microbial Biosciences

Washington University in St. Louis, 2023

Professor Ram Dixit, Chair

Directional growth in plants is primarily determined by the axis of cell expansion, which is specified by the net orientation of cortical microtubules. Microtubules guide the deposition of cellulose and other cell wall materials. In rapidly elongating cells, transversely oriented microtubules create material anisotropy in the cell wall that prevents radial cell expansion, channeling cell expansion in the longitudinal direction. Mutations perturbing microtubule organization frequently lead to aberrant cell growth in land plants, with some mutations leading to helical growth patterns (called ‘twisted mutants’), often in roots. This phenotype manifests as right-handed or left-handed twisting of cell files along the long axis of plant organs, which correlates with rightward or leftward organ growth, respectively. Helical growth is a common occurrence in the plant kingdom and serves a variety of purposes, but the molecular mechanisms that produce helical growth and define handedness are not well understood. Furthermore, how molecular-level processes propagate across spatial scales to control organ-level growth is undefined. Here, I used the model plant *Arabidopsis thaliana* as an experimentally tractable system, focusing on the root organ to study the mechanisms underlying helical growth in plants.

In this work, I used roots as a model plant organ to investigate the molecular mechanisms that control symmetry maintenance and symmetry breaking in plants. Arabidopsis roots are ideally suited for this work because of their simple, concentric ring-like cellular anatomy and well-defined process of development. I selected two Arabidopsis twisted mutants with opposite chirality to study whether the emergence of right-handed and left-handed helical growth involves conserved or distinct mechanisms. Cortical microtubules are skewed in the right-handed *spr1* mutant, which lacks a microtubule plus end-associated protein that regulates polymerization dynamics. In contrast, cortical microtubules tend to be laterally displaced in the left-handed *cmu1* mutant, which lacks a protein that contributes to the attachment of cortical microtubules to the plasma membrane. Using a cell-type specific complementation approach, I showed that both *SPR1* and *CMU1* gene expression in the epidermis alone is sufficient to maintain wild-type-like straight cell files and root growth. In addition, epidermal expression of *SPR1* restores both the morphology and skew of the cortical cell file to wild-type-like. By genetically disrupting cell-cell adhesion in the *spr1* mutant, I found that a physical connection between epidermal and cortical cells is required for the epidermis to cause organ-level skewed growth. Together, these data demonstrate that the epidermis plays a central role in maintaining straight root growth, suggesting that twisted plant growth in nature could arise by altering microtubule behavior in the epidermis alone and does not require null alleles in all cells.

To examine whether cortical microtubule defects in the *spr1-3* mutant affect cell growth, I conducted morphometry analysis. I found that while skewed cortical microtubule orientation correlates with asymmetric epidermal cell morphology and growth in the *spr1-3* mutant root meristem, cell file twisting is not manifested until the differentiation zone of the root where cell growth slows down and root hairs emerge. Furthermore, I demonstrated that cell file twisting is

not sufficient to generate skewed growth at the organ level, which requires that the root is grown on an agar medium, a mechanically heterogeneous environment. Increasing the stiffness of the agar medium caused the *spr1-3* and *cmu1* mutant roots to grow straight, indicating that mechanical stimuli influence twisted root growth. Despite their important role in root anchorage, root hairs on the epidermis are not required for skewed root growth, nor for reorienting root skewing in response to changes in the mechanical environment. Overall, this work provides new insights into how symmetry breaking affects root mechanoresponse.

Spatial heterogeneity in the composition and organization of the plant cell wall affects its mechanics to control cell shape and directional growth. In the last chapter of this work, I describe a new methodology for imaging plant primary cell walls at the nanoscale using atomic force microscopy coupled with infrared spectroscopy (AFM-IR). I contributed to generating a novel sample preparation technique and employed AFM-IR and spectral deconvolution to generate high-resolution spatial maps of the mechanochemical signatures of the Arabidopsis epidermal cell wall. Cross-correlation analysis of the spatial distribution of chemical and mechanical properties suggested that the carbohydrate composition of cell wall junctions correlates with increased local stiffness. In developing this methodology, this chapter provides an essential foundation for applying AFM-IR to understand the complex mechanochemistry of intact plant cell walls at nanometer resolution.

Chapter 1: Introduction

Biological symmetry and asymmetry are widely prevalent across spatial scales and kingdoms. Asymmetry in plants is often presented as helical growth, such as twisted tree trunks and coiling tendrils that provide structural rigidity, and circular movement of growing roots to better explore the soil environment. The cortical microtubule cytoskeleton orchestrates plant growth directionality, but exactly how molecular changes at the microtubule level propagate across cell and tissue scales to control organ-level growth is yet unclear. The thesis presented here explores the cellular and tissue-scale mechanisms underlying symmetry maintenance and the consequences of fixed asymmetry in plant roots.

1.1 Symmetry Breaking in Biology

1.1.1 Symmetry and Symmetry Breaking

Symmetry comes from the Greek word ‘simmetria,’ meaning good proportions and harmony (Darvas, 2007), but a more modern definition is ‘invariance under specified transformations’ (Brading et al., 2021; Merriam-Webster, 2023). Ancient Greeks admired the beauty and harmony in symmetry and emphasized it through artwork and architecture (Simon Mittman, 2019). Mathematicians and physicists are excited by hidden symmetries in the laws of nature that enable a deeper understanding of forces and particle behavior (Macleod, 2015; *What’s so Special about the Higgs Boson?*, 2023). In biology, symmetry exists across all scales. At the nanoscale, symmetry is present in numerous molecular structures, including H₂O molecules and many oligomeric proteins (Kellman, 1996; Goodsell & Olson, 2000; André et al.,

2007). The evolution of multicellularity eventually led to symmetry at a larger scale, and there are diverse types of symmetry seen at the organ and whole organism levels. Plant tissues (roots and shoots) and fungi are often radially symmetric, which enables these organisms to respond to environmental forces from every direction (Holló & Novák, 2012). Bilateral symmetry, which evolved about 600 million years ago (Hecht, 2004), is necessary for mobility in animals (Holló & Novák, 2012).

The prevalence of symmetry in biology is likely matched by the occurrence of symmetry breaking, which is found across the molecular to organism scales and in both unicellular and multicellular organisms (Buschmann & Borchers, 2020; Huang et al., 2012; Inaki et al., 2016; Smyth, 2016). Molecular asymmetry is presented in multiple ways. One form is a difference in electrical charge across the molecule (i.e., polarity or dipole moment), including in H₂O molecules and certain proteins. Another type of asymmetry is exemplified by cytoskeletal filaments such as actin filaments and microtubules, which are formed by the head-to-tail polymerization of subunits, leading to a structural polarity that is important for force generation (Mullins, 2010). Molecules can also exhibit asymmetry in the form of chiral structures. Molecules can also exhibit asymmetry in the form of chiral structures. Nearly all amino acids (except glycine) are chiral, which can subsequently induce chirality at the protein level in the form of helices and other handed higher-order structures (Efimov, 2018). Asymmetries at the cellular level serve important roles in organismal development. In bacterial cells, the polar localization of some proteins is carefully orchestrated and essential for a variety of functions, including signal transduction, pili assembly, and flagella formation (Shapiro et al., 2002). In plant cells, polar transport of the phytohormone auxin is important for various tropic growth

responses and organogenesis a process mediated by the asymmetric distribution of auxin transport proteins such as the PIN family auxin efflux carriers (Adamowski & Friml, 2015).

Symmetry breaking is fundamental for mammalian development. The helical alignment of the heart's musculature induces an overall helical shape (Buckberg, 2002), which is important for appropriate cardiac function as evidenced by diseases that arise due to more circumferential tissue alignment (Chang et al., 2022). The left-right asymmetric arrangement of organs in mammals is determined at the embryonic stage by the handedness of ciliary-guided fluid flow (Nonaka et al., 1998; Y. Okada et al., 1999; Takeda et al., 1999; Hirokawa et al., 2009). Large-scale morphological asymmetries are also widely prevalent in plants and serve a variety of purposes, from improved structural support to effective seed dispersal (Smyth, 2016). In summary, the maintenance and breaking of symmetry are widespread and functionally relevant across kingdoms. While asymmetry evolved independently in prokaryotes, plants, and animals, its molecular origin often traces back to cytoskeletal activities (Henley, 2012).

1.1.2 The Cytoskeleton's Role in Symmetry Breaking

The cytoskeleton is a dynamic network of filaments within a cell that guide the transport of proteins and vesicles, generate forces on organelles and membranes, and provide structural support. The three major components of the cytoskeleton are microtubules, filamentous actin (F-actin), and intermediate filaments (Pollard & Goldman, 2018). While only animals developed intermediate filaments, homologous forms of microtubules and actin exist in all three kingdoms (Pollard & Goldman, 2018). All three polymers have distinct mechanical properties and functions. F-actin is the thinnest cytoskeletal element (6 nm diameter), a highly flexible helix of polymerized globular actin (G-actin) subunits. In contrast, microtubules are thicker (25 nm

diameter), hollow tube-like structures consisting of laterally associated linear protofilaments formed by the polymerization of $\alpha\beta$ -tubulin heterodimers. Both F-actin and microtubules have intrinsic polarity with one end being more dynamic than the other ('barbed' end for F-actin, plus end for microtubules), which is important for directing motor protein movement (Pollard & Goldman, 2018). Intermediate filaments (10 nm diameter) are highly flexible, braided polymers of polypeptide tetramers that stack with opposing orientations, resulting in no net polarity and no association with motor proteins (Pollard & Goldman, 2018).

In bacteria such as *Helicobacter pylori*, generation of the naturally occurring helical cell shape involves cytoskeletal filaments called bactofilin that are highly stable (Deng et al., 2019; Sichel et al., 2022), unlike dynamic actin and microtubule filaments. The helical shape of *H. pylori* is essential for its ability to colonize the stomach, however, the underlying mechanism is unclear (Sycuro et al., 2010) since helical cell shape does not aid in bacterial motility (Padgett et al., 1983; Constantino et al., 2016). *Escherichia coli*, a rod-shaped bacteria, naturally elongates in a chiral manner due to helical ordering of the MreB cytoskeleton (Varma et al., 2007; S. Wang et al., 2012), a homolog of the eukaryotic actin that guides the local insertion of cell wall material.

In animals, handedness is determined at the embryonic stage by both the actomyosin and microtubule cytoskeletal systems. For example, the myosin 1D (Myo1D) actin motor protein is an evolutionarily conserved determinant of left-right symmetry in animals (Juan et al., 2018). *Drosophila melanogaster* mutants lacking Myo1D exhibit reversed orientation of visceral organs (Hozumi et al., 2006; Spéder et al., 2006). Overexpression of Myo1D in the epidermis of *D. melanogaster* larva induces right-handed twisting of the whole larval body (Lebreton et al., 2018). Myo1D likely induces organismal-level torsion through chiral molecular interactions with

actin filaments that lead to chiral cell and organ morphologies (Lebreton et al., 2018). Control of the left-right asymmetric arrangement of organs also involves kinesin family members (KIF), which are microtubule-associated motor proteins essential for ciliary assembly (Hirokawa et al., 2009; Cullen et al., 2021). Mutations in *Kif* genes affect ciliary morphology and motility (Nonaka et al., 1998; Y. Okada et al., 1999; Takeda et al., 1999; Hirokawa et al., 2009). Cilia in *Kif3* mutant mice move rotationally, as opposed to beating in a wavelike manner in wild-type mice, which thus inverses the handedness of fluid flow (Hirokawa et al., 2009). As a result, *Kif3* mutant mice exhibit a reversed left-right asymmetry in organ arrangement, a disease called ‘situs inversus’ when it occurs in humans (Mishra et al., 2012).

Handedness in plant development often manifests as helical or chiral growth patterns in aerial tissues, which are widely prevalent across plant species and organs (Smyth, 2016). In contrast to animals, the origin of handedness in plants typically involves the microtubule cytoskeleton (Nakamura & Hashimoto, 2020), with a few notable exceptions involving cell wall modifications (Reiter et al., 1997; Saffer et al., 2017; Schindelman et al., 2001; Sedbrook et al., 2002). How microtubule-level modifications generate helical growth at the organ and whole plant level is not fully understood and will be explored in the section below.

1.2 Helical Growth in Plants

1.2.1 A Historical Perspective

Helical shapes and motions of plants have been appreciated by biologists for over 150 years. Charles Darwin was amongst the first (preceded by Asa Gray in 1858 and Ludwig H. Palm and Hugo von Mohl in 1827) to observe and experimentally test the prevalence and relevance of helical plant growth. In his notable publication, *On the Movement and Habits of*

Climbing Plants, Darwin extensively documents the movements of over one hundred plants he classified as spirally twining, leaf climbers, and tendril bearers (Darwin, 1865). Darwin was fascinated by the helical motion of plant tips and its correlation with the axial twisting of the plant organ itself. Mohl considered that twining plants were ‘irritable,’ in that they bend toward any object they touch, but Darwin disproved this by rubbing tendrils to excite movement and finding no result (Darwin, 1865). Darwin also disputed that axial torsion is the cause of plant twining, and listed several examples of tendril-bearing plants that do not twist (e.g., *Pisum sativum*, *Echinocystis lobata*, *Bigonia capreolata*) (Darwin, 1865).

To date, the molecular mechanisms of axial twisting in plant organs are not fully understood, nor how organ twisting contributes to helical growth. However, significant technological advancements since Darwin’s time have helped address these knowledge gaps. Modern approaches to studying helical plant growth employ timelapse imaging, as seen in recent work on maize (Del Dottore et al., 2017) and rice (I. Taylor et al., 2021) root circumnutation, which uncovered *HISTIDINE KINASE 1* as a necessary gene for this helical growth phenomenon (I. Taylor et al., 2021). High-resolution microscopy is used to visualize twisted cell files and cellular morphologies (Buschmann & Borchers, 2020), which also allows for three-dimensional reconstruction and analysis of organ structure (Otsuka & Tsukaya, 2021). The model plant *Arabidopsis thaliana* has proved a useful tool for studying chiral growth in recent decades given the dozens of characterized mutants exhibiting twisted growth in various organs (Buschmann & Borchers, 2020). These *Arabidopsis* mutants have pointed to clear roles for the microtubule cytoskeleton and cell wall in twisted growth, and this will be explored further in Section 1.5.

1.2.2 The Purpose of Helical Growth

Helical growth, often observed in aerial tissues (stems, leaves, tendrils, flowers), is widespread in the plant kingdom, including examples in the fossil record (Zhou et al., 2019), but what is the purpose of this developmental phenomenon? Darwin considered that the helical morphology serves a structural purpose, in that stems twine to gain rigidity and carry their own weight (Darwin, 1865). Tendrils, found in grapevines and Cucurbita, coil around supports to facilitate the growth of climbing plants (Smyth, 2016). However, structural integrity is not the only functional purpose of helical growth. Some plants have helically-arranged petals (e.g., Norfolk Island hibiscus), which may serve to attract pollinators (Endress, 1999). There are numerous examples of spiral-shaped seed pods (e.g., *Medicago orbicularis*) and seed pods that spin as they float down (e.g., *Ginkgo biloba*, with helically-orientated cellulose microfibrils in the seed shell (Y. Zhang et al., 2022)), perhaps to facilitate seed dispersal. Many leaves and petals resupinate, or twist by approximately 180° during opening, and while the purpose of this is largely unknown (Smyth, 2016), it may serve as a protective advantage during development or to position petals for pollinator landing (Darwin, 1862).

Naturally-occurring helical growth in plants is most commonly observed in aerial tissues, but helical growth can also occur below ground in the root system. Roots circumnutate at their tips to explore and penetrate the surrounding soil environment (Migliaccio et al., 2009; I. Taylor et al., 2021). Charles and Francis Darwin first describe root circumnutation in their 1880 book, *The Power of Movement in Plants* (Darwin et al., 1880). This movement at each independent root tip leads to a complex root system architecture that stretches deep into the soil and across long distances, acquiring water and nutrients and providing structural stability.

1.3 The Plant Root System

1.3.1 Root System Function and Development

From food crops to giant sequoias that reach over 80 meters high (U.S. National Park Service, 2021), proper root system development is essential for plant health. To understand root system development, which can span meters, scientists often scale down their field of view to focus on the root tip, a few millimeters in length. At the cell level, the root tip is highly symmetrical, and the genetic and molecular mechanisms defining its development are well understood (Figure 1.3.1. *Arabidopsis thaliana* ('Arabidopsis') is a commonly-used model plant for studying roots given its highly reduced cellular architecture consisting of an epidermis, cortex, endodermis, pericycle, and stele tissue (Scheres & Wolkenfelt, 1998; Benfey & Scheres, 2000; Petricka et al., 2012). Roots of young (3-day-old) *Arabidopsis* seedlings are about ~1 cm in length, and with their well-defined anatomy, are highly amenable to quantitative morphological analysis. The epidermal cell layer is in direct contact with the surrounding environment and produces hair-like protrusions in specific cells (called trichoblasts) to improve anchorage and increase surface area for nutrient uptake (Datta et al., 2011). The stele contains vasculature elements (xylem, protoxylem, metaxylem) that transport water and nutrients to and from the shoot. Cell layers surrounding the stele are radially symmetric, but the stele tissue is bilaterally symmetric, with vasculature elements at the center axis (Petricka et al., 2012).

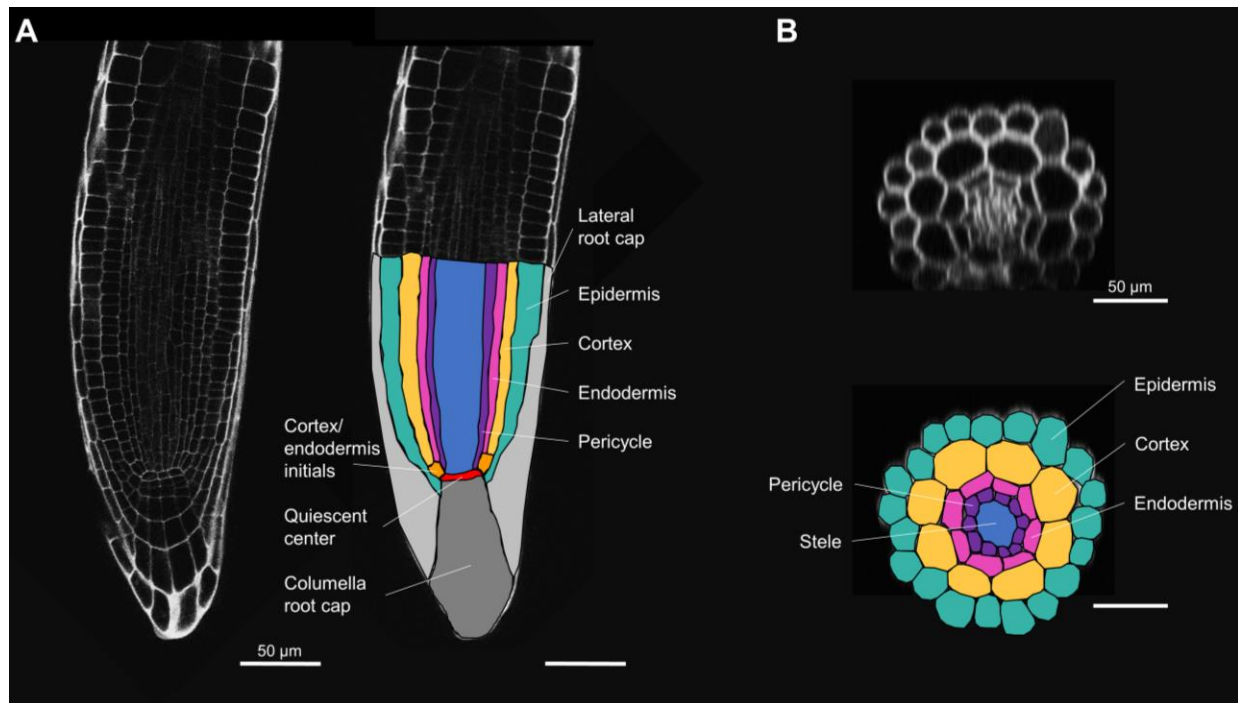


Figure 1.3.1 Arabidopsis root anatomy. (A) X,Y cross-section of a wild-type Col-0 root meristem, stained with propidium iodide and imaged using confocal microscopy. Scale bar = 50 μm. (B) X,Z cross-section of a wild-type Col-0 root differentiation zone, stained with propidium iodide and imaged using confocal microscopy. Scale bar = 50 μm.

Cell division and cell fate determination occur at the root apical meristem (RAM). The RAM consists of undifferentiated stem cells that give rise to the different cell layers of the root. Within the RAM exists a set of less mitotically-active cells, called the quiescent center (QC), which uses short-range signaling mechanisms to maintain stem cell identity of surrounding cells (van den Berg et al., 1997). Cortical and endodermal initial cells are part of this stem cell niche and give rise to these cell layers through tight spatiotemporal regulation of transcription factor (SHORTROOT and SCARECROW) signaling and periclinal cell division that defines cell identities (Benfey et al., 1993; Helariutta et al., 2000). Epidermis and lateral root cap initial cells are positioned laterally to the quiescent center and, like the cortical and endodermal initials, give rise to these cell layers through transcription factor (FEZ and SOMBRERO) signaling and periclinal cell division (Willemsen et al., 2008).

After cell division and cell fate are determined, RAM cells enter a ‘transition zone’ of slow growth, where cells are morphologically isotropic and become competent for rapid elongation (Verbelen et al., 2006). Above the quiescent center, the total length of the Arabidopsis RAM and the transition zone is about 500 μm . Following the transition zone, cells enter a phase of rapid growth in the ‘elongation zone’ where they grow anisotropically and double in size every hour, reaching lengths of about 140 μm (Verbelen et al., 2006). The elongation zone is about 300 μm in length, and the end of rapid elongation is marked by the production of root hairs from trichoblast cells ~900 μm above the quiescent center. Once root hairs begin to emerge, cell growth dramatically slows, and cells enter the ‘differentiation zone.’

1.3.2 Root Mechanobiology

Roots grow in a mechanically heterogeneous soil environment, filled with obstacles (e.g., rocks, other roots, trash) and other mechanical forces (compact soil) that impede root growth (Monshausen & Gilroy, 2009). Soil compaction, which results from changes in weather and heavy machinery use, is a significant mechanical challenge that impairs soil fertility and root system development (Colombi & Keller, 2019; Bello-Bello et al., 2022). Roots sense and respond to these mechanical stimuli (‘mechanoresponse’) to direct growth, enabling deeper soil penetration that anchors the plant and improves nutrient and water acquisition (Bello-Bello et al., 2022). Understanding root mechanoresponse is highly agriculturally relevant as it informs appropriate farming practices and may aid in the development of crop species with improved mechanoresponse (Iijima et al., 2007; Colombi & Keller, 2019).

The bulk of mechanoperception occurs at the root tip. With no mechanical impedances, growth at the root tip follows the gravity vector (‘gravitropism’), with cells elongating at equal

rates and maintaining radial symmetry. However, when the tip encounters an impenetrable obstacle, it quickly redirects its trajectory by tipping the cell growth balance. Cell expansion is slowed on one side of the root elongation zone, redirecting the root around the barrier (Massa & Gilroy, 2003). When tracking along a flat barrier, like a glass coverslip, wild-type *Arabidopsis* roots reorient and maintain a tip angle of $\sim 136^\circ$ relative to the barrier (Massa & Gilroy, 2003). Mutants with mechanosensory defects tend to flatten in response to the barrier, such as the *calmodulin-like 24/touch2* (*cml24/tch2*) mutant with a functionally-perturbed CML24 calcium-binding protein (Tsai et al., 2007; Y. Wang et al., 2011). Calcium (Ca^{2+}) is an essential secondary messenger in plants that regulates a wide variety of abiotic stress responses (Dodd et al., 2010; Nakagawa et al., 2007; Xu et al., 2022). Mechanical stimuli, like touch, immediately trigger a transient release of Ca^{2+} from the cell wall and vacuole into the cytosol in roots and other plant organs (Demarty et al., 1984; Legué et al., 1997; Toyota et al., 2008; Monshausen et al., 2009; Dodd et al., 2010; Xu et al., 2022). Another example of a mutant with altered mechanosensation is *piezo1*, which lacks a mechanosensitive Ca^{2+} ion channel and has difficulty penetrating stiff agar (Mousavi et al., 2021). Mutants in other cellular processes have also been shown to have defective barrier responses, including those defective in reactive oxygen species (*rbohD1*), ethylene (*eir1*), and auxin signaling (*aux1*) (Jacobsen et al., 2021).

Root waving and skewing are mechanoresponses that differ from barrier sensing (Figure 1.3.2). The Darwins were the first to describe root waving using seedlings grown on smoked-glass plates (Darwin et al., 1880). Waving and skewing are surface-dependent root phenotypes that are thought to result from a combination of thigmotropism and gravitropism (K. Okada & Shimura, 1990; Simmons et al., 1995; Blancaflor & Masson, 2003; Thompson & Holbrook, 2004; Oliva & Dunand, 2007; Vaughn & Masson, 2011; Roy & Bassham, 2014; Z. Zhang et al.,

2022). The exact mechanisms driving root waving and skewing are not fully understood, but the process involves circumnutation at the root tip (Roy & Bassham, 2014). Roots grown on tilted plates containing agar growth medium are responding to two forces: the force of gravity that directs downward growth, and the force of the agar that pushes the root upward. As the root follows the gravity vector downward it is met with the opposing force of the agar, which imposes a friction force that halts tip movement while the elongation zone keeps growing (Thompson & Holbrook, 2004), resulting in a curve in the root. The root tip is then deflected away from the agar, and as the tip grows, it circumnutates and meets the surface of the agar again. This process repeats, causing more waves along the length of the root (Thompson & Holbrook, 2004). Increasing the incline of the plate amplifies the root waving phenotype (Simmons et al., 1995), but it is important to note that root waving is not observed in all plant species (Simmons et al., 1995).

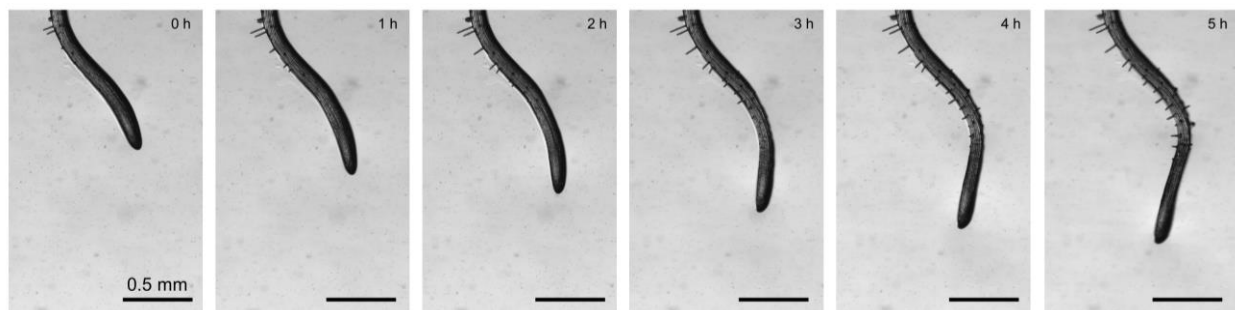


Figure 1.3.2 Arabidopsis root waving during growth. 4-day-old wild-type Col-0 root growing vertically along an agar nutrient gel imaged once per hour.

Root skewing is the leftward or rightward slanting of the root as a whole, relative to the vertical. More pronounced root skewing is often associated with twisting (‘rotation’) at the cell file level (Nakamura & Hashimoto, 2020; Roy & Bassham, 2014), but cell file twisting is not essential to induce skewed growth (Buer et al., 2003). Wild-type Columbia-0 (Col-0) naturally

adopts a slight leftward skew (viewed from the front of the plate) when grown vertically on agar plates, but exhibits straight cell files (Rutherford & Masson, 1996; Schultz et al., 2017). Skewed root growth is commonly observed across many wild-type *Arabidopsis* ecotypes, and while the degree of skewing ranges across ecotypes, the vast majority skew leftward (Vaughn & Masson, 2011). While many *Arabidopsis* mutants with skewed root growth have been identified over the decades (Benfey et al., 1993; Bisgrove et al., 2008; Furutani et al., 2000; Ishida et al., 2007; Korolev et al., 2007; Nakajima et al., 2004; Nakamura & Hashimoto, 2009; Rutherford & Masson, 1996; Sedbrook et al., 2002; Thitamadee et al., 2002; Y. Wang et al., 2011; Whittington et al., 2001; Yuen et al., 2003), only a few studies have explored the genetic basis for controlling skewed growth. Using quantitative trait locus mapping and microarrays, Vaughn and Masson narrowed down a region on chromosome 2 between 9.3 and 11.2 Mb that is associated with rightward skewing in the wild-type ecotype Cvi (Vaughn & Masson, 2011). Schultz et al. narrowed this down even further, using a transcription microarray analysis to identify 11 genes likely involved in skewing (Schultz et al., 2017). These highly probably skew gene candidates are involved in a variety of cellular processes, including sucrose transport (*SWEET11*, *ASNI*), iron ion binding (*MIOX4*), salt tolerance (*SIS*), and more. At the molecular level, there is extensive evidence that the cortical microtubule cytoskeleton is important for generating skewed root growth (Nakamura & Hashimoto, 2020), and this will be explored in the next section.

1.3.3 Next-Generation Methods for Studying Roots

The pace of root system phenotyping has not kept up with the advancements made in genetic analyses, which imposes a bottleneck on developing high-yielding crops that grow in challenging soil and climate conditions (Furbank & Tester, 2011; Topp et al., 2016). The ultimate goal is high-throughput, in-field phenotyping (Araus & Cairns, 2014), but root systems

are inherently challenging to study given their complex three-dimensional (3-D) morphology, hidden by the surrounding soil. Traditional methods for studying root system architecture in the field are destructive and time-consuming (H. M. Taylor et al., 1991; Trachsel et al., 2011; Maeght et al., 2013). 3-D image analysis has been an important tool driving RSA research in recent decades (Tollner et al., 1994; Downie et al., 2015; Piñeros et al., 2016; Topp et al., 2016; Jiang et al., 2019; Atkinson et al., 2019). 3-D imaging can be accomplished using X-ray computed tomography (Heeraman et al., 1997; Taina et al., 2008; Mooney et al., 2012; Pfeifer et al., 2015; Teramoto et al., 2020), which visualizes roots in the soil using differences in the attenuation of X-rays between materials (Teramoto et al., 2020). X-ray computed tomography signals can clearly distinguish between root tissue and the surrounding substrate, but segmenting out root tissue has traditionally been a time-consuming process until recently (Teramoto et al., 2020). X-ray signal is computed to reconstruct slice images, which are virtually stacked to create 3-D volumetric projections (Teramoto et al., 2020).

Advancements in rapid, image-based root phenotyping have produced a variety of tools for studying roots in 2-D paradigms (i.e., on agar plates) (Atkinson et al., 2019), including DART (Le Bot et al., 2010), SmartRoot (Lobet et al., 2011), RootNav (Pound et al., 2013; Yasrab et al., 2019), RootTrace (French et al., 2009; Naeem et al., 2011), DIRT (Bucksch et al., 2014), BRAT (Slovak et al., 2014). These tools process 2-D images of roots by computationally segmenting the root from the agar using color thresholding, creating a skeleton of the root, and producing quantitative morphological data on the root architecture (e.g., root length, tip angles, number of roots). Some software has been further developed for kinematic analyses (Spalding & Miller, 2013), tracking root growth rates and root tip reorientation during gravitropism (Miller et al., 2007; Durham Brooks et al., 2010). While sensitivity to noise remains an issue in root

phenotyping (Atkinson et al., 2019), the output of data at high resolution has greatly expanded biologists' understanding of root growth behavior.

1.4 Cytoskeletal Control of Plant Directional Growth

1.4.1 Cortical Microtubule Cytoskeleton

Plant growth above and below ground is determined by the combined action of cell division (particularly, the rate of division and orientation of the division plane) and cell expansion (particularly, the rate and direction of elongation). In most plant tissues, cell expansion is anisotropic. Directional growth in plant cells is determined by the axis of cell elongation, which is specified by the net orientation of cortical microtubules (Green, 1962; Baskin, 2001, 2005; Lloyd, 2011). The large (up to 90% of cell volume) water-filled vacuole in mature plant cells pushes cytoplasmic material to the cell cortex. In plant cells, the majority of microtubules are present at the cell cortex (Cyr & Palevitz, 1995) and are physically tethered to the plasma membrane via specific proteins (Liu et al., 2016). Plasma membrane-bound cellulose synthase complexes (CSCs) are attached to cortical microtubules via protein linkers (Paredes et al., 2006; Lloyd, 2006; Gu et al., 2010; Bringmann et al., 2012; S. Li et al., 2012; Pedersen et al., 2023). As cellulose is synthesized directly into the cell wall it assembles into microfibrils (Haigler et al., 2014) that associate with each other and surrounding wall material, generating a force that propels CSCs along microtubules (Diotallevi & Mulder, 2007). As a result, the orientation of extracellular cellulose microfibrils matches the orientation of intracellular cortical microtubules. In *Arabidopsis* mutants lacking proteins that tether microtubules to the plasma membrane, the force exerted by catalytically active CSCs that remain attached to microtubules causes lateral displacement of microtubules (Liu et al., 2016).

How exactly does the orientation of microtubules dictate the orientation of cell growth? Cellulose microfibrils associate laterally in the wall, forming a lattice of cellulose layers ('lamellae') that is highly resistant to tensile stress (Brett, 2000; Baskin, 2005). High hydrostatic ('turgor') pressure from the water-filled vacuole is exerted isotropically on the plant cell wall. This pressure (up to 2 MPa) exceeds that of the inside of car tires, yet because of cellulose and other cell wall material, the cell does not explode (Beauzamy et al., 2014). Turgor pressure, which is maintained by osmotic regulation, provides much of the mechanical rigidity for living plant tissues and is utilized to drive cell growth, which is directed by localized reinforcement of the cell wall (Alberts et al., 2002). In rapidly elongating cells, cellulose microfibril alignment matches transversely-aligned cortical microtubules, creating material anisotropy in the cell wall that prevents radial cell expansion, channeling growth in the perpendicular direction (Baskin, 2005; Bou Daher et al., 2018; Peaucelle et al., 2015). Microtubule orientation aligns along the axis of maximal stress in the cell (Hamant et al., 2008). As cells mature, microtubules reorient longitudinally, slowing cell elongation as cellulose microfibrils resist expansion. Microtubule reorientation is particularly evident during the transition from root cell elongation to cell differentiation in the root (Adamowski et al., 2019).

1.4.2 Cell Wall Composition and Mechanics

The initial cell wall produced by all plant cells is called the primary cell wall. The primary cell wall is thin and extensible, which is important for facilitating cell growth. The secondary cell wall, which is highly rigid, is produced later in certain terminally differentiated cell types, like xylem vessels. Adjacent plant cells are cemented to each other by a gelatinous, pectin-rich structure called the middle lamella. Plant cell walls are highly dynamic structures that are primarily composed of sugar-based polymers, interwoven in a complex meshwork with

highly heterogeneous mechanical properties (Majda et al., 2017; Cosgrove, 2018; Phyto et al., 2017; Grones et al., 2019). The primary cell wall contains cellulose microfibrils, hemicellulose (e.g., xyloglucan), pectin (e.g., rhamnogalacturonan, polygalacturonan), and proteins. Secondary cell walls are distinguished by the presence of lignin, a hydrophobic phenolic compound that provides rigidity and confers resistance against pathogens (Cosgrove, 2005; Fry, 2010; Lampugnani et al., 2018; Anderson & Kieber, 2020). While cortical microtubules facilitate the directionality of cellulose synthesis, both actin and microtubules guide the delivery of other materials to the cell wall, including non-cellulosic polysaccharides, structural proteins, and enzymes (Fukuda, 1997; Ganguly et al., 2020; Kong et al., 2015; McFarlane et al., 2008; Takenaka et al., 2018; C. Zhu et al., 2015; Chebli et al., 2021).

The primary cell wall is elastic, can stiffen and soften, and is capable of plastic deformation. Cellulose microfibrils move in response to mechanical stress by straightening, curving, sliding, bundling, and reorienting (Y. Zhang et al., 2021). Cell wall dynamics are also facilitated by enzymatic activity that modifies non-cellulosic polysaccharides by enabling or disabling their ability to crosslink, or directly cleave the backbone of the polysaccharide (Anderson & Kieber, 2020). Cell wall stiffness can also be altered by regulating the crosslinking of the pectin homogalacturonan. Calcium ions facilitate crosslinking of adjacent homogalacturonan polymers by attaching to galacturonic acid residues along each chain. Homogalacturonan is delivered to the cell wall in a methylated state which deters Ca^{2+} -based crosslinking. Demethylation by pectin methylesterase enzymes, which remove methyl groups on galacturonic acid residues, enable calcium binding and crosslinking. The activity of pectin methylesterases is regulated by pH and inhibitory proteins that dynamically bind and release pectin methylesterases in response to signals (Wormit & Usadel, 2018; Anderson & Kieber,

2020). Other cell wall-modifying enzymes include lyases, which cleave pectins, and endotransglucosylases, which cleave xyloglucan (Anderson & Kieber, 2020). Expansins, on the other hand, loosen the cell wall by breaking the load-bearing hydrogen bonds that connect xyloglucan to cellulose (Cosgrove, 2000; Sandt et al., 2007). These limited interactions between closely-intertwined xyloglucan and cellulose are considered to be ‘biomechanical hotspots’ that may play an important role in dictating overall wall mechanics (Park & Cosgrove, 2015).

Analysis of the plant cell wall to determine correlations among its composition, organization, and mechanics has been challenging. Common label-dependent methodologies for imaging the plant cell wall include fluorescent stains (calcofluor, S4B, propidium iodide) and metabolic click labeling (Anderson et al., 2010; Anderson & Wallace, 2012). However, these methods are limited by the diffraction-limited resolution of standard light microscopy (~200-250 nm) and do not measure cell wall mechanical properties. Atomic force microscopy (AFM) is used as a label-free technique to map cell wall topography and mechanical properties at the nanoscale, often coupled with targeted enzymatic treatments to distinguish the contribution of different cell wall components (Cosgrove, 2018; Peaucelle et al., 2015; T. Zhang et al., 2016, 2019; Zheng et al., 2017). Nonetheless, AFM cannot directly detect cell wall chemical components.

AFM coupled with nano-infrared spectroscopy (AFM-IR) is an emerging technique to perform nanoscale multimodal imaging of physical, chemical, and mechanical material features (Dazzi et al., 2005, 2012; Dazzi & Prater, 2017; Kurouski et al., 2020). AFM-IR uses a tunable IR laser focused on the sample at the AFM tip. When the wavelength of the IR laser matches the excitation wavelength of the sample beneath the AFM tip, the sample absorbs the IR energy and undergoes thermal expansion which is detected by the AFM tip in contact with the sample

surface. This can provide chemical images at selected IR wavelengths with nanoscale spatial resolution. AFM is simultaneously used to collect high-resolution topographical and mechanical maps. AFM-IR was first developed to perform nanoscale multimodal imaging of physical, chemical, and mechanical features of composite materials (Dazzi et al., 2012; Dazzi & Prater, 2017; Kurouski et al., 2020) and is primarily used to study synthetic compositions, such as nanofilms, but has also been applied to some biological systems (Dazzi & Prater, 2017; Pereira et al., 2018b). Recently, AFM-IR has been used to image biological specimens such as triacylglycerol-containing vesicles from bacteria, yeast, and microalga (Dazzi & Prater, 2017), extracellular vesicles from animal stem cells (Kim et al., 2018), bone (Gourion-Arsiquaud et al., 2014), and breast cancer cells (Clède et al., 2013; Dazzi & Prater, 2017). In plants, the application of AFM-IR has so far been limited to secondary cell walls which are more readily amenable to sectioning and sample preparation (Farahi et al., 2017; Tetard et al., 2010, 2011, 2012, 2015).

1.5 Arabidopsis ‘Twisted’ Mutants

1.5.1 A Plethora of Twisted Mutants

Given the importance of cortical microtubules in controlling plant cell morphology (Dixit & Cyr, 2004), mutations perturbing microtubule organization frequently lead to aberrant cell growth in *Arabidopsis*. These mutations typically occur in genes encoding for tubulin or microtubule-associated proteins (MAPs). Some mutations lead to isotropic cell expansion, like in the *botero1* (*bot1*) and *microtubule organization 1* (*mor1*) mutants (Bichet et al., 2001; Whittington et al., 2001). The *bot1* mutant lacks the microtubule severing protein, katanin, leading to disorganized cortical microtubules and increased radial expansion of cells, resulting in dwarfed stems, hypocotyls, and roots (Bichet et al., 2001; Reed et al., 1998). The temperature-sensitive *mor1* mutant contains a point mutation that disrupts the microtubule binding of a

microtubule plus-end polymerase that belongs to the evolutionarily conserved MAP215 family, disrupting cortical microtubule length and organization at the restrictive temperature and inducing extreme cell swelling and dwarfism (Whittington et al., 2001).

Other microtubule-based mutations lead to symmetry breaking and helical plant growth ('twisted mutants') (Buschmann & Borchers, 2020; Smyth, 2016). There are over 30 characterized *Arabidopsis* twisted mutants (and several in other species) exhibiting helical growth in hypocotyls, leaves, stems, petals, trichomes, and most commonly, roots (Buschmann & Borchers, 2020). The handedness of helical growth is typically fixed, and the majority of twisted mutants display some type of microtubule defect. Some twisted mutants contain skewed cortical microtubule arrays in elongating cells, leading to right-handed or left-handed cell file twisting that correlates with either rightward or leftward organ growth, respectively (Ishida et al., 2007). Examples of mutants with skewed microtubules include *spiral2/tortifolia1* (*spr2/tor1*) (Buschmann et al., 2004; Y. Fan et al., 2018; Furutani et al., 2000; Shoji et al., 2004), *calmodulin-like 24/touch2* (*cml24/tch2*) (Delk et al., 2005; Y. Wang et al., 2011), and *spiral1* (*spr1*) (Balkunde et al., 2019; Furutani et al., 2000; Galva et al., 2014; Nakajima et al., 2004, 2006; Sedbrook et al., 2004). *spr2/tor1* is a null mutant lacking a microtubule minus-end stabilizing protein and shows left-handed skewed microtubules in petiole epidermal cells, correlating with right-handed cell file twisting and counter-clockwise rotation of leaves (Buschmann et al., 2004; Y. Fan et al., 2018; Furutani et al., 2000; Shoji et al., 2004). The *cml24* mutant, with a loss-of-function mutation in a calcium-binding protein implicated in touch response (see Section 1.3.2), shows left-handed skewed microtubules in root epidermal cells and strong right-handed cell file and root skewing (Y. Wang et al., 2011). The *spr1* mutant exhibits a

right-handed root skewing phenotype similar to the *cml24* mutant and will be explored in detail below.

Not all twisted mutants contain skewed microtubules. The *cellulose synthase interacting 1* (*csi1*) (Bringmann et al., 2012; Landrein et al., 2013; Liu et al., 2016; X. Zhu et al., 2018) and *cellulose microtubule uncoupling 1* (*cmu1*) (Liu et al., 2016; Ganguly et al., 2020) mutants exhibit disorganized or floppy microtubules, respectively. *csi1* is a null mutant lacking a MAP that physically links cortical microtubules and CSCs, resulting in misalignment between cortical microtubules and nascent cellulose microfibrils (Bringmann et al., 2012). Interestingly, the handedness of helical growth in the *csi1* mutant depends on the organ type, with right-handed cell files in etiolated hypocotyls and left-handed cell files in roots (Bringmann et al., 2012). In some cases, twisted growth can occur with wild-type-like microtubules. The *ramnose biosynthesis 1* mutant contains reduced levels of the pectin rhamnogalacturonan-I and has twisted petals and petal epidermal cells but wild-type-like microtubule orientation (Saffer et al., 2017). The abundance of characterized twisted mutants (Buschmann & Borchers, 2020) suggests there are many molecular mechanisms, often related to cortical microtubules and cell wall composition, that function to maintain straight growth. While the molecular mechanisms of many of the proteins involved in twisted growth have been studied, how biochemical defects at the nanoscale propagate across cell and tissue scales to perturb directional growth at the organ and organism scale is yet unclear.

1.5.2 Arabidopsis *spirall* and *cmu1* Mutants

SPR1 is a plant-specific gene expressed in most tissues in Arabidopsis and throughout all cell layers in the root (Nakajima et al., 2004). The *spr1* mutant was first identified by Takashi

Hashimoto's lab in 2000. They isolated the *spr1-1* and *spr1-3* mutant alleles from the Landsberg *erecta* (Ler) and Col-0 ecotypes, respectively, using fast-neutron irradiation-mediated mutagenesis (Furutani et al., 2000). Fast-neutron irradiation is an effective genetic knockout technique that induces deletions ranging between 1 – 30,000 base pairs throughout the genome (Moody, 2017). The *spr1-3* mutant allele contains a 10-base pair deletion in an exon-intron junction, resulting in a genetic knockout (Nakajima et al., 2004). *Spr1* mutant seedlings have left-handed skewed cortical microtubule arrays that correlate with strong, right-handed cell file twisting spanning multiple cell layers in roots and etiolated hypocotyls (Furutani et al., 2000; Weizbauer et al., 2011). The entire root organ in *spr1* mutant seedlings skews sharply rightward when grown on the surface of an agar medium (Figure 1.5.1) (Furutani et al., 2000). SPR1 is a MAP that autonomously tracks the growing plus ends of microtubules, however, it is not fully understood why lacking SPR1 results in skewed microtubule orientation (Galva et al., 2014; Sedbrook et al., 2004; Wong & Hashimoto, 2017; Balkunde et al., 2019). Cell file twisting in the *spr1* mutant is strongest in the epidermis and decreases moving toward inner cell layers (Weizbauer et al., 2011). In addition, cortical cells are isotropically expanded in the *spr1* mutant, leading to roots and etiolated hypocotyls with increased diameter compared to the wild-type (Furutani et al., 2000). Hashimoto's group originally hypothesized that epidermal cell files skew to compensate for reduced anisotropy in the underlying cortex (Furutani et al., 2000), but Schulz's group used computational modeling to suggest the inverse — cortical cells must expand radially due to geometric constraints imposed by a skewed epidermis. To date, both of these models have not been tested experimentally and hence the relative contribution of each cell layer in determining twisted growth remains unknown.

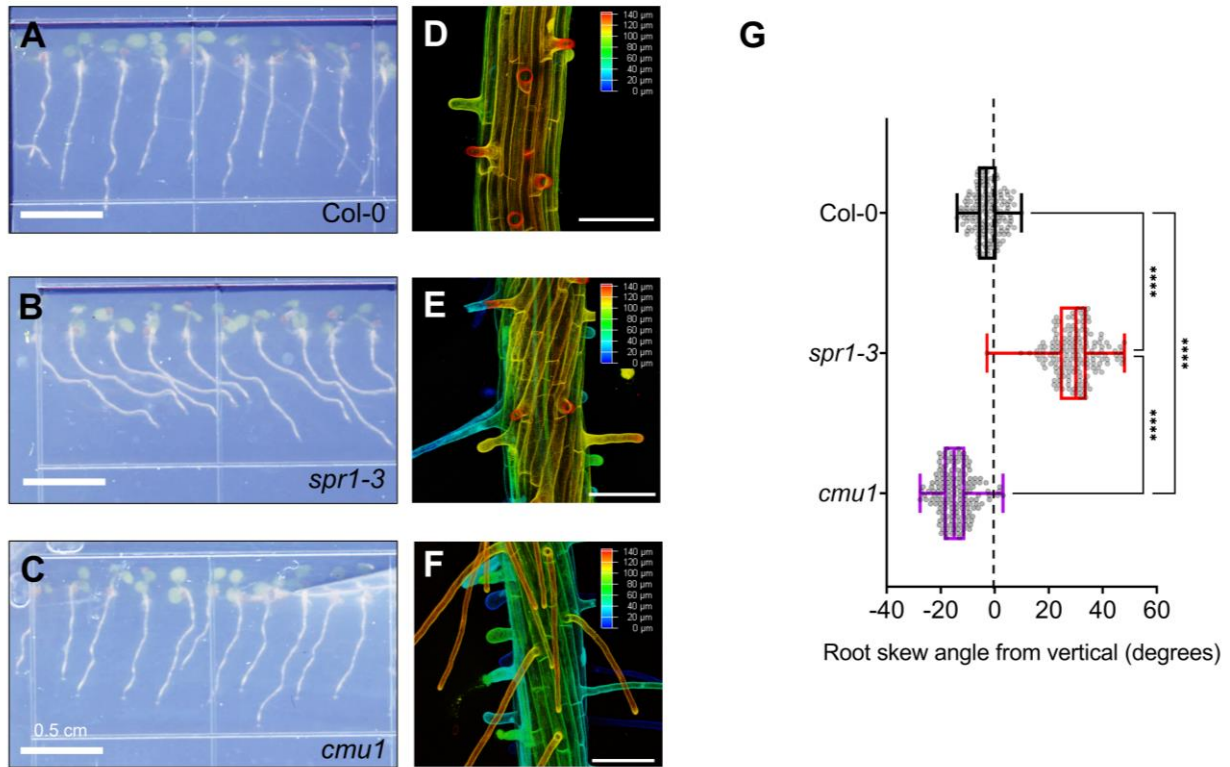


Figure 1.5.1 *spirall* and *cmu1* Arabidopsis twisted mutants exhibit opposing chirality. (A-C) Root skewing phenotype of 3-day-old Col-0 (A), *spr1-3* (B), and *cmu1* (C) seedlings grown vertically on agar plates. (D-F) Maximum projection images of cell files in the differentiation zone of Col-0 (D), *spr1-3* (E), and *cmu1* (F) seedlings stained with propidium iodide, imaged with confocal microscopy. Roots are depth-coded, with red cells appearing at the surface of the roots. Scale bar = 100 μm. (G) Root skewing angle of 3-day-old seedlings grown vertically on agar plates. Plots show mean ± SD, n = 159, 163, 159 roots for Col-0, *spr1-3*, and *cmu1* respectively. Statistics represent Kruskal-Wallis test with a Dunn's multiple comparison test; **** $P < 0.0001$.

CMU1, also known as KINESIN LIGHT CHAIN-RELATED-1 (KLCR1), was first identified by Steffen Abel's group using a yeast two-hybrid screen to identify proteins interacting with IQD67 DOMAIN 1 (IQD1) (Bürstenbinder et al., 2013). *IQD1* is induced by mechanical stimuli and encodes for a protein that associates with microtubules and calmodulin to regulate calcium signaling during defense response (Levy et al., 2005). CMU1 is a MAP that contains a tetratricopeptide repeat domain with homology to the light-chain subunit on kinesin motor proteins (Bürstenbinder et al., 2013; Verhey et al., 2011). CMU1, which localizes in a punctate pattern along the length of microtubules, works in complex with CMU2 to tether

microtubules to the plasma membrane and prevent their lateral displacement by motile cellulose synthase complexes (Liu et al., 2016). CMU1 also interacts with the FRAGILE-FIBER 1 kinesin to facilitate the deposition of cell wall material (Ganguly et al., 2020). *cmu1* mutants exhibit left-handed skewed cell files in etiolated hypocotyls and roots (Figure 1.5.1), correlated with leftward skewed root growth (Ganguly et al., 2020; Liu et al., 2016). Compared to the *spr1* mutant, the root skewing phenotype in the *cmu1* mutant is more subtle. Nonetheless, the *spr1* and *cmu1* mutants together are useful tools to investigate whether mechanisms responsible for tissue and organ level twisting are conserved or distinct between right-handed and left-handed mutants.

1.6 Outstanding Questions Regarding Twisted Plant Growth

Both symmetry and symmetry-breaking span scales, developmental stages, and kingdoms. The broad prevalence of naturally occurring twisted growth in the plant kingdom suggests that twisting is an advantageous trait as discussed in Section 1.2.2. Despite being a topic of interest to plant biologists for nearly 200 years, we still do not fully understand the underlying mechanisms and benefits (or consequences) of twisted plant growth.

For plants that naturally produce twisted organ growth (aside from circumnutation), how do they know when to break symmetry? Specifically, what are the developmental and cellular cues for breaking symmetry? Moreover, what determines the handedness of twisted growth? The plant's ability to determine when and where symmetry is broken is thought to involve the microtubule cytoskeleton and cell wall. However, twisting can arise from many different kinds of mutations, often (but not always) related to microtubules and the cell wall. Is this why twisted growth is so common in plants? How exactly do molecular processes coordinate to generate

organ-level twisting, or relatedly, maintain straight growth? Adjacent plant cells share a cell wall and are physically adhered to each other, which enables cells to respond to mechanical forces imparted by their neighbors. Does contiguous mechanical coupling throughout the plant tissue play a role in maintaining or breaking growth symmetry?

Plant roots, in particular, rely on their anatomical symmetry to control growth directionality. However, cell file twisting and skewed root growth are common developmental defects observed in *Arabidopsis* twisted mutants. What are the consequences, if any, of fixed twisted growth in roots? The vast majority of research on *Arabidopsis* twisted mutants uses seedlings grown on agar plates – a two-dimensional environment. Do twisted mutants exhibit a three-dimensional growth defect that affects the entire root system architecture? What does this look like in a soil environment?

In summary, there are many important questions surrounding the origin and function of twisted growth. The work accomplished by this thesis provides answers to some of these questions while raising new questions that will guide future research on twisted plant growth and its potential application to agriculture.

1.7 Objectives and Significance of the Thesis

This thesis work aimed to understand the cellular mechanisms and developmental consequences of symmetry breaking in plants, using *Arabidopsis* roots as a model system. In addition, this thesis developed a novel methodology for high-resolution analysis of the plant cell wall, which controls directional cell and organ growth. The three chapters of this thesis are:

- i. Microtubule-generated anisotropy in the epidermis is required for maintaining anatomical symmetry in *Arabidopsis* roots

- ii. Twisted growth impairs Arabidopsis root mechanoresponse
- iii. Correlated mechanochemical maps of Arabidopsis primary cell walls using atomic force microscope-infrared spectroscopy

In Chapter 2, I used a cell type-specific genetic complementation approach in two Arabidopsis twisted mutants (*spr1* and *cmu1*) and demonstrated that the epidermis alone is sufficient to maintain wild-type-like straight cell files and root growth, regardless of handedness. In addition, epidermal expression of SPR1 restores both the morphology and skew of the cortical cell file to wild-type-like. By genetically disrupting cell-cell adhesion in the *spr1* mutant, I found that a physical connection between epidermal and cortical cells is required for the ability of the epidermis to entrain cortical cell morphology and generate skewed root growth. I hypothesized that root hairs on the epidermis played a role in organ-level directional growth, but through generating a root hairless *spr1* mutant, I found that root hairs were not required for generating skewed growth. Together, these data highlight the importance of the epidermis in driving twisted growth and suggest that twisted plant growth in nature could arise by altering microtubule behavior in the epidermis alone.

In Chapter 3, I show that the *spr1* mutant twisted root phenotype is also present in lateral roots, demonstrating that this mutation affects the root system as a whole, perhaps leading to greater developmental consequences in a soil environment. I demonstrated that cell file twisting in the *spr1* mutant is not sufficient to generate skewed growth at the organ level, which requires a heterogeneous external mechanical input. Increasing the stiffness of the agar medium caused *spr1* mutant roots to grow straight, indicating that external mechanical stimuli influence twisted root growth. Despite their important role in root anchorage, root hairs on the epidermis are not

required for reorienting root skewing in response to changes in the mechanical environment.

Overall, this work provides new insights into how symmetry breaking affects root mechanoresponse.

In Chapter 4, I established new methodologies for sample preparation, data acquisition, and multivariate statistical analyses for AFM-IR on *Arabidopsis* primary cell walls. This sample preparation method was effective at eliminating spectral contamination and obtaining a section suitable for AFM-IR. This work also demonstrated a novel application of non-negative matrix factorization (NMF) to analyze AFM-IR datasets, detecting factors representing the chemical functionality of neutral sugars of cell wall carbohydrates, acidic sugars of cell wall carbohydrates, and amino and carbonyl groups of cell wall proteins. Furthermore, cross-correlation analysis of the spatial distribution of NMFs and wall mechanical properties showed that the neutral sugar-containing carbohydrate composition in the epidermal cell wall correlates with increased local stiffness. Future improvement of AFM-IR spatial resolution and spectral range may reveal more subtle patterns in component organization that are important for defining the local mechanical properties of the cell wall. With the methodologies developed in this chapter, AFM-IR can be used to explore and understand phenotypic alterations to specific plant tissues in nanoscale resolution caused by environmental stresses or genetic mutations.

Chapter 2: Microtubule-generated anisotropy in the epidermis is required for maintaining anatomical symmetry in Arabidopsis roots

2.1 Abstract

Plant roots, composed of multiple concentric cell layers, rely on their highly symmetrical cellular anatomy to control growth directionality. However, chiral root growth can arise due to mutations targeting microtubules, which play a critical role in directing plant cell growth. It is yet unclear how microtubule-level defects propagate across spatial scales to drive chirality, and how different cell layers contribute to controlling root growth. Here, we used a cell type-specific genetic complementation approach in two *Arabidopsis thaliana* twisted mutants, *spr1* and *cmu1*, to demonstrate that the epidermis alone is sufficient to maintain wild-type-like straight cell files and root growth, regardless of handedness. By genetically disrupting cell-cell adhesion in the *spr1* and *cmu1* mutants, we found that physical coupling between adjacent epidermal cells and the epidermis and cortex is required for the ability of the epidermis to entrain cortical cell morphology and generate skewed root growth. We hypothesized that root hairs on the epidermis played a role in directing root growth, but through generating a root hairless *spr1* mutant, we found that root hairs were not required for root skewing. Together, these data highlight the importance of the epidermis in driving twisted growth and suggest that twisted plant growth in nature could arise by altering microtubule behavior in the epidermis alone.

2.2 Introduction

Left-right asymmetry or chirality is widespread in unicellular and multicellular organisms (Buschmann & Borchers, 2020; Huang et al., 2012; Inaki et al., 2016; Smyth, 2016). While this trait evolved independently in prokaryotes, plants and animals, its molecular origin often traces back to cytoskeletal activities. In bacteria such as *Helicobacter pylori*, the generation of the naturally occurring helical cell shape involves cytoskeletal filaments called bactofilin (Sichel et al., 2022). Normally rod-shaped bacteria such as *E. coli* can also acquire chiral morphology through mutations in the MreB cytoskeleton (Varma et al., 2007; S. Wang et al., 2012). In animals, handedness frequently arises due to the actomyosin cytoskeletal system. For example, overexpression of the myosin 1D motor protein in the epidermis of *Drosophila melanogaster* larva induces right-handed twisting of the whole larval body (Spéder et al., 2006; Lebreton et al., 2018). By contrast, the origin of handedness in plants typically involves the microtubule cytoskeleton (Nakamura & Hashimoto, 2020), with a few notable exceptions involving non-microtubule-based mechanisms for helical plant growth (Reiter et al., 1997; Saffer et al., 2017; Schindelman et al., 2001; Sedbrook et al., 2002).

Directional growth of plant organs is primarily determined by the axis of cell expansion, which is specified by the net orientation of cortical microtubules (Baskin, 2001, 2005; Bou Daher et al., 2018; Green, 1962; Lloyd, 2011; Peaucelle et al., 2015; Wasteneys, 2000). Cortical microtubules spatially guide the deposition of cellulose and other cell wall materials (Fukuda, 1997; Ganguly et al., 2020; Kong et al., 2015; McFarlane et al., 2008; Takenaka et al., 2018; C. Zhu et al., 2015). In rapidly elongating cells, transversely oriented cortical microtubules create material anisotropy in the cell wall that resists radial cell expansion, channeling growth in the

longitudinal direction (Baskin, 2005). This process produces straight cell files and symmetric plant organs. Mutations in microtubule-associated genes frequently act to break symmetry, resulting in the twisted growth of plant organs (Smyth, 2016; Buschmann & Borchers, 2020). This phenotype manifests as right-handed or left-handed helical cell files which correlate with either rightward or leftward organ growth, respectively. How microtubule-based symmetry-breaking at the cellular level leads to chiral growth of plant tissues and organs remains a long-standing conundrum. To investigate this question, we examined roots of the right-handed *spiral1* (Balkunde et al., 2019; Furutani et al., 2000; Galva et al., 2014; Nakajima et al., 2004, 2006; Sedbrook et al., 2004) and left-handed *cmu1* (Ganguly et al., 2020; Liu et al., 2016) mutants of the model plant *Arabidopsis thaliana*. Our genetic and developmental studies reveal the underlying mechanisms with the epidermis playing a central role by entraining the growth direction and anisotropy of the underlying cell layer and by facilitating mechanical interactions between the root and its environment.

2.3 Materials and Methods

2.3.1 Plant Materials and Growth Conditions

All *Arabidopsis thaliana* plants that were used in this study are listed in Table 2.3.1. For all plant growth experiments, seeds were surface-sterilized using a 25% bleach solution, resuspended in 0.1% agarose, and stratified at 4°C for 2 days. Sterilized seeds were grown vertically on agar medium containing 1% w/v Phytoblend agar (Caisson Labs), 0.3% w/v sucrose, and half-strength Murashige and Skoog basal medium (Caisson Labs), pH 5.7. under 16/8-h light/dark photoperiod (120 $\mu\text{mol m}^{-2} \text{sec}^{-1}$ light intensity) at 24°C. All experiments used seedlings after 3-4 days of growth.

Table 2.3.1. *Arabidopsis thaliana* lines used in Chapter 2.

Line Name	Description	Source
Col-0	Wild-type background	N/A
<i>spr1-3</i> (At2g03680)	<i>spr1</i> null mutant (fast-neutron mutagenized)	(Nakajima et al., 2004)
<i>spr1-6</i> (At2g03680)	<i>spr1</i> null mutant (T-DNA insert)	(Sedbrook et al., 2004)
<i>cmu1/kler1</i> (At4g10840)	<i>cmu1/kler1</i> null mutant (T-DNA insert)	(Liu et al., 2016) ABRC: CS924251
Col-0 35S::LTI6B-GFP	Wild-type expressing plasma membrane marker	ABRC: CS84726
<i>spr1-3</i> 35S::LTI6B-GFP	<i>spr1</i> null mutant expressing plasma membrane marker	This study
Col-0 35S::RFP-TUB6	Wild-type expressing RFP microtubule marker	(Balkunde et al., 2019)
<i>spr1-3</i> 35S::RFP-TUB6	<i>spr1</i> null mutant expressing RFP microtubule marker	This study
Col-0 <i>pUBIQUITINQ10::GFP-TUB6</i>	Wild-type expressing GFP microtubule marker	(Y. Fan et al., 2018)
<i>spr1-3</i> <i>pUBIQUITINQ10::GFP-TUB6</i>	<i>spr1</i> null mutant expressing GFP microtubule marker	This study
<i>spr1-3</i> <i>pSHR::SPR1-GFP</i>	<i>spr1</i> null mutant with <i>SPR1-GFP</i> under <i>SHR</i> promoter	This study
<i>spr1-3</i> <i>pSCR::SPR1-GFP</i>	<i>spr1</i> null mutant with <i>SPR1-GFP</i> under <i>SCR</i> promoter	This study
<i>spr1-3</i> <i>pWER::SPR1-GFP</i>	<i>spr1</i> null mutant with <i>SPR1-GFP</i> under <i>WER</i> promoter	This study
<i>spr1-3</i> <i>pPEP::SPR1-GFP</i>	<i>spr1</i> null mutant with <i>SPR1-GFP</i> under <i>PEP</i> promoter	This study
<i>cmu1</i> <i>pWER::GFP-CMU1</i>	<i>cmu1/kler1</i> null mutant with <i>GFP-CMU1</i> under <i>WER</i> promoter	This study
<i>cpc try</i> (At2g46410, At5g53200)	<i>cpc try</i> double null mutant (T-DNA + EMS)	ABRC: CS66489
<i>spr1-6 cpc try</i>	<i>spr1 cpc try</i> triple null mutant (T-DNA + EMS)	This study

2.3.2 Construction of Plasmids and Generation of Transgenic Plants

To generate *spr1-3* cell layer-specific complemented lines, promoters ~2 kb upstream of the *SHORTROOT* (*SHR*), *SCARECROW* (*SCR*), *WEREWOLF* (*WER*), and *ENDOPEPTIDASE* (*PEP*) genes were PCR amplified from Col-0 genomic DNA and cloned into pDONR-P1P5r by means of Gateway BP clonase recombination. All promoters were recombined with pGAG entry vector, pDONR-*SPRI-GFP* (Balkunde et al., 2019), and pDONR-*NosGent* using Gateway LR clonase recombination. Primer sequences for cloning can be found in Table 2.3.2. All constructs created using PCR were verified by enzymatic digest, colony PCR, and sequencing. *spr1-3* mutant plants were transformed with each *PROMOTER::SPRI-GFP* expression construct using *Agrobacterium tumefaciens* dip technique. Homozygous T3 lines were selected on Gentamycin-containing growth medium. Cell layer-specific complemented *cmu1* lines were generated using the same method, but entry constructs were combined with pDONR-*GFP-CMU1* to generate *PROMOTER::GFP-CMU1* expression constructs, each carrying a Gentamycin resistance gene for plant selection. To generate plasma membrane marker lines, the *spr1-3* mutant was crossed with wild-type Col-0 containing LTI6b-GFP. Homozygous F3 lines were selected on Basta-containing (10 µg/mL) growth medium for selecting *spr1-3* x LTI6b-GFP plants. To generate microtubule marker lines, Col-0 and *spr1-3* mutant plants were transformed with a *35S::RFP-TUB6* expression construct (Balkunde et al., 2019) using *Agrobacterium tumefaciens* dip technique. T2 lines were selected on Kanamycin-containing growth medium.

Table 2.3.2. Primers for amplifying cell layer-specific promoters from Col-0 genomic DNA. Bolded nucleotides are complementary to the promoter sequence.

Primer Name	Primer Sequence (5' to 3'; complementary region bolded)	Purpose
SHR attB1	GGGGACAAGTTTGTACAAAAAAGCAGGCTTT aagaagcagagcgtgggggtt	Amplification of <i>SHR</i> promoter for Gateway cloning

SHR attB5r	GGGGACAACCTTTTGTATACAAAGTTGTatcagcatcatgtgtgtcttg	Amplification of <i>SHR</i> promoter for Gateway cloning
WER attB1	GGGGACAAGTTTGTACAAAAAAGCAGGCTTTgagccttgctaaatctccaatggc	Amplification of <i>WER</i> promoter for Gateway cloning
WER attB5r	GGGGACAACCTTTTGTATACAAAGTTGTcctttttgttctttgaatgatagacgagaga	Amplification of <i>WER</i> promoter for Gateway cloning
SCR attB1	GGGGACAAGTTTGTACAAAAAAGCAGGCTTTaaggtagaggaagaggactttg	Amplification of <i>SCR</i> promoter for Gateway cloning
SCR attB5r	GGGGACAACCTTTTGTATACAAAGTTGTaattaatttgagtttgaaaaataataaaaat	Amplification of <i>SCR</i> promoter for Gateway cloning
PEP attB1	GGGGACAAGTTTGTACAAAAAAGCAGGCTTTtaaggctagacaacgtccataggtg	Amplification of <i>PEP</i> promoter for Gateway cloning
PEP attB5r	GGGGACAACCTTTTGTATACAAAGTTGTtttagggcctgtgtatatatccat	Amplification of <i>PEP</i> promoter for Gateway cloning

2.3.3 Image Acquisition and Analysis

Root skewing. Three-day-old seedlings were used for all analyses. For organ-level skewing measurements, seedlings were grown vertically on nutrient agar plates and scanned from behind using a CanoScan 4400F scanner (Canon) at 300 DPI. Images were digitally reversed prior to measuring root skewing angle from vertical (0 degrees) using FIJI (Schindelin et al., 2012). Statistical analyses (ANOVA and Kruskal-Wallis tests) and graph generation were performed using GraphPad Prism software.

GFP signal and cellular morphometry in *spr1-3* and *cmu1* cell layer-specific complemented lines. For imaging SPR1-GFP and GFP-CMU1 signal in *spr1-3* and *cmu1* complemented lines, respectively, seedlings were stained with propidium iodide (Rounds et al., 2011) (PI; 10 ug/mL in distilled H₂O) for 15 minutes, mounted in sterile milliQ water, and

imaged using a Leica SP8 confocal inverted microscope equipped with a 40x oil immersion objective (NA 1.0). GFP was excited by 488 nm laser (detected 500 – 545 nm) and PI was excited by 552 nm laser (detected 562 – 725 nm). To image cellular morphometry in these lines, seedlings were stained with PI (10 ug/mL in distilled H₂O) and imaged using a Leica multiphoton upright microscope equipped with a 40x water immersion objective (NA 5.0). PI was excited by using aligned lasers, 832 nm and 1046 nm. For both experiments, Z-stacks were collected at a pixel resolution of 512 x 512 and a 3 µm slice separation.

Cortical microtubule orientation in Col-0, *spr1-3*, and cell-layer specific complemented *spr1-3*. For imaging cortical microtubules in Col-0 and *spr1-3* mutant seedlings expressing *p35S::RFP-TUB6*, seedlings were mounted in sterile milliQ water and imaged using a Leica SP8 confocal inverted microscope equipped with a 40x oil immersion objective (NA 1.0). RFP was excited by 552 nm laser (detected 562 – 725 nm). Z-stacks were collected at a pixel resolution of 1024 x 1024 and a 2 µm slice separation. Images were digitally reversed and roots were digitally straightened to align the root tip perpendicular to the bottom x-axis of the image, prior to measuring microtubule orientation using the FibrilTool plug-in (Boudaoud et al., 2014) for FIJI (Schindelin et al., 2012).

Cellular morphometry and growth of Col-0 and *spr1-3* root elongation zone cells. For imaging cellular morphometry and growth in Col-0 and *spr1-3* mutant expressing *p35S::LTI6b-GFP*, seedlings were mounted in sterile liquid nutrient media (1/2 MS + 0.3% sucrose, pH 5.7) and imaged using a Leica multiphoton upright microscope equipped with a 40x water immersion objective (NA 1.0). Z-stacks were collected at a pixel resolution of 512 x 512 and a 3 µm slice separation. GFP was excited by 488 nm laser (detected 500 – 600 nm). Plants were imaged at timepoints 0 hours and 2 hours. Images were digitally reversed prior to

measuring cell wall lengths and angles using FIJI (Schindelin et al., 2012). To obtain wall growth rates, cell wall length at 0 hours was subtracted from the length at 2 hours for each cell.

2.4 Results

2.4.1 Epidermal Complementation of the *spr1-3* and *cmu1* Mutants Rescues Straight Root Growth

How microtubule-based symmetry-breaking at the cellular level propagates across spatial scales to generate chiral growth of plant tissues and organs remains a long-standing conundrum. To investigate this question, we examined the roots of *spiral1* (Balkunde et al., 2019; Furutani et al., 2000; Galva et al., 2014; Nakajima et al., 2004, 2006; Sedbrook et al., 2004) and *cmu1* (Ganguly et al., 2020; Liu et al., 2016) mutants of the model plant *Arabidopsis thaliana*, which show right-handed and left-handed skewing, respectively, at the organ (Figure 2.6.1A) and cell file (Figure 2.6.1B) levels. Roots are cylindrical structures consisting of concentrically arranged cell layers that are adhered to each other and grow in a coordinated manner (termed symplastic growth). To evaluate the contribution of the different cell layers in generating twisted root growth, we complemented the *spr1-3* mutant with *SPR1-GFP* driven by promoters of the *SHORTROOT* (p*SHR*), *SCARECROW* (p*SCR*), *ENDOPEPTIDASE* (p*PEP*), and *WEREWOLF* (p*WER*) genes, which are expressed in the stele, endodermis, cortex, and epidermis, respectively (Marquès-Bueno et al., 2016; Petricka et al., 2012). The cell layer-specific promoters resulted in *SPR1-GFP* signal exclusively in the specified cell layers (Figure. 2.4.1, B to E), in contrast to the native *SPR1* promoter which resulted in *SPR1-GFP* signal in all cell layers (Figure 2.4.1A) as previously reported (Sedbrook et al., 2004). We found that plants expressing *SPR1-GFP* in either the stele, endodermis, or cortex showed right-handed growth of roots (Figure 2.4.1, F and G) and cell files (Figure 2.4.1, I to K), similar to the *spr1-3* null mutant. In striking contrast, plants

expressing SPR1-GFP in the epidermis showed straight growth of roots (Figure 2.4.1, F and G) and cell files (Figure 2.4.1L), similar to wild-type Col-0 plants (Figure 2.4.1F) and native promoter-complemented *spr1-6* mutant plants (Figure 2.4.1, F to H). Furthermore, epidermal complementation of the *spr1-3* mutant resulted in transverse microtubule orientation in the epidermis, similar to wild-type, whereas cortical complementation did not rescue the skewed microtubule orientation in the *spr1-3* epidermal cells (Figure 2.6.2). Complementation of the *cmu1* mutant with pWER::*CMU1-GFP* also resulted in straight root and cell file growth similar to wild-type plants (Figure 2.4.2). Together, these data demonstrate that epidermal expression alone is sufficient to rescue both right-handed and left-handed twisted mutants.

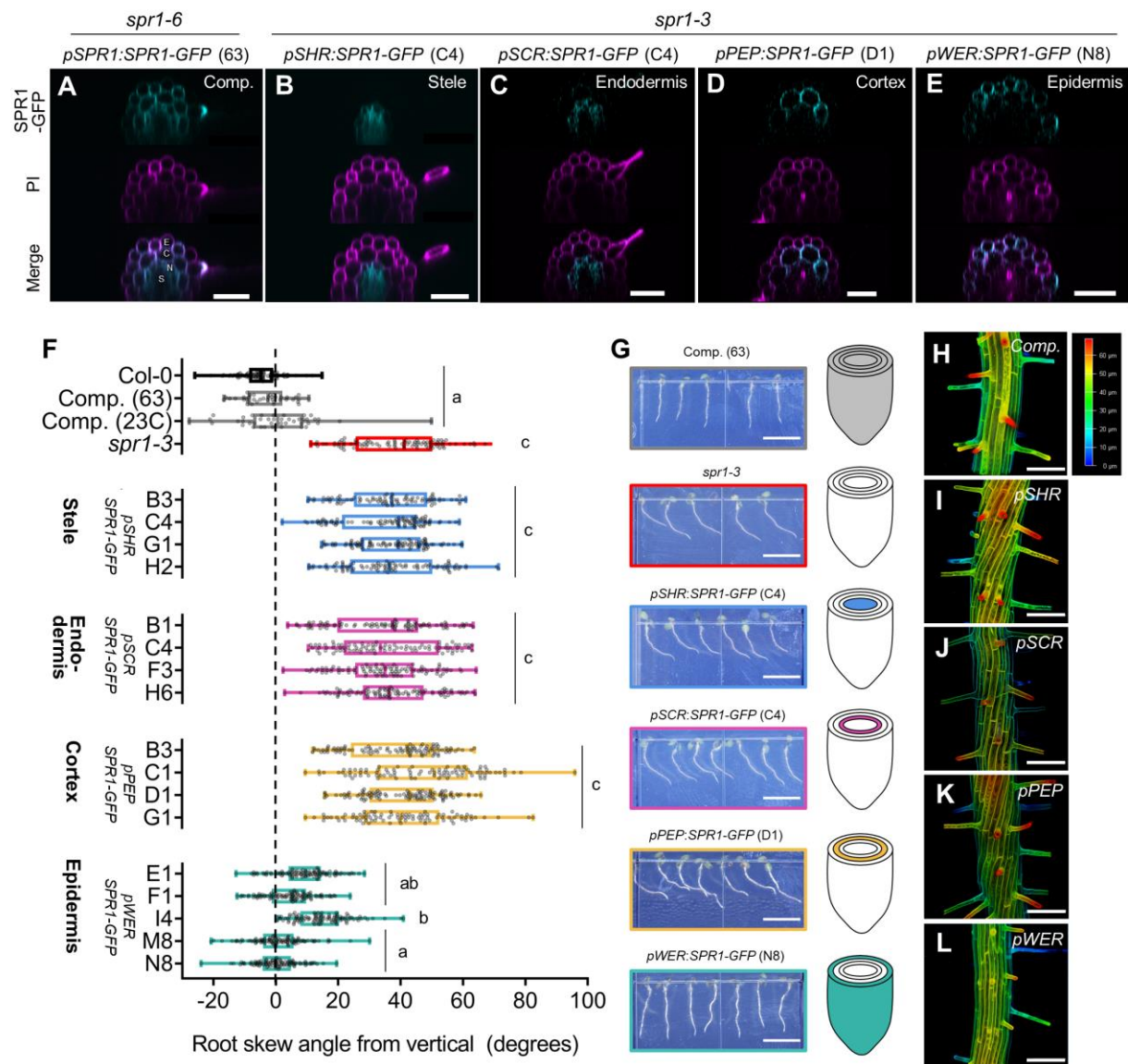


Figure 2.4.1. Expression of *SPR1*-GFP in the epidermis alone is sufficient to maintain root anatomical and growth symmetry. (A-E) Confocal x-z images of *SPR1*-GFP signal (cyan) in propidium iodide (PI)-stained (magenta) roots. E = epidermis, C = cortex, N = endodermis, S = stele. Scale bar = 50 μ m. (F) Root skewing angle of 3-day-old seedlings grown vertically on agar medium. Positive and negative angles indicate rightward and leftward root growth, respectively. The gray, blue, magenta, yellow, and teal boxplots represent independent transgenic lines expressing *SPR1*-GFP under the control of either the native *SPR1* promoter (Comp.), or *SHR*, *SCR*, *PEP* and *WER* promoters, respectively. Plots show mean \pm SD, $n > 80$ roots for all genotypes except Comp. ($n > 38$). Statistics represent Kruskal-Wallis test with a Dunn's multiple comparison test ($P < 0.05$). (G) Representative images of 3-day-old seedlings grown vertically on agar medium. Icons on the right indicate which cell layers express *SPR1*-GFP. Scale bar = 0.5 cm. (H-L) Maximum projection confocal images of PI-stained roots. Scale bar = 100 μ m. Color bar represents distance in the z-direction.

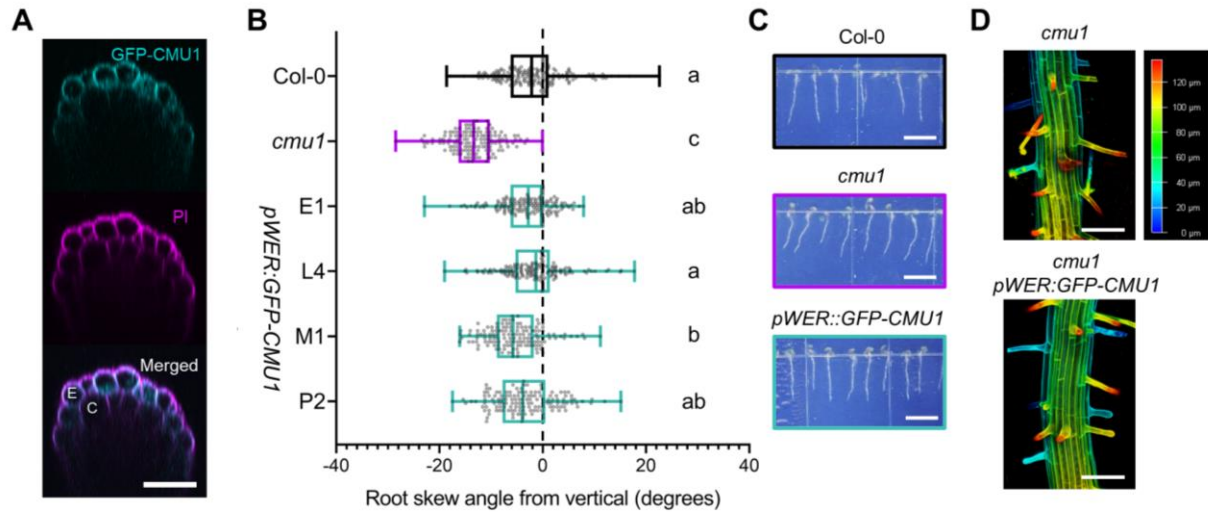


Figure 2.4.2. Expression of GFP-CMU1 in the epidermis alone is sufficient to maintain root anatomical and growth symmetry. (A) Confocal x-z images of GFP-CMU1 signal (cyan) in propidium iodide (PI)-stained (magenta) roots. E = epidermis, C = cortex. Scale bar = 50 μm . (B) Root skewing angle of 3-day-old seedlings grown vertically on agar medium. Positive and negative angles indicate rightward and leftward root growth, respectively. The teal boxplots represent independent transgenic lines expressing GFP-CMU1 under the control of the *WER* promoter. Plots show mean \pm SD, $n > 120$ roots for all genotypes. Statistics represent Kruskal-Wallis test with a Dunn's multiple comparison test ($P < 0.05$). (C) Representative images of 3-day-old seedlings grown vertically on agar medium. Scale bar = 0.5 cm. (D) Maximum projection confocal images of PI-stained roots. Scale bar = 100 μm . Color bar represents distance in the z-direction.

We next determined whether epidermal complementation influences underlying cell layers. For this analysis, we focused on the differentiation zone of the *spr1-3* mutant due to its strong skewing phenotype (Figure 2.6.1B). In line N8, which fully complements the twisted root phenotype, both the epidermal and cortical cell layers are straight (Figure 2.4.3, A and B). Likewise, in the partially complementing line I4, both the epidermal and cortical cell layers only partly return to straight growth (Figure 2.4.3, A and B). The growth anisotropy of epidermal cells is only marginally different between distinct complementation lines, which is unsurprising given the small difference in epidermal growth anisotropy between wild-type and *spr1-3* roots (Figure 2.4.3C). Unexpectedly, the growth anisotropy of cortical cells was significantly restored to wild-type-like in both epidermal complementation lines (Figure 2.4.3D). In contrast, the expression of SPR1-GFP in the cortical cell layer did not significantly alter the skewed growth and anisotropy

of either the cortical or epidermal cells (Figure 2.4.3, A and B). Thus, the epidermis influences the growth directionality and anisotropy of cortical cells and not the other way around as proposed previously (Furutani et al., 2000).

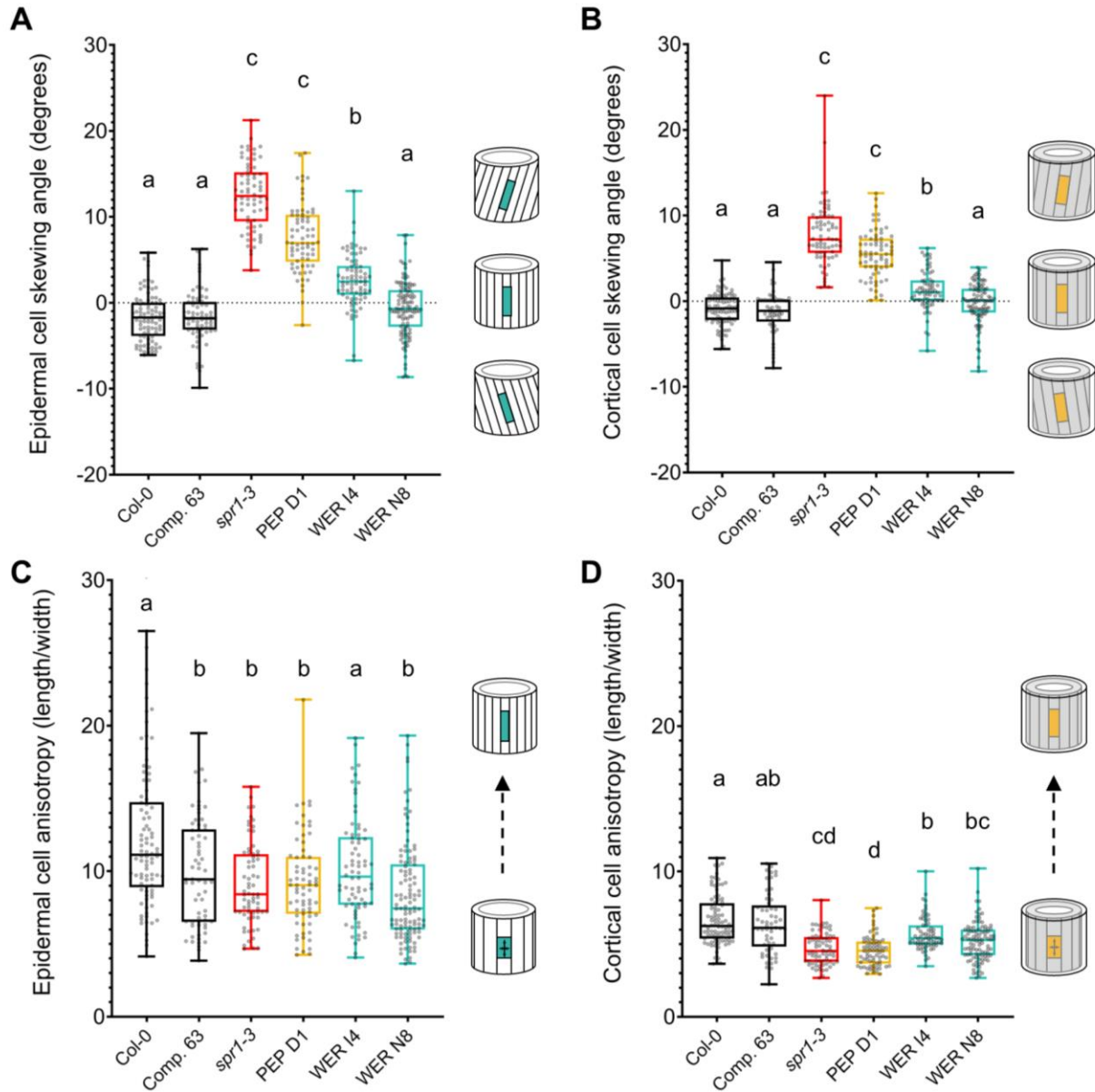


Figure 2.4.3. Epidermal complementation of the *spr1-3* mutant restores the skewing and anisotropy of both epidermal and cortical cells to wild-type-like. (A, B) Skewing angle from vertical of individual epidermal (A) and cortical (B) cells in the differentiation zone of 3-day-old propidium iodide-stained roots. Positive and negative angles indicate rightward and leftward cell skewing, respectively. (C, D) Cellular anisotropy (length/width ratio) of epidermal (C) and cortical (D) cells in the differentiation zone. Root models to the right of each figure represent cell

skewing (A, B) and cell anisotropy (C, D) of epidermal (teal) and cortical (yellow) cells. All plots show mean \pm SD, $n > 65$ cells for all genotypes. Statistics represent Kruskal-Wallis test with a Dunn's multiple comparison test ($P < 0.05$).

2.4.2 Reduced Epidermal Cell Adhesion Suppresses Skewed Root Growth

Epidermal entrainment of the cortex could be due to geometric constraints imposed by symplastic growth of plant tissues (Weizbauer et al., 2011). Such a mechanism requires tight adhesion between adjacent cell layers. Cell-cell adhesion in land plants is mediated by a pectin-rich cell wall structure called the middle lamella (Bethke et al., 2016; Daher & Braybrook, 2015; Du et al., 2020). The *quasimodo1* (*qual-1*) mutant, which contains reduced levels of homogalacturonan pectin, impairs adhesion between epidermal cells and between epidermal and cortical cells (Bouton et al., 2002). This mutant was found to suppress twisted growth in the hypocotyl and petioles of the *spr2-2* mutant (Verger et al., 2019). Therefore, we generated *spr1-3 qual-1* and *cmu1 qual-1* double mutants, both of which exhibited significant epidermal cell peeling due to partial loss of cell adhesion (Figure 2.4.4, A to I). Introduction of the *qual-1* mutation strongly suppressed right-handed root skewing in the *spr1-3* mutant and completely rescued left-handed root skewing in the *cmu1* mutant (Figure 2.4.4J). Notably, suppression of root skewing was not due to diminished torsion of epidermal cells (Figure 2.4.4K). In addition, cortical cell anisotropy was fully rescued in the *spr1-3 qual-1* double mutant (Figure 2.4.4L). Thus, the integrity of the epidermis and its adhesion to the cortex is required for root twisting and epidermal control of cortical cell morphology. Cell adhesion might enable coordinated growth of root tissue through mechanical coupling of cell layers and/or by facilitating the movement of proteins and small molecules through plasmodesmata.

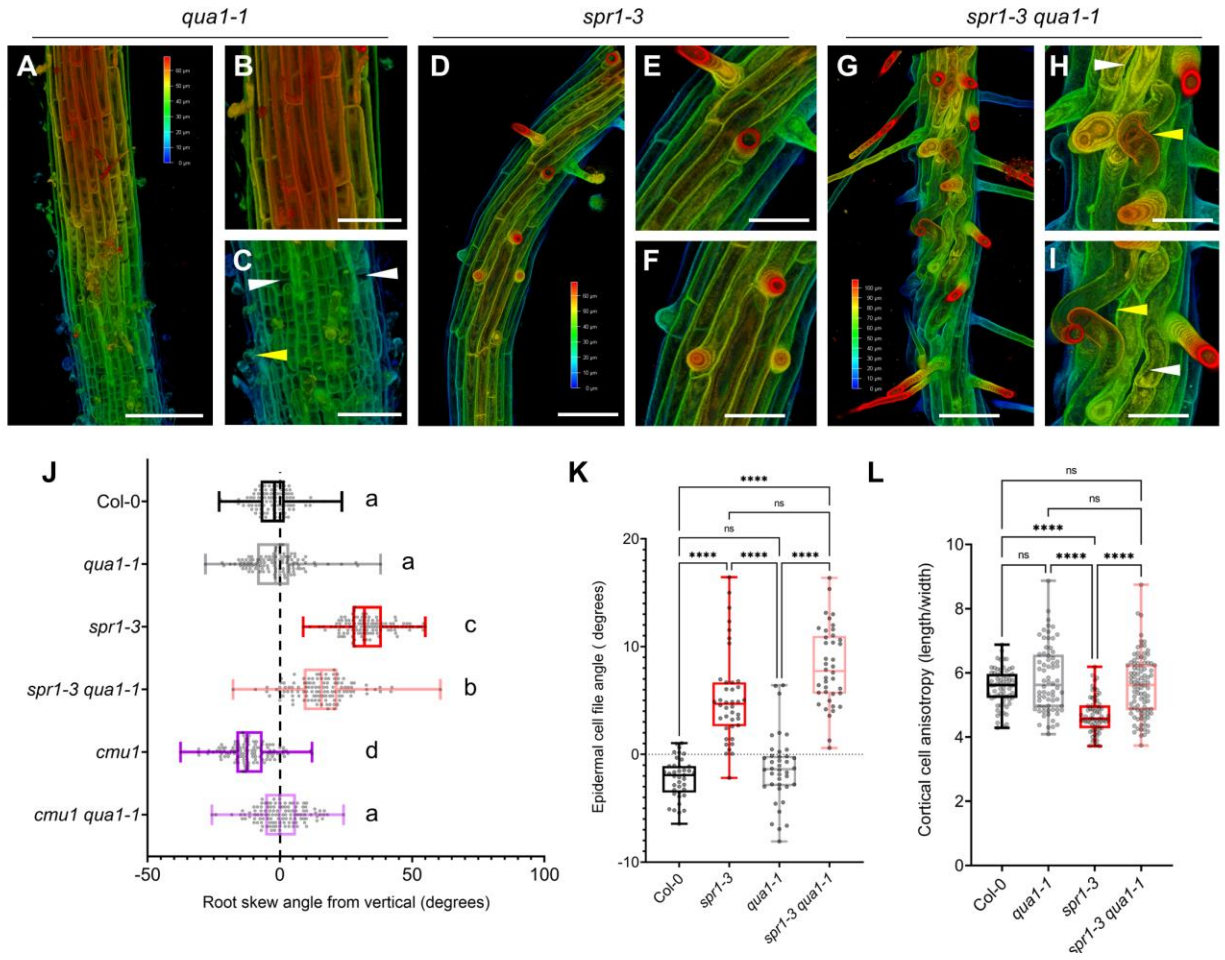


Figure 2.4.4. Cell adhesion is required for twisted growth of *spr1-3* and *cmu1* mutant roots. (A, D, G) Maximum projection, depth-coded confocal images of propidium iodide-stained roots. Color bar represents distance in the z-direction. Scale bar = 100 μ m. (B, C, E, F, H, I) Closeup images of impaired epidermal cell adhesion. Scale bar = 50 μ m. White and yellow arrowheads point to partial and near-complete loss of cell adhesion, respectively. (J) Root skewing angle of 3-day-old seedlings grown vertically on agar medium. Positive and negative angles indicate rightward and leftward root growth, respectively. Plots show mean \pm SD, $n = 112, 116, 116, 116, 115$, and 119 roots for Col-0, *qua1-1*, *spr1-3*, *spr1-3 qua1-1*, *cmu1*, and *cmu1 qua1-1*, respectively. (K) Epidermal cell file angle of 3-day-old seedlings grown vertically on agar medium. In the *qua1-1* and *spr1-3 qua1-1* roots, only intact epidermal cells were measured. Plots show mean \pm SD, $n = 39, 40, 40$, and 40 roots for Col-0, *spr1-3*, *qua1-1*, and *spr1-3 qua1-1*, respectively. (L) Anisotropy (length/width ratio) of cortical cells with lengths between 100-150 μ m in the differentiation zone. Plots show mean \pm SD, $n = 69, 68, 67$, and 96 cells for Col-0, *qua1-1*, *spr1-3*, and *spr1-3 qua1-1*, respectively. Statistics in J-L represent Kruskal-Wallis test with a Dunn's multiple comparison test ($P < 0.05$); **** $P < 0.0001$, ns = not significant.

2.4.3 Skewed Microtubules and Cell Morphology Precedes Cell File Twisting

Since the epidermis drives directional root growth, we wanted to compare the morphology and growth of epidermal cells between wild-type and twisted mutants. For this purpose, we introduced *p35S::GFP-LTI6b*, a plasma membrane marker that delineates the cell periphery (Cutler et al., 2000; Sassi et al., 2014), into wild-type Col-0 and *spr1-3* plants. We focused on cell geometry in the elongation zone since tilted microtubule arrays (Figure 2.6.2) are first detectable in this region of the root. Unlike the symmetric cells in Col-0 roots, *spr1-3* cells had a right-handed skewed morphology as demonstrated by the ratio of end wall angles (Figure 2.4.5, A and B). In addition, the left lateral wall was longer than the right lateral wall in the *spr1-3* mutant compared to Col-0 (Figure 2.4.5C), probably due to their asymmetric growth in *spr1-3* (Figure 2.4.5D). As the orientation of cortical microtubules directs cellulose deposition (Baskin, 2005), the skewed morphology of *spr1-3* cells is likely attributed to a skewed material anisotropy of the cell wall constraining cell growth.

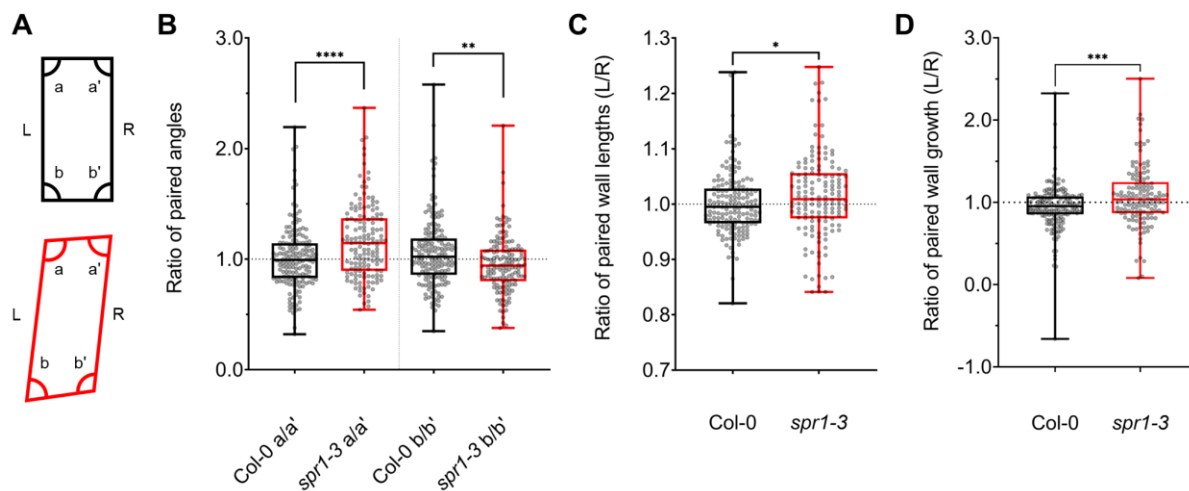


Figure 2.4.5. Cortical microtubule and cell skewing precedes twisted growth in the *spr1-3* mutant. (A) Cell morphometry model denoting paired end-wall angles (a and a', b and b') and paired lateral wall lengths (L and R) in root elongation zone cells. (B) Ratio of paired end-wall angles. Plots show mean \pm SD, n = 164 and 147 cells for Col-0 and *spr1-3*, respectively. (C) Ratio of paired wall lengths. Plots show mean \pm SD, n = 164 and 147 cells for

Col-0 and *spr1-3*, respectively. (D) Ratio of paired wall growth rates over the course of 2 hours. Plots show mean \pm SD, $n = 165$ and 137 cells for Col-0 and *spr1-3*, respectively. Statistics in B-D represent unpaired Mann-Whitney test between genotypes; * $P < 0.05$; ** $P < 0.01$; *** $P < 0.001$; **** $P < 0.0001$.

2.4.4 Cell File Twisting and a Heterogeneous Mechanical Environment Together Promote Root Skewing

In stark contrast to skewed roots when growth on the surface of an agar medium, *spr1-3* and *cmu1* roots are straight when grown within the agar medium (Figure 2.4.6, A and B), even though epidermal cells are similarly skewed under both conditions (Figure 2.4.6C). Thus, cell file twisting is not sufficient to generate skewed roots. When grown in soil, *spr1-3* and *cmu1* roots once again showed skewed growth (Figure 2.6.3). Together, these data indicate that a heterogeneous growth environment is essential for the skewed root phenotype.

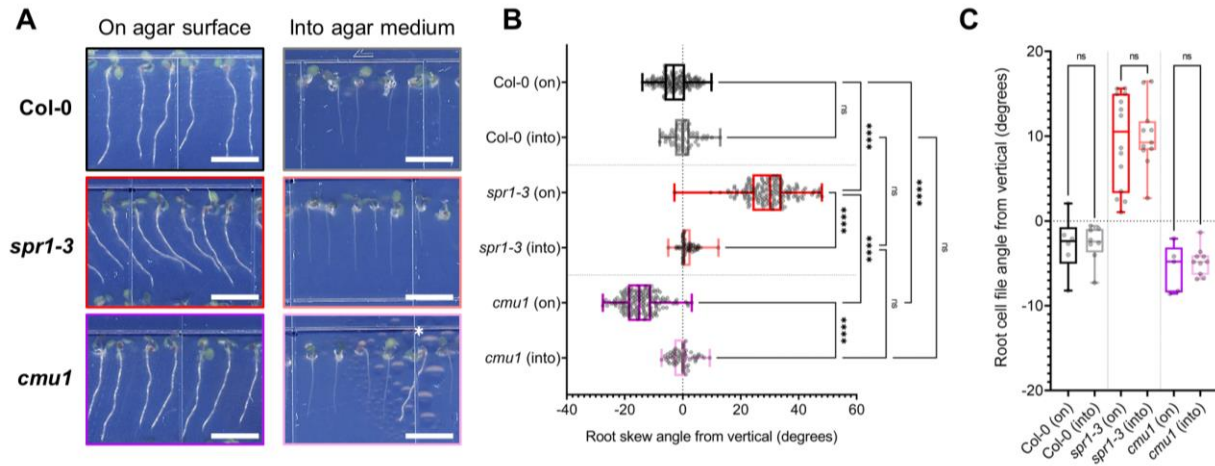


Figure 2.4.6. Root twisting requires a heterogeneous environment. (A) Representative images of 3-day-old seedlings grown vertically on or into 1% agar medium. Scale bar = 0.5 cm. Asterisk denotes seedling that did not penetrate agar during growth. (B) Root skewing angle of 3-day-old seedlings grown vertically on or into 1% agar medium. Plots show mean \pm SD, $n = 159$, 163 , and 159 roots for Col-0, *spr1-3*, and *cmu1* seedlings grown on agar, respectively. Plots show mean \pm SD, $n = 62$, 68 , and 63 roots for Col-0, *spr1-3*, and *cmu1* grown inside of agar, respectively. Positive and negative angles indicate rightward and leftward root growth, respectively. Statistics represent Kruskal-Wallis test with a Dunn's multiple comparison test; **** $P < 0.0001$, ns = not significant. (C) Cell file angles of 3-day-old seedlings grown vertically on or into 1% agar medium. Plots show mean \pm SD, $n = 6$, 14 , and 5 roots for Col-0, *spr1-3*, and *cmu1* seedlings grown on agar, respectively. Plots show mean \pm SD, $n = 8$, 11 , and 11 roots for Col-0, *spr1-3*, and *cmu1* grown inside of agar, respectively; ns = not significant.

To determine the mechanistic origin of root skewing, we imaged the interaction of roots with the surface of an agar medium. We observed that root hairs on the left side of *spr1-3* roots contacted the agar surface more frequently than on the right side, whereas wild-type and *cmu1* roots did not show laterally biased root hair-agar interactions (Figure 2.6.4, A to D). To test whether biased root hair-agar interaction is functionally significant, we crossed the *spr1-6* mutant, whose roots skew similar to *spr1-3* (Figure 2.6.1A), with *cpc try*, a root hairless mutant (Kirik et al., 2004). We found that the hairless roots of the *spr1-6 cpc try* triple mutant skew to the same degree as the hirsute *spr1-6* roots (Figure 2.6.4E), demonstrating that root hairs are dispensable for skewed root growth.

2.5 Discussion

This work provides strong experimental evidence in support of the epidermal-growth-control theory proposed for embryonic and adult stem elongation (Kutschera & Niklas, 2007), and demonstrates that the epidermis also plays a dominant role in controlling the growth of roots. In a cylindrical object like a plant root, resistance to torque and bending scales as the fourth power of the radius from the center axis. Thus, the epidermis as the outermost cell layer should have the highest contribution to twisted growth. Arabidopsis roots are minimalistic and contain a single cortical cell layer, unlike other plants which commonly possess multiple cortical layers. Whether the epidermal control of growth applies to roots containing multiple cortical cell layers remains to be determined.

Our results offer a new perspective on the wide prevalence of twisted growth in the plant kingdom. Rather than requiring a null mutation to produce twisted growth, our results suggest that modulation of gene expression in the epidermis alone is sufficient to generate a helical growth habitat at the organ level. The ability to fine-tune the direction of root growth might be

particularly advantageous in soil which is highly heterogeneous in terms of its mechanical microenvironment and water and nutrient availability. Recently, Yu et al. showed that phosphorylation of SPIRAL2-LIKE (SP2L), a microtubule-associated protein and close homolog of SPIRAL2 (Y. Fan et al., 2018; Shoji et al., 2004), mediates cortical microtubule reorientation in the root transition zone to produce twisted cell expansion during halotropism (Yu et al., 2022). Similarly, salt stress causes right-handed root skewing in *Arabidopsis* (C. Wang et al., 2007), which is associated with rapid proteasome-dependent degradation of SPR1 and restructuring of cortical microtubule arrays (Shoji et al., 2004; C. Wang et al., 2007; S. Wang et al., 2011). Thus, plants might dynamically regulate microtubule-associated genes and/or proteins in the epidermis to promote root twisting as part of hydrotropism and halotropism. Inducing twisted growth might also aid in soil penetration and growth past obstacles, akin to circumnutation of the root tip enhancing root exploration (I. Taylor et al., 2021). On the other hand, constitutive cell file twisting is likely detrimental for root mechanoresponse as demonstrated by the inability of the *spr1* mutant to maintain straight root growth trajectory in a mechanically heterogeneous environment.

2.6 Supplementary Information

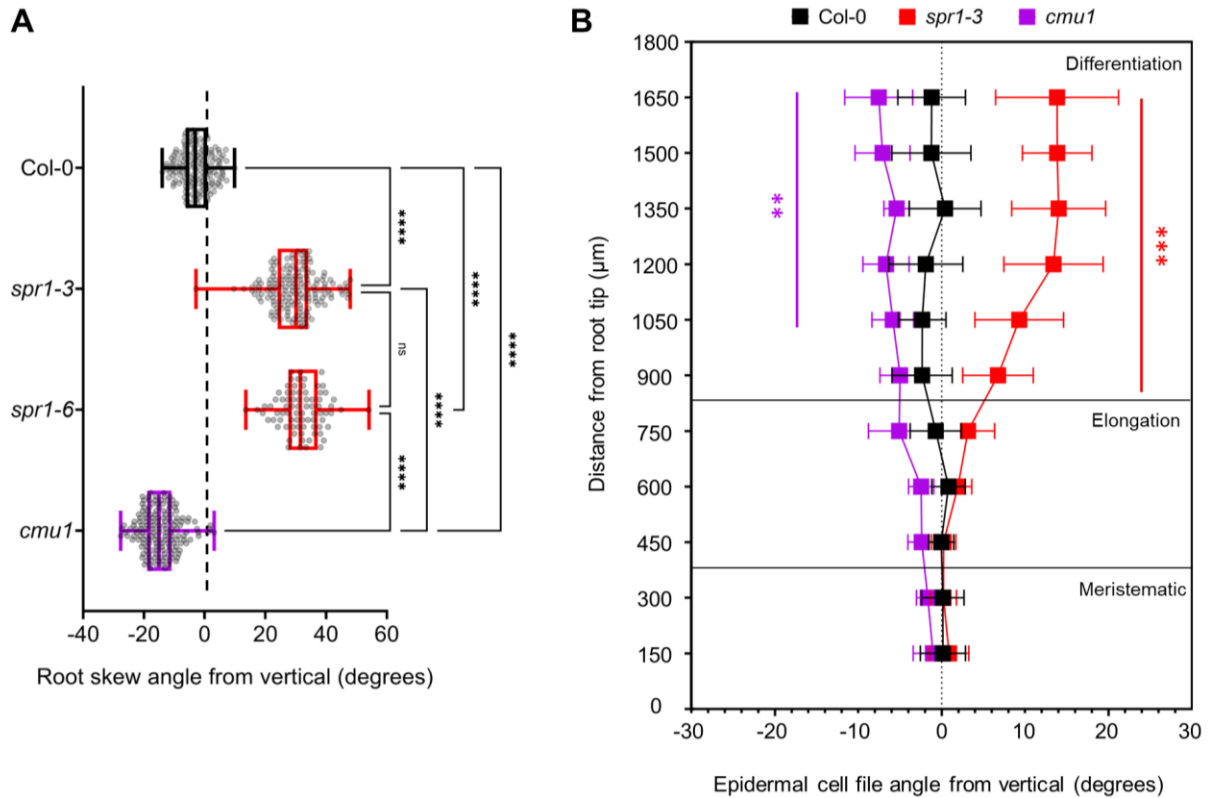


Figure 2.6.1. *spr1* and *cmu1* roots skew with opposing chirality. (A) Root skewing angle of 3-day-old seedlings grown vertically on agar medium. Positive and negative angles indicate rightward and leftward root growth, respectively. Plots show mean \pm SD, $n = 159, 163, 79, 159$ roots for Col-0, *spr1-3*, *spr1-6*, and *cmu1* respectively. Data reproduced from Figure 6B. Statistics represent Kruskal-Wallis test with a Dunn's multiple comparison test; **** $P < 0.0001$, ns = not significant. (B) Epidermal cell file angles of propidium iodide-stained Col-0, *spr1-3*, and *cmu1* seedlings ($n = 12$), grown vertically for 3 days on agar medium prior to imaging. Cell file angles were measured in 150 μm intervals from root tip. Positive and negative angles indicate right-handed and left-handed cell file twisting, respectively. Statistics represent unpaired T-test between *spr1-3* and Col-0 (red asterisks) and *cmu1* and Col-0 (purple asterisks); ** $P < 0.01$; *** $P < 0.001$

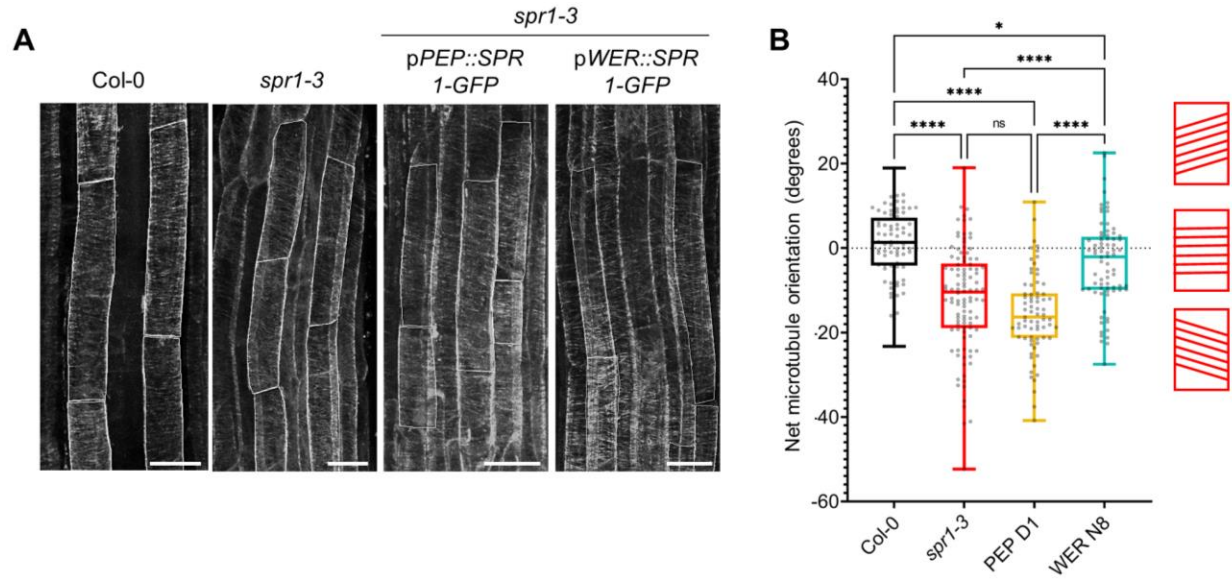


Figure 2.6.2. Epidermal complementation of the *spr1-3* mutant restores transverse microtubule orientation. (A) Maximum projection confocal images of root epidermal cells from p35S::RFP-TUB6 expressing seedlings grown vertically for 3 days on agar medium. Scale bar = 25 μ m. Cells outlined in white were used to measure the net microtubule orientation using the FibrilTool plugin. (B) Net microtubule orientation in epidermal cells of the root elongation zone. Positive and negative angles represent right- and left-handed microtubule orientation, respectively, matching the icons on the right. Plots represent mean \pm SD, n = 81, 106, 73, and 77 cells for Col-0, *spr1-3*, PEP D1, and WER N8, respectively; * P < 0.05, **** P < 0.0001, ns = not significant.

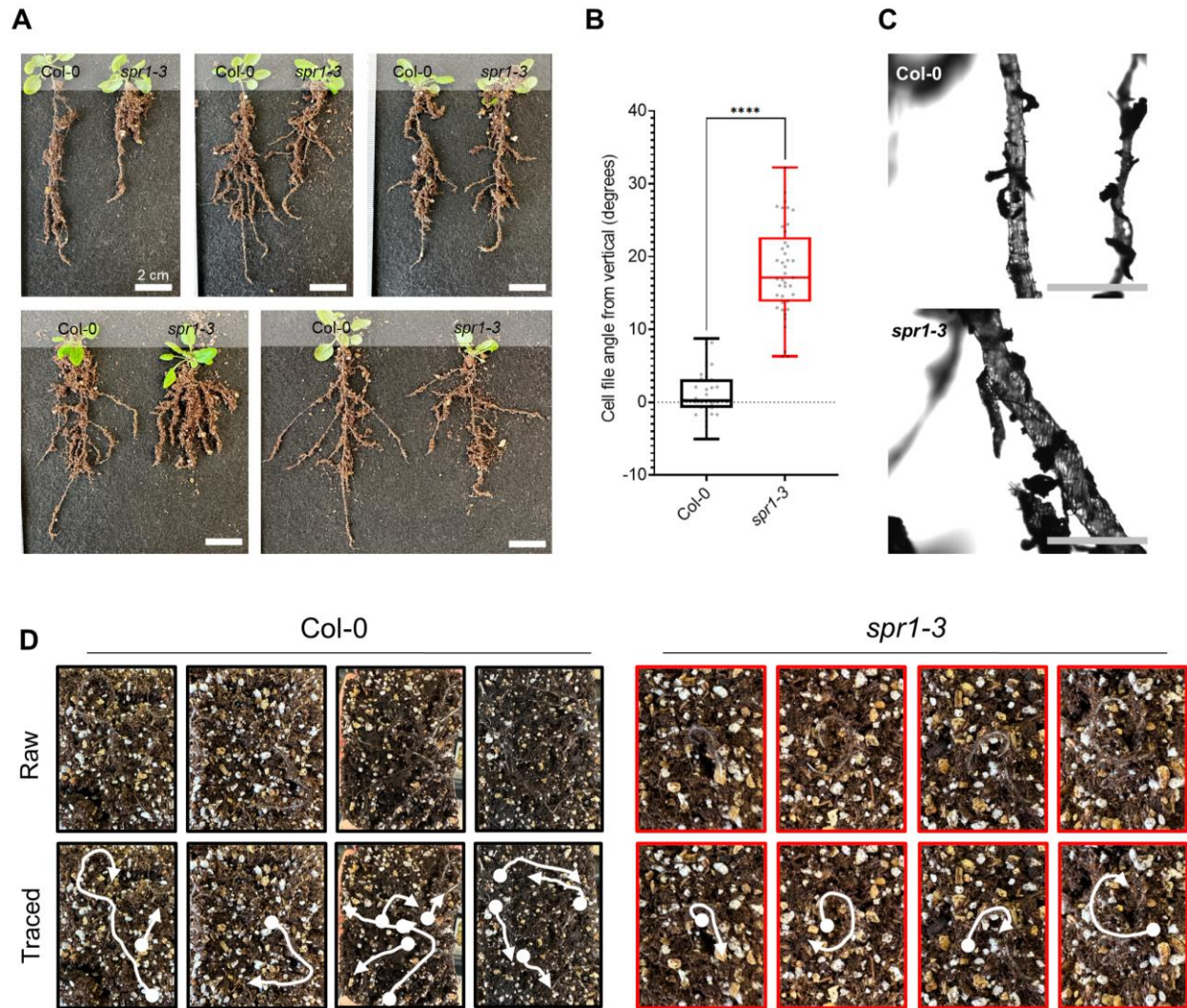


Figure 2.6.3. Soil-grown *spr1-3* roots maintain skewed cell files. (A) 3-week-old seedlings removed from soil pots and laid flat on black felt. Roots were spread out as much as possible. *spr1-3* roots consistently curled at the tips. The directionality of curl depended on how roots were laid and thus handedness was not assigned. Scale bar = 1 cm. (B) Cell file angles of mature Col-0 and *spr1-3* roots. Plots show mean \pm SD, $n = 37$ and 41 for Col-0 and *spr1-3*, respectively. Statistics represent unpaired t-test; **** $P < 0.0001$. (C) Representative raw images of cell file twisting in soil-grown roots. Scale bar = $500\ \mu\text{m}$. (D) Col-0 roots follow a random growth pattern along the base of the pot, whereas *spr1-3* roots follow a clockwise growth pattern. Line end symbols represent the start of the root exiting the soil (circle) and the root tip (arrowhead).

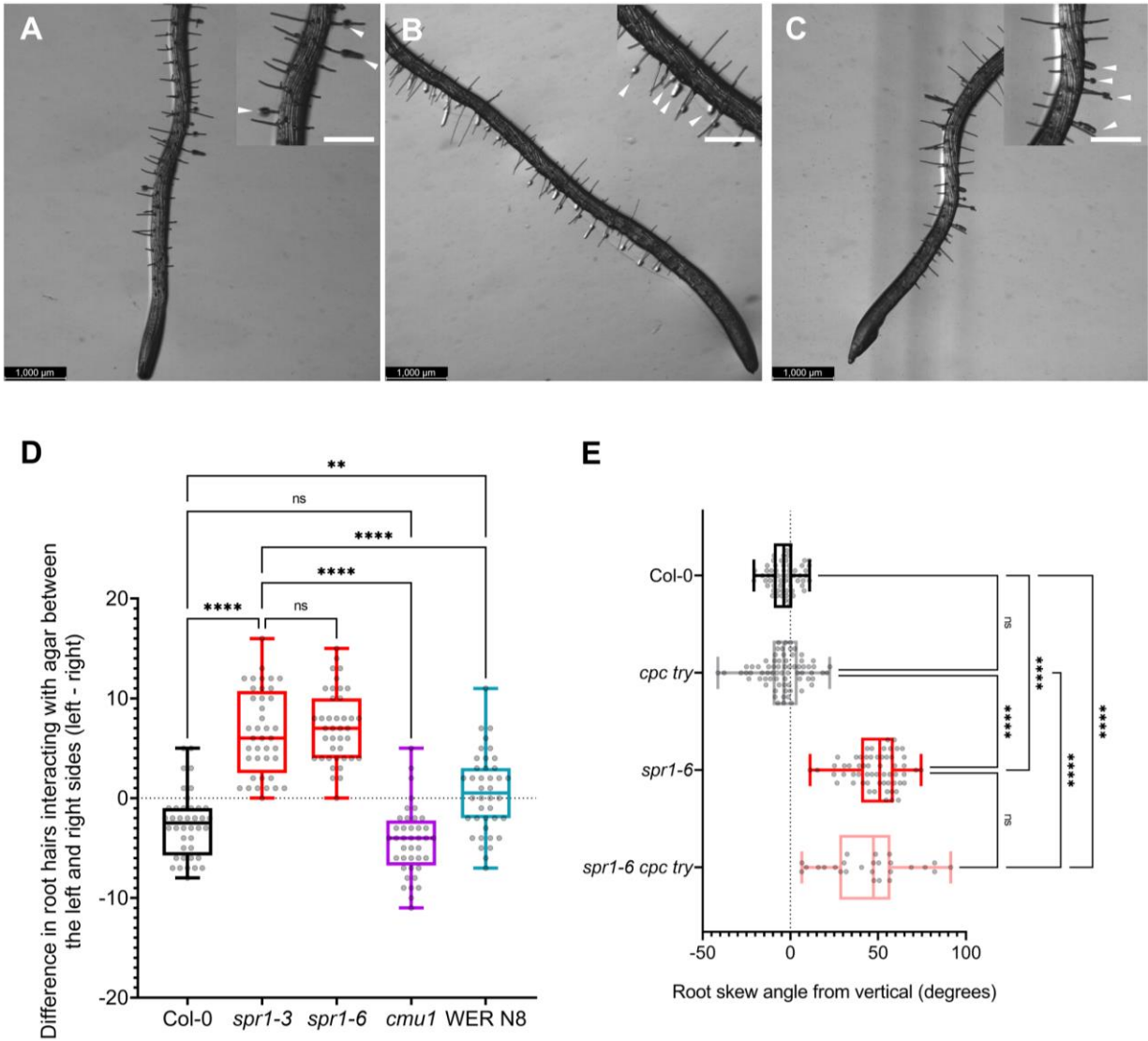


Figure 2.6.4. Biased root hair-agar interaction in *spr1* mutant does not contribute to skewed root growth. (A-C) Representative images of 3-day-old Col-0 (A), *spr1-3* (B), and *cmu1* (C) seedlings grown on top of agar. Change in light reflection shows root hair-agar contact sites. Root hair-agar interactions are denoted with a white arrowhead. Scale bar = 500 μm . (D) Total number of left-side (L) versus right-side (R) agar-interacting root hairs. Plots show mean \pm SD, $n = 40$ roots for each genotype. Statistics represent unpaired Mann-Whitney t-test; **** $P < 0.0001$; ns = not significant. (E) Root skewing angle of 3-day-old seedlings grown vertically on agar medium. Positive and negative angles indicate rightward and leftward root growth, respectively. Plots show mean \pm SD, $n = 63, 71, 60$ and 26 roots for Col-0, *cpc try*, *spr1-6*, and *spr1-6 cpc try* roots, respectively. Statistics represent one-way ANOVA test with Tukey's multiple comparison test; **** $P < 0.0001$; ns = not significant.

Chapter 3: Twisted growth impairs

Arabidopsis root mechanoresponse

3.1 Abstract

The high complexity of the plant root system can be attributed to disparate growth patterns of individual roots, which must navigate various mechanostimuli while obtaining nutrients and water. Mutations targeting microtubules, which play a critical role in directing plant cell growth, can induce chiral root growth. Here, we show that the *Arabidopsis thaliana* *spiral1* mutant, which contains skewed cortical microtubules, exhibits fixed right-handed cell file twisting and skewed root growth in both primary and lateral roots. Similar to other Arabidopsis twisted mutants, we found that *spiral1* exhibits an abnormal growth response to plastic barriers, indicating that fixed twisted growth disrupts root mechanoresponse. Organ-level root skewing requires a heterogeneous external mechanical input, which can be achieved by growing seedlings on an agar substrate. To further understand how *spiral1* roots respond to changes in the mechanical environment, we increased the stiffness of the agar medium and found that *spiral1* root growth directionality was unstable, switching from right- to left-handed on stiffer agar. Right-handed cell file twisting, however, remained unchanged across growth conditions. Despite their important role in root anchorage, we found that root hairs on the epidermis are not required for reorienting *spiral1* roots on stiffer agar. Overall, this work provides new insights into the consequences of microtubule-based symmetry breaking for root mechanoresponse.

3.2 Introduction

Vascular plants, including all major crops, build extensive root systems that are vital for nutrient acquisition, water uptake, and soil anchorage. These plants either have taproot or fibrous root systems below ground, with some plants forming adventitious roots above ground from other tissues (Bellini et al., 2014). The overall architecture of the root system largely depends on the soil environment, which is mechanically, chemically, and biologically heterogeneous. Warmer temperatures associated with climate change are expected to significantly impact soil properties, posing a critical threat to agricultural practices across the globe (Seleiman et al., 2021). For example, warmer temperatures will enhance water evaporation in the soil's top layer, which houses at least 50% of root tissue in crops (J. Fan et al., 2016). There is growing interest in modifying the root system architecture to aid in crop adaptation to climate change (B. Li et al., 2022; Lynch, 2018). Kirkegaard et al. showed that increased root growth in wheat enables deeper soil penetration for greater water uptake and improved grain yield (Kirkegaard et al., 2007). Similarly, Ogura et al. showed that genetically-modified *Arabidopsis* plants with altered auxin signaling grew deeper roots and were more drought-resistant (Ogura et al., 2019). Genetically modifying or selecting root systems that can dig deeper will likely be an advantageous farming strategy for crop production in expectedly warmer future climate conditions.

For roots to dig deeper, they must be able to successfully grow through compact soil and navigate around obstacles such as rocks. Plants are exposed to a variety of mechanical stimuli ('mechanostimuli'), from wind to sound vibration, and respond and adapt accordingly during development (Monshausen & Gilroy, 2009). In the soil environment, roots use touch response (i.e., thigmotropism) to avoid obstacles such as rocks (Braam, 2005), a process facilitated by auxin signaling (H.-J. Lee et al., 2020). Since mechanostimuli can vary across millimeter-scale

distances in the soil, generating a desired root system to support healthy crop growth is contingent upon engineering root development at this scale. *Arabidopsis thaliana* ('Arabidopsis') roots, given their simple architecture and accessibility to microscopy, are well-suited as a model to study how mechanical inputs direct root growth (Scheres & Wolkenfelt, 1998).

Arabidopsis has been extensively used for assessing root mechanoresponse, including thigmotropism (H.-J. Lee et al., 2020; Massa & Gilroy, 2003; K. Okada & Shimura, 1990; Tanaka et al., 2006) and gravitropism (Blancaflor, 2015; Durham Brooks et al., 2010; Simmons et al., 1995; Y. Zhang & Friml, 2020). In the lab, growth on top of agar medium is a mechanically heterogeneous environment known to enhance root skewing in twisted mutants (Oliva & Dunand, 2007; Rutherford & Masson, 1996; Schultz et al., 2017; Simmons et al., 1995), and this input is required for generating skewed root growth in the *spr1-3* mutant (Chapter 2) (Furutani et al., 2000). A well-characterized root growth mechanoresponse is barrier avoidance, during which the root tip forms a step-like structure and reorients growth around the barrier (Massa & Gilroy, 2003). The right-handed twisted mutant, *calmodulin-like 24* (*cml24*), has a defective barrier response (Y. Wang et al., 2011), suggesting that fixed twisted growth may be disadvantageous in mechanically heterogeneous environments. Here, we show that the right-handed *spr1-3* mutant exhibits twisted growth at the root system level and has a defective barrier response similar to *cml24*. In addition, we demonstrate that *spr1-3* root growth trajectory is highly sensitive to the stiffness of the agar medium compared to wild-type, with robust straight root growth. Despite their role in root anchorage, root hairs are not essential for guiding root growth directionality. Thus, twisted growth influences the development and mechanoresponsiveness of roots.

3.3 Materials and Methods

3.3.1 Plant Growth Conditions

All *Arabidopsis thaliana* plants used in this study are listed in Table 3.3.1. For all plant growth experiments, seeds were surface-sterilized using a 25% bleach solution, resuspended in 0.1% agarose, and stratified at 4°C for 2 days. Sterilized seeds were grown vertically on agar medium containing 1% w/v Phytoblend agar (Caisson Labs), 0.3% w/v sucrose, and half-strength Murashige and Skoog basal medium (Caisson Labs), pH 5.7. under 16/8-h light/dark photoperiod ($120 \mu\text{mol m}^{-2} \text{sec}^{-1}$ light intensity) at 24°C.

Table 3.3.1. *Arabidopsis thaliana* lines used in Chapter 3.

Line Name	Description	Source
Col-0	Wild-type background	N/A
<i>spr1-3</i> (At2g03680)	<i>spr1</i> null mutant (fast-neutron mutagenized)	Furutani et. al., 2000
<i>spr1-6</i> (At2g03680)	<i>spr1</i> null mutant (T-DNA insert)	Sedbrook et. al, 2004
<i>wer</i> (At5g14750)	<i>werewolf</i> null mutant (T-DNA insert)	SALK_044925
<i>spr1-6 wer</i>	<i>spr1 wer</i> double null mutant	This study
<i>cpc try</i> (At2g46410, At5g53200)	<i>cpc try</i> double null mutant	ABRC: CS66489
<i>spr1-6 cpc try</i>	<i>spr1 cpc try</i> triple null mutant	This study

3.3.2 Agar Gradient Assay

Arabidopsis seeds were surface sterilized and stratified as stated in Section 3.3.1 and plated on agar growth medium containing either 1%, 3%, or 5% Phytoblend agar (Caisson Labs). Seedlings were grown vertically in conditions stated in Section 3.3.1 and imaged at 3 days of

growth from the front-side of the plate using a stereo dissecting light microscope (Leica) to image cell files and scanned at 300 DPI (Canoscan 4400F scanner) to image whole roots. Organ-level root skewing was measured from vertical (0 degrees) using FIJI (Schindelin et al., 2012). FIJI was also used to measure cell file angles in the differentiation zone, relative to the orientation of the primary root. Statistical analysis and graph generation were performed using GraphPad Prism software.

3.4 Results

3.4.1 Root Skewing is Present at the Root System Level in the *spr1-3* Mutant

We previously showed that in a mechanically-heterogeneous environment, skewed epidermal cell growth propagates macroscopically to cause chiral bending of the primary root of the Arabidopsis *spr1-3* mutant (Chapter 2). However, whether the microtubule-based right-handed helical growth of epidermal cells affects the entire root system of *spr1-3* plants has not been examined.

When grown on top of an agar medium, the lateral roots of the *spr1-3* mutant exhibit skewed growth at the organ and cell file levels, similar to primary roots, indicating that twisted growth is a root system phenotype (Figure 3.4.1A, Figure 3.6.1). While *spr1-3* lateral roots that emerge from the left and right sides of the primary root eventually adopt similar rightward skewing angles, the initial emergence and tip angles of lateral roots are strikingly different between the two sides. Lateral roots forming on the left side of *spr1-3* roots show significantly greater emergence angles compared to Col-0 roots, whereas lateral roots forming on the right side of *spr1-3* roots show significantly lower emergence angles compared to Col-0 roots (Figure 3.4.1A). In Col-0 plants, lateral root tips on both sides of the primary root start off at an angle of

about 50° and gradually reorient vertically due to gravitropism (Figure 3.4.1B, C). In contrast, in *spr1-3* plants, left-side lateral roots start out growing nearly vertically and adopt a rightward bend over time (Figure 3.4.1B). Conversely, right-side lateral roots of the *spr1-3* mutant start nearly parallel to the primary root and continue to maintain the rightward growth trajectory (Figure 3.4.1C).

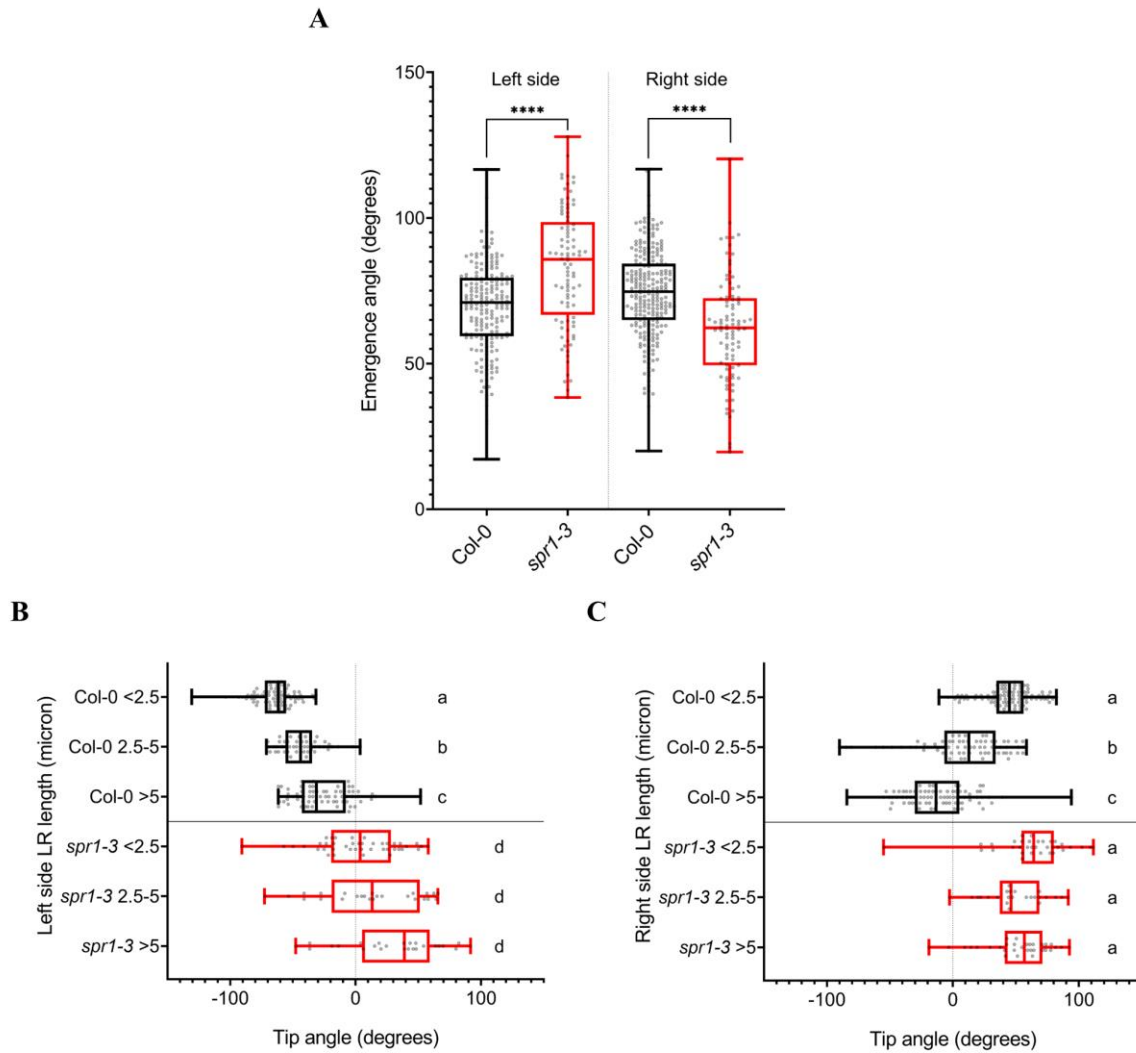


Figure 3.4.1. The spatial orientation of lateral roots in *spr1-3* affects root emergence and tip angles. (A) Lateral root (LR) emergence angles in Col-0 and *spr1-3* 11-day-old seedlings grown vertically on agar medium. For each genotype, LRs were grouped based on spatial orientation on the left or right side of the primary root. Plots show mean \pm SD, n = 201, 92, 243, and 90 for Col-0 left side, *spr1-3* left side, Col-0 right side, and *spr1-3* right side,

respectively. Statistics represent unpaired Mann-Whitney t-tests; **** $P < 0.0001$. (B, C) LR tip angles, relative to vertical (0 degrees) oriented to the left (B) or right (C) sides of primary roots in Col-0 and *spr1-3* 11-day-old seedlings grown vertically on agar medium. LRs were groups based on LR length of less than 2.5 μm , between 2.5 and 5 μm , and greater than 5 μm . For B, plots show mean \pm SD, $n = 75, 54, 72, 42, 25$, and 25 LRs for Col-0 < 2.5 , Col-0 2.5-5, Col-0 > 5 , *spr1-3* < 2.5 , *spr1-3* 2.5-5, and *spr1-3* > 5 , respectively. For C, plots show mean \pm SD, $n = 94, 70, 79, 34, 24$, and 32 LRs for Col-0 < 2.5 , Col-0 2.5-5, Col-0 > 5 , *spr1-3* < 2.5 , *spr1-3* 2.5-5, and *spr1-3* > 5 , respectively. For B and C, Statistics represent Kruskal-Wallis test with Dunn's multiple comparison test ($P < 0.05$).

3.4.2 Stiffness of the Agar Medium Affects Organ-Level Directional Root Growth in the *spr1-3* Mutant

Twisted mutants, such as *cml24*, have been previously shown to have defective root mechano-response, as assessed by their inability to sense and avoid glass coverslip barriers in their growth path (Y. Wang et al., 2011). To examine how *spr1-3* roots respond to obstacles, we placed hard plastic barriers in the path of growing *spr1-3* roots. Unlike wild-type roots which show a characteristic bend upon encountering the barrier, *spr1-3* roots flatten along the barrier (Figure 3.6.2), similar to the barrier avoidance response of the *cml24* mutant (Y. Wang et al., 2011). *spr1-3* roots that hit the flat barrier consistently grow rightward (data not shown), a response that resembles the clockwise growth trajectory of *spr1-3* roots that hit the base of the plant pot, as described in Chapter 2 (Figure 2.6.3D).

The above data motivated us to test whether the stiffness of the growth medium affects the growth trajectory of *spr1-3* roots. For this experiment, we grew seedlings on media containing either 1%, 3%, or 5% agar. Increasing agar concentration increased the shear modulus, or the force tangential to the root surface, of the growth medium from 1.33×10^3 Pa (1% agar), 1.52×10^4 Pa (3% agar), to 2.16×10^4 Pa (5% agar). While Col-0 roots grew relatively straight on all three types of media, *spr1-3* roots switched from right-handed to left-handed skewing as shear modulus increased (Figure 3.4.2A, B). To determine whether this root response is potentially due to osmotic stress caused by increasing agar concentration (Verger et

al., 2018, 2019), seedlings were grown on 1% agar medium containing different amounts of mannitol. 100 mM mannitol did not affect the growth angle of Col-0 and *spr1-3* roots. In the presence of 200 mM and 300 mM mannitol, Col-0 roots changed growth direction slightly, however, the rightward skew of *spr1-3* roots was not significantly affected (Figure 3.6.3). Based on these data, we conclude that mechanical cues (due to increasing shear modulus) and not osmotic stress are responsible for changing the growth direction of *spr1-3* roots with increasing agar concentration. We found that while *spr1-3* roots grow rightward, straight, and leftward on 1%, 3%, and 5% agar media, respectively, the root epidermal cell files showed similar right-handed skewing under all three conditions (Figure 3.4.2C). Thus, the increased shear force of the agar medium can uncouple cell file twisting from directional root growth in the *spr1-3* mutant.

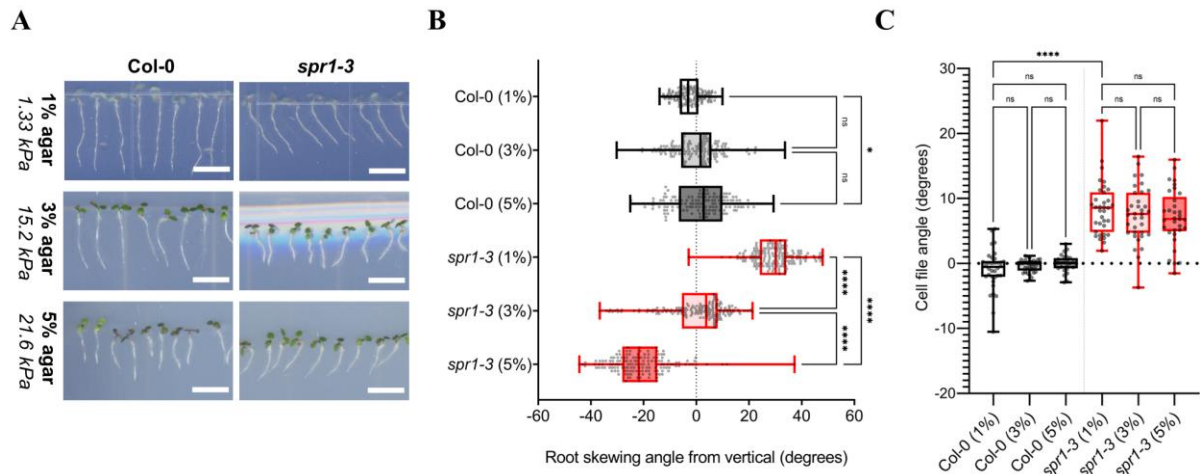
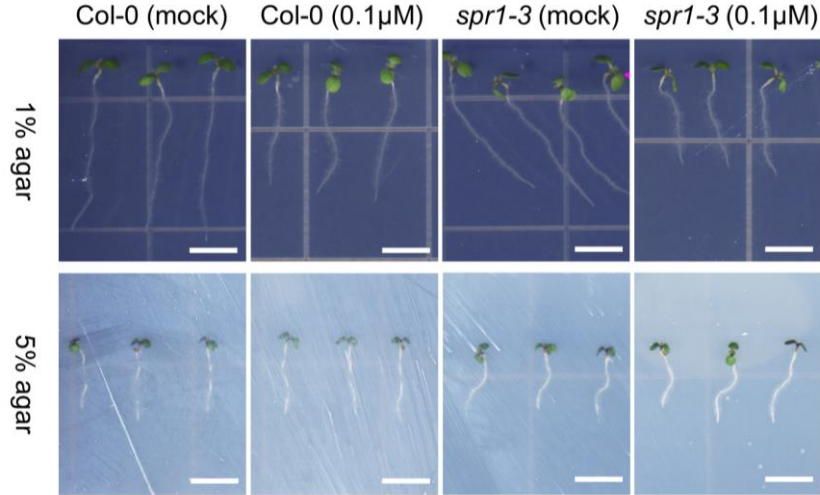


Figure 3.4.2. *spr1-3* root skewing shifts from right- to left-handed on agar with increasing shear modulus. (A) Representative images of Col-0 and *spr1-3* seedlings on each agar type. Scale bar = 0.5 cm. kPa = kilopascals. (B) Root skewing angle, relative to vertical (0 degrees) of Col-0 and *spr1-3* 3-day-old seedlings grown vertically on agar medium with increasing agar concentration. Plots show mean \pm SD, $n = 159, 159, 157, 163, 160,$ and 154 roots for Col-0 1%, Col-0 3%, Col-0 5%, *spr1-3* 1%, *spr1-3* 3%, and *spr1-3* 5%, respectively. Statistics represent Kruskal-Wallis test with a Dunn's multiple comparison test; $*P < 0.05$, $****P < 0.0001$, ns = not significant. (C) Average cell file angle from vertical measured at the basal differentiation zone. Statistics represent Kruskal-Wallis test with a Dunn's multiple comparison test; $*P < 0.05$, $****P < 0.0001$, ns = not significant.

3.4.3 ACC-induced Root Hair Production Straightens *spr1-3* Mutant Roots on 1% Agar

Previously, we showed that while root hairs interact with the agar surface in a biased fashion in the *spr1-3* mutant, root hair-agar interaction is not required for generating skewed root growth (Chapter 2). However, given that root hairs function to anchor the root (Bailey et al., 2002; Bengough et al., 2016), we wanted to investigate if root hairs influenced *spr1-3* root skewing under conditions of increased mechanical force from the growth medium. We hypothesized that increased root hair production would stabilize root skewing in the *spr1-3* mutant. To test this hypothesis, we treated Col-0 and *spr1-3* seedlings grown on 1% or 5% agar with 0.1 μ M 1-aminocyclopropane-1-carboxylic acid (ACC). ACC is a soluble ethylene precursor that induces ectopic root hair production from atrichoblast cell files and enhances root hair growth (Shibata & Sugimoto, 2019). We found that in the presence of ACC, *spr1-3* roots were hairier and significantly straighter on both 1% and 5% agar (Figure 3.4.3A). However, ACC also caused both Col-0 and *spr1-3* roots to be stunted even on 1% agar (Figure 3.4.3B), consistent with the inhibition of root growth by ethylene (Růžicka et al., 2007). While these results point to a potential role of root hairs in stabilizing root directional growth, the impact of ACC on root growth may be indirectly affecting root mechanoresponse.

A



B

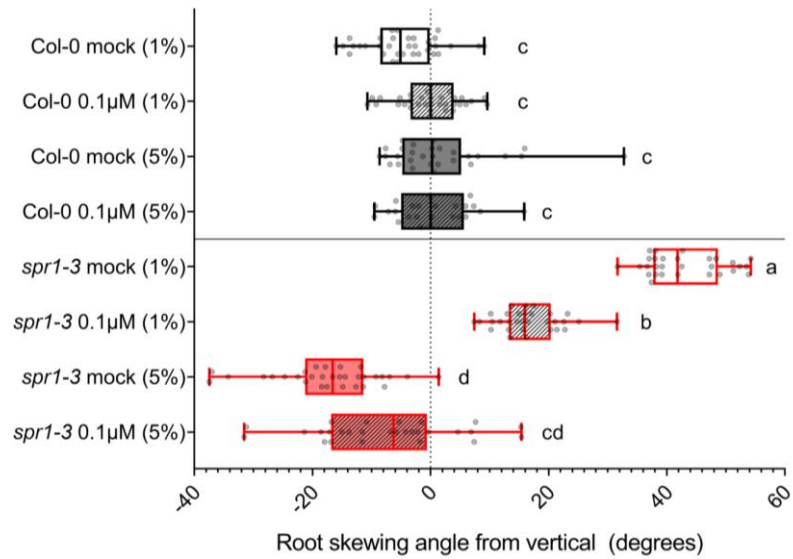


Figure 3.4.3. Hairy *spr1-3* roots induced by exogenous ACC treatment affect root mechanoresponse. (A) Representative images of Col-0 and *spr1-3* seedlings for each treatment type. Scale bar = 0.5 cm. (B) Root skewing angle, relative to vertical (0 degrees) of Col-0 and *spr1-3* 5-day-old seedlings grown vertically on agar medium with increasing agar concentration and in the presence or absence of ACC. Plots show mean \pm SD, $n = 34, 33, 29, 24, 29, 31, 31,$ and 28 roots for Col-0 mock (1%), Col-0 0.1 μM (1%), Col-0 mock (5%), Col-0 0.1 μM (5%), *spr1-3* mock (1%), *spr1-3* 0.1 μM (1%), *spr1-3* mock (5%), and *spr1-3* 0.1 μM (5%), respectively. Statistics represent Kruskal-Wallis test with a Dunn's multiple comparison test ($P < 0.05$).

3.4.3 Root Hairs are Not necessary for Root Skewing in the *spr1* Mutant

To avoid unwanted effects of ACC on root growth, we used a genetic approach to directly assess the effect of root hairs on root mechanoresponse. We generated *spr1* lines without root hairs by crossing the T-DNA insertion allele, *spr1-6*, with the hairless double mutant, *caprice (cpc) tryptichon (try)* (Kirik et al., 2004). We also crossed *spr1-6* with *werewolf (wer)* to produce a *spr1-6 wer* double mutant which has increased root hair production (M. M. Lee & Schiefelbein, 1999). When grown on media containing either 1% or 5% agar, the *wer* single mutant and *cpc try* double mutant roots grew straight, similar to wild-type roots. In contrast, the *spr1-6*, *spr1-6 wer*, and *spr1-6 cpc try* mutants all showed similar rightward skew on 1% agar and essentially straight growth on 5% agar (Figure 3.4.4). Interestingly, 5% agar promoted root hair elongation in all genotypes, except *cpc try* and *spr1-6 cpc try* (Figure 3.4.4). Taken together, these results demonstrate that root hairs are dispensable for influencing the directional growth of roots in response to increased shear force from the substrate. Furthermore, redirecting root directional growth only requires interactions between the epidermis and the surrounding substrate.

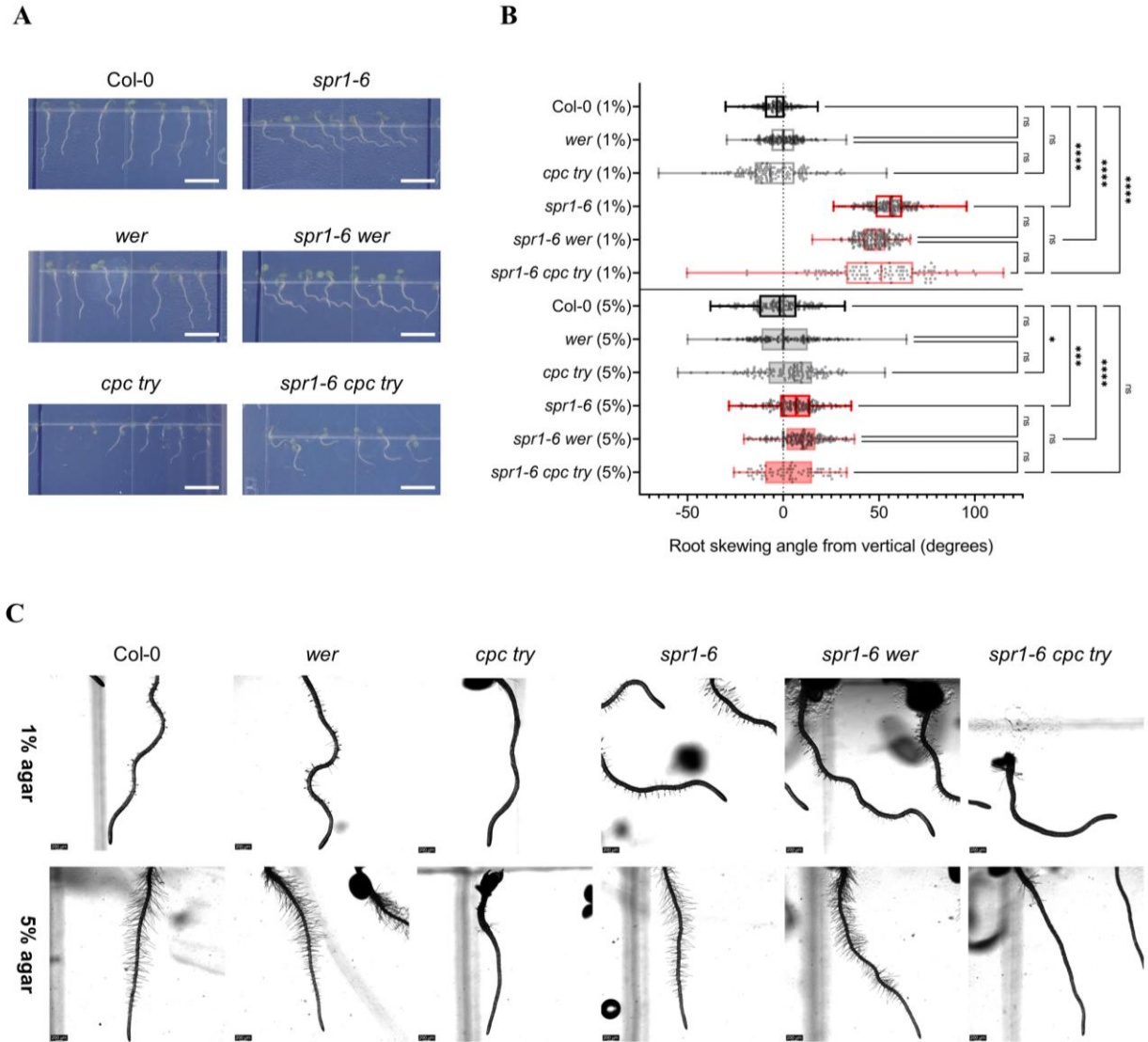


Figure 3.4.4. Root hairs are not required for reorientation of *spr1-6* root skewing in response to increased shear modulus. (A) Representative images of seedlings grown on 1% agar plates. Scale bar = 0.5 cm. (B) Root skewing angle, relative to vertical (0 degrees) of 3-day-old seedlings grown vertically on agar medium with increased agar concentration (1% versus 5%). Plots show mean \pm SD, $n = 176, 183, 133, 178, 182, 102, 177, 187, 120, 182, 186$, and 73 roots for Col-0 1%, *wer* 1%, *cpc try* 1%, *spr1-6* 1%, *spr1-6 wer* 1%, *spr1-6 cpc try* 1%, Col-0 5%, *wer* 5%, *cpc try* 5%, *spr1-6* 5%, *spr1-6 wer* 5%, and *spr1-6 cpc try* 5%, respectively. Statistics represent Kruskal-Wallis test with a Dunn's multiple comparison test; **** $P < 0.0001$, ns = not significant. (C) Close-up images of seedlings on 1% or 5% agar. Scale bar = 200 μ m.

3.5 Discussion

Helical movement, or circumnutation, plays an important role in root exploration through mechanically heterogeneous environments, such as soil (Del Dottore et al., 2017; I. Taylor et al., 2021). Using the Arabidopsis twisted mutant, *spr1*, our findings demonstrate that microtubule-based chiral root growth impairs root mechanoresponse. In Chapter 2, we showed that *spr1-3* roots that hit the base of the pot always grow in a clockwise pattern, whereas wild-type Col-0 root growth trajectory was randomized. This result resembles the coiling defect seen in the rice *histidine kinase-1* mutant, which has defective circumnutation and a reduced capacity for surface exploration (I. Taylor et al., 2021), but the *spr1-3* mutant is not likely defective in circumnutation as these roots still wave (Simmons et al., 1995). Fixed handedness in the *spr1* mutant may restrict the variability in directional growth response that may be important for exploring the soil or responding to disparate environmental forces. Supporting this, here we show that while the growth trajectory of wild-type roots is robust to changing shear modulus of the growth medium, the growth trajectory of *spr1-3* roots is highly sensitive to increased shear modulus. Surprisingly, the increased sensitivity of the *spr1-3* roots to their mechanical environment occurs without any change in the epidermal cell file angle. Future work will address the relationship of twisted growth in *spr1-3* to the mechanics of differential root bending.

We found that increased agar stiffness induced root hair elongation in all genotypes except the hairless mutants (*cpc try* and *spr1-6 cpc try*). This phenomenon may be an adaptive response to promote root adhesion to the agar surface since root hairs play an important role in root anchorage (Bengough et al., 2016). Consistent with this idea, seedlings grown on stiffer agar tended to fall off (data not shown), which occurred more frequently in the hairless mutants. Nonetheless, we show that root hairs are not required for *spr1* root straightening on stiff agar,

further supporting the finding in Chapter 2 that root hairs do not play a role in guiding root directional growth.

We show that wild-type roots remained relatively straight along the gravity vector despite changes in shear force from the substrate. It is unclear whether the maintenance of straight growth is advantageous in a highly heterogeneous mechanical environment, such as soil. Recent work from Yu et al. shows that microtubules reorient in the root elongation zone to generate helical growth in wild-type roots as a mechanism to avoid salt stress (Yu et al., 2022). Perhaps the ability to turn on and off helical growth in roots is advantageous for navigating the complex soil environment. To better assess the benefits and drawbacks of twisted growth, it will be important to analyze *spr1* root system development in 3-D agar gels with varying mechanical properties and in soil. Future work should employ advanced imaging technology developed in recent decades, such as computed tomography and X-ray imaging (Tollner et al., 1994; Downie et al., 2015; Piñeros et al., 2016; Topp et al., 2016; Jiang et al., 2019; Atkinson et al., 2019).

3.6 Supplementary Information

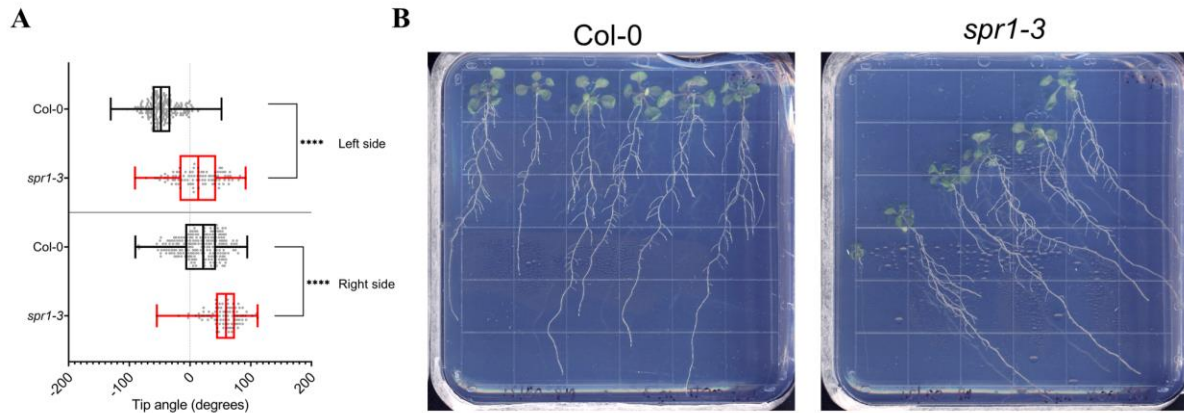


Figure 3.6.1. LRs skew rightward in *spr1-3* seedlings. (A) Average LR tip angle from vertical on the left and right sides of Col-0 and *spr1-3* primary roots, measured at 11 days post germination. Plots show mean \pm SD, $n = 201, 92, 243$, and 90 LR for Col-0 left side, *spr1-3* left side, Col-0 right side, and *spr1-3* right side, respectively, across 15-20 seedlings for each genotype. Statistics represent Kruskal-Wallis test with a Dunn's multiple comparison test; $***P < 0.0001$, ns = not significant. (B) Representative raw images of seedlings used for LR morphometry were imaged from behind the plate and digitally flipped along the horizontal axis. *spr1-3* seeds were plated along an angle to prevent roots from touching during growth.

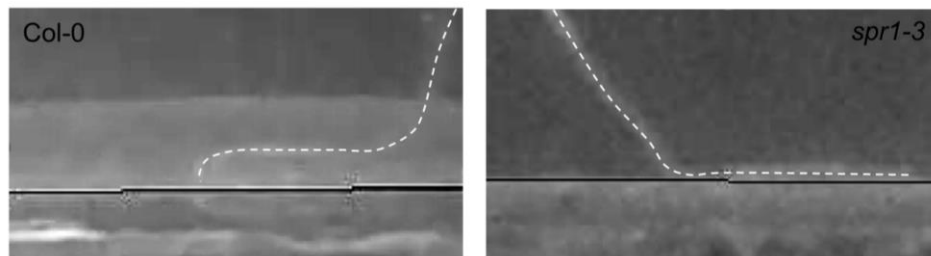


Figure 3.6.2. *spr1-3* roots flatten along plastic barriers during growth. Col-0 and *spr1-3* seeds were germinated on vertical plates in Raspberry Pi imaging devices, and at four days of growth, a plastic barrier was inserted a few millimeters below the roots. Root growth was imaged once per hour for 24 hours.

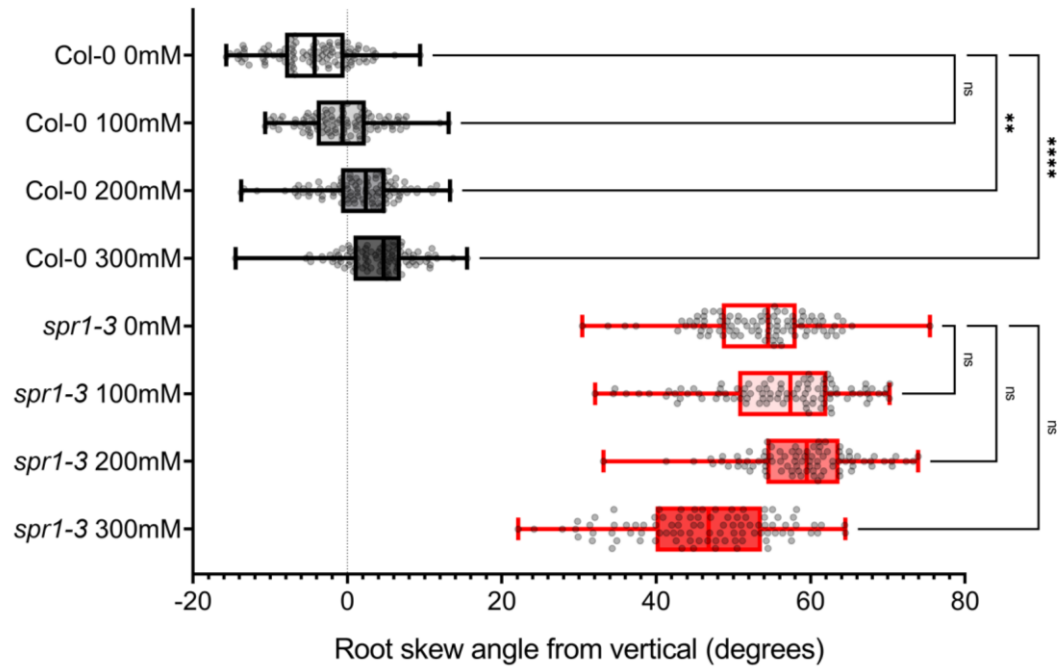


Figure 3.6.3. Root skewing in the *spr1-3* mutant is unaffected by increasing osmotic stress. Root skewing angle, relative to vertical (0 degrees) of 3-day-old seedlings grown vertically on agar medium containing up to 300 mM of mannitol. Plots show mean \pm SD, $n = 96, 99, 98, 93, 94, 96, 89,$ and 94 roots for Col-0 0 mM, Col-0 100 mM, Col-0 200 mM, Col-0 300 mM, *spr1-3* 0 mM, *spr1-3* 100 mM, *spr1-3* 200 mM, and *spr1-3* 300 mM, respectively. Statistics represent Kruskal-Wallis test with a Dunn's multiple comparison test; **** $P < 0.0001$, ns = not significant.

Chapter 4: Correlated mechanochemical maps of Arabidopsis primary cell walls using atomic force microscope-infrared spectroscopy¹

4.1 Abstract

Spatial heterogeneity in the composition and organization of the primary cell wall affects its mechanics to generate cell shape. However, directly correlating cell wall composition, organization, and mechanics has been challenging. To overcome this barrier, we applied atomic force microscopy coupled with infrared spectroscopy (AFM-IR) to generate spatially correlated maps of paraformaldehyde-fixed, intact *Arabidopsis thaliana* epidermal cell wall mechanical and chemical properties. AFM-IR spectra were deconvoluted by non-negative matrix factorization (NMF) into a linear combination of IR spectral factors representing sets of chemical groups comprising different cell wall components. This approach enables the quantification of chemical composition from IR spectral signatures and visualization of chemical heterogeneity at nanometer resolution. Cross-correlation analysis of the spatial distribution of NMFs and mechanical properties suggests that the carbohydrate composition of cell wall junctions correlates with increased local stiffness. Together, our work establishes a new methodology to use AFM-IR for the mechanochemical analysis of intact plant cell walls.

¹ This chapter has been adapted from Bilkey et al., 2022 (Bilkey et al., 2022).

4.2 Introduction

Cell walls are a defining feature of plant cells and play a critical role in protecting plants against environmental stress, providing structural support, and determining the direction of growth. All plant cells have an extensible primary cell wall, which forms first and underlies cell growth and morphogenesis. Certain cell types, such as tracheids and fiber cells in the vasculature of the plant, develop a thick and non-extensible secondary cell wall during their differentiation. The primary cell wall consists of polysaccharides such as cellulose, hemicellulose, and pectin, along with some proteins (Cosgrove, 2005; Lampugnani et al., 2018). Cells control the synthesis and deposition of individual cell wall components to modulate the composition of the cell wall. Spatial heterogeneity in cell wall composition is particularly important in defining the mechanical properties of the wall (Cosgrove, 2018; Grones et al., 2019; Majda et al., 2017; Phyto et al., 2017).

Cellulose is a linear polymer of β -1,4-linked glucose (Glc) that forms microfibrils that resist tensile stress and control the axis of turgor-driven cell expansion (Cosgrove, 2018). Cellulose microfibrils are believed to be mechanically coupled to each other at sites called ‘biomechanical hotspots’ where hemicelluloses, such as xyloglucan (XG), are thought to form tight linkages between microfibrils (Cosgrove, 2014; Park & Cosgrove, 2012). XG is the major hemicellulose in primary cell walls of *Arabidopsis thaliana* and other eudicots (Park & Cosgrove, 2015) that consists of a β -1,4-Glc backbone substituted at regular positions with α -D-xylose (Xyl). The Xyl monomers in XG are further substituted with β -D-galactose (Gal) and α -L-fucose (Fuc). Another hemicellulose found in the primary cell walls of *A. thaliana* is glucuronoarabinoxylans (GAX), which consists of a β -1,4-xylose monomer backbone with sidechains of α -D-arabinose (Ara) and/or α -D-glucuronic acid (GlcA) monomers (Zabackis et

al., 1995). The cellulose microfibrils and hemicellulose network is surrounded by a hydrophilic pectin matrix that aids in cell wall extensibility, strength, and porosity (Atmodjo et al., 2013; Cosgrove, 2014; Mohnen, 2008; Willats et al., 2001). Pectin is a highly branched polymer consisting of anionic sugars such as α -D-galacturonic acid (GalA) and can undergo reversible methyl esterification to modulate cell wall elasticity (Höfte et al., 2012; Peaucelle et al., 2015). The main pectin in *A. thaliana* includes homogalacturonan (HGA), rhamnogalacturonan I (RG-I), and rhamnogalacturonan II (RG-II). Adjacent cells are adhered to each other via a pectin-rich middle lamella that is important for maintaining the structural integrity of plants (Bouton et al., 2002; Daher & Braybrook, 2015). Approximately 10% of the mass of the plant primary cell wall is comprised of enzymes and structural proteins. Some structural proteins, such as arabinogalactan proteins (AGPs) (Jamet et al., 2006), are glycosylated by oligosaccharides composed mainly of neutral sugars and a small number of GlcA monomers.

A variety of techniques have been developed to spatially visualize plant cell wall composition. For example, metabolic labeling with an alkynylated fucose analog is used to fluorescently label the location of rhamnogalacturonan pectin in the cell wall (Anderson et al., 2012; Anderson & Wallace, 2012). Fluorescent dyes, such as propidium iodide and Pontamine fast scarlet 4SB, are used to stain and image the location of homogalacturonan pectin and cellulose, respectively (Anderson et al., 2010; Rounds et al., 2011; Thomas et al., 2013). Since these methods enable live imaging, they reveal real-time spatial locations and concentrations of specific wall components. However, these methods require labeling and typically focus on one cell wall epitope or component at a time.

Spectroscopy has been used as a label-free method to spatially analyze the cell wall composition of plant cells and tissues. For example, IR and Raman spectroscopy, which detect

molecular vibrations via light absorption and inelastic scattering of photons, respectively, have enabled chemical imaging of plant cell walls and other biological materials (Baker et al., 2014; Gierlinger, 2014, 2017). Fourier-transform infrared spectroscopy (FTIR) and attenuated total reflection (ATR)-FTIR microspectroscopy methods have been used to map cellulose- and lignin-rich regions in *Populus* wood cell walls (Canteri et al., 2019; Cuello et al., 2020; Gierlinger, 2017). Confocal Raman microspectroscopy has also been used to map cellulose and lignin-rich regions in multiple plant types (Agarwal, 2006; Gierlinger, 2014, 2017; Gierlinger & Schwanninger, 2006; Prats Mateu et al., 2016; Schmidt et al., 2010). While these label-free techniques can simultaneously detect multiple cell wall components, they cannot offer insights into how these cell wall components correlate with cell wall mechanical properties (e.g., stiffness).

Atomic force microscopy (AFM) is a label-free method that can surpass the visible-light diffraction limit to visualize cell wall topography and mechanical properties at the nanoscale (T. Zhang et al., 2016). However, AFM does not directly provide chemical information, and cell wall composition can only be indirectly inferred from mechanical information and/or through changes in mechanical properties following treatments that degrade specific cell wall components or linkages (Marga et al., 2005; T. Zhang et al., 2016, 2017, 2019). AFM coupled with IR (AFM-IR) is an emerging technique to perform nanoscale multimodal imaging of physical, chemical, and mechanical material features (Dazzi et al., 2005; Dazzi & Prater, 2017; Kurouski et al., 2020). This technique has been primarily used to generate correlated mechano-chemical maps of polymer composites, films, fibers, and blends (Centrone, 2015; Dazzi & Prater, 2017). AFM-IR uses a tunable IR laser focused on the sample at the AFM tip. When the wavelength of the IR laser matches the excitation wavelength of the sample beneath the AFM

tip, the sample absorbs the IR energy and undergoes thermal expansion which is detected by the AFM tip in contact with the sample surface. This can provide chemical images at selected IR wavelengths with nanoscale spatial resolution. Recently, AFM-IR has been used to image biological specimens such as triacylglycerol-containing vesicles from bacteria, yeast, and microalga (Dazzi & Prater, 2017), extracellular vesicles from animal stem cells (Kim et al., 2018), bone (Gourion-Arsiquaud et al., 2014), and breast cancer cells (Clède et al., 2013; Dazzi & Prater, 2017). In plants, the application of AFM-IR has so far has been limited to secondary cell walls (Farahi et al., 2017; Tetard et al., 2010, 2011, 2012, 2015).

In this work, we establish a new methodology for applying AFM-IR to simultaneously measure the mechanical and chemical properties of the primary cell wall of *A. thaliana* epidermal cells. We provide a sample preparation technique suited for AFM-IR on *A. thaliana* stem sections, which eliminates chemical contamination. Since many plant cell wall components have overlapping spectral features and because IR spectral imaging creates large and complex datasets, we applied non-negative matrix factorization (NMF) to reduce the dimensionality of the AFM-IR data into a more manageable number of components (Borodinov et al., 2019; Montcuquet et al., 2010). These non-negative matrix factors were used to identify the IR spectral features representing different cell wall components. By correlating the spatial distribution of chemical groups with nanomechanical properties, this study reveals how the spatial variation in cell wall composition relates to the spatial variation in cell wall mechanics.

4.3 Materials and Methods

4.3.1 Sample Preparation

Arabidopsis thaliana ecotype Columbia-0 (Col-0) plants were grown under continuous light conditions ($120 \mu\text{Em}^{-2}\text{s}^{-1}$) for six weeks. Apical regions of inflorescence stems were sectioned and fixed overnight with 3% paraformaldehyde solution in phosphate buffered saline (PBS, 1.4 M NaCl, 1 mM KCl, 100 mM Na_2PO_4 , 18 mM KH_2PO_4 pH 7.4). Fixed stem pieces were placed in a cryomold box containing room temperature 10% low-melting deep-sea cold fish gelatin (Cat. No. G7041, Sigma, St. Louis, USA) in deionized water. Stems were flash frozen in liquid nitrogen while held upright. Frozen gelatin blocks were sectioned using a cryostat (CM1850, Leica Microsystems) at $10 \mu\text{m}$ thickness using a Leica 819 microtome blade (Leica Biosystems Nussloch GmbH, Germany), washed three times with deionized water, and then adhered to a zinc sulfide block and dried overnight in the fume hood. Sections were stored at room temperature until imaging.

4.3.2 AFM-IR Measurement

IR spectral measurements were collected using a Nano-IR2-s instrument in contact resonance mode located at the Center for Nanophase Materials Sciences at Oak Ridge National Laboratory. Analysis Studio software (Bruker Corporation, Billerica, MA) monitored IR absorbance at wavenumber regions of 922-1170, 1301-1410, and 1504-1720 cm^{-1} . Soft IR probes with a nominal spring constant of 0.04 N/m were used. The phase-locked loop (PLL) frequency was tuned to 60 kHz and the laser spot was optimized to the AFM tip with the largest IR absorption at 1030 cm^{-1} . Scans for topography, PLL frequency, phase shift, lateral deflection, and deflection were first collected over a large $25 \times 25 \mu\text{m}^2$ region on epidermal cells at a scan

rate of 0.5 Hz with a resolution of 128×128 pixel points and 8 co-averages in contact resonance mode. Within this region, the same scan types were then collected over a small $3 \times 3 \mu\text{m}^2$ region at a scan rate of 0.2 Hz with a resolution of 256×256 pixel points and 8 co-averages. A 30×30 IR array was collected in the small region with 4 co-averages and a spectral resolution of 1 cm^{-1} .

4.3.3 NMF and Cross-Correlation with Phase Shift

NMF analysis was conducted using factors varying in number from two to six to determine the optimal number of NMF factors, in part, based on cophenetic correlation coefficients and residual sum of squares. Once the optimized number of NMF factors was determined, the NMF factor spectra (loading) and factor distribution coefficients (score) were exported. The solved NMF factor spectra were compared to the FTIR spectra of the standards using principal component analysis (PCA). Then, NMF factor distribution maps were generated to visualize the factor spatial distribution. The phase shift map (originally 256×256 pixel points) collected on the $3 \times 3 \mu\text{m}^2$ region was reduced, by average data binning, to 30×30 pixel points, matching the NMF factor distribution map. Cross-correlation analysis between phase shift and the difference in NMF factor scores between factor 1 and sum of factors 2 and 3 was then performed similar to the protocol used in Borodinov et al., 2019.

4.4 Results and Discussion

4.4.1 AFM-IR Imaging of *A. thaliana* Epidermal Cell Walls

The spatial resolution and signal quality of AFM-IR images depends greatly on sample thickness and roughness (Pereira et al., 2018a). For example, in thick samples ($>1 \mu\text{m}$) of poor thermal conductivity, insufficient decay of thermal expansion with respect to scan rate can reduce spatial resolution and signal quality (Kurouski et al., 2020). Most AFM-IR studies have

involved spun-cast polymer thin films rather than complex biological specimens. As a result, our study required special considerations for sample preparation.

Resin embedding is a commonly used technique to obtain thin sections with well-preserved cellular structures (Verhertbruggen et al., 2017). However, epoxy resin has strong IR absorption in the $1720 - 922\text{ cm}^{-1}$ region, which would interfere with the IR signatures useful in our study (Coste et al., 2021; González et al., 2012; Pereira et al., 2018a). Therefore, paraformaldehyde (PFA) tissue fixation and low melting-temperature gelatin were used to embed apical portions of *A. thaliana* stems. A cryostat was then used to obtain cross sections from a frozen block of gelatin-embedded stem with controlled and uniform thickness ($\sim 10\text{ }\mu\text{m}$) and surface roughness ($< 100\text{ nm}$). This method resulted in sections that had intact epidermis, phloem, and xylem cells; but softer tissues, like the pith and cortex, were less well preserved (Figure 4.6.1A). AFM-IR imaging was conducted on the epidermal cell wall because the epidermis is composed of mostly primary cell walls (Cosgrove, 2018). Because sections were obtained perpendicular to the periclinal cell walls, the mechanical properties detected by AFM are unaffected by turgor pressure. PFA-fixed sections demonstrate minimal spectral difference from *A. thaliana* stem tissue that had undergone no sample preparation (Figure 4.6.2). Therefore, the sample preparation method devised here was suitable for generating plant stem sections for AFM-IR with no detectable spectral contamination.

Topographical (Figures 4.4.1A, B) and phase (Figure 4.4.1C) images obtained via contact resonance mode AFM imaging were used to locate an epidermal cell wall. The topographical map of a $25 \times 25\text{ }\mu\text{m}^2$ region shows the wall between two adjoining epidermal cells and corresponds to the AFM-IR image collected (Figure 4.4.1B). Phase images report the difference

in AFM cantilever drive and response oscillation that is sensitive to the surface stiffness and adhesion of the surface to the AFM tip (Ye & Zhao, 2010). Generally, softer samples result in a negative phase shift and stiffer samples result in a positive phase shift (Dong & Yu, 2003). Phase shift can be sensitive to cell wall composition and has been previously used to capture different cell wall ultrastructural features in young poplar stems (Farahi et al., 2017). Similarly, in the *A. thaliana* sample from this study, the phase map (Figure 4.4.1C) showed striations along the wall, presumably with regions of softer and stiffer material. The spatial variation in sample surface and subsurface properties indicated by phase shift can be attributed to spatial variation in cell wall mechanics and/or adhesion (Bidhendi & Geitmann, 2019), which are thought to be determined by wall composition and organization (Bidhendi et al., 2019; Bidhendi & Geitmann, 2019; Bou Daher et al., 2018; Cosgrove, 2018; Peaucelle et al., 2011). For example, streaks in the phase shift maps indicate regions where the tip goes from an attractive (stiff) to a repulsive (soft) material (Figure 4.4.1D-F).

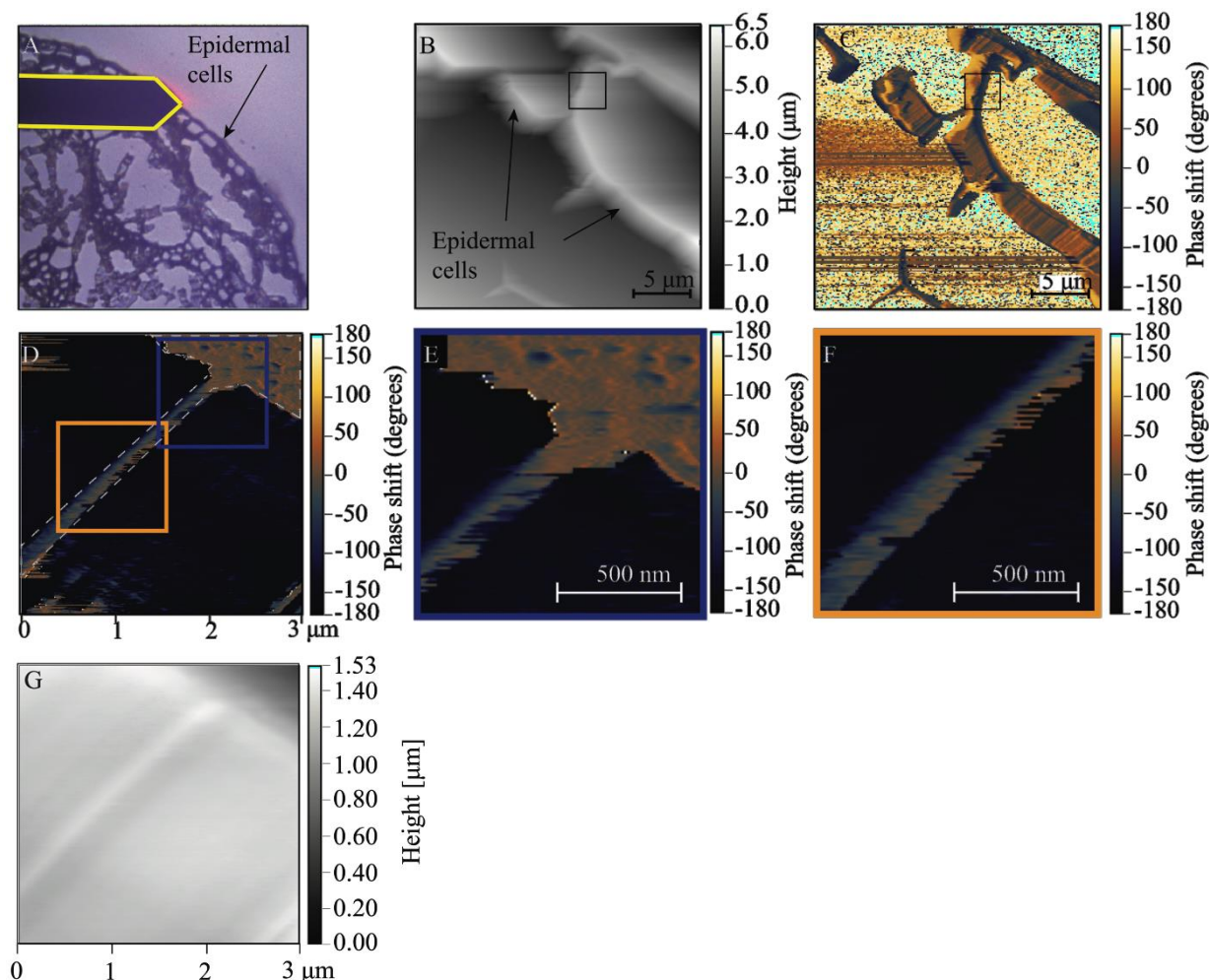


Figure 4.4.1. AFM-IR imaging of an epidermal cell wall in a PFA-fixed *A. thaliana* stem sample. (A) Image of sample region from the AFM camera. AFM cantilever tip is outlined in yellow. (B, C) Contact resonance mode AFM height image and phase shift map of the large scan region ($25 \times 25 \mu\text{m}^2$) showing epidermal cells. Positive shifts in phase indicates increasing sample stiffness. Black box represents where AFM-IR measurements (30×30 spectral array) were collected. Scale bar = $5 \mu\text{m}$. (D) Phase 2 map of the small scan region ($3 \times 3 \mu\text{m}^2$) where AFM-IR measurements were collected. White dashed line is outlining a region of increased stiffness at the junction between two epidermal cells. (E, F) Zoomed-in images of two regions of varying phase shift along cell-cell junction, indicated in D. Scale bar = 500 nm . (G) Height map was obtained of a $3 \times 3 \mu\text{m}^2$ region where AFM-IR data was collected.

Chemical information on a shared epidermal cell wall was acquired with a 30×30 array (900 AFM-IR pixel points or spectra) over a $3 \times 3 \mu\text{m}^2$ region, collecting a matrix of spectra every 100 nm in the x- and y-dimension (black square in Figures 4.4.1B, C). Although the spatial resolution of our AFM-IR acquisition could not be determined, it nonetheless offered multimodal

images to correlate cell wall chemical and mechanical properties. Within the scan region, images (256 × 256 pixel map over a 3 × 3 μm² region) were collected for phase shift (Figure 4.4.1D), height (Figure 4.4.1G), phase-locked loop (PLL) frequency (Figure 4.6.1B), and deflection (Figures 4.6.1C, E). Continuous adjustment in PLL frequency is necessary to maintain the resonance enhanced condition throughout the scan. Hence, PLL monitors changes in contact resonance frequency which occur due to changes in sample surface stiffness and adhesion (Stan & Soares, 2014). Deflection is a direct measure of cantilever-surface interaction force and is used to produce a three-dimensional image of the sample surface (Vadillo-Rodríguez et al., 2004). Based on Figure 4.4.1, the stiff portion of the wall, indicated by high positive phase shift, is outlined by a white dashed line (Figure 4.4.1D). This region appears slightly raised in the height map (Figure 4.4.1G), with more distinct three-dimensional structure in the deflection (Figure 4.6.1C) and lateral deflection (Figure 4.6.1D) maps. Based on the orientation of the sample, this region was determined to be the junction between the anticlinal cell walls of two epidermal cells. Figures 4.4.1E and 4.4.1F show enlarged phase shift images of the cell-cell junction, suggesting a stiffer boundary between the cells and softer regions on either side. This stiff cell-cell junction likely represents the middle lamella, a pectin-rich region that acts as a ‘glue’ between shared cell walls (Daher & Braybrook, 2015; Zamil & Geitmann, 2017). Previous work by Zamil et al. using a micro-stretching technique also found that the middle lamella between epidermal cells is significantly stronger than the rest of the cell wall (Zamil et al., 2014).

4.4.2 Determining the Spatial Variation in Primary Cell Wall Composition by AFM-IR

In our experiments, the available lasers for AFM-IR spectral acquisition were limited to a range of 922-1170, 1301-1410, and 1504-1720 cm⁻¹. All Fourier-transform infrared spectroscopy

(FTIR) and AFM-IR spectra in this study were pre-processed applying spectral smoothing, baseline correction, and normalization approaches (Gautam et al., 2015) (see Supporting Information and Figure 4.6.3). To ensure that spectra produced by AFM-IR are similar to those obtained by traditional FTIR, PCA was used to compare FTIR and AFM-IR spectra of carbohydrate standards obtained from plant primary cell walls. The results show that the FTIR and AFM-IR spectra of the carbohydrate standards are statistically indistinguishable (Figure 4.6.2). Therefore, the AFM-IR spectra accurately reflect cell wall IR response and chemistry.

The IR spectra of the primary cell wall is complex because the different polymeric components each have intricate chemical functionality. FTIR spectra of cell wall standards were used to establish IR band assignments to specific primary cell wall components. Commercially available XG, RG-I, cellulose, xylan, and polygalacturonic acid (PGA) samples extracted from various plant sources were used as representative examples of cellulose, pectin, and hemicellulose. Lignin was not included as a cell wall standard since it is not abundant in the epidermal cell walls of *A. thaliana* apical stems (C. Zhu et al., 2015). Further, imaging of lignin autofluorescence (Decou et al., 2017) demonstrated that there is essentially no lignin in the epidermis (Figure 4.6.4). FTIR spectra of each standard are shown in Figure 4.3.2A, and major IR bands observed for each cell wall standard are detailed in Table 4.6.1. To further facilitate interpretation of AFM-IR spectral data, FTIR spectra of *A. thaliana* primary cell wall reference fractions were obtained. Oxalate, 1 M KOH, and 4 M KOH extracts, were isolated from alcohol-insoluble residues generated from *A. thaliana* seedling by sequential extraction (Figure 4.6.5). Previously, Peralta et al. performed sequential extractions followed by glycome profiling on the apical section of an *A. thaliana* stem (Pattathil et al., 2012; Peralta et al., 2017). It was found that the oxalate extract was enriched in RG-I and AG epitopes (Peralta et al., 2017). Similarly, in this

study, the oxalate extract isolated from *A. thaliana* seedlings was found to consist mainly of Gal (39%), Ara (25%), and GalA (20%) residues (Table 4.6.2). In addition to carbohydrates, this extract also contained a significant amount of protein (see Table 4.6.3). Therefore, the oxalate extract, in this study, likely contains pectins, AGPs, and other cell wall proteins. Peralta et al. found that the subsequent carbonate and 1 M NaOH extracts were enriched in epitopes associated with xylans, HGA, RG-I, and AG (Peralta et al., 2017). In this study, the polysaccharides in the 1 M KOH extract were composed mainly of Xyl (35%), Ara (21%), Gal (20%), GalA (8%), and Glc (6%) residues (Table 4.6.2). The 1 M KOH extract also contains a significant amount of protein (Table 4.6.3). Therefore, the 1 M KOH extract, in this study, likely contains xylans, pectins, and cell wall proteins. Lastly, Peralta et al. reported that a 4 M NaOH extract was enriched in epitopes associated with non-fucosylated XGs, fucosylated XGs, and xylan (Peralta et al., 2017). In this study, the polysaccharides in the 4 M KOH extract were composed mainly of GalA (25%), Xyl (24%), Ara (14%), Gal (13%), and Glc (10%) residues (see Table 4.6.2). In addition, the 4 M KOH extract lacked significant amounts of protein (Table 4.6.3). This dataset suggests that the 4 M KOH extract, in this study, likely consists of XGs, pectins, and xylans.

The cellulose, xylan, and XG standards exhibit strong IR absorption between ~ 975 - 1170 cm^{-1} (Figure 4.4.2A). As shown in Table 4.4.1, these IR bands are related to: (1) sugar ring ether O-C-O, (2) primary and secondary alcohol C-O, and (3) glycosidic ether O-C-O stretching commonly observed in the neutral residues and polysaccharide linkages of cell wall carbohydrates. The oxalate, 1 M KOH, and 4 M KOH reference extracts, as well as the mean AFM-IR spectrum of the *A. thaliana* epidermal cell wall, also show strong IR absorption in the ~ 975 - 1170 cm^{-1} region (Figure 4.6.5 and Figure 4.4.2B), suggesting the presence of

carbohydrates. The mean *A. thaliana* AFM-IR spectrum contains prominent bands with peak maxima at: (1) 1310 cm^{-1} assigned to alcohol O-H bending and/or the amide III band; (2) 1380 cm^{-1} assigned to alcohol O-H bending, aliphatic C-H bending, and/or carboxylic acid symmetric stretching; (3) 1525 cm^{-1} assigned to the amine II band; and (4) 1670-1660 cm^{-1} assigned to adsorbed water O-H bending, carboxylic acid antisymmetric stretching, and/or the amine I band. Prominent IR bands at 1310, 1380, 1525, and 1657 cm^{-1} are also observed for the soy protein standard (Figure 4.4.2A), indicating the presence of cell wall proteins in the *A. thaliana* epidermal cell wall spectrum. While the oxalate, 1 M KOH, and 4 M KOH reference extracts also absorb at 1525 cm^{-1} (Figure 4.6.5), the relative absorption peak intensity at 1525 to 1075 cm^{-1} for the 4 M KOH reference extract is much lower than for oxalate and 1 M KOH reference extracts. The lower intensity in this region suggests that the 4 M KOH reference extract contains significantly less protein. Pectin cell wall standards (i.e., PGA and RG-I) show strong IR bands at ~1407 and 1604 cm^{-1} , which are assigned to carboxylic acid symmetric and antisymmetric stretching (Figure 4.4.2A). Although IR absorption at ~1407 and 1604 cm^{-1} is observed in the mean *A. thaliana* AFM-IR spectrum (Figure 4.4.2B) and in the oxalate, 1 M KOH, and 4 M KOH reference extracts (Figure 4.6.5), these bands overlap with the IR absorption of proteins, which makes resolving the presence of acidic sugars on pectin based on carboxylic acid functionality difficult. PCA analysis further specifies the extent of the chemical similarity between cell wall reference fractions, cell wall standards, and the *A. thaliana* epidermal cell wall regions (Figure 4.6.6).

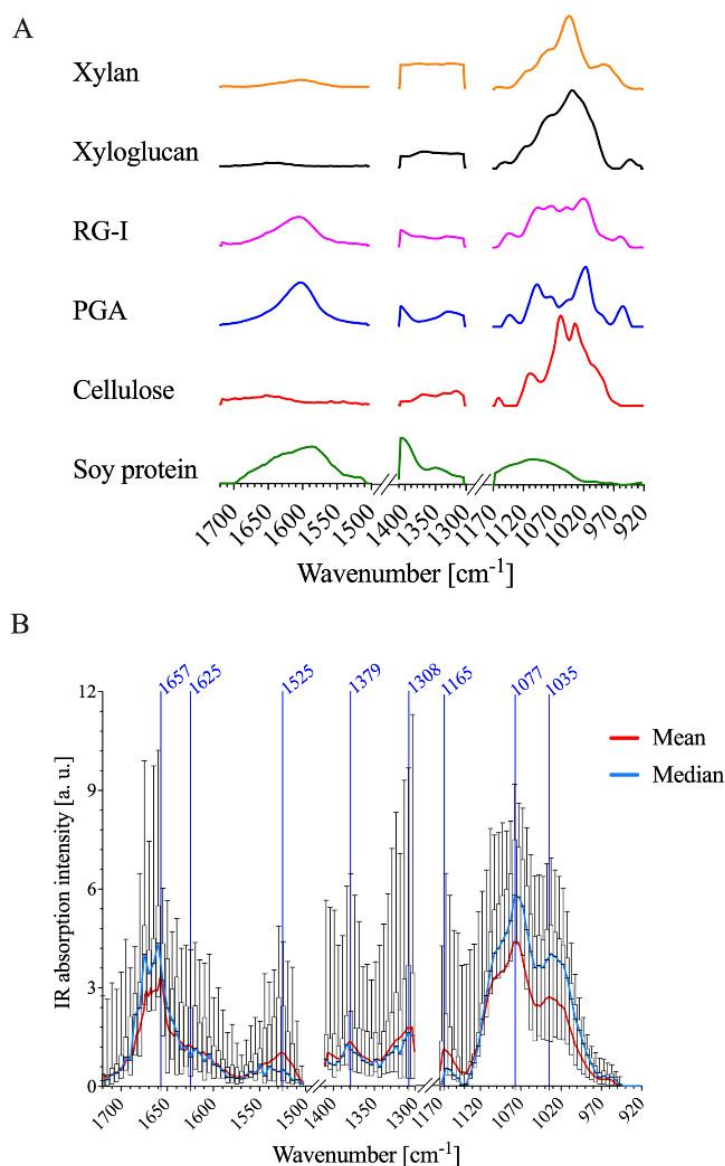


Figure 4.4.2. AFM-IR data of PFA-fixed *A. thaliana* stem epidermal cell wall show similar absorption patterns to FTIR spectra of cell wall standards. (A) Normalized FTIR spectra of cellulose, soy protein, PGA, RG-I, xylan and xyloglucan. FTIR absorption between 1300 - 1171 cm⁻¹ and 1503 - 1411 cm⁻¹ was removed for comparison with AFM-IR data. (B) a box plot of the AFM-IR spectra collected on the epidermal cell wall sample surface by binning 30 × 30 pixels into 15 × 15 pixels and by binning spectral wavenumbers 8×. The red and blue line represent the mean and median AFM-IR spectra, respectively. There was no AFM-IR absorption between 1503 – 1411 cm⁻¹ and 1300 – 1171 cm⁻¹.

The variance of IR absorption intensity across measured wavenumbers is substantial (Figure 4.4.2B), suggesting that there is chemical complexity and heterogeneity as a function of AFM-IR pixel location. Single wavenumber maps (Figure 4.4.3) were generated to depict the

spatial variation in IR absorption of specific functional groups associated with different cell wall standards (Table 4.4.1): neutral sugars in carbohydrates (C-O; 1075 cm^{-1}); amide II in proteins (C-N; 1525 cm^{-1}); and acidic sugar in carbohydrates, amide I in protein, and/or adsorbed water (1660 cm^{-1}). While both 1075 and 1660 cm^{-1} appear to have high absorption intensity across the majority of the AFM-IR scan region, there are clear differences in the level of absorption at these wavenumbers and their spatial distribution. For example, the area that shows the strongest absorption at 1075 cm^{-1} shows the weakest absorption at 1525 and 1660 cm^{-1} . Similarly, the region towards the bottom of the map that shows strong absorption at 1660 cm^{-1} , also shows weak absorption at 1075 and 1525 cm^{-1} . By contrast, in the top third of the map (the region between $2.5\text{--}3.0\text{ }\mu\text{m}$ in the y-dimension), there is a relatively equal spatial distribution of all three wavenumbers. Thus, single wavenumber maps can distinguish between the spatial distribution and concentration of spectrally resolved functional groups, such as C-O and C=O. However, these functional groups are found in multiple cell wall components. Therefore, single wavenumber maps are insufficient to fully capture the spatial and chemical complexity of cell wall components.

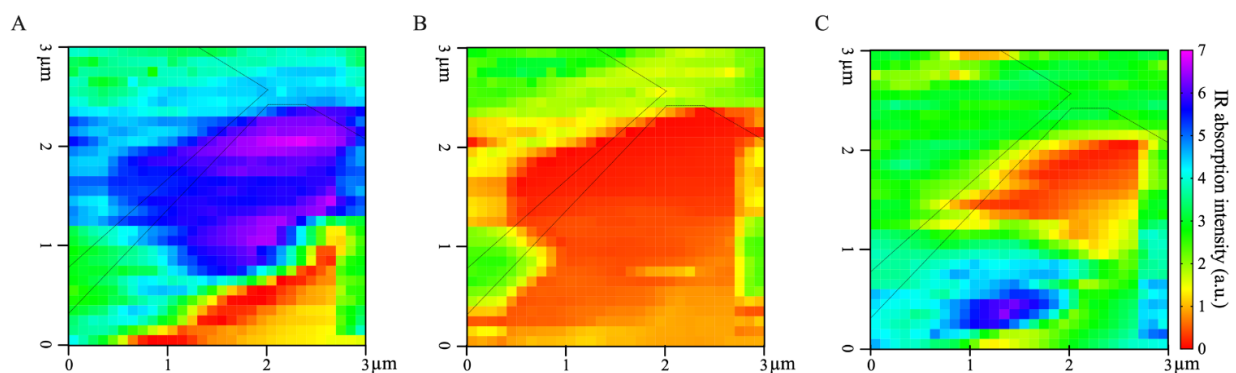


Figure 4.4.3. Fixed wavenumber maps at (A) 1075 cm^{-1} , (B) 1525 cm^{-1} , and (C) 1660 cm^{-1} . The black dashed outline represents the cell-cell junction highlighted in Figure 4.4.1D. a.u. = arbitrary units.

Table 4.4.1. IR assignments of the average Arabidopsis AFM-IR spectrum compared to commercial standards.

Wavenumber range (cm ⁻¹)	Wavenumber maxima (cm ⁻¹)	Band Assignments	Commercial Standards
1706-1631	1657	amide I (C=O stretch weakly coupled with C-N stretch and N-H bending)	soy protein
1631-1598	1625	adsorbed water O-H bending	cellulose, xylan, xyloglucan
		COO- antisymmetric stretching adsorbed water O-H bending	PGA, RG-I
1567-1504	1525	amide II (C-N stretch strongly coupled with N-H bending)	soy protein
1394-1351	1379	alcohol O-H bending aliphatic C-H bending	cellulose, xylan, xyloglucan, PGA, RG-I
		COO- symmetric stretching	PGA, RG-I
1342-1301	1308	C-H bending alcohol O-H bending	cellulose, xylan, xyloglucan, PGA, RG-I
		amide III (N-H in plane bending coupled with C-N stretching)	soy protein
1170-1145	1165	glycosidic O-C-O vibrations	
1137-1045	1077	sugar ring ether O-C-O stretching C-O stretching (secondary alcohol)	cellulose, xylan, xyloglucan, PGA, RG-I
1045-944	1035	C-O and C-C stretching (primary/secondary alcohol)	

4.4.3 Deconvoluting AFM-IR Spectra for Mechanochemical Correlations

To more accurately delineate local concentrations of specific cell wall functional groups and components, NMF spectral deconvolution was applied (Borodinov et al., 2019; Kulkarni et al., 2018; Labbe et al., 2005; Lin et al., 2018; Montcuquet et al., 2010; T. Zhang et al., 2018). NMF of the AFM-IR dataset (i.e., input matrix) requires a subjective, user-specified number of factors. The cophenetic correlation coefficient and residual sum of squares for a given solution represents the extent to which the residual data (i.e., the data from the input matrix that was not recreated by linear combinations of the factors) can be explained by best-fit linear combinations

of solution factors. For example, Brunet et al. proposed that the cophenetic correlation coefficients demonstrate the stability of NMF solutions or how accurately the NMF solution describes the dataset (Brunet et al., 2004). Hutchins et al. proposed that the proper NMF solution occurs when the residual sum of squares, or the variation between the target matrix and the NMF solution, is minimized (Hutchins et al., 2008). However, these measures alone cannot solely inform which is the ‘best’ solution or number of factors. In this study, NMF solutions were generated with the number of factors ranging from two to six. Distinctive factor spectra were generated up to the three-factor solution, but following that point, increasing factor number resulted simply in factor splitting. Furthermore, the cophenetic correlation coefficient and residual sum of squares values were relatively low for the three-factor solution (Figure 4.6.7). Therefore, the three-factor NMF solution was used to analyze the *A. thaliana* AFM-IR dataset.

Key IR absorption bands in the NMF spectra were analyzed and used to attribute the origin of NMFs (Figure 4.4.4A and Table 4.4.2). Factor 1 spectrum exhibited strong absorption for sugar ring ether O-C-O and primary alcohol C-O stretching at IR bands between 975-1091 cm^{-1} , which are absorption signatures associated with cell wall carbohydrates (Figure 4.4.4A). Absorption in this region was also seen in the FTIR spectra of carbohydrate standards and reference extracts. Notably, similar to cellulose, XG, and xylan, the Factor 1 spectrum did not show strong absorption in regions related to carboxylic acids (1407 and 1604 cm^{-1}). Factor 1 thus primarily represents a set of chemical groups that comprise neutral sugars on primary cell wall carbohydrate components; although, there are likely spectral elements attributed to cellulose, XG, and xylan in Factor 2. The Factor 2 spectrum contained IR absorption bands between (1) 1063-1170 cm^{-1} with peak maxima at 1110 and 1165 cm^{-1} that are attributed to glycosidic ether O-C-O and/or secondary alcohol C-O stretching, and (2) 1301-1346 cm^{-1} with a peak maximum

at 1310 cm^{-1} that is attributed to alcohol O-H bending and/or the amide III band. These two IR absorption band regions are found in the FTIR spectra of both carbohydrate and protein standards. Factor 2 thus represents specific moieties on primary cell wall carbohydrate components, mainly glycosidic linkages, and N-H groups of amides on proteins. The Factor 3 spectrum contained IR absorption bands between (1) $1324\text{-}1410\text{ cm}^{-1}$ with peak maxima at 1380 and 1403 cm^{-1} that are attributed to alcohol O-H bending, aliphatic C-H bending, and/or carboxylic acid symmetric stretching, (2) $1504\text{-}1570\text{ cm}^{-1}$ with a peak maximum at 1525 cm^{-1} that is attributed to the amide II band, and (3) $1596\text{-}1696\text{ cm}^{-1}$ with peak maxima 1610 and 1660 cm^{-1} that are attributed to carboxylic acid anti-symmetric stretching, adsorbed water O-H bending, and/or the amide I band. Factor 3 thus represents the acidic sugars on primary cell wall carbohydrate components, mainly carbonyls, as well as C-N and C=O groups of amides on proteins. The FTIR of RG-I and PGA suggest that the IR band for carboxylic acid anti-symmetric stretching is centered closer to 1600 cm^{-1} . Accordingly, a major IR absorption feature of the spectra of Factor 3 is located more towards 1660 cm^{-1} is likely more characteristic of the presence of a protein amide I band or protein-adsorbed water. Factor 1 loading was mapped in Figure 4.4.4B. As expected for the plant cell wall, neutral sugars represented by Factor 1 are present throughout most of the AFM-IR scan region. The NMF loading maps for Factors 2 and 3 are shown in 6×6 pixel squares, in agreement with the cell wall being a composite material (Figure 4.6.8) (Burton et al., 2010).

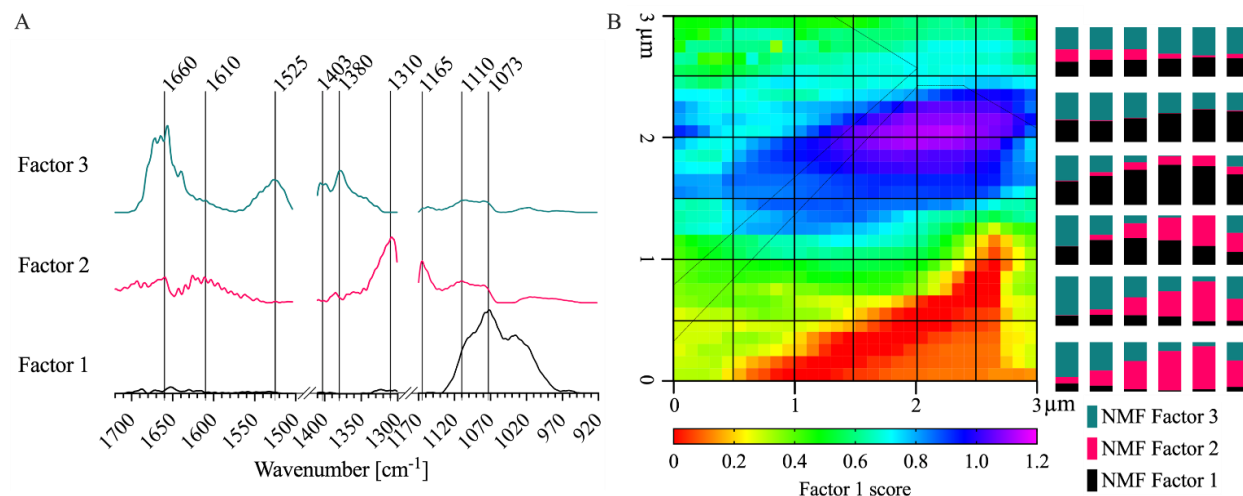


Figure 4.4.4. NMF factor spectra represent carbohydrate-rich and protein-like regions in the epidermal cell wall. (A) NMF factor spectra plot for the 3-factor NMF solution. Peaks in each NMF factor spectrum are labeled with vertical lines. There was no AFM-IR absorption between 1503 – 1411 cm^{-1} and 1300 – 1171 cm^{-1} . (B) Distribution map of Factor 1 representing its concentration (absolute value) in each pixel, with stacked bar plots displaying the ratio of NMF scores of Factors 1, 2 and 3 binned across 6×6 pixels (one box of the grid). Black dashed outline represents the cell-cell junction highlighted in Figure 4.4.1D.

Table. 4.4.2. IR assignments of NMF factors.

Factor	Wavenumber range (cm^{-1})	Wavenumber maxima (cm^{-1})	Band Assignments
3	1696-1596	1660, 1610	amide I (C=O stretch weakly coupled with C-N stretch and N-H bending) carboxylic acid O=C-O stretching adsorbed water O-H bending
2	1648-1543	1610	carboxylic acid O=C-O stretching adsorbed water O-H bending
3	1571-1504	1525	amide II (C-N stretch strongly coupled with N-H bending)
3	1410-1324	1403, 1380	alcohol O-H bending carboxylic acid O-H bending aliphatic C-H bending
2	1346-1301	1310	alcohol O-H bending amide III (N-H in plane bending coupled with C-N stretching) carboxylic acid O=C-O stretching

2	1170-1063	1165, 1110	glycosidic ether O-C-O stretching secondary alcohol C-O stretching
1	1091-975	1073	sugar ring ether O-C-O stretching primary alcohol C-O stretching

The left and top edges of the *A. thaliana* AFM-IR image are enhanced in the abundance of Factor 3 spectral features, whereas the bottom-right corner of the *A. thaliana* AFM-IR is enhanced in the abundance of Factor 2 spectral features. To better visualize these differences, we generated a map of the difference between Factor 1 score and the sum of Factors 2 and 3 scores (Figure 4.4.5A). Although an operation of this type with NMF loading values is ill-defined, it can be used to visualize which locations are enhanced in Factor 1 versus Factors 2 and 3 or vice versa. Positive values indicate locations where the IR spectra are enhanced in Factor 1, while negative values indicate locations with IR spectra are enhanced in Factors 2 and 3. In this map, Factor 1 dominates an oval-shaped region along the cell-cell junction (cyan and blue pixels), suggesting a high relative abundance of neutral sugars in this region. This map suggests that cellulose, xyloglucan, and xylan are present at higher concentrations than proteins and pectins within this region. By contrast, proteins and pectins represented by Factors 2 and 3 together appear to dominate the bottom third of the AFM-IR image (yellow and red pixels). Plants contain various cell wall proteins that make up 5-10% of the cell wall (Albenne et al., 2013; Amos & Mohnen, 2019; Daher & Braybrook, 2015; Keller, 1993). Localized deposition of cell wall proteins was previously demonstrated by Smallwood et al., who performed immunohistochemical staining of extensin and showed it localizes as puncta in the root epidermal cell wall (Smallwood et al., 1995). Without the need for immunostaining, our results

further support that cell wall proteins may be preferentially deposited in certain regions of the cell wall. The remaining light-green colored pixels in the map depict an equal mixture of Factor 1 and Factors 2 + 3, indicating that in some regions of the cell wall, the concentration of cell wall components is more balanced. These results show that NMF is a useful statistical tool to deconvolute AFM-IR spectral datasets to identify the major chemical components of cell walls and to distinguish their spatial organization and concentration.

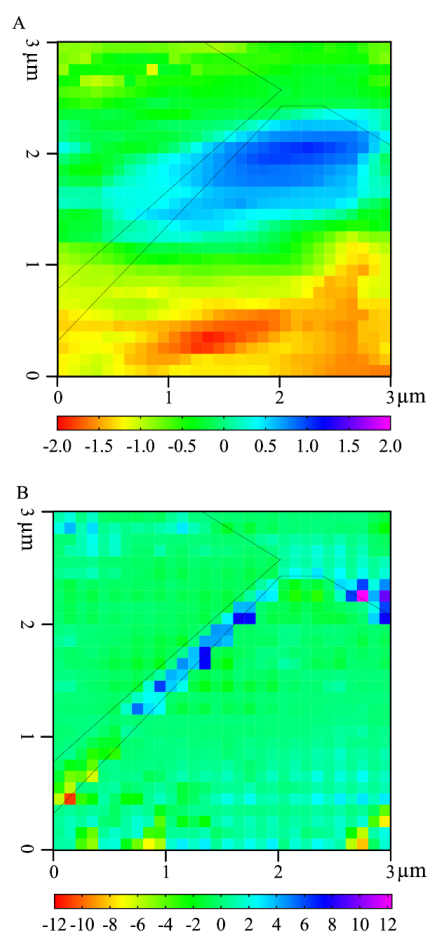


Figure 4.4.5. Higher relative presence of NMF Factor 1 positively correlates with cell wall stiffness. (A) NMF distribution difference between Factor 1 score and sum of Factors 2 and 3 scores. (B). Correlation between phase shift and the NMF distribution difference between Factor 1 score and sum of Factors 2 and 3 scores as seen in Figure 4A for each pixel. Black dashed outline represents cell-cell junction highlighted in Figure 4.4.1D.

4.4.4 Correlating Cell Wall Composition and Stiffness

An advantage of AFM-IR is its use in co-registering chemical and nanomechanical information. Cross-correlation coefficients can be used to evaluate the relationship between local mechanical properties, measured by cantilever phase shift, and chemical fingerprints (Borodinov et al., 2019). In this study, a positive cross-correlation value at a given pixel could result from either an increase in both the relative Factor 1 score and phase shift, or an increase in relative combined Factors 2 and 3 scores and a decrease in phase shift. Conversely, a negative cross-correlation value at a given pixel could result from either an increase in the relative Factor 1 score but a decrease in phase shift, or an increase in both the relative combined Factors 2 and 3 scores and phase shift. The former result would suggest that cell wall components described by Factor 1 correlate to cell wall stiffening while the cell wall components described by Factors 2 and 3 correlate to cell wall softening, while the latter result would suggest the reverse. The magnitude of the cross-correlation value is indicative of the strength of the correlation.

The epidermal cell-cell junction displayed a distinguishable topological feature (Figure 4.4.1G) as well as appeared stiffer than the rest of the scanned region, as indicated by a positive phase shift (Figure 4.4.1D). Cross-correlation analysis showed that a higher relative abundance of neutral sugars represented by Factor 1 correlates with cell wall stiffening, specifically along the cell-cell junction (blue pixels; Figure 4.4.5B). It is possible that around the cell-cell junction, a higher concentration of crystalline cellulose is driving wall stiffening (Rongpipi et al., 2019). Combined Factors 2 and 3 scores correlate with cell wall stiffening in a small region along the cell-cell junction (red and yellow pixels; Figure 4.4.5B). NMF factor score and phase shift in regions adjacent to the cell-cell junction are not strongly correlated, suggesting that softening of

the cell is not due to the concentration of a particular cell wall component or, at least, the loading of a Factor 1 or Factors 2 + 3.

4.5 Supplementary Information

4.5.1 Supplementary Methods

Arabidopsis cell wall alcohol insoluble residue (AIR) preparation (Guo, 2018; Phyto et al., 2017; Ruiz-Matute et al., 2011; Yeats et al., 2016). *Arabidopsis thaliana* Col-0 seeds were surface sterilized using a 25% (v/v) bleach solution prepared in sterile deionized (DI) water. For oxalate, 1 M KOH, and 4 M KOH extracts, seedlings were grown vertically on 1/2 Murashige and Skoog medium (Caisson Laboratories) with 1% agar, 0.3% sucrose, pH 5.7 for 2 weeks in 16 h / 8 h light conditions ($120 \mu\text{Em}^{-2}\text{s}^{-1}$), at 24°C. Seedling tissue was ground to a powder using a mortar and pestle at liquid nitrogen temperature. The powder was transferred into a 50 mL falcon tube filled with 40 mL of 80% ethanol, extracted for 30 minutes on ice, and then aliquoted into 2 mL Eppendorf tubes. Samples were pelleted by centrifugation at $15,000 \times g$ for 10 min at room temperature and the supernatant was discarded. Pellets were resuspended in cold 80% ethanol and centrifuged multiple times until the sample changed from green to gray-white. 1 mL of 1:1 (v:v) chloroform:methanol was added to each tube and thoroughly vortexed. Samples were extracted for 10 min at room temperature, centrifuged at $15,000 \times g$ for 10 min, and solvent was removed. This was repeated for a total of 3 washes with chloroform:methanol. After the last disposal of the chloroform:methanol solution, 1 mL of acetone was added to each sample tube. The pellets were disrupted with vortexing and samples were centrifuged at $15,000 \times g$ for 10 min. The final AIR pellets were air-dried overnight in a fume hood.

Cell wall component extraction. This was performed by the University of Georgia Complex Carbohydrate Research Center (UGA CCRC).

Polysaccharide extraction. Destarched AIR material from Arabidopsis Col-0 seedlings (384.1 mg) was suspended in 38 mL of 0.25% ammonium oxalate and gently mixed by tube rotator overnight at RT. The mixture was centrifuged at 1,200 x g for 15 min and the supernatant was transferred for dialysis (MWCO: 6-8 kDa). The resulting Oxalate extract was lyophilized after dialysis and weighed (28.15 mg, 7.4% yield). The pellet was dispersed in ~40 mL of 1 M potassium hydroxide (KOH) with 0.1% (w/v) NaBH₄ and mixed overnight, followed by centrifugation (1,200 x g, 15 min). The supernatant was removed and transferred for dialysis (MWCO: 1 kDa). The extracted material (1 M KOH) was lyophilized and weighed (66.02 mg, 17.2% yield) for further analysis. The residue pellet was resuspended in ~40 mL of 4 M KOH and mixed overnight to extract the second fraction of hemicellulose (4 M KOH). The sample was centrifuged (1,200 x g, 15 min) and the supernatant was collected and dialyzed (MWCO: 1 kDa). The extracted material (4 M KOH) was lyophilized and weighed (31 mg, 8.1% yield).

For a glycosyl composition analysis by TMS derivatization, the three carbohydrate extracts (Oxalate: 0.28 mg; 1 M KOH: 0.32 mg; 4 M KOH: 0.28 mg) were then spiked with 20 µg of inositol (internal standard) and heated with 500 µL of 1 M methanolic HCl in a sealed screw-top glass test tube for 18 h at 80 °C. After cooling and removal of the solvent under a stream of nitrogen, the sample was treated with 200 µL of methanol, 100 µL of pyridine, and 100 µL of acetic anhydride for 30 min. The solvent was evaporated, and the sample derivatized with 200 µL of Tri-Sil HTP (Pierce) at 80 °C for 30 min. The GC-MS analysis of the resulting TMS methyl glycosides was performed on an Agilent 7890A GC interfaced to a 5975C MSD, using a Supelco Equity-1 fused silica capillary column (30 m × 0.25 mm ID) and the temperature was programmed as listed in Table 4.6.2. The results of the glycosyl composition analysis are included in Table 4.6.3.

Protein extraction. The protein extraction followed the procedure described previously by Liang and Christeller, 2004 (Christeller & Laing, 2005), and Koontz, 2014 (Koontz, 2014), with slight adjustment. The Arabidopsis seedling (5 g) was ground into smaller granules by Hamilton coffee grinder and grind these granules by pestle and mortar with 100 mL of extraction buffer, composed of 200 mM HEPES (pH 7), 1% polyvinyl pyrrolidone, 10% glycerol, 2 mM dithiothreitol and 500 μ L of proteinase inhibitor cocktail (Sigma-Aldrich). The extraction buffer was stored at 4°C before use. The mixture was filtered through a nylon mesh (pore size: 100 μ m), and the insoluble part was washed by 50 mL of buffer again. Both filtrates were combined and centrifuged at 30,000 x g for 15 min (4°C) twice. The pellet was washed by 50 mL of extraction buffer again, and the supernatants were combined for dialysis (MWCO = 3.5 kDa) in 20-50 mM ammonium bicarbonate (pH 7.2) to remove salt and polyphenol, followed by lyophilization. The pellet was re-extract three times with the extraction buffer. The supernatants were combined and underwent benzonase (450 U) digestion at 37 °C overnight. The sample was then dialyzed again in 20 mM ammonium bicarbonate to remove the salt and nucleotides and resuspended in ~15 mL of water. The sample was preceded with trichloroacetic acid (TCA) precipitation by adding 1.6 mL of 94% TCA in the solution of the sample. The solution was stored at -20 °C for 15 min and centrifuge at 10,000 x g for 10 min to remove the supernatant. The pellet was washed by acetone three times to remove TCA and dried by a stream of nitrogen. The weight of the pellet was 37 mg.

Total carbohydrate and protein analysis. Total carbohydrate levels in the Arabidopsis cell wall extracts were quantified using a phenol-sulfuric acid assay. As a reference standard for total carbohydrate analysis, a 100 mg/L glucose solution was prepared using α -D-Glucose from Sigma, St. Louis, USA. In test tubes, around 5 mg of the extracts was weighed separately and

added, while 100, 200, 400, 600 and 800 μL of the 100 mg/L glucose standard solution were pipetted into other test tubes. An empty tube was used as control. The volume in each tube was made up to 1 mL with DI water. Then, 1 mL 5 % (w/v) phenol solution was added into each tube and mixed on a shaker for 5 min. 5 mL of 96 weight percent sulfuric acid was then added to each tube with continuous shaking for 10 min. After the tubes showed different color levels, 2 μL of each solution was pipetted to each well in a well plate with 3 replicates each. Then, 198 μL control solution was added to each well followed by tapping a few times to mix well. The well plate was then placed in an oven at 90°C for 5 min. After cooling down to room temperature, the absorbance values at a UV wavelength of 490 nm were measured using a Tecan Infinite M200Pro plate reader for total carbohydrate analysis. After a calibration of the glucose standards, the linear regression coefficient had a value of 0.9871. The parameters from the regression analysis were used to interpolate the total carbohydrate percentages of the extracts.

Protein levels were quantified in cell wall extracts using the PierceTM BCA Protein Assay Kit (ThermoFisher Scientific) using the test-tube procedure. Extracts were dissolved in milliQ water and diluted to a concentration of 2 mg/mL. Bovine serum albumin (BSA) standards were prepared per the PierceTM BCA Protein Assay protocol at a working range of 20 - 2,000 $\mu\text{g/mL}$. Absorbance was measured using a spectrophotometer at a wavelength of 562 nm. The linear regression coefficient of the BSA standard curve had a value of 0.974. Samples were measured in duplicate and a positive control of 300 $\mu\text{g/mL}$ BSA (BioRad) was used to confirm accuracy. The results of the total carbohydrate and protein analyses are included in Table 4.6.3.

Preparation of standard pellets. To make hydraulic-pressed pellets, around 5 mg of dry commercial plant cell wall standards (cellulose, polygalacturonic acid (PGA), rhamnogalacturonic acid I (RGI), and xyloglucan, Megazyme Ltd.), Arabidopsis cell wall extracts (Oxalate, 1 M

KOH, and 4 M KOH) were mixed with 100 mg of KBr and placed on a hydraulic press die. Pressure of 3 metric tons was applied for 5 minutes. Pellets were stored in a desiccator until FTIR measurements were collected.

Preparation of spin-coated films. Silicon wafers were rinsed with DI water and air dried for 10 min. PGA, RGI and xyloglucan were dissolved with DI water to a concentration of 10 g/L and filtered using a 0.22 μm syringe. The solutions were each spin coated onto the precleaned silicon wafers at 1000 rpm for 40 s. The spin coating program is: 400 rpm for the first 10 s, 1000 rpm for the next 40 s, 400 rpm for the last 10 s, with 100 rpm acceleration speed. Spin coated wafers were vacuum dried at 80 °C for 3 hours and stored in a desiccator until AFM-IR measurement. The films were measured to have a thickness of at least 80 nm by a profilometer.

FTIR measurements. FTIR spectra were collected on standard pellets (cellulose and Arabidopsis cell wall extracts) and spin-coated standard films (PGA, RGI, and xyloglucan). DI water was used to clean a Thermo Scientific® Nicolet 470 FTIR spectrometer before FTIR measurements. The parameters for FTIR measurements were set as follows: resolution as 1 cm^{-1} , number of scans as 64 per sample and the mode as attenuated total reflection. Background spectra were obtained in ambient air before the measurements. FTIR spectra of samples were measured at each corner to ensure reproducibility of the spectra and exported for further analysis.

Pre-processing of IR spectra. FTIR spectral range was reduced to match the range of AFM-IR. FTIR and AFM-IR spectra were divided into three separate spectral regions for pre-processing: 922-1170 cm^{-1} , 1301-1410 cm^{-1} , and 1504-1720 cm^{-1} . No outlier spectra were detected using principal component analysis at a 95% confidence level. Separate spectral regions were smoothed using a zeroth order Savitzky–Golay (SG) smoothing filter with a window of 7

points to reduce the effect of noise. A first-order automatic weighted least square approach for baseline correction was applied to obtain a baseline-corrected dataset. Smoothed IR spectra were normalized with an extended multiplicative scatter correction algorithm using Eigenvector® SOLO software. The separate spectral regions were rescaled according to the baseline-corrected dataset and combined into a single spectral document for multivariate analyses. AFM-IR and FTIR spectra were smoothed again using a zeroth order SG smoothing filter with a window of 7 points to reduce noise for plotting purposes.

Principal component analysis (PCA). The number of principal components (PCs) was set as 3 for PCA using a nonlinear iterative partial least squares algorithm via Python. The significant PCs were determined from their individual contribution to total variances. PC scores and PC spectra (loading) were exported for each significant PC. To visualize the point-to-point variations in the region of interest, PC scores of two PC components were plotted on a 2D plane, such as PC1 score versus PC2 score.

4.5.2 Supplementary Figures and Tables

Table 4.5.1. IR assignments of commercial standards.

Wavenumber Range (cm ⁻¹)	Wavenumber Maxima (cm ⁻¹)	Band Assignments	Peaks Observed in the Extracts
1720-1586	1652	H–O–H bending vibration of absorbed water	cellulose
1407-1350	1370	CH ₂ bending	
1350-1328	1334	CH ₂ symmetric bending	
1328-1303	1316	CH ₂ symmetric bending	
1167-1151	1161	glycosidic O–C–O vibrations	
1131-1092	1109	C–O stretching	
		C–C stretching	
1092-1044	1058	C–O stretching	
		C–C stretching	
1044-1007	1034	C–O stretching	

1007-959	1004	C–C stretching C–O stretching C–C stretching	
1717--1507	1604	COO- antisymmetric stretching	PGA
1409-1378	1407	COO- symmetric stretching	
1378-1303	1329	CH ₂ bending	
1156-1126	1143	glycosidic O-C-O vibrations	
1126-1082	1097	C–O stretching C–C stretching	
1082-1061	1076	C–O stretching C–C stretching	
1061-1044	1045	C–O stretching C–C stretching	
1044-998	1017	C–O stretching C–C stretching	
998-958	992	C–O stretching C–C stretching	
958-940	955	CO bending	
1705-1507	1604	COO- antisymmetric stretching	RG-I
1409-1381	1407	COO- symmetric stretching	
1381-1350	1378	CH ₂ bending	
1350-1303	1331	ring vibrations	
1166-1126	1143	glycosidic O-C-O vibrations	
1126-1086	1095	C–O stretching C–C stretching	
1086-1060	1073	C–O stretching C–C stretching	
1060-1039	1048	C–O stretching C–C stretching	
1039-972	1020	C–O stretching C–C stretching	
972-940	959	CO bending	
1701-1619	1628	amide I (C=O stretch weakly coupled with C-N stretch and N-H bending)	soy protein
1520-1507	1517	amide II (protein N–H bend, C–N stretch)	
1363-1304	1350	amide III (N-H in plane bending coupled with C-N stretching)	
1685-1537	1605	COO- antisymmetric stretching	xylan
1408-1365	1384	CH ₂ bending	
1342-1309	1328	C-H and O-H bending	
1167-1153	1160	glycosidic O-C-O vibrations	
1148-1106	1117	C–O stretching C–C stretching	

1106-1075	1078	C–O stretching C–C stretching	xyloglucan
1075-1007	1043	C–O stretching C–C stretching	
1007-933	987	C–O stretching C–C stretching	
1706-1594	1651	H–O–H bending vibration of absorbed water	
1397-1323	1371	CH ₂ bending	
1164-1144	1150	glycosidic O–C–O vibrations	
1148-1106	1115	C–O stretching C–C stretching	
1106-1075	1078	C–O stretching C–C stretching	xyloglucan
1072-973	1038	C–O stretching C–C stretching	
959-925	942	Ring vibration	

Table 4.5.2. The glycosyl composition analysis results of the three Arabidopsis cell wall reference extracts (Oxalate, 1 M KOH, and 4 M KOH), performed by the UGA CCRC.

Extract	Oxalate		1 M KOH		4 M KOH	
	Mass (µg)	Mol % ¹	Mass (µg)	Mol % ¹	Mass (µg)	Mol % ¹
Glycosyl residue						
Arabinose (Ara)	28.7	25.5	7.5	20.8	16.4	14.1
Ribose (Rib)	0.6	0.5	n.d.	-	n.d.	-
Rhamnose (Rha)	3	2.5	1.4	3.6	8.7	6.8
Fucose (Fuc)	1.4	1.1	0.8	2.1	2.2	1.7
Xylose (Xyl)	3.4	3	12.7	35.3	28	24
Glucuronic Acid (GlcA)	1.9	1.3	0.5	1	1.2	0.8
Galacturonic acid (GalA)	27.8	19.2	3.5	7.5	37	24.6
Mannose (Man)	1.3	1	0.6	1.5	4.1	3
Galactose (Gal)	52.5	38.9	8.5	19.7	18.9	13.5
Glucose (Glc)	4.3	3.2	2.5	5.8	14.3	10.2
N-Acetyl Glucosamine (GlcNAc)	0.8	0.5	0.3	0.5	0.1	0.1
Methyl Galacturonic acid (Me-GalA)	5.1	3.3	1.1	2.2	1.9	1.2

SUM	130.7	100	39.3	100	132.9	100
Total Carbohydrate % by weight	44.90%		12%		46.80%	

¹Values are expressed as mole percent of total carbohydrates. The total percentage may not add to exactly 100 % due to rounding.

Table 4.5.3. Total carbohydrate and protein percentages of the three Arabidopsis cell wall reference extracts (Oxalate, 1 M KOH, and 4 M KOH).

Extract	Oxalate	1 M KOH	4 M KOH
Total carbohydrate percentage (wt%)	23.3 ± 4.3	33.0 ± 3.9	92.2 ± 6.7
Protein percentage (wt%)	33.6 ± 1.3	44.0 ± 7.3	14.4 ± 1.5

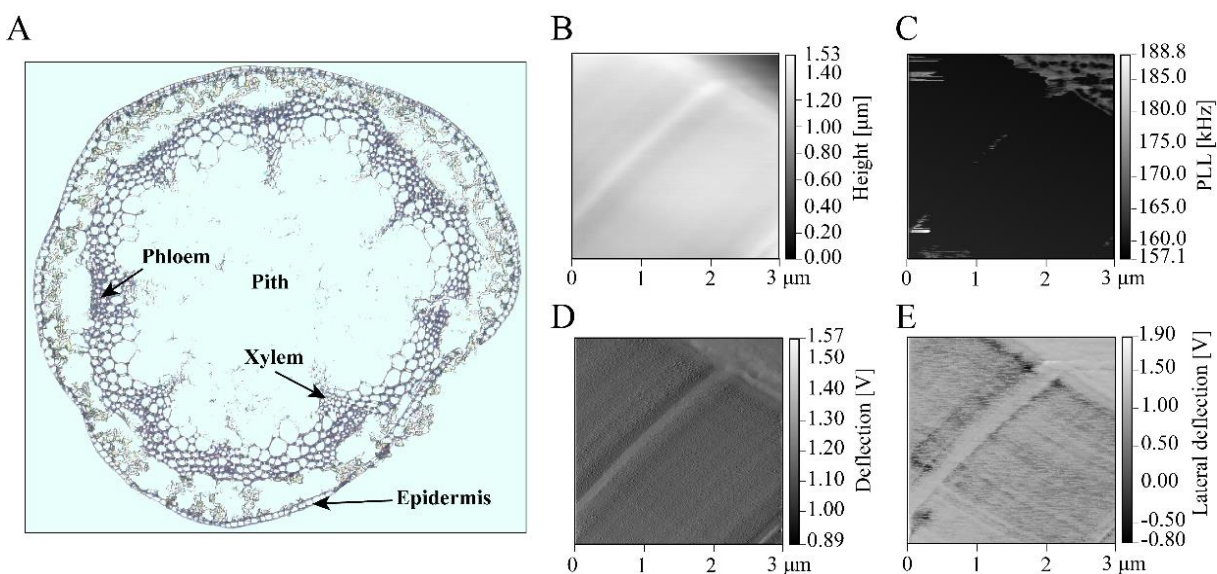


Figure 4.5.1. The epidermis and vasculature of PFA fixed stem sections maintain cell shape and tissue integrity. (A) PFA-fixed stem section with cell layers labeled. Height (B), phase-locked-loop (C), deflection (D), and lateral deflection (E) maps were obtained of a 3 x 3 μm^2 region where AFM-IR data was collected.

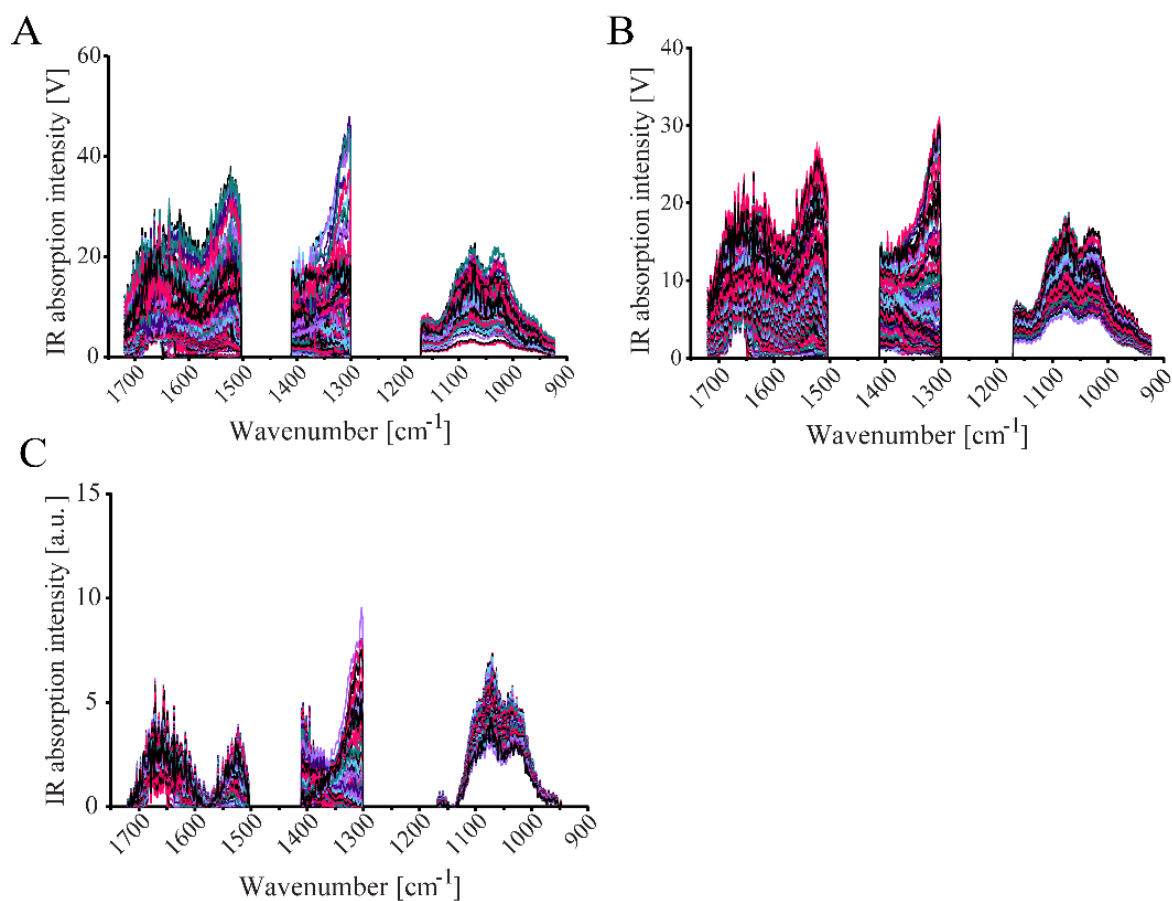


Figure 4.5.2. Pre-processing steps used for FTIR and AFM-IR spectra. 900 raw AFM-IR spectra (A) were first smoothed 5pt (B), and then EMSC normalized (C). There was no AFM-IR absorption between 1503 - 1411 cm^{-1} and 1300 - 1171 cm^{-1} , thus absorption = 0 a.u. (arbitrary units) in these regions of the spectra.

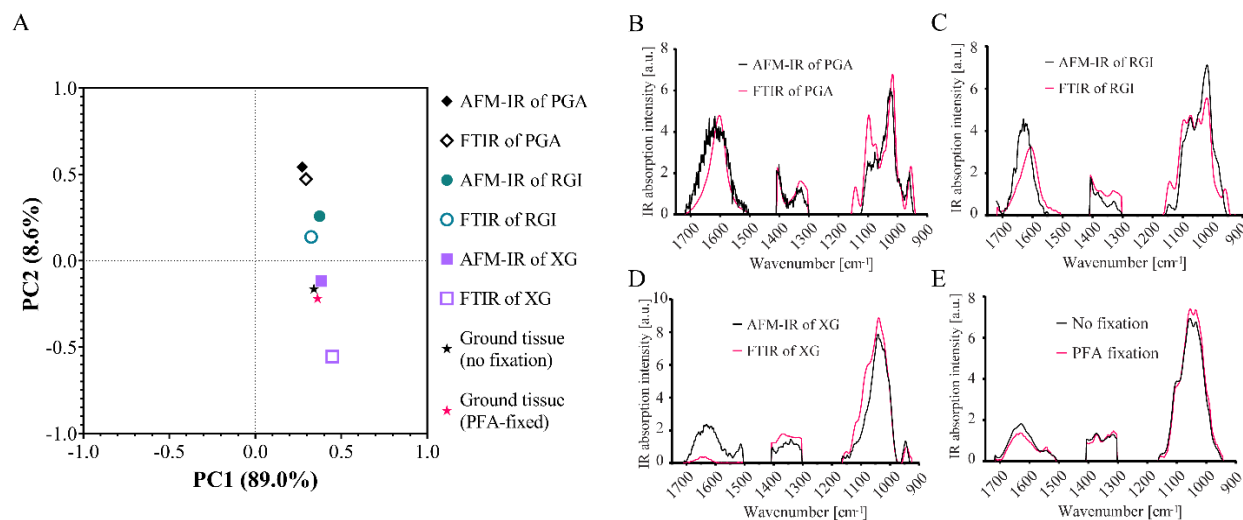


Figure 4.5.3. PCA of AFM-IR spectra and FTIR spectra of the same carbohydrate standards show highly similar IR signatures. (A) PCA score plot of FTIR and AFM-IR of selected commercial standards, and dehydrated ground tissue from PFA-fixed and unfixed Arabidopsis stem. (B-D) AFM-IR and FTIR spectra for commercial standards (polygalacturonic acid, PGA; rhamnogalacturonan I, RGI; and xyloglucan, XG) used in PCA. AFM-IR signature closely matches the signature of FTIR. (E) Comparison of FTIR spectra of unfixed ground stem tissue and of PFA-fixed ground stem tissue. Unfixed stem tissue is chemically indistinguishable from PFA-fixed stem tissue. There was no AFM-IR absorption between $1503 - 1411 \text{ cm}^{-1}$ and $1300 - 1171 \text{ cm}^{-1}$, thus absorption = 0 a.u. (arbitrary units) in these regions of the spectra.

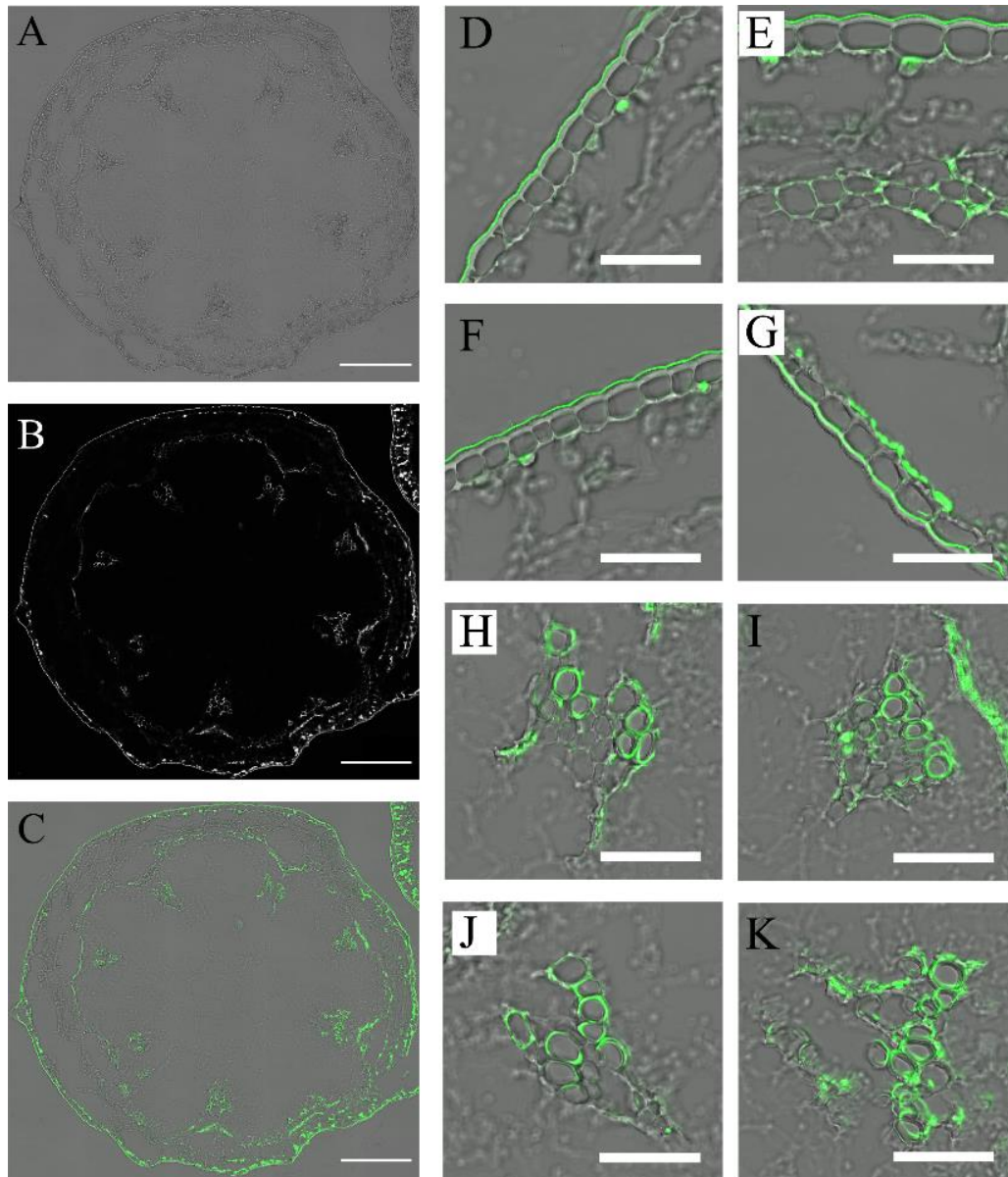


Figure 4.5.4. Lignin autofluorescence in Col-0 stem section. Lignin autofluorescence (excitation wavelength = 405 nm and emission wavelength = 450-650 nm) in a PFA-fixed Col-0 stem section prepared on a microscope slide. (A) Transmitted light channel, (B) fluorescence emission channel, and (C) overlay of transmitted light (gray) and fluorescence (green). Enlarged images of epidermal cells (D-G) show autofluorescence of the waxy cuticle but no autofluorescence in the anticlinal and inner periclinal walls. In contrast, enlarged images of xylem vessels (H-K) show high levels of autofluorescence throughout their cell walls. Scale bar = 200 μ m (A-C) and 50 μ m (D-K).

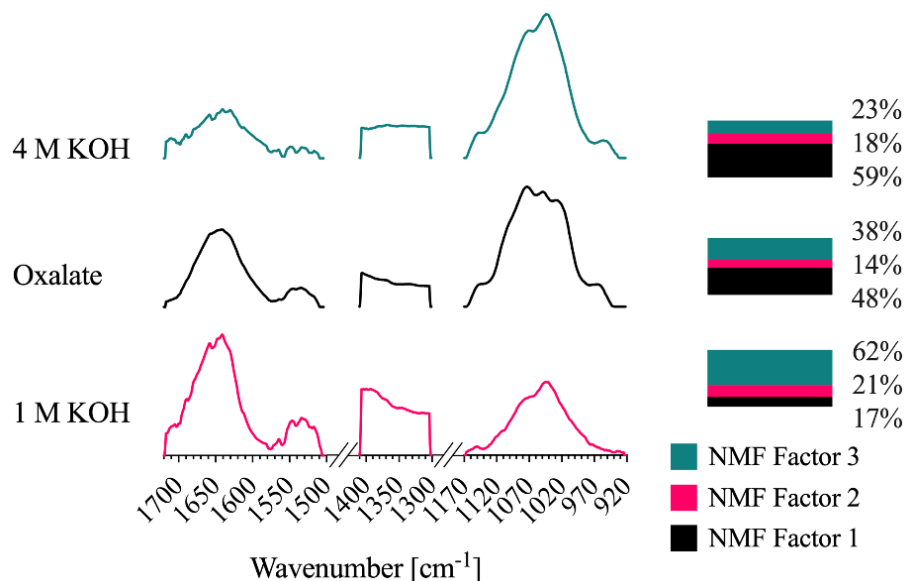


Figure 4.5.5. FTIR spectra of extracts from Arabidopsis seedling tissue. FTIR spectra of cell wall extracts obtained using 4M KOH, oxalate and 1M KOH. The NMF factor score percentages for each extract are shown on the right. FTIR absorption between 1503 - 1411 cm^{-1} and 1300 - 1171 cm^{-1} was removed to match AFM-IR spectral measurements, thus absorption = 0 a.u. (arbitrary units) in these regions of the spectra.

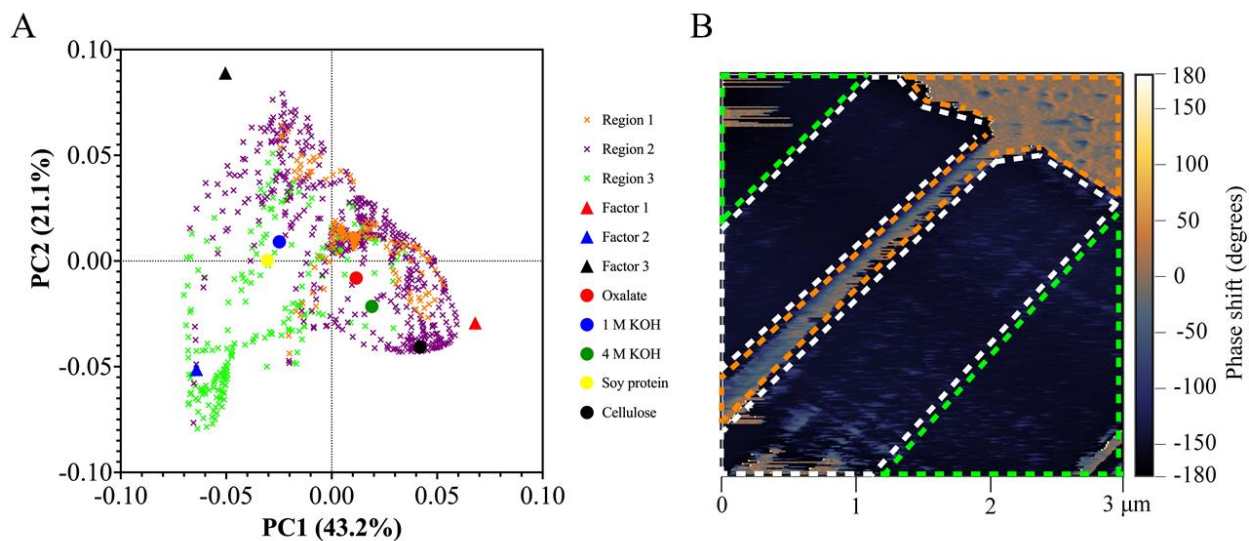


Figure 4.5.6. PCA shows chemical heterogeneity within the epidermal cell wall. (A) PC score plot (PC1 versus PC2) of cell wall standards together with 900 Arabidopsis AFM-IR spectra and 3 NMF factor spectra. Scores for AFM-IR pixel spectra are colored based on phase 2 image in B. (B) Phase 2 map of epidermal wall where AFM-IR data was collected, divided into three regions: cell-cell junction (orange, Region 1), within 1 μm of the cell-cell junction (white, Region 2), and more than 1 μm from the cell-cell junction (green, Region 3).

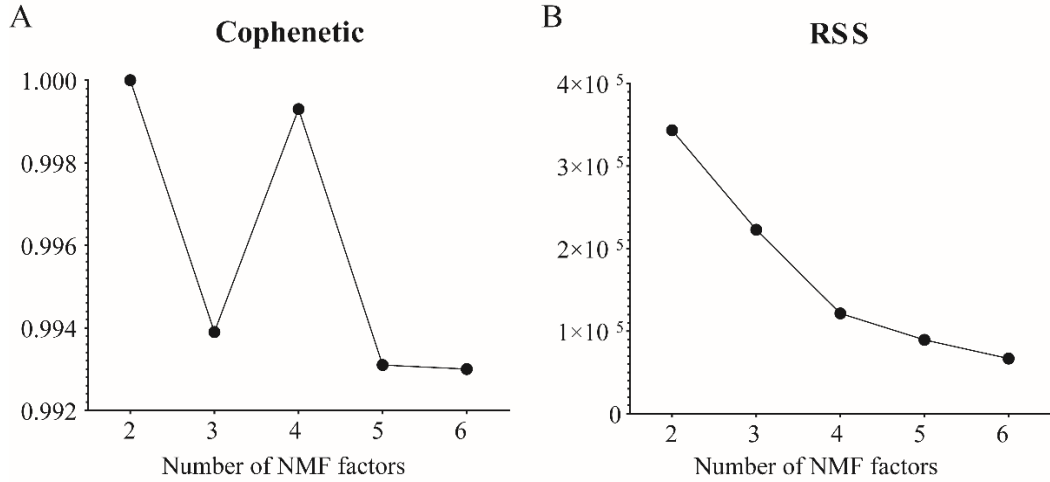


Figure 4.5.7. Cophenetic coefficient of variation (A) and residual sum of squares (RSS, B) for NMF factors ranging from 2 to 6. There is a local minimum when the number of NMF factors is set to 3. At this local minimum, RSS continues to decrease. This supports that the 3-factor solution is best for NMF analysis (Brunet et al., 2004).

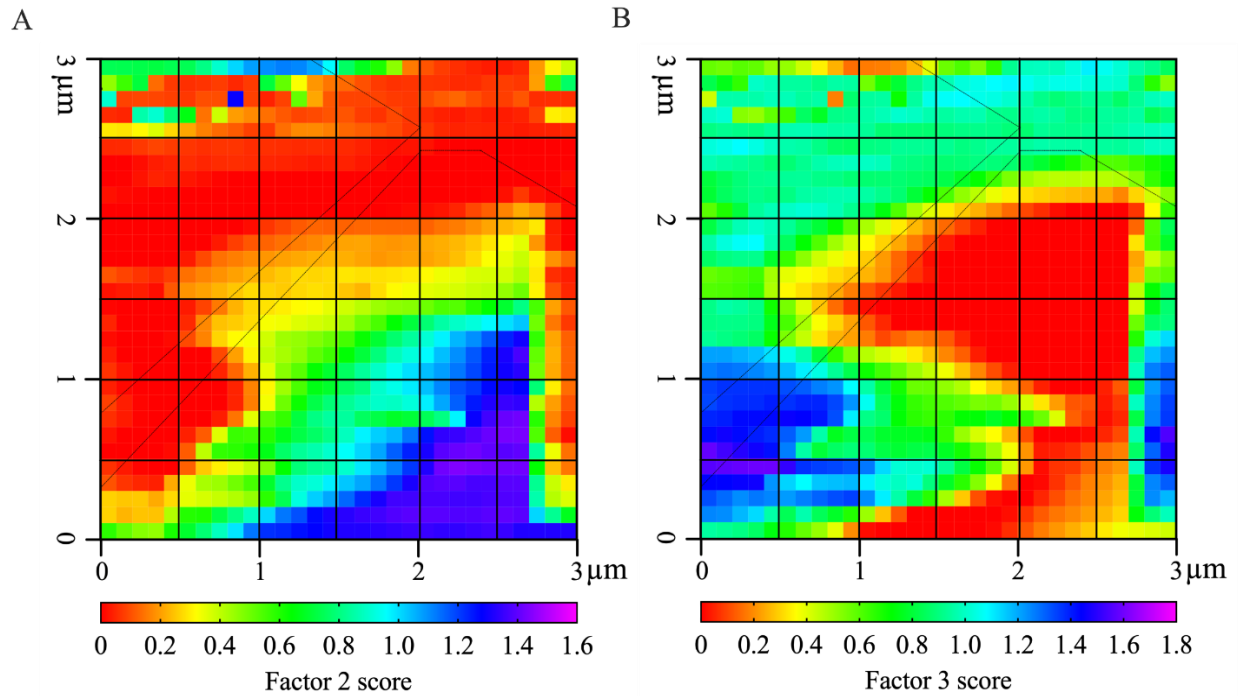


Figure 4.5.8. Distribution maps of Factor 2 (A) and Factor 3 (B) representing their concentrations (absolute value) in each pixel. Black dashed outline represents cell-cell junction highlighted in Figure 4.4.1D. A 6 x 6 box is outlined to represent the binned pixels as in Figure 4.4.4.

Chapter 5: Conclusions and Future Directions

Plant root systems adopt highly complex three-dimensional architectures in their quest to acquire water and nutrients, navigate the mechanically-heterogeneous soil environment, and provide structure support that stabilizes the plant. Root system development depends on directional growth at each root tip, which is defined by the microtubule cytoskeleton and relies on the root's inherent anatomical symmetry. Using Arabidopsis twisted mutants, *spr1* and *cmu1*, I found that directional root growth can be defined by the epidermal cell layer alone, which also controls the morphology of inner tissues. The epidermis interacts directly with the surrounding environment and requires a heterogeneous mechanical input to generate chiral growth, impacting the architecture of the root system as a whole. Intriguingly, root hairs, a feature unique to the epidermis that provides anchorage, are not necessary for guiding root growth trajectory. I found that chiral growth negatively impacts multiple root mechanoresponses, as the *spr1* mutant exhibits both defective root barrier avoidance and enhanced sensitivity to increased stiffness of the agar medium, which modulates its organ-level growth phenotype. Wild-type root growth, in contrast, is more resilient to conditions with varying mechanical stresses. Overall, this thesis work provides new insights into how morphological changes resulting from mutations affecting the microtubule cytoskeleton propagate across spatial scales to generate chiral growth at the root organ level, and how chiral growth consequently influences root mechanoresponse. The following sections summarize the main findings of Chapters 2-4 and outline key next steps to address outstanding questions.

5.1 The Epidermis Controls Root Directional Growth

In Chapter 2, I used a cell layer-specific genetic complementation approach in right-handed (*spr1*) and left-handed (*cmu1*) Arabidopsis twisted mutants and demonstrated that the epidermis alone is sufficient to maintain wild-type-like straight cell files and root growth, regardless of the handedness of twisted growth. Twisted growth in the *spr1* mutant was originally attributed to the reduced anisotropy of this mutant's cortical cell layer, which appears expanded in etiolated hypocotyls (Furutani et al., 2000). Furutani et al. theorized that the isotropic expansion of the cortex forces the longer epidermal cells to tilt as a compensatory mechanism to maintain tissue integrity. However, my results show that the epidermis, and not the cortex, dictates symmetry maintenance in the root. This finding is consistent with the second moment of area principle which states that resistance to torque and bending scales as the fourth power of the radius from the center. Furthermore, epidermal expression of *SPR1* restored both the anisotropy and skew of the cortical cell file to wild-type-like in the *spr1-3* mutant. These results indicate that the epidermis entrains the morphology of the cortex, and in contrast to Furutani's original theory, it can be concluded that the isotropic expansion of cortical cells in the *spr1* mutant is a compensatory response to the twisting of the epidermis. By genetically disrupting epidermal and cortical cell adhesion in the *spr1-3* mutant, I found that isotropic expansion of the cortex requires a physical connection with the epidermis. In addition, disrupting epidermal cell adhesion suppressed root skewing in the *spr1-3* mutant, indicating that the integrity of the epidermis is important for directing organ-level growth. In conclusion, epidermal control of internal tissue morphology and root growth directionality is facilitated by cell-cell adhesion, which maintains contiguous mechanical coupling and possibly mediates symplastic communication between cells. These data suggest that twisted plant growth in nature could arise

by altering microtubule behavior in the epidermis alone and does not require null alleles that might perturb other developmental and physiological processes in unwanted ways.

Future Direction 1: Does the thickness of the cortical cell layer affect the ability of the epidermis to maintain root symmetry? While my work points to a clear role for the epidermis in controlling root directional growth, this work was conducted in *Arabidopsis*, which contains a simple root cellular anatomy with one cortical cell layer. Most land plants, including agriculturally important species such as maize and rice (*Oryza sativa*, *Os*), contain more complex root anatomy consisting of 8 to 15 layers of cortical cells (Hochholdinger et al., 2004). Cortical cell division is controlled by the *SHORTROOT* (*SHR*) and *SCARECROW* (*SCR*) genes (Helariutta et al., 2000). I hypothesize that the thickness of the cortex does not affect the ability of the epidermis to control root growth because with a thicker cortex, the increased distance of the epidermis from the center axis will enhance its resistance to torsion, as dictated by the second moment of area principle. To test this hypothesis, future work should generate *spr1-3* lines that ectopically express *OsSHR2* under the control of a constitutive promoter, which induces multiple cortical cell layers in *Arabidopsis* roots (Wu et al., 2014). I expect that there will be no difference in cell file twisting or root skewing between *spr1-3* and *spr1-3/OsSHR2* plants. Furthermore, complementing the *spr1-3/OsSHR2* mutant in the epidermis alone by expressing *pWER::SPR1-GFP* should rescue straight growth, as was seen in Chapter 2. However, it would be interesting to see if complementing *spr1-3/OsSHR2* in the cortex alone by expressing *pPEP::SPR1-GFP* would partially rescue straight growth, as a thicker cortex may contribute more to controlling root growth.

Future Direction 2: Can the epidermis control symmetry breaking in the root?

While my work demonstrated that epidermal expression of *SPR1* or *CMU1* is necessary to

maintain root growth symmetry, whether loss of *SPR1* or *CMU1* in the epidermis alone is sufficient to drive twisted root growth remains unknown. Thus, an ideal complementary experiment would be a cell layer-specific knockout approach, specifically in the epidermis. Decaestecker et al. recently developed a CRISPR system for tissue-specific knockout (CRISPR-TSKO) in *Arabidopsis* (Decaestecker et al., 2019). This technique, which expresses the Cas9 nuclease and guide RNA under the control of tissue-specific promoters, generated somatic mutations with high efficiency in the first generation. It is important to note with this technique that each cell technically experiences different CRISPR-based mutations (typically small indels) that are not inheritable, but the tissue-specific expression of the Cas9 cassette is inherited. Future experiments should use CRISPR-TSKO to conduct epidermis-specific knockout of *SPR1* and *CMU1* using the respective *pSPR1::SPR1-GFP* and *pCMU1::GFP-CMU1* lines. The loss of GFP signal in the epidermis will signify the successful knockout of each gene in this cell layer. I predict that these lines will exhibit skewed cell files and roots as seen in the respective mutant lines.

Future Direction 3: What is the relationship between cellular growth rate and the origin of cell file twisting in the *spr1* mutant? I found that in the elongation zone of *spr1-3* roots, the skewed organization of cortical microtubules in the epidermis correlates with asymmetric cell growth, which precedes cell file twisting. Interestingly, the onset of cell file twisting correlates with the slowing down of cell elongation. Specifically, cell file twisting initiates during the transition between the distal elongation zone and the differentiation zone, a phenotype previously reported in other twisted mutants (Thitamadee et al., 2002). How do root cell growth patterns differ between the *spr1* mutant and wild-type? What exactly is the relationship between cell growth and cell file twisting in the *spr1* mutant? My work has

narrowed down which cell layer and developmental zone future work should focus on to answer these questions.

I hypothesize that through rapid cell elongation, skewed microtubule orientation creates material anisotropy of the cell wall that builds torsional stress along the cell file, which is relieved through cell file twisting as growth slows down. Future experiments should employ exogenous hormone treatments to either enhance or decrease root cell growth and evaluate how changes in growth rate influence cell file twisting. For example, auxin reduces the rate of cell elongation in primary roots in a dose-dependent manner, leading to a shorter elongation zone (Rahman et al., 2007). I hypothesize that reducing the rate of elongation will reduce torsional stress along the cell file in the *spr1* mutant, thus suppressing cell file twisting. These experiments can be complemented by computational modeling to quantitatively evaluate the mechanical stresses imposed by rapid cell elongation and whether and how they might yield twisted growth.

5.2 Mechanisms of Twisted Root Growth and Consequences on Root System Architecture

How does twisting of the epidermis cause roots to bend in a specific direction? One notable feature of the root epidermis is the production of root hairs from trichoblast cell files. In Chapter 2, I found that in *spr1-3* seedlings grown on top of agar, root hairs interacted with the agar in an asymmetric manner. Intriguingly, *spr1-3* mutant roots that penetrated and grew inside the agar did not skew, despite maintaining twisted cell files. Inside agar, root hairs likely experience equal forces in all directions that average out, leading to straight root growth. These observations suggested a model in which biased mechanical interactions between root hairs and the surface of the agar provides the motive force to deflect roots in the opposite direction.

However, when I tested this model by generating a root hairless *spr1* mutant (*spr1-6 cpc try*), I found that root hairs were not required to generate skewed root growth. Therefore, some other feature of epidermal cells is responsible for deflecting roots when grown on an agar medium. One can imagine that in a highly heterogenous mechanical environment, like the soil, the interaction between the epidermis and surrounding substrate might vary in space and time, leading to complex root structures. However, even in the simple growth conditions of an agar plate, it is unclear exactly how the interaction between epidermal cells and the agar confers such an extreme organ-level phenotype in the *spr1* mutant.

Future Direction 1: How does the twisted epidermis in the *spr1* mutant interact with the agar to generate the root-skewing phenotype? My work demonstrated that the epidermis-agar interactions are sufficient to cause directional root bending. I hypothesize that the chiral twisting of epidermal cells in the *spr1* mutant creates asymmetric microscale interactions between the root surface and agar that deflect the root. In Chapter 2, I used standard widefield microscopy to visualize agar indentation around root hairs but could not detect smaller agar indentations around the root with this imaging approach. A potentially useful tool to apply in future work is polarized light. Agar is a birefringent (a transparent, molecularly-ordered material through which light is double-refracted), linear elastic gel with predictable stress and strain properties (Lemon et al., 2017). Polarizing filters force light waves to adopt one alignment. When polarized light passes through agar, any stress applied to the agar will rotate the axis of polarized light to a degree dependent on the applied force (Full et al., 1995). This detectable shift in light polarity can be mapped across the surface of the agar. Hence, it may be possible to visualize the stress induced by a root growing along the agar surface. To compare potential differences in stress applied by *spr1* mutant and wild-type roots to an agar surface, it will be

important to use polarized light microscopy at cell file-level resolution, focused on the differentiation zone of the root where twisted growth is most obvious. If stress differences are detectable between genotypes, it would be interesting to image how stress changes around the transition between cell elongation and differentiation which correlates with detectable twisted growth.

Future Direction 2: How does the *spr1* mutation impact three-dimensional root development and mechanoresponse? Arabidopsis twisted mutants have previously been shown to have defective root mechanoresponse in barrier avoidance (Y. Wang et al., 2011), and I confirmed a similar defect in the *spr1-3* mutant. Here, I explored whether the stiffness of the growth environment also affected root mechanoresponse by growing seedlings on plates containing different agar concentrations. Increasing the concentration of agar increased the stiffness of the medium and caused *spr1-3* root skewing to progressively switch from rightward to leftward, indicating that organ-level directional growth was less stable in the *spr1-3* mutant compared to wild-type Col-0, which sustained straight growth across all treatments. Surprisingly, leftward-skewed *spr1-3* roots on stiff agar maintained right-handed twisted cell files, demonstrating that even in a heterogeneous mechanical environment, cell file twisting is an intrinsic feature of roots that can be de-coupled from organ-level growth response. Lastly, despite their important role in root anchorage (Bengough et al., 2016), I found that root hairs on the epidermis are not required for reorienting *spr1-6* root skewing on stiff agar.

My thesis work demonstrates that twisted growth in *spr1-3* affects the root system as a whole. In Chapter 3, I show that *spr1* lateral roots exhibit similar cell file twisting and root skewing as the primary root when grown on agar plates, supporting findings in Chapter 2 that describe cell file twisting and fixed clockwise growth trajectories of soil-grown *spr1* roots. While

seedlings grown on agar are experimentally tractable, this growth method does not recapitulate the complexity of a soil environment. The opacity of soil poses a significant barrier to high-resolution root imaging. However, X-ray computed tomography (CT) is an advanced, 3-D imaging tool that has been extensively used to image soil-grown roots in recent decades (Heeraman et al., 1997; Taina et al., 2008; Mooney et al., 2012; Pfeifer et al., 2015; Teramoto et al., 2020). CT imaging, which easily distinguishes between root tissue and the surrounding substrate, can be used to reconstruct a precise 3-D volumetric projection of the root system, from which root system architecture can be quantified (Paya et al., 2015; Teramoto et al., 2020; Herrero-Huerta et al., 2022). Thus, future work to understand the implications of twisted growth on root system development should employ CT imaging. This approach should enable a comparison of root system architecture of the *spr1* mutant and wild-type plants under controlled conditions such as in compact versus loose soil. In addition, this approach would allow assessment of how roots respond to barriers in a 3-D soil environment and whether twisted roots interact differently with barriers than wild-type roots.

A complementary approach would be to compare root system architecture in agar gels of varying stiffnesses, or in an agar gel that increases in stiffness with depth. For this experiment, it is important to remember that *spr1* roots grown inside of agar do not skew rightward, as seen on top of agar, but still maintain twisted cell files. This experiment may answer the following questions: How does increased stiffness of the surrounding root environment impact root system development? Does fixed twisted growth in the *spr1* mutant enable deeper root penetration? Quantifying the 3-D root system architecture and its development over time should provide insights into the possible benefits of twisted root growth on soil penetration, obstacle avoidance, and overall plant health.

Future Direction 3: Does the *spr1* mutation impact auxin distribution in the root?

Gravitropism, or growth along the gravity vector, is a characteristic root mechanoresponse. This response is sensitive to developmental and environmental cues, and roots of different species typically exhibit a specific gravitropic setpoint angle (GSA) or root skewing angle. *Spr1-3* roots adopt a large, rightward GSA compared to wild-type. Previously, fixed twisted growth was found to impact root gravitropism in another Arabidopsis mutant with defective auxin transport, *twisted dwarf1* (B. Wang et al., 2013). I found that the *spr1-3* mutant exhibits a similar defect. Specifically, *spr1-3* roots show reduced root bending in response to a reorientation of the gravity vector, but the kinematics of *spr1-3* root bending was similar to wild-type. A transient change in the lateral distribution of auxin plays a critical role in mediating root growth (Went, 1974; Y. Zhang & Friml, 2020). Therefore, it would be interesting to explore if the differential distribution of auxin helps define the right-handed skewing angle (or GSA) adopted by *spr1* roots.

A gravitropic stimulus is easy to apply to plate-grown seedlings by simply rotating the plate. Upon a 90° rotation, starch-filled granules in the root apex sense the change in gravity vector, signaling a change in auxin transport from symmetric to asymmetric distribution along the length of the root elongation zone (Friml et al., 2003; Baster et al., 2013; Y. Zhang & Friml, 2020). Given the gravitropic defect I found in *spr1-3*, it would be important to determine if auxin distribution is perturbed in *spr1-3* roots. To facilitate these experiments, I have introduced a widely-used fluorescent reporter to visualize auxin transport, *pDR5::GFP* (Chen et al., 2013), into both *spr1-3* and *cmu1* mutants. Future work should use a fluorescent stereomicroscope to visualize GFP signal in the elongation zone of *spr1-3/pDR5::GFP* and *cmu1/pDR5::GFP* roots grown on agar plates to determine if auxin distribution is asymmetric and correlates with handedness in these mutants. Furthermore, it will be important to assess how the distribution of

auxin changes in response to a gravitropic stimulus. External mechanical forces have been shown to cause the reorientation of cortical microtubules and redistribution of PIN family auxin efflux carriers (Heisler et al., 2010). Therefore, auxin movement may be perturbed in twisted mutants due to changes in the tissue stress pattern caused by twisted growth. In either case, these experiments will shed light on whether auxin distribution plays a role in the root growth of twisted mutants.

Future Direction 4: Do mutations in microtubule-associated genes contribute to naturally-occurring twisted growth in plants? My thesis work demonstrates that *SPR1* and *CMU1* are necessary for symmetry-maintenance in Arabidopsis roots — mutations in the *spr1* and *cmu1* genes result in right- or left-handed root growth, respectively. A caveat of this work is that all experiments were performed using Arabidopsis plants in the wild-type Col-0 ecotype background. Can these findings be translated to naturally-occurring twisted growth? To test this, future work should utilize the Arabidopsis ‘1001 Genomes’ database (<https://1001genomes.org/>) to investigate variation in gene expression in wild-type Arabidopsis ecotypes that naturally skew right-ward or left-ward. This database contains transcriptomic (AraRNAseq) and phenotypic (AraPheno) data across at least 1001 Arabidopsis ecotypes. I looked through this database for phenotypes related to root skewing of seedlings grown vertically on agar plates and discovered a study performed by Julkowska et al. that compared root architecture remodeling in response to salt stress (Julkowska et al., 2017). The AraPheno database summarized root skewing data of 328 accessions on the control medium (0 mM NaCl) in this study (<https://arapheno.1001genomes.org/phenotype/643/>). The most leftward-skewing ecotype was Co-2 from Portugal, and the most rightward-skewing ecotype was Kro-0 from Germany (Julkowska et al., 2017). Using the AraRNAseq database, the transcriptional profiles of these

ecotypes (and a few others with similar phenotypes) should be compared to see if the expression of microtubule-associated genes, such as *CMUI* and *SPRI*, are reduced or absent in Co-2 and Kro-0. If so, this would suggest that naturally-occurring twisted growth may be directly due to genetic variations that reduce the expression of microtubule-associated genes. It would also be important to assess the expression of other genes, not necessarily related to microtubules, that are associated with twisted growth, summarized in a 2020 review by Buschmann and Borchers (Buschmann & Borchers, 2020).

5.3 AFM-IR Can Be Used to Study Plant Cell Wall Mechanochemistry at the Nanoscale

In Chapter 4, I contributed to the development of new methodologies for sample preparation, data acquisition, and multivariate statistical analyses for AFM-IR on *A. thaliana* primary cell walls. A method using gelatin embedding and cryostat sectioning of PFA-fixed *A. thaliana* stems was effective at eliminating spectral contamination and obtaining a section suitable for AFM-IR. Through the adaptation of this sample preparation and sectioning method, AFM-IR may be applied to other genotypes, plant species, and plant tissues to assess local cell wall mechanochemical properties. This work also demonstrated a novel application of non-negative matrix factorization (NMF) to analyze AFM-IR datasets. NMF deconvolution of AFM-IR spectra across the epidermal cell wall detected factors representing chemical functionality of neutral sugars of cell wall carbohydrates, acidic sugars of cell wall carbohydrates, and amino and carbonyl groups of cell wall proteins. Ultimately, cross-correlation analysis of the spatial distribution of NMFs and mechanical properties showed that the neutral sugar-containing carbohydrate composition of cell wall junctions between neighboring *A. thaliana* epidermal cells correlates with increased local stiffness. Future improvement of AFM-IR spatial resolution and

spectral range may reveal more subtle patterns in component organization that are important for defining the local mechanical properties of the cell wall. With these advances in methodologies for sample preparation, data acquisition, and multivariate statistical analyses, AFM-IR can be used to explore and understand phenotypic alterations to specific plant tissues in nanoscale resolution caused by environmental stresses or genetic mutations.

Future Direction: Use Arabidopsis cell wall-deficient mutants to improve AFM-IR data analysis. As highlighted throughout this thesis, the Arabidopsis root is an excellent model system to understand plant growth and development. In Chapter 4, we used the apical region of an Arabidopsis stem for AFM-IR application because the stem is physically easy to manipulate for sample preparation, compared to the root. However, the root contains simpler cellular anatomy, with one cell layer per tissue type, and the stages of cell development are easy to define. The next step of this work should adapt our current sample preparation methodology to be used on Arabidopsis roots grown on agar plates. For this, I have produced root samples for Huiyong Li (Dr. Marcus Foston's lab) for troubleshooting a new sample preparation methodology and conducting AFM-IR experiments.

In addition, our ongoing work is using cell wall-deficient mutants to help identify IR spectral signatures associated with specific cell wall components. For this work, we are using xyloglucan-deficient *xxt1xxt2* (Cavalier et al., 2008), cellulose-deficient *proctuse1/cesa6* (Fagard et al., 2000), and pectin-deficient *quasimodo2* (Mouille et al., 2007) Arabidopsis mutants. Using the power of AFM-IR to generate correlated mechanochemical maps of the cell wall, we expect to better attribute localized mechanical properties to the prevalence of specific cell wall components. In the future, this analysis should be applied to epidermal cells of twisted mutants such as *spr1-3* and *cmu1* to determine how microtubule-related mutations affect cell wall

composition and mechanics at the nanoscale, to gain a better understanding of the origin of skewed growth at the cell level. Furthermore, it will be important to create mechanochemical maps in different cell types and developmental regions of the root, perhaps under various treatment conditions, to more closely understand how cell wall mechanochemical properties at the nanoscale impact root development.

References

- Adamowski, M., & Friml, J. (2015). PIN-Dependent Auxin Transport: Action, Regulation, and Evolution. *The Plant Cell*, 27(1), 20–32. <https://doi.org/10.1105/tpc.114.134874>
- Adamowski, M., Li, L., & Friml, J. (2019). Reorientation of Cortical Microtubule Arrays in the Hypocotyl of *Arabidopsis thaliana* Is Induced by the Cell Growth Process and Independent of Auxin Signaling. *International Journal of Molecular Sciences*, 20(13), 3337. <https://doi.org/10.3390/ijms20133337>
- Agarwal, U. P. (2006). Raman imaging to investigate ultrastructure and composition of plant cell walls: Distribution of lignin and cellulose in black spruce wood (*Picea mariana*). *Planta*, 224(5), 1141. <https://doi.org/10.1007/s00425-006-0295-z>
- Albenne, C., Canut, H., & Jamet, E. (2013). Plant cell wall proteomics: The leadership of *Arabidopsis thaliana*. *Frontiers in Plant Science*, 4, 111. <https://doi.org/10.3389/fpls.2013.00111>
- Alberts, B., Johnson, A., Lewis, J., Raff, M., Roberts, K., & Walter, P. (2002). The Plant Cell Wall. *Molecular Biology of the Cell*. 4th Edition. <https://www.ncbi.nlm.nih.gov/books/NBK26928/>
- Amos, R. A., & Mohnen, D. (2019). Critical Review of Plant Cell Wall Matrix Polysaccharide Glycosyltransferase Activities Verified by Heterologous Protein Expression. *Frontiers in Plant Science*, 10. <https://doi.org/10.3389/fpls.2019.00915>
- Anderson, C. T., Carroll, A., Akhmetova, L., & Somerville, C. (2010). Real-Time Imaging of Cellulose Reorientation during Cell Wall Expansion in *Arabidopsis* Roots. *Plant Physiology*, 152(2), 787–796. <https://doi.org/10.1104/pp.109.150128>

- Anderson, C. T., & Kieber, J. J. (2020). Dynamic Construction, Perception, and Remodeling of Plant Cell Walls. *Annual Review of Plant Biology*, 71(1), 39–69.
<https://doi.org/10.1146/annurev-arplant-081519-035846>
- Anderson, C. T., & Wallace, I. S. (2012). Illuminating the wall: Using click chemistry to image pectins in Arabidopsis cell walls. *Plant Signaling & Behavior*, 7(6), 661–663.
<https://doi.org/10.4161/psb.19939>
- Anderson, C. T., Wallace, I. S., & Somerville, C. R. (2012). Metabolic click-labeling with a fucose analog reveals pectin delivery, architecture, and dynamics in Arabidopsis cell walls. *Proceedings of the National Academy of Sciences*, 109(4), 1329–1334.
<https://doi.org/10.1073/pnas.1120429109>
- André, I., Bradley, P., Wang, C., & Baker, D. (2007). Prediction of the structure of symmetrical protein assemblies. *Proceedings of the National Academy of Sciences*, 104(45), 17656–17661. <https://doi.org/10.1073/pnas.0702626104>
- Araus, J. L., & Cairns, J. E. (2014). Field high-throughput phenotyping: The new crop breeding frontier. *Trends in Plant Science*, 19(1), 52–61.
<https://doi.org/10.1016/j.tplants.2013.09.008>
- Atkinson, J. A., Pound, M. P., Bennett, M. J., & Wells, D. M. (2019). Uncovering the hidden half of plants using new advances in root phenotyping. *Current Opinion in Biotechnology*, 55, 1–8. <https://doi.org/10.1016/j.copbio.2018.06.002>
- Atmodjo, M. A., Hao, Z., & Mohnen, D. (2013). Evolving Views of Pectin Biosynthesis. *Annual Review of Plant Biology*, 64(1), 747–779. <https://doi.org/10.1146/annurev-arplant-042811-105534>

- Bailey, P. H. J., Currey, J. D., & Fitter, A. H. (2002). The role of root system architecture and root hairs in promoting anchorage against uprooting forces in *Allium cepa* and root mutants of *Arabidopsis thaliana*. *Journal of Experimental Botany*, 53(367), 333–340. <https://doi.org/10.1093/jexbot/53.367.333>
- Baker, M. J., Trevisan, J., Bassan, P., Bhargava, R., Butler, H. J., Dorling, K. M., Fielden, P. R., Fogarty, S. W., Fullwood, N. J., Heys, K. A., Hughes, C., Lasch, P., Martin-Hirsch, P. L., Obinaju, B., Sockalingum, G. D., Sulé-Suso, J., Strong, R. J., Walsh, M. J., Wood, B. R., ... Martin, F. L. (2014). Using Fourier transform IR spectroscopy to analyze biological materials. *Nature Protocols*, 9(8), 1771–1791. <https://doi.org/10.1038/nprot.2014.110>
- Balkunde, R., Foroughi, L., Ewan, E., Emenecker, R., Cavalli, V., & Dixit, R. (2019). Mechanism of microtubule plus-end tracking by the plant-specific SPR1 protein and its development as a versatile plus-end marker. *The Journal of Biological Chemistry*, 294(44), 16374–16384. <https://doi.org/10.1074/jbc.RA119.008866>
- Baskin, T. I. (2001). On the alignment of cellulose microfibrils by cortical microtubules: A review and a model. *Protoplasma*, 215(1–4), 150–171. <https://doi.org/10.1007/BF01280311>
- Baskin, T. I. (2005). Anisotropic Expansion of the Plant Cell Wall. *Annual Review of Cell and Developmental Biology*, 21(1), 203–222. <https://doi.org/10.1146/annurev.cellbio.20.082503.103053>
- Baster, P., Robert, S., Kleine-Vehn, J., Vanneste, S., Kania, U., Grunewald, W., Rybel, B. D., Beeckman, T., & Friml, J. (2013). SCFTIR1/AFB-auxin signalling regulates PIN vacuolar trafficking and auxin fluxes during root gravitropism. *The EMBO Journal*, 32(2), 260. <https://doi.org/10.1038/emboj.2012.310>

- Beauzamy, L., Nakayama, N., & Boudaoud, A. (2014). Flowers under pressure: Ins and outs of turgor regulation in development. *Annals of Botany*, 114(7), 1517–1533.
<https://doi.org/10.1093/aob/mcu187>
- Bellini, C., Pacurar, D. I., & Perrone, I. (2014). Adventitious Roots and Lateral Roots: Similarities and Differences. *Annual Review of Plant Biology*, 65(1), 639–666.
<https://doi.org/10.1146/annurev-arplant-050213-035645>
- Bello-Bello, E., López-Arredondo, D., Rico-Chambrón, T. Y., & Herrera-Estrella, L. (2022). Conquering compacted soils: Uncovering the molecular components of root soil penetration. *Trends in Plant Science*, 27(8), 814–827.
<https://doi.org/10.1016/j.tplants.2022.04.001>
- Benfey, P. N., Linstead, P. J., Roberts, K., Schiefelbein, J. W., Hauser, M.-T., & Aeschbacher, R. A. (1993). Root development in *Arabidopsis*: Four mutants with dramatically altered root morphogenesis. *Development*, 119, 57–70.
- Benfey, P. N., & Scheres, B. (2000). Root development. *Current Biology*, 10(22), R813–R815.
[https://doi.org/10.1016/S0960-9822\(00\)00814-9](https://doi.org/10.1016/S0960-9822(00)00814-9)
- Bengough, A. G., Loades, K., & McKenzie, B. M. (2016). Root hairs aid soil penetration by anchoring the root surface to pore walls. *Journal of Experimental Botany*, 67(4), 1071–1078. <https://doi.org/10.1093/jxb/erv560>
- Bethke, G., Thao, A., Xiong, G., Li, B., Soltis, N. E., Hatsugai, N., Hillmer, R. A., Katagiri, F., Kliebenstein, D. J., Pauly, M., & Glazebrook, J. (2016). Pectin Biosynthesis Is Critical for Cell Wall Integrity and Immunity in *Arabidopsis thaliana*. *The Plant Cell*, 28(2), 537–556. <https://doi.org/10.1105/tpc.15.00404>

- Bichet, A., Desnos, T., Turner, S., Grandjean, O., & Höfte, H. (2001). BOTERO1 is required for normal orientation of cortical microtubules and anisotropic cell expansion in *Arabidopsis*. *The Plant Journal*, 25(2), 137–148. <https://doi.org/10.1111/j.1365-313X.2001.00946.x>
- Bidhendi, A. J., Altartouri, B., Gosselin, F. P., & Geitmann, A. (2019). Mechanical Stress Initiates and Sustains the Morphogenesis of Wavy Leaf Epidermal Cells. *Cell Reports*, 28(5), 1237-1250.e6. <https://doi.org/10.1016/j.celrep.2019.07.006>
- Bidhendi, A. J., & Geitmann, A. (2019). Methods to quantify primary plant cell wall mechanics. *Journal of Experimental Botany*, 70(14), 3615–3648. <https://doi.org/10.1093/jxb/erz281>
- Bilkey, N., Li, H., Borodinov, N., Ievlev, A. V., Ovchinnikova, O. S., Dixit, R., & Foston, M. (2022). Correlated mechanochemical maps of *Arabidopsis thaliana* primary cell walls using atomic force microscope infrared spectroscopy. *Quantitative Plant Biology*, 3, e31. <https://doi.org/10.1017/qpb.2022.20>
- Bisgrove, S. R., Lee, Y.-R. J., Liu, B., Peters, N. T., & Kropf, D. L. (2008). The Microtubule Plus-End Binding Protein EB1 Functions in Root Responses to Touch and Gravity Signals in *Arabidopsis*. *The Plant Cell*, 20(2), 396–410. <https://doi.org/10.1105/tpc.107.056846>
- Blancaflor, E. B. (Ed.). (2015). *Plant Gravitropism* (Vol. 1309). Springer New York. <https://doi.org/10.1007/978-1-4939-2697-8>
- Blancaflor, E. B., & Masson, P. H. (2003). Plant Gravitropism. Unraveling the Ups and Downs of a Complex Process. *Plant Physiology*, 133(4), 1677–1690.
- Borodinov, N., Bilkey, N., Foston, M., Ievlev, A. V., Belianinov, A., Jesse, S., Vasudevan, R. K., Kalinin, S. V., & Ovchinnikova, O. S. (2019). Application of pan-sharpening algorithm

- for correlative multimodal imaging using AFM-IR. *Npj Computational Materials*, 5(1).
<https://doi.org/10.1038/s41524-019-0186-z>
- Bou Daher, F., Chen, Y., Bozorg, B., Clough, J. H., Jönsson, H., & Braybrook, S. A. (2018). *Anisotropic growth is achieved through the additive mechanical effect of material anisotropy and elastic asymmetry*. <https://doi.org/10.1101/316364>
- Boudaoud, A., Burian, A., Borowska-Wykręt, D., Uyttewaal, M., Wrzalik, R., Kwiatkowska, D., & Hamant, O. (2014). FibrilTool, an ImageJ plug-in to quantify fibrillar structures in raw microscopy images. *Nature Protocols*, 9(2), Article 2.
<https://doi.org/10.1038/nprot.2014.024>
- Bouton, S., Leboeuf, E., Mouille, G., Leydecker, M.-T., Talbotec, J., Granier, F., Lahaye, M., Höfte, H., & Truong, H.-N. (2002). QUASIMODO1 Encodes a Putative Membrane-Bound Glycosyltransferase Required for Normal Pectin Synthesis and Cell Adhesion in Arabidopsis. *The Plant Cell*, 14(10), 2577–2590. <https://doi.org/10.1105/tpc.004259>
- Braam, J. (2005). In touch: Plant responses to mechanical stimuli. *New Phytologist*, 165(2), 373–389. <https://doi.org/10.1111/j.1469-8137.2004.01263.x>
- Brading, K., Castellani, E., & Teh, N. (2021). Symmetry and Symmetry Breaking. In E. N. Zalta (Ed.), *The Stanford Encyclopedia of Philosophy* (Fall 2021). Metaphysics Research Lab, Stanford University. <https://plato.stanford.edu/archives/fall2021/entries/symmetry-breaking/>
- Brett, C. T. (2000). Cellulose microfibrils in plants: Biosynthesis, deposition, and integration into the cell wall. In *International Review of Cytology* (Vol. 199, pp. 161–199). Elsevier.
[https://doi.org/10.1016/S0074-7696\(00\)99004-1](https://doi.org/10.1016/S0074-7696(00)99004-1)

- Bringmann, M., Li, E., Sampathkumar, A., Kocabek, T., Hauser, M.-T., & Persson, S. (2012). POM-POM2/CELLULOSE SYNTHASE INTERACTING1 Is Essential for the Functional Association of Cellulose Synthase and Microtubules in Arabidopsis. *The Plant Cell*, 24(1), 163–177. <https://doi.org/10.1105/tpc.111.093575>
- Brunet, J.-P., Tamayo, P., Golub, T. R., & Mesirov, J. P. (2004). Metagenes and molecular pattern discovery using matrix factorization. *Proceedings of the National Academy of Sciences*, 101(12), 4164–4169. <https://doi.org/10.1073/pnas.0308531101>
- Buckberg, G. D. (2002). Basic science review: The helix and the heart. *The Journal of Thoracic and Cardiovascular Surgery*, 124(5), 863–883. <https://doi.org/10.1067/mtc.2002.122439>
- Bucksch, A., Burridge, J., York, L. M., Das, A., Nord, E., Weitz, J. S., & Lynch, J. P. (2014). Image-Based High-Throughput Field Phenotyping of Crop Roots. *PLANT PHYSIOLOGY*, 166(2), 470–486. <https://doi.org/10.1104/pp.114.243519>
- Buer, C. S., Wasteneys, G. O., & Masle, J. (2003). Ethylene Modulates Root-Wave Responses in Arabidopsis. *Plant Physiology*, 132(2), 1085–1096. <https://doi.org/10.1104/pp.102.019182>
- Bürstenbinder, K., Savchenko, T., Müller, J., Adamson, A. W., Stamm, G., Kwong, R., Zipp, B. J., Dinesh, D. C., & Abel, S. (2013). Arabidopsis Calmodulin-binding Protein IQ67-Domain 1 Localizes to Microtubules and Interacts with Kinesin Light Chain-related Protein-1*. *Journal of Biological Chemistry*, 288(3), 1871–1882. <https://doi.org/10.1074/jbc.M112.396200>
- Burton, R. A., Gidley, M. J., & Fincher, G. B. (2010). Heterogeneity in the chemistry, structure and function of plant cell walls. *Nature Chemical Biology*, 6(10), 724–732. <https://doi.org/10.1038/nchembio.439>

- Buschmann, H., & Borchers, A. (2020). Handedness in plant cell expansion: A mutant perspective on helical growth. *New Phytologist*, 225(1), 53–69.
<https://doi.org/10.1111/nph.16034>
- Buschmann, H., Fabri, C. O., Hauptmann, M., Hutzler, P., Laux, T., Lloyd, C. W., & Schäffner, A. R. (2004). Helical Growth of the Arabidopsis Mutant *tortifolia1* Reveals a Plant-Specific Microtubule-Associated Protein. *Current Biology*, 14(16), 1515–1521.
<https://doi.org/10.1016/j.cub.2004.08.033>
- Canteri, M. H. G., Renard, C. M. G. C., Le Bourvellec, C., & Bureau, S. (2019). ATR-FTIR spectroscopy to determine cell wall composition: Application on a large diversity of fruits and vegetables. *Carbohydrate Polymers*, 212, 186–196.
<https://doi.org/10.1016/j.carbpol.2019.02.021>
- Cavalier, D. M., Lerouxel, O., Neumetzler, L., Yamauchi, K., Reinecke, A., Freshour, G., Zabortina, O. A., Hahn, M. G., Burgert, I., Pauly, M., Raikhel, N. V., & Keegstra, K. (2008). Disrupting Two Arabidopsis thaliana Xylosyltransferase Genes Results in Plants Deficient in Xyloglucan, a Major Primary Cell Wall Component. *The Plant Cell*, 20(6), 1519–1537. <https://doi.org/10.1105/tpc.108.059873>
- Centrone, A. (2015). Infrared Imaging and Spectroscopy Beyond the Diffraction Limit. *Annual Review of Analytical Chemistry*, 8(1), 101–126. <https://doi.org/10.1146/annurev-anchem-071114-040435>
- Chang, H., Liu, Q., Zimmerman, J. F., Lee, K. Y., Jin, Q., Peters, M. M., Rosnach, M., Choi, S., Kim, S. L., Ardoña, H. A. M., MacQueen, L. A., Chantre, C. O., Motta, S. E., Cordoves, E. M., & Parker, K. K. (2022). Recreating the heart's helical structure-function

- relationship with focused rotary jet spinning. *Science*, 377(6602), 180–185.
<https://doi.org/10.1126/science.abl6395>
- Chebli, Y., Bidhendi, A. J., Kapoor, K., & Geitmann, A. (2021). Cytoskeletal regulation of primary plant cell wall assembly. *Current Biology*, 31(10), R681–R695.
<https://doi.org/10.1016/j.cub.2021.03.092>
- Chen, Y., Yordanov, Y. S., Ma, C., Strauss, S., & Busov, V. B. (2013). DR5 as a reporter system to study auxin response in *Populus*. *Plant Cell Reports*, 32(3), 453–463.
<https://doi.org/10.1007/s00299-012-1378-x>
- Christeller, J., & Laing, W. (2005). Plant Serine Proteinase Inhibitors. *Protein & Peptide Letters*, 12(5), 439–447.
- Clède, S., Lambert, F., Sandt, C., Kascakova, S., Unger, M., Harté, E., Plamont, M.-A., Saint-Fort, R., Deniset-Besseau, A., Gueroui, Z., Hirschmugl, C., Lecomte, S., Dazzi, A., Vessièrès, A., & Policar, C. (2013). Detection of an estrogen derivative in two breast cancer cell lines using a single core multimodal probe for imaging (SCoMPI) imaged by a panel of luminescent and vibrational techniques. *Analyst*, 138(19), 5627–5638.
<https://doi.org/10.1039/C3AN00807J>
- Colombi, T., & Keller, T. (2019). Developing strategies to recover crop productivity after soil compaction—A plant eco-physiological perspective. *Soil and Tillage Research*, 191, 156–161. <https://doi.org/10.1016/j.still.2019.04.008>
- Constantino, M. A., Jabbarzadeh, M., Fu, H. C., & Bansil, R. (2016). Helical and rod-shaped bacteria swim in helical trajectories with little additional propulsion from helical shape. *Science Advances*, 2(11), e1601661. <https://doi.org/10.1126/sciadv.1601661>

- Cosgrove, D. J. (2000). Expansive growth of plant cell walls. *Plant Physiology and Biochemistry*, 38(1), 109–124. [https://doi.org/10.1016/S0981-9428\(00\)00164-9](https://doi.org/10.1016/S0981-9428(00)00164-9)
- Cosgrove, D. J. (2005). Growth of the plant cell wall. *Nature Reviews Molecular Cell Biology*, 6(11), 850–861. <https://doi.org/10.1038/nrm1746>
- Cosgrove, D. J. (2014). Re-constructing our models of cellulose and primary cell wall assembly. *Current Opinion in Plant Biology*, 22, 122–131. <https://doi.org/10.1016/j.pbi.2014.11.001>
- Cosgrove, D. J. (2018). Nanoscale structure, mechanics and growth of epidermal cell walls. *Current Opinion in Plant Biology*, 46, 77–86. <https://doi.org/10.1016/j.pbi.2018.07.016>
- Coste, R., Soliman, M., Bercu, N. B., Potiron, S., Lasri, K., Aguié-Béghin, V., Tetard, L., Chabbert, B., & Molinari, M. (2021). Unveiling the impact of embedding resins on the physicochemical traits of wood cell walls with subcellular functional probing. *Composites Science and Technology*, 201, 108485. <https://doi.org/10.1016/j.compscitech.2020.108485>
- Cuello, C., Marchand, P., Laurans, F., Grand-Perret, C., Lainé-Prade, V., Pilate, G., & Déjardin, A. (2020). ATR-FTIR Microspectroscopy Brings a Novel Insight Into the Study of Cell Wall Chemistry at the Cellular Level. *Frontiers in Plant Science*, 11. <https://doi.org/10.3389/fpls.2020.00105>
- Cullen, C. L., O'Rourke, M., Beasley, S. J., Auderset, L., Zhen, Y., Pepper, R. E., Gasperini, R., & Young, K. M. (2021). Kif3a deletion prevents primary cilia assembly on oligodendrocyte progenitor cells, reduces oligodendrogenesis and impairs fine motor function. *Glia*, 69(5), 1184. <https://doi.org/10.1002/glia.23957>
- Cutler, S. R., Ehrhardt, D. W., Griffiths, J. S., & Somerville, C. R. (2000). Random GFP::cDNA fusions enable visualization of subcellular structures in cells of Arabidopsis at a high

- frequency. *Proceedings of the National Academy of Sciences*, 97(7), 3718–3723.
<https://doi.org/10.1073/pnas.97.7.3718>
- Cyr, R. J., & Palevitz, B. A. (1995). Organization of cortical microtubules in plant cells. *Current Opinion in Cell Biology*, 7(1), 65–71. [https://doi.org/10.1016/0955-0674\(95\)80046-8](https://doi.org/10.1016/0955-0674(95)80046-8)
- Daher, F. B., & Braybrook, S. A. (2015). How to let go: Pectin and plant cell adhesion. *Frontiers in Plant Science*, 6. <https://doi.org/10.3389/fpls.2015.00523>
- Darvas, G. (2007). *Symmetry: Cultural-historical and Ontological Aspects of Science-Arts Relations; the Natural and Man-made World in an Interdisciplinary Approach*. Springer Science & Business Media.
- Darwin, C. (1862). *On the various contrivances by which British and foreign orchids are fertilised by insects, and on the good effects of intercrossing*. John Murray. <http://darwin-online.org.uk/content/frameset?pageseq=1&itemID=F800&viewtype=text>
- Darwin, C. (1865). On the Movements and Habits of Climbing Plants. *Journal of the Linnean Society of London, Botany*, 9(33–34), 1–118. <https://doi.org/10.1111/j.1095-8339.1865.tb00011.x>
- Darwin, C., Darwin, F., & University of Leeds. (1880). *The Power of Movement in Plants*. John Murray. <https://doi.org/10.5962/bhl.title.102319>
- Datta, S., Kim, C. M., Pernas, M., Pires, N. D., Proust, H., Tam, T., Vijayakumar, P., & Dolan, L. (2011). Root hairs: Development, growth and evolution at the plant-soil interface. *Plant and Soil*, 346(1), 1–14. <https://doi.org/10.1007/s11104-011-0845-4>
- Dazzi, A., & Prater, C. B. (2017). AFM-IR: Technology and Applications in Nanoscale Infrared Spectroscopy and Chemical Imaging. *Chemical Reviews*, 117(7), 5146–5173.
<https://doi.org/10.1021/acs.chemrev.6b00448>

- Dazzi, A., Prater, C. B., Hu, Q., Chase, D. B., Rabolt, J. F., & Marcott, C. (2012). AFM-IR: Combining atomic force microscopy and infrared spectroscopy for nanoscale chemical characterization. *Applied Spectroscopy*, 66(12), 1365–1384. <https://doi.org/10.1366/12-06804>
- Dazzi, A., Prazeres, R., Glotin, F., & Ortega, J. M. (2005). Local infrared microspectroscopy with subwavelength spatial resolution with an atomic force microscope tip used as a photothermal sensor. *Optics Letters*, 30(18), 2388. <https://doi.org/10.1364/OL.30.002388>
- Decaestecker, W., Buono, R. A., Pfeiffer, M. L., Vangheluwe, N., Jourquin, J., Karimi, M., Van Isterdael, G., Beeckman, T., Nowack, M. K., & Jacobs, T. B. (2019). CRISPR-TSKO: A Technique for Efficient Mutagenesis in Specific Cell Types, Tissues, or Organs in Arabidopsis[OPEN]. *The Plant Cell*, 31(12), 2868–2887. <https://doi.org/10.1105/tpc.19.00454>
- Decou, R., Serk, H., Ménard, D., & Pesquet, E. (2017). Analysis of Lignin Composition and Distribution Using Fluorescence Laser Confocal Microspectroscopy. In M. de Lucas & J. P. Etchells (Eds.), *Xylem: Methods and Protocols* (pp. 233–247). Springer. https://doi.org/10.1007/978-1-4939-6722-3_17
- Del Dottore, E., Mondini, A., Sadeghi, A., Mattoli, V., & Mazzolai, B. (2017). An efficient soil penetration strategy for explorative robots inspired by plant root circumnutation movements. *Bioinspiration & Biomimetics*, 13(1), 015003. <https://doi.org/10.1088/1748-3190/aa9998>
- Delk, N. A., Johnson, K. A., Chowdhury, N. I., & Braam, J. (2005). CML24, Regulated in Expression by Diverse Stimuli, Encodes a Potential Ca²⁺ Sensor That Functions in

- Responses to Absciscic Acid, Daylength, and Ion Stress. *Plant Physiology*, 139(1), 240–253. <https://doi.org/10.1104/pp.105.062612>
- Demarty, M., Morvan, C., & Thellier, M. (1984). Calcium and the cell wall. *Plant, Cell & Environment*, 7(6), 441–448. <https://doi.org/10.1111/j.1365-3040.1984.tb01434.x>
- Deng, X., Llamazares, A. G., Wagstaff, J., Hale, V. L., Cannone, G., McLaughlin, S. H., Kureisaite-Ciziene, D., & Löwe, J. (2019). The structure of bactofilin filaments reveals their mode of membrane binding and lack of polarity. *Nature Microbiology*, 4(12), 2357–2368. <https://doi.org/10.1038/s41564-019-0544-0>
- Diotallevi, F., & Mulder, B. (2007). The Cellulose Synthase Complex: A Polymerization Driven Supramolecular Motor. *Biophysical Journal*, 92(8), 2666–2673. <https://doi.org/10.1529/biophysj.106.099473>
- Dixit, R., & Cyr, R. (2004). The Cortical Microtubule Array: From Dynamics to Organization. *The Plant Cell*, 16(10), 2546–2552. <https://doi.org/10.1105/tpc.104.161030>
- Dodd, A. N., Kudla, J., & Sanders, D. (2010). The Language of Calcium Signaling. *Annual Review of Plant Biology*, 61(1), 593–620. <https://doi.org/10.1146/annurev-arplant-070109-104628>
- Dong, R., & Yu, L. E. (2003). Investigation of Surface Changes of Nanoparticles Using TM-AFM Phase Imaging. *Environmental Science & Technology*, 37(12), 2813–2819. <https://doi.org/10.1021/es034071k>
- Downie, H. F., Adu, M. O., Schmidt, S., Otten, W., Dupuy, L. X., White, P. J., & Valentine, T. A. (2015). Challenges and opportunities for quantifying roots and rhizosphere interactions through imaging and image analysis. *Plant, Cell & Environment*, 38(7), 1213–1232. <https://doi.org/10.1111/pce.12448>

- Du, J., Kirui, A., Huang, S., Wang, L., Barnes, W. J., Kiemle, S. N., Zheng, Y., Rui, Y., Ruan, M., Qi, S., Kim, S. H., Wang, T., Cosgrove, D. J., Anderson, C. T., & Xiao, C. (2020). Mutations in the Pectin Methyltransferase QUASIMODO2 Influence Cellulose Biosynthesis and Wall Integrity in Arabidopsis. *The Plant Cell*, 32(11), 3576–3597. <https://doi.org/10.1105/tpc.20.00252>
- Durham Brooks, T. L., Miller, N. D., & Spalding, E. P. (2010). Plasticity of Arabidopsis Root Gravitropism throughout a Multidimensional Condition Space Quantified by Automated Image Analysis. *PLANT PHYSIOLOGY*, 152(1), 206–216. <https://doi.org/10.1104/pp.109.145292>
- Efimov, A. V. (2018). Chirality and Handedness of Protein Structures. *Biochemistry (Moscow)*, 83(1), S103–S110. <https://doi.org/10.1134/S0006297918140092>
- Endress, P. K. (1999). Symmetry in Flowers: Diversity and Evolution. *International Journal of Plant Sciences*, 160(S6), S3–S23. <https://doi.org/10.1086/314211>
- Fagard, M., Desnos, T., Desprez, T., Goubet, F., Refregier, G., Mouille, G., McCann, M., Rayon, C., Vernhettes, S., & Höfte, H. (2000). PROCUSTE1 Encodes a Cellulose Synthase Required for Normal Cell Elongation Specifically in Roots and Dark-Grown Hypocotyls of Arabidopsis. *The Plant Cell*, 12(12), 2409–2423.
- Fan, J., McConkey, B., Wang, H., & Janzen, H. (2016). Root distribution by depth for temperate agricultural crops. *Field Crops Research*, 189, 68–74. <https://doi.org/10.1016/j.fcr.2016.02.013>
- Fan, Y., Burkart, G. M., & Dixit, R. (2018). The Arabidopsis SPIRAL2 Protein Targets and Stabilizes Microtubule Minus Ends. *Current Biology*, 28(6), 987-994.e3. <https://doi.org/10.1016/j.cub.2018.02.014>

- Farahi, R. H., Charrier, A. M., Tolbert, A., Lereu, A. L., Ragauskas, A., Davison, B. H., & Passian, A. (2017). Plasticity, elasticity, and adhesion energy of plant cell walls: Nanometrology of lignin loss using atomic force microscopy. *Scientific Reports*, 7(1). <https://doi.org/10.1038/s41598-017-00234-4>
- French, A., Ubeda-Tomás, S., Holman, T. J., Bennett, M. J., & Pridmore, T. (2009). High-Throughput Quantification of Root Growth Using a Novel Image-Analysis Tool. *Plant Physiology*, 150(4), 1784–1795. <https://doi.org/10.1104/pp.109.140558>
- Friml, J., Vieten, A., Sauer, M., Weijers, D., Schwarz, H., Hamann, T., Offringa, R., & Jürgens, G. (2003). Efflux-dependent auxin gradients establish the apical–basal axis of Arabidopsis. *Nature*, 426(6963), Article 6963. <https://doi.org/10.1038/nature02085>
- Fry, S. C. (2010). Cell Wall Polysaccharide Composition and Covalent Crosslinking. In *Annual Plant Reviews* (pp. 1–42). John Wiley & Sons, Ltd. <https://doi.org/10.1002/9781444391015.ch1>
- Fukuda, H. (1997). Tracheary Element Differentiation. *The Plant Cell*, 9(7), 1147–1156.
- Full, R. J., Yamauchi, A., & Jindrich, D. L. (1995). Maximum single leg force production: Cockroaches righting on photoelastic gelatin. *Journal of Experimental Biology*, 198(12), 2441–2452. <https://doi.org/10.1242/jeb.198.12.2441>
- Furbank, R. T., & Tester, M. (2011). Phenomics – technologies to relieve the phenotyping bottleneck. *Trends in Plant Science*, 16(12), 635–644. <https://doi.org/10.1016/j.tplants.2011.09.005>
- Furutani, I., Watanabe, Y., Prieto, R., Masukawa, M., Suzuki, K., Naoi, K., Thitamadee, S., Shikanai, T., & Hashimoto, T. (2000). The SPIRAL genes are required for directional control of cell elongation in Arabidopsis thaliana. *Development*, 127, 4443–4453.

- Galva, C., Kirik, V., Lindeboom, J. J., Kaloriti, D., Rancour, D. M., Hussey, P. J., Bednarek, S. Y., Ehrhardt, D. W., & Sedbrook, J. C. (2014). The Microtubule Plus-End Tracking Proteins SPR1 and EB1b Interact to Maintain Polar Cell Elongation and Directional Organ Growth in *Arabidopsis*. *The Plant Cell*, 26(11), 4409–4425.
<https://doi.org/10.1105/tpc.114.131482>
- Ganguly, A., Zhu, C., Chen, W., & Dixit, R. (2020). FRA1 Kinesin Modulates the Lateral Stability of Cortical Microtubules Through Cellulose Synthase-Microtubule Uncoupling Protein. *The Plant Cell*, tpc.00700.2019. <https://doi.org/10.1105/tpc.19.00700>
- Gautam, R., Vanga, S., Ariese, F., & Umapathy, S. (2015). Review of multidimensional data processing approaches for Raman and infrared spectroscopy. *EPJ Techniques and Instrumentation*, 2(1). <https://doi.org/10.1140/epjti/s40485-015-0018-6>
- Gierlinger, N. (2014). Revealing changes in molecular composition of plant cell walls on the micron-level by Raman mapping and vertex component analysis (VCA). *Frontiers in Plant Science*, 5. <https://doi.org/10.3389/fpls.2014.00306>
- Gierlinger, N. (2017). New insights into plant cell walls by vibrational microspectroscopy. *Applied Spectroscopy Reviews*, 53(7), 517–551.
<https://doi.org/10.1080/05704928.2017.1363052>
- Gierlinger, N., & Schwanninger, M. (2006). Chemical Imaging of Poplar Wood Cell Walls by Confocal Raman Microscopy. *Plant Physiology*, 140(4), 1246–1254.
<https://doi.org/10.1104/pp.105.066993>
- González, M. G., Cabanelas, J. C., & Baselga, J. (2012). Applications of FTIR on Epoxy Resins—Identification, Monitoring the Curing Process, Phase Separation and Water

- Uptake. In T. Theophanides (Ed.), *Infrared Spectroscopy—Materials Science, Engineering and Technology*. InTech. <https://doi.org/10.5772/36323>
- Goodsell, D. S., & Olson, A. J. (2000). Structural Symmetry and Protein Function. *Annual Review of Biophysics and Biomolecular Structure*, 29(1), 105–153.
<https://doi.org/10.1146/annurev.biophys.29.1.105>
- Gourion-Arsiquaud, S., Marcott, C., Hu, Q., & Boskey, A. L. (2014). Studying Variations in Bone Composition at Nano-Scale Resolutions: A Preliminary Report. *Calcified Tissue International*, 95(5), 413–418. <https://doi.org/10.1007/s00223-014-9909-9>
- Green, P. B. (1962). Mechanism for Plant Cellular Morphogenesis. *Science*, 138(3548), 1404–1405. <https://doi.org/10.1126/science.138.3548.1404>
- Grones, P., Raggi, S., & Robert, S. (2019). FORCE-ing the shape. *Current Opinion in Plant Biology*, 52, 1–6. <https://doi.org/10.1016/j.pbi.2019.05.008>
- Gu, Y., Kaplinsky, N., Bringmann, M., Cobb, A., Carroll, A., Sampathkumar, A., Baskin, T. I., Persson, S., & Somerville, C. R. (2010). Identification of a cellulose synthase-associated protein required for cellulose biosynthesis. *Proceedings of the National Academy of Sciences*, 107(29), 12866–12871. <https://doi.org/10.1073/pnas.1007092107>
- Guo, Y. (Ed.). (2018). *Plant Senescence: Methods and Protocols* (Vol. 1744). Springer New York. <https://doi.org/10.1007/978-1-4939-7672-0>
- Haigler, C. H., Grimson, M. J., Gervais, J., Moigne, N. L., Höfte, H., Monasse, B., & Navard, P. (2014). Molecular Modeling and Imaging of Initial Stages of Cellulose Fibril Assembly: Evidence for a Disordered Intermediate Stage. *PLOS ONE*, 9(4), e93981.
<https://doi.org/10.1371/journal.pone.0093981>

- Hamant, O., Heisler, M. G., Jönsson, H., Krupinski, P., Uyttewaal, M., Bokov, P., Corson, F., Sahlin, P., Boudaoud, A., Meyerowitz, E. M., Couder, Y., & Traas, J. (2008). Developmental Patterning by Mechanical Signals in Arabidopsis. *Science*, 322(5908), 1650–1655. <https://doi.org/10.1126/science.1165594>
- Hecht, J. (2004, June 3). *Tiny fossils reveal key step in animal evolution*. New Scientist. <https://www.newscientist.com/article/dn5070-tiny-fossils-reveal-key-step-in-animal-evolution/>
- Heeraman, D. A., Hopmans, J. W., & Clausnitzer, V. (1997). Three dimensional imaging of plant roots in situ with X-ray Computed Tomography. *Plant and Soil*, 189(2), 167–179. <https://doi.org/10.1023/B:PLSO.0000009694.64377.6f>
- Heisler, M. G., Hamant, O., Krupinski, P., Uyttewaal, M., Ohno, C., Jönsson, H., Traas, J., & Meyerowitz, E. M. (2010). Alignment between PIN1 Polarity and Microtubule Orientation in the Shoot Apical Meristem Reveals a Tight Coupling between Morphogenesis and Auxin Transport. *PLOS Biology*, 8(10), e1000516. <https://doi.org/10.1371/journal.pbio.1000516>
- Helariutta, Y., Fukaki, H., Wysocka-Diller, J., Nakajima, K., Jung, J., Sena, G., Hauser, M.-T., & Benfey, P. N. (2000). The SHORT-ROOT Gene Controls Radial Patterning of the Arabidopsis Root through Radial Signaling. *Cell*, 101(5), 555–567. [https://doi.org/10.1016/S0092-8674\(00\)80865-X](https://doi.org/10.1016/S0092-8674(00)80865-X)
- Henley, C. L. (2012). Possible Origins of Macroscopic Left-Right Asymmetry in Organisms. *Journal of Statistical Physics*, 148(4), 741–775. <https://doi.org/10.1007/s10955-012-0520-z>

- Herrero-Huerta, M., Raunonen, P., & Gonzalez-Aguilera, D. (2022). 4DRoot: Root phenotyping software for temporal 3D scans by X-ray computed tomography. *Frontiers in Plant Science*, 13. <https://www.frontiersin.org/articles/10.3389/fpls.2022.986856>
- Hirokawa, N., Tanaka, Y., & Okada, Y. (2009). Left–Right Determination: Involvement of Molecular Motor KIF3, Cilia, and Nodal Flow. *Cold Spring Harbor Perspectives in Biology*, 1(1), a000802. <https://doi.org/10.1101/cshperspect.a000802>
- Hochholdinger, F., Park, W. J., Sauer, M., & Woll, K. (2004). From weeds to crops: Genetic analysis of root development in cereals. *Trends in Plant Science*, 9(1), 42–48. <https://doi.org/10.1016/j.tplants.2003.11.003>
- Höfte, H., Peaucelle, A., & Braybrook, S. (2012). Cell wall mechanics and growth control in plants: The role of pectins revisited. *Frontiers in Plant Science*, 3, 121. <https://doi.org/10.3389/fpls.2012.00121>
- Holló, G., & Novák, M. (2012). The manoeuvrability hypothesis to explain the maintenance of bilateral symmetry in animal evolution. *Biology Direct*, 7(1), 22. <https://doi.org/10.1186/1745-6150-7-22>
- Hozumi, S., Maeda, R., Taniguchi, K., Kanai, M., Shirakabe, S., Sasamura, T., Spéder, P., Noselli, S., Aigaki, T., Murakami, R., & Matsuno, K. (2006). An unconventional myosin in *Drosophila* reverses the default handedness in visceral organs. *Nature*, 440(7085), Article 7085. <https://doi.org/10.1038/nature04625>
- Huang, K. C., Ehrhardt, D., & Shaevitz, J. W. (2012). The molecular origins of chiral growth in walled cells. *Current Opinion in Microbiology*, 15(6), 707–714. <https://doi.org/10.1016/j.mib.2012.11.002>

- Hutchins, L. N., Murphy, S. M., Singh, P., & Graber, J. H. (2008). Position-dependent motif characterization using non-negative matrix factorization. *Bioinformatics*, 24(23), 2684–2690. <https://doi.org/10.1093/bioinformatics/btn526>
- Iijima, M., Kato, J., & Taniguchi, A. (2007). Combined Soil Physical Stress of Soil Drying, Anaerobiosis and Mechanical Impedance to Seedling Root Growth of Four Crop Species. *Plant Production Science*, 10(4), 451–459. <https://doi.org/10.1626/pps.10.451>
- Inaki, M., Liu, J., & Matsuno, K. (2016). Cell chirality: Its origin and roles in left–right asymmetric development. *Philosophical Transactions of the Royal Society B: Biological Sciences*, 371(1710), 20150403. <https://doi.org/10.1098/rstb.2015.0403>
- Ishida, T., Kaneko, Y., Iwano, M., & Hashimoto, T. (2007). Helical microtubule arrays in a collection of twisting tubulin mutants of *Arabidopsis thaliana*. *Proceedings of the National Academy of Sciences*, 104(20), 8544–8549. <https://doi.org/10.1073/pnas.0701224104>
- Jacobsen, A. G. R., Jervis, G., Xu, J., Topping, J. F., & Lindsey, K. (2021). Root growth responses to mechanical impedance are regulated by a network of ROS, ethylene and auxin signalling in *Arabidopsis*. *The New Phytologist*, 231(1), 225–242. <https://doi.org/10.1111/nph.17180>
- Jamet, E., Canut, H., Boudart, G., & Pont-Lezica, R. F. (2006). Cell wall proteins: A new insight through proteomics. *Trends in Plant Science*, 11(1), 33–39. <https://doi.org/10.1016/j.tplants.2005.11.006>
- Jiang, N., Floro, E., Bray, A. L., Laws, B., Duncan, K. E., & Topp, C. N. (2019). Three-Dimensional Time-Lapse Analysis Reveals Multiscale Relationships in Maize Root

- Systems with Contrasting Architectures. *The Plant Cell*, 31(8), 1708–1722.
<https://doi.org/10.1105/tpc.19.00015>
- Juan, T., Géminard, C., Coutelis, J.-B., Cerezo, D., Polès, S., Noselli, S., & Fürthauer, M. (2018). Myosin1D is an evolutionarily conserved regulator of animal left–right asymmetry. *Nature Communications*, 9(1), Article 1. <https://doi.org/10.1038/s41467-018-04284-8>
- Julkowska, M. M., Koevoets, I. T., Mol, S., Hoefsloot, H., Feron, R., Tester, M. A., Keurentjes, J. J. B., Korte, A., Haring, M. A., de Boer, G.-J., & Testerink, C. (2017). Genetic Components of Root Architecture Remodeling in Response to Salt Stress[OPEN]. *The Plant Cell*, 29(12), 3198–3213. <https://doi.org/10.1105/tpc.16.00680>
- Keller, B. (1993). Structural Cell Wall Proteins. *Plant Physiology*, 101(4), 1127–1130.
<https://doi.org/10.1104/pp.101.4.1127>
- Kellman, M. E. (1996). Symmetry in chemistry from the hydrogen atom to proteins. *Proceedings of the National Academy of Sciences*, 93(25), 14287–14294.
<https://doi.org/10.1073/pnas.93.25.14287>
- Kim, S. Y., Khanal, D., Tharkar, P., Kalionis, B., & Chrzanowski, W. (2018). None of us is the same as all of us: Resolving the heterogeneity of extracellular vesicles using single-vesicle, nanoscale characterization with resonance enhanced atomic force microscope infrared spectroscopy (AFM-IR). *Nanoscale Horizons*, 3(4), 430–438.
<https://doi.org/10.1039/C8NH00048D>
- Kirik, V., Simon, M., Huelskamp, M., & Schiefelbein, J. (2004). The ENHANCER OF TRY AND CPC1 gene acts redundantly with TRIPTYCHON and CAPRICE in trichome and

- root hair cell patterning in *Arabidopsis*. *Developmental Biology*, 268(2), 506–513.
<https://doi.org/10.1016/j.ydbio.2003.12.037>
- Kirkegaard, J. A., Lilley, J. M., Howe, G. N., Graham, J. M., Kirkegaard, J. A., Lilley, J. M.,
 Howe, G. N., & Graham, J. M. (2007). Impact of subsoil water use on wheat yield.
Australian Journal of Agricultural Research, 58(4), 303–315.
<https://doi.org/10.1071/AR06285>
- Kong, Y., Peña, M. J., Renna, L., Avci, U., Pattathil, S., Tuomivaara, S. T., Li, X., Reiter, W.-D.,
 Brandizzi, F., Hahn, M. G., Darvill, A. G., York, W. S., & O'Neill, M. A. (2015).
 Galactose-Depleted Xyloglucan Is Dysfunctional and Leads to Dwarfism in *Arabidopsis*.
Plant Physiology, 167(4), 1296–1306. <https://doi.org/10.1104/pp.114.255943>
- Koontz, L. (2014). Chapter One—TCA Precipitation. In J. Lorsch (Ed.), *Methods in Enzymology*
 (Vol. 541, pp. 3–10). Academic Press. <https://doi.org/10.1016/B978-0-12-420119-4.00001-X>
- Korolev, A. V., Buschmann, H., Doonan, J. H., & Lloyd, C. W. (2007). AtMAP70-5, a divergent
 member of the MAP70 family of microtubule-associated proteins, is required for
 anisotropic cell growth in *Arabidopsis*. *Journal of Cell Science*, 120(13), 2241–2247.
<https://doi.org/10.1242/jcs.007393>
- Kulkarni, P., Dost, M., Bulut, Ö. D., Welle, A., Böcker, S., Boland, W., & Svatoš, A. (2018).
 Secondary ion mass spectrometry imaging and multivariate data analysis reveal co-
 aggregation patterns of *Populus trichocarpa* leaf surface compounds on a micrometer
 scale. *The Plant Journal*, 93(1), 193–206. <https://doi.org/10.1111/tpj.13763>

- Kurouski, D., Dazzi, A., Zenobi, R., & Centrone, A. (2020). Infrared and Raman chemical imaging and spectroscopy at the nanoscale. *Chemical Society Reviews*.
<https://doi.org/10.1039/c8cs00916c>
- Kutschera, U., & Niklas, K. J. (2007). The epidermal-growth-control theory of stem elongation: An old and a new perspective. *Journal of Plant Physiology*, 164(11), 1395–1409.
<https://doi.org/10.1016/j.jplph.2007.08.002>
- Labbe, N., Rials, T. G., Kelley, S. S., Cheng, Z.-M., Kim, J.-Y., & Li, Y. (2005). FT-IR imaging and pyrolysis-molecular beam mass spectrometry: New tools to investigate wood tissues. *Wood Science and Technology*, 39(1), 61–76. <https://doi.org/10.1007/s00226-004-0274-0>
- Lampugnani, E. R., Khan, G. A., Somssich, M., & Persson, S. (2018). Building a plant cell wall at a glance. *Journal of Cell Science*, 131(2), jcs207373.
<https://doi.org/10.1242/jcs.207373>
- Landrein, B., Lathe, R., Bringmann, M., Vouillot, C., Ivakov, A., Boudaoud, A., Persson, S., & Hamant, O. (2013). Impaired Cellulose Synthase Guidance Leads to Stem Torsion and Twists Phyllotactic Patterns in Arabidopsis. *Current Biology*, 23(10), 895–900.
<https://doi.org/10.1016/j.cub.2013.04.013>
- Le Bot, J., Serra, V., Fabre, J., Draye, X., Adamowicz, S., & Pagès, L. (2010). DART: A software to analyse root system architecture and development from captured images. *Plant and Soil*, 326(1), 261–273. <https://doi.org/10.1007/s11104-009-0005-2>
- Lebreton, G., Géminard, C., Lapraz, F., Pyrpassopoulos, S., Cerezo, D., Spéder, P., Ostap, E. M., & Noselli, S. (2018). Molecular to organismal chirality is induced by the conserved myosin 1D. *Science*, 362(6417), 949–952. <https://doi.org/10.1126/science.aat8642>

- Lee, H.-J., Kim, H.-S., Park, J. M., Cho, H. S., & Jeon, J. H. (2020). PIN-mediated polar auxin transport facilitates root–obstacle avoidance. *New Phytologist*, 225(3), 1285–1296.
<https://doi.org/10.1111/nph.16076>
- Lee, M. M., & Schiefelbein, J. (1999). WEREWOLF, a MYB-Related Protein in Arabidopsis, Is a Position-Dependent Regulator of Epidermal Cell Patterning. *Cell*, 99(5), 473–483.
[https://doi.org/10.1016/S0092-8674\(00\)81536-6](https://doi.org/10.1016/S0092-8674(00)81536-6)
- Legué, V., Blancaflor, E., Wymer, C., Perbal, G., Fantin, D., & Gilroy, S. (1997). Cytoplasmic free Ca²⁺ in Arabidopsis roots changes in response to touch but not gravity. *Plant Physiology*, 114(3), 789–800.
- Lemon, D. J., Yang, X., Srivastava, P., Luk, Y.-Y., & Garza, A. G. (2017). Polymertropism of rod-shaped bacteria: Movement along aligned polysaccharide fibers. *Scientific Reports*, 7(1), Article 1. <https://doi.org/10.1038/s41598-017-07486-0>
- Levy, M., Wang, Q., Kaspi, R., Parrella, M. P., & Abel, S. (2005). Arabidopsis IQD1, a novel calmodulin-binding nuclear protein, stimulates glucosinolate accumulation and plant defense. *The Plant Journal*, 43(1), 79–96. <https://doi.org/10.1111/j.1365-313X.2005.02435.x>
- Li, B., Zhang, X., Morita, S., Sekiya, N., Araki, H., Gu, H., Han, J., Lu, Y., & Liu, X. (2022). Are crop deep roots always beneficial for combating drought: A review of root structure and function, regulation and phenotyping. *Agricultural Water Management*, 271, 107781.
<https://doi.org/10.1016/j.agwat.2022.107781>
- Li, S., Lei, L., Somerville, C. R., & Gu, Y. (2012). Cellulose synthase interactive protein 1 (CSI1) links microtubules and cellulose synthase complexes. *Proceedings of the National Academy of Sciences*, 109(1), 185–190. <https://doi.org/10.1073/pnas.1118560109>

- Lin, H., Zhang, Y., Wang, Q., Li, B., Fan, S., & Wang, Z. (2018). Species identification of bloodstains by ATR-FTIR spectroscopy: The effects of bloodstain age and the deposition environment. *International Journal of Legal Medicine*, 132(3), 667–674.
<https://doi.org/10.1007/s00414-017-1634-2>
- Liu, Z., Schneider, R., Kesten, C., Zhang, Y., Somssich, M., Zhang, Y., Fernie, A. R., & Persson, S. (2016). Cellulose-Microtubule Uncoupling Proteins Prevent Lateral Displacement of Microtubules during Cellulose Synthesis in Arabidopsis. *Developmental Cell*, 38(3), 305–315. <https://doi.org/10.1016/j.devcel.2016.06.032>
- Lloyd, C. (2006). Microtubules Make Tracks for Cellulose. *Science*, 312(5779), 1482–1483.
<https://doi.org/10.1126/science.1128903>
- Lloyd, C. (2011). Chapter seven—Dynamic Microtubules and the Texture of Plant Cell Walls. In K. W. Jeon (Ed.), *International Review of Cell and Molecular Biology* (Vol. 287, pp. 287–329). Academic Press. <https://doi.org/10.1016/B978-0-12-386043-9.00007-4>
- Lobet, G., Pagès, L., & Draye, X. (2011). A Novel Image-Analysis Toolbox Enabling Quantitative Analysis of Root System Architecture1[W][OA]. *Plant Physiology*, 157(1), 29–39. <https://doi.org/10.1104/pp.111.179895>
- Lynch, J. P. (2018). Rightsizing root phenotypes for drought resistance. *Journal of Experimental Botany*, 69(13), 3279–3292. <https://doi.org/10.1093/jxb/ery048>
- Macleod, K. (2015, August 13). *How Does Symmetry Shape Nature's Laws?* Quanta Magazine.
<https://www.quantamagazine.org/videos/how-does-symmetry-shape-natures-laws-2/>
- Maeght, J.-L., Rewald, B., & Pierret, A. (2013). How to study deep roots—And why it matters. *Frontiers in Plant Science*, 4.
<https://www.frontiersin.org/articles/10.3389/fpls.2013.00299>

- Majda, M., Grones, P., Sintorn, I.-M., Vain, T., Milani, P., Krupinski, P., Zagórska-Marek, B., Viotti, C., Jönsson, H., Mellerowicz, E. J., Hamant, O., & Robert, S. (2017). Mechanochemical Polarization of Contiguous Cell Walls Shapes Plant Pavement Cells. *Developmental Cell*, 43(3), 290-304.e4. <https://doi.org/10.1016/j.devcel.2017.10.017>
- Marga, F., Grandbois, M., Cosgrove, D. J., & Baskin, T. I. (2005). Cell wall extension results in the coordinate separation of parallel microfibrils: Evidence from scanning electron microscopy and atomic force microscopy. *The Plant Journal*, 43(2), 181–190. <https://doi.org/10.1111/j.1365-313X.2005.02447.x>
- Marquès-Bueno, M. M., Morao, A. K., Cayrel, A., Platre, M. P., Barberon, M., Caillieux, E., Colot, V., Jaillais, Y., Roudier, F., & Vert, G. (2016). A versatile Multisite Gateway-compatible promoter and transgenic line collection for cell type-specific functional genomics in Arabidopsis. *The Plant Journal*, 85(2), 320–333. <https://doi.org/10.1111/tpj.13099>
- Massa, G. D., & Gilroy, S. (2003). Touch modulates gravity sensing to regulate the growth of primary roots of *Arabidopsis thaliana*. *The Plant Journal*, 33(3), 435–445. <https://doi.org/10.1046/j.1365-313X.2003.01637.x>
- McFarlane, H. E., Young, R. E., Wasteneys, G. O., & Samuels, A. L. (2008). Cortical microtubules mark the mucilage secretion domain of the plasma membrane in Arabidopsis seed coat cells. *Planta*, 227(6), 1363–1375. <https://doi.org/10.1007/s00425-008-0708-2>
- Merriam-Webster. (2023, January 21). *Definition of SYMMETRY*. <https://www.merriam-webster.com/dictionary/symmetry>

- Migliaccio, F., Fortunati, A., & Tassone, P. (2009). Arabidopsis root growth movements and their symmetry: Progress and problems arising from recent work. *Plant Signaling & Behavior*, 4(3), 183–190. <https://doi.org/10.4161/psb.4.3.7959>
- Miller, N. D., Parks, B. M., & Spalding, E. P. (2007). Computer-vision analysis of seedling responses to light and gravity. *The Plant Journal*, 52(2), 374–381. <https://doi.org/10.1111/j.1365-313X.2007.03237.x>
- Mishra, M., Kumar, N., Jaiswal, A., Verma, A. K., & Kant, S. (2012). Kartagener's syndrome: A case series. *Lung India : Official Organ of Indian Chest Society*, 29(4), 366–369. <https://doi.org/10.4103/0970-2113.102831>
- Mohnen, D. (2008). Pectin structure and biosynthesis. *Current Opinion in Plant Biology*, 11(3), 266–277. <https://doi.org/10.1016/j.pbi.2008.03.006>
- Monshausen, G. B., Bibikova, T. N., Weisenseel, M. H., & Gilroy, S. (2009). Ca²⁺ Regulates Reactive Oxygen Species Production and pH during Mechanosensing in Arabidopsis Roots. *The Plant Cell*, 21(8), 2341. <https://doi.org/10.1105/tpc.109.068395>
- Monshausen, G. B., & Gilroy, S. (2009). Feeling green: Mechanosensing in plants. *Trends in Cell Biology*, 19(5), 228–235. <https://doi.org/10.1016/j.tcb.2009.02.005>
- Montcuquet, A.-S., Hervé, L., Garcia, F. P. N. Y., Dinten, J.-M., & Mars, J. I. (2010). Nonnegative matrix factorization: A blind spectra separation method for in vivo fluorescent optical imaging. *Journal of Biomedical Optics*, 15(5), 056009. <https://doi.org/10.1117/1.3491796>
- Moody, S. (2017, May 10). *Plant Seed Mutagenesis*. The McClellan Nuclear Research Center. <https://mnrc.ucdavis.edu/plant-seed-mutagenesis>

- Mooney, S. J., Pridmore, T. P., Helliwell, J., & Bennett, M. J. (2012). Developing X-ray Computed Tomography to non-invasively image 3-D root systems architecture in soil. *Plant and Soil*, 352(1), 1–22. <https://doi.org/10.1007/s11104-011-1039-9>
- Mouille, G., Ralet, M.-C., Cavelier, C., Eland, C., Effroy, D., Hématy, K., McCartney, L., Truong, H. N., Gaudon, V., Thibault, J.-F., Marchant, A., & Höfte, H. (2007). Homogalacturonan synthesis in *Arabidopsis thaliana* requires a Golgi-localized protein with a putative methyltransferase domain. *The Plant Journal*, 50(4), 605–614. <https://doi.org/10.1111/j.1365-313X.2007.03086.x>
- Mousavi, S. A. R., Dubin, A. E., Zeng, W.-Z., Coombs, A. M., Do, K., Ghadiri, D. A., Keenan, W. T., Ge, C., Zhao, Y., & Patapoutian, A. (2021). PIEZO ion channel is required for root mechanotransduction in *Arabidopsis thaliana*. *Proceedings of the National Academy of Sciences*, 118(20), e2102188118. <https://doi.org/10.1073/pnas.2102188118>
- Mullins, R. D. (2010). Cytoskeletal Mechanisms for Breaking Cellular Symmetry. *Cold Spring Harbor Perspectives in Biology*, 2(1), a003392. <https://doi.org/10.1101/cshperspect.a003392>
- Naeem, A., French, A. P., Wells, D. M., & Pridmore, T. P. (2011). High-throughput feature counting and measurement of roots. *Bioinformatics*, 27(9), 1337–1338. <https://doi.org/10.1093/bioinformatics/btr126>
- Nakagawa, Y., Katagiri, T., Shinozaki, K., Qi, Z., Tatsumi, H., Furuichi, T., Kishigami, A., Sokabe, M., Kojima, I., Sato, S., Kato, T., Tabata, S., Iida, K., Terashima, A., Nakano, M., Ikeda, M., Yamanaka, T., & Iida, H. (2007). *Arabidopsis* plasma membrane protein crucial for Ca²⁺ influx and touch sensing in roots. *Proceedings of the National Academy*

- of Sciences of the United States of America*, 104(9), 3639–3644.
<https://doi.org/10.1073/pnas.0607703104>
- Nakajima, K., Furutani, I., Tachimoto, H., Matsubara, H., & Hashimoto, T. (2004). SPIRAL1 Encodes a Plant-Specific Microtubule-Localized Protein Required for Directional Control of Rapidly Expanding Arabidopsis Cells. *The Plant Cell*, 16(5), 1178–1190.
<https://doi.org/10.1105/tpc.017830>
- Nakajima, K., Kawamura, T., & Hashimoto, T. (2006). Role of the SPIRAL1 Gene Family in Anisotropic Growth of Arabidopsis thaliana. *Plant and Cell Physiology*, 47(4), 513–522.
<https://doi.org/10.1093/pcp/pcj020>
- Nakamura, M., & Hashimoto, T. (2009). A mutation in the Arabidopsis γ -tubulin-containing complex causes helical growth and abnormal microtubule branching. *Journal of Cell Science*, 122(13), 2208–2217. <https://doi.org/10.1242/jcs.044131>
- Nakamura, M., & Hashimoto, T. (2020). Mechanistic Insights into Plant Chiral Growth. *Symmetry*, 12(12), Article 12. <https://doi.org/10.3390/sym12122056>
- Nonaka, S., Tanaka, Y., Okada, Y., Takeda, S., Harada, A., Kanai, Y., Kido, M., & Hirokawa, N. (1998). Randomization of Left–Right Asymmetry due to Loss of Nodal Cilia Generating Leftward Flow of Extraembryonic Fluid in Mice Lacking KIF3B Motor Protein. *Cell*.
- Ogura, T., Goeschl, C., Filiault, D., Mirea, M., Slovak, R., Wolhrab, B., Satbhai, S. B., & Busch, W. (2019). Root System Depth in Arabidopsis Is Shaped by EXOCYST70A3 via the Dynamic Modulation of Auxin Transport. *Cell*, 178(2), 400–412.e16.
<https://doi.org/10.1016/j.cell.2019.06.021>

- Okada, K., & Shimura, Y. (1990). Reversible Root Tip Rotation in Arabidopsis Seedlings Induced by Obstacle-Touching Stimulus. *Science*, 250(4978), 274–276.
<https://doi.org/10.1126/science.250.4978.274>
- Okada, Y., Nonaka, S., Tanaka, Y., Saijoh, Y., Hamada, H., & Hirokawa, N. (1999). Abnormal Nodal Flow Precedes Situs Inversus in iv and inv mice. *Molecular Cell*, 4(4), 459–468.
[https://doi.org/10.1016/S1097-2765\(00\)80197-5](https://doi.org/10.1016/S1097-2765(00)80197-5)
- Oliva, M., & Dunand, C. (2007). Waving and skewing: How gravity and the surface of growth media affect root development in Arabidopsis. *New Phytologist*, 176(1), 37–43.
<https://doi.org/10.1111/j.1469-8137.2007.02184.x>
- Otsuka, Y., & Tsukaya, H. (2021). Three-dimensional quantification of twisting in the Arabidopsis petiole. *Journal of Plant Research*, 134(4), 811–819.
<https://doi.org/10.1007/s10265-021-01291-7>
- Padgett, P. J., Friedman, M. W., & Krieg, N. R. (1983). Straight Mutants of *Spirillum volutans* Can Swim. *Journal of Bacteriology*, 153(3), 1543–1544.
<https://doi.org/10.1128/jb.153.3.1543-1544.1983>
- Paredez, A. R., Somerville, C. R., & Ehrhardt, D. W. (2006). Visualization of Cellulose Synthase Demonstrates Functional Association with Microtubules. *Science*, 312(5779), 1491–1495. <https://doi.org/10.1126/science.1126551>
- Park, Y. B., & Cosgrove, D. J. (2012). A Revised Architecture of Primary Cell Walls Based on Biomechanical Changes Induced by Substrate-Specific Endoglucanases. *Plant Physiology*, 158(4), 1933–1943. <https://doi.org/10.1104/pp.111.192880>

- Park, Y. B., & Cosgrove, D. J. (2015). Xyloglucan and its Interactions with Other Components of the Growing Cell Wall. *Plant and Cell Physiology*, 56(2), 180–194.
<https://doi.org/10.1093/pcp/pcu204>
- Pattathil, S., Avci, U., Miller, J. S., & Hahn, M. G. (2012). Immunological approaches to plant cell wall and biomass characterization: Glycome Profiling. *Methods in Molecular Biology (Clifton, N.J.)*, 908, 61–72. https://doi.org/10.1007/978-1-61779-956-3_6
- Paya, A. M., Silverberg, J. L., Padgett, J., & Bauerle, T. L. (2015). X-ray computed tomography uncovers root–root interactions: Quantifying spatial relationships between interacting root systems in three dimensions. *Frontiers in Plant Science*, 6.
<https://www.frontiersin.org/articles/10.3389/fpls.2015.00274>
- Peaucelle, A., Braybrook, S. A., Le Guillou, L., Bron, E., Kuhlemeier, C., & Höfte, H. (2011). Pectin-Induced Changes in Cell Wall Mechanics Underlie Organ Initiation in Arabidopsis. *Current Biology*, 21(20), 1720–1726.
<https://doi.org/10.1016/j.cub.2011.08.057>
- Peaucelle, A., Wightman, R., & Höfte, H. (2015). The Control of Growth Symmetry Breaking in the Arabidopsis Hypocotyl. *Current Biology*, 25(13), 1746–1752.
<https://doi.org/10.1016/j.cub.2015.05.022>
- Pedersen, G. B., Blaschek, L., Frandsen, K. E. H., Noack, L. C., & Persson, S. (2023). Cellulose synthesis in land plants. *Molecular Plant*, 16(1), 206–231.
<https://doi.org/10.1016/j.molp.2022.12.015>
- Peralta, A. G., Venkatachalam, S., Stone, S. C., & Pattathil, S. (2017). Xylan epitope profiling: An enhanced approach to study organ development-dependent changes in xylan structure,

- biosynthesis, and deposition in plant cell walls. *Biotechnology for Biofuels*, 10(1), 245.
<https://doi.org/10.1186/s13068-017-0935-5>
- Pereira, L., Flores-Borges, D. N. A., Bittencourt, P. R. L., Mayer, J. L. S., Kiyota, E., Araújo, P., Jansen, S., Freitas, R. O., Oliveira, R. S., & Mazzafera, P. (2018a). Infrared Nanospectroscopy Reveals the Chemical Nature of Pit Membranes in Water-Conducting Cells of the Plant Xylem. *Plant Physiology*, 177(4), 1629–1638.
<https://doi.org/10.1104/pp.18.00138>
- Pereira, L., Flores-Borges, D. N. A., Bittencourt, P. R. L., Mayer, J. L. S., Kiyota, E., Araújo, P., Jansen, S., Freitas, R. O., Oliveira, R. S., & Mazzafera, P. (2018b). Infrared Nanospectroscopy Reveals the Chemical Nature of Pit Membranes in Water-Conducting Cells of the Plant Xylem. *Plant Physiology*, 177(4), 1629–1638.
<https://doi.org/10.1104/pp.18.00138>
- Petricka, J. J., Winter, C. M., & Benfey, P. N. (2012). Control of Arabidopsis Root Development. *Annual Review of Plant Biology*, 63, 563–590.
<https://doi.org/10.1146/annurev-arplant-042811-105501>
- Pfeifer, J., Kirchgessner, N., Colombi, T., & Walter, A. (2015). Rapid phenotyping of crop root systems in undisturbed field soils using X-ray computed tomography. *Plant Methods*, 11, 41. <https://doi.org/10.1186/s13007-015-0084-4>
- Phyo, P., Wang, T., Kiemle, S. N., O'Neill, H., Pingali, S. V., Hong, M., & Cosgrove, D. J. (2017). Gradients in Wall Mechanics and Polysaccharides along Growing Inflorescence Stems. *Plant Physiology*, 175(4), 1593–1607. <https://doi.org/10.1104/pp.17.01270>
- Piñeros, M. A., Larson, B. G., Shaff, J. E., Schneider, D. J., Falcão, A. X., Yuan, L., Clark, R. T., Craft, E. J., Davis, T. W., Pradier, P.-L., Shaw, N. M., Assaranurak, I., McCouch, S. R.,

- Sturrock, C., Bennett, M., & Kochian, L. V. (2016). Evolving technologies for growing, imaging and analyzing 3D root system architecture of crop plants. *Journal of Integrative Plant Biology*, 58(3), 230–241. <https://doi.org/10.1111/jipb.12456>
- Pollard, T. D., & Goldman, R. D. (2018). Overview of the Cytoskeleton from an Evolutionary Perspective. *Cold Spring Harbor Perspectives in Biology*, 10(7), a030288. <https://doi.org/10.1101/cshperspect.a030288>
- Pound, M. P., French, A. P., Atkinson, J. A., Wells, D. M., Bennett, M. J., & Pridmore, T. (2013). RootNav: Navigating Images of Complex Root Architectures. *Plant Physiology*, 162(4), 1802–1814. <https://doi.org/10.1104/pp.113.221531>
- Prats Mateu, B., Hauser, M. T., Heredia, A., & Gierlinger, N. (2016). Waterproofing in Arabidopsis: Following Phenolics and Lipids In situ by Confocal Raman Microscopy. *Frontiers in Chemistry*, 4. <https://doi.org/10.3389/fchem.2016.00010>
- Rahman, A., Bannigan, A., Sulaman, W., Pechter, P., Blancaflor, E. B., & Baskin, T. I. (2007). Auxin, actin and growth of the Arabidopsis thaliana primary root. *The Plant Journal*, 50(3), 514–528. <https://doi.org/10.1111/j.1365-313X.2007.03068.x>
- Reed, J. W., Elumalai, R. P., & Chory, J. (1998). Suppressors of an Arabidopsis thaliana phyB mutation identify genes that control light signaling and hypocotyl elongation. *Genetics*, 148(3), 1295–1310.
- Reiter, W.-D., Chapple, C., & Somerville, C. (1997). Mutants of Arabidopsis thaliana with altered cell wall polysaccharide composition. *The Plant Journal*, 12(2), 335–345.
- Rongpipi, S., Ye, D., Gomez, E. D., & Gomez, E. W. (2019). Progress and Opportunities in the Characterization of Cellulose – An Important Regulator of Cell Wall Growth and Mechanics. *Frontiers in Plant Science*, 9, 1894. <https://doi.org/10.3389/fpls.2018.01894>

- Rounds, C. M., Lubeck, E., Hepler, P. K., & Winship, L. J. (2011). Propidium Iodide Competes with Ca^{2+} to Label Pectin in Pollen Tubes and Arabidopsis Root Hairs1[W][OA]. *Plant Physiology*, 157(1), 175–187. <https://doi.org/10.1104/pp.111.182196>
- Roy, R., & Bassham, D. C. (2014). Root growth movements: Waving and skewing. *Plant Science*, 221–222, 42–47. <https://doi.org/10.1016/j.plantsci.2014.01.007>
- Ruiz-Matute, A. I., Hernández-Hernández, O., Rodríguez-Sánchez, S., Sanz, M. L., & Martínez-Castro, I. (2011). Derivatization of carbohydrates for GC and GC–MS analyses. *Journal of Chromatography B*, 879(17–18), 1226–1240. <https://doi.org/10.1016/j.jchromb.2010.11.013>
- Rutherford, R., & Masson, P. H. (1996). Arabidopsis thaliana sku Mutant Seedlings Show Exaggerated Surface-Dependent Alteration in Root Growth Vector. *Plant Physiology*, 111(4), 987–998. <https://doi.org/10.1104/pp.111.4.987>
- Růžicka, K., Ljung, K., Vanneste, S., Podhorská, R., Beeckman, T., Friml, J., & Benková, E. (2007). Ethylene Regulates Root Growth through Effects on Auxin Biosynthesis and Transport-Dependent Auxin Distribution. *The Plant Cell*, 19(7), 2197. <https://doi.org/10.1105/tpc.107.052126>
- Saffer, A. M., Carpita, N. C., & Irish, V. F. (2017). Rhamnose-Containing Cell Wall Polymers Suppress Helical Plant Growth Independently of Microtubule Orientation. *Current Biology*, 27(15), 2248–2259.e4. <https://doi.org/10.1016/j.cub.2017.06.032>
- Sandt, V. S. T. V., Suslov, D., Verbelen, J.-P., & Vissenberg, K. (2007). Xyloglucan Endotransglucosylase Activity Loosens a Plant Cell Wall. *Annals of Botany*, 100(7), 1467. <https://doi.org/10.1093/aob/mcm248>

- Sassi, M., Ali, O., Boudon, F., Cloarec, G., Abad, U., Cellier, C., Chen, X., Gilles, B., Milani, P., Friml, J., Vernoux, T., Godin, C., Hamant, O., & Traas, J. (2014). An Auxin-Mediated Shift toward Growth Isotropy Promotes Organ Formation at the Shoot Meristem in *Arabidopsis*. *Current Biology*, 24(19), 2335–2342.
<https://doi.org/10.1016/j.cub.2014.08.036>
- Scheres, B., & Wolkenfelt, H. (1998). The *Arabidopsis* root as a model to study plant development. *Plant Physiology and Biochemistry*, 36(1–2), 21–32.
[https://doi.org/10.1016/S0981-9428\(98\)80088-0](https://doi.org/10.1016/S0981-9428(98)80088-0)
- Schindelin, J., Arganda-Carreras, I., Frise, E., Kaynig, V., Longair, M., Pietzsch, T., Preibisch, S., Rueden, C., Saalfeld, S., Schmid, B., Tinevez, J.-Y., White, D. J., Hartenstein, V., Eliceiri, K., Tomancak, P., & Cardona, A. (2012). Fiji: An open-source platform for biological-image analysis. *Nature Methods*, 9(7), 676–682.
<https://doi.org/10.1038/nmeth.2019>
- Schindelman, G., Morikami, A., Jung, J., Baskin, T. I., Carpita, N. C., Derbyshire, P., McCann, M. C., & Benfey, P. N. (2001). COBRA encodes a putative GPI-anchored protein, which is polarly localized and necessary for oriented cell expansion in *Arabidopsis*. *Genes & Development*, 15(1115–1127), 14.
- Schmidt, M., Schwartzberg, A. M., Carroll, A., Chaibang, A., Adams, P. D., & Schuck, P. J. (2010). Raman imaging of cell wall polymers in *Arabidopsis thaliana*. *Biochemical and Biophysical Research Communications*, 395(4), 521–523.
<https://doi.org/10.1016/j.bbrc.2010.04.055>

- Schultz, E. R., Zupanska, A. K., Sng, N. J., Paul, A.-L., & Ferl, R. J. (2017). Skewing in Arabidopsis roots involves disparate environmental signaling pathways. *BMC Plant Biology*, 17(1). <https://doi.org/10.1186/s12870-017-0975-9>
- Sedbrook, J. C., Carroll, K. L., Hung, K. F., Masson, P. H., & Somerville, C. R. (2002). The Arabidopsis SKU5 Gene Encodes an Extracellular Glycosyl Phosphatidylinositol–Anchored Glycoprotein Involved in Directional Root Growth. *The Plant Cell*, 14(7), 1635–1648. <https://doi.org/10.1105/tpc.002360>
- Sedbrook, J. C., Ehrhardt, D. W., Fisher, S. E., Scheible, W.-R., & Somerville, C. R. (2004). The Arabidopsis SKU6/SPIRAL1 Gene Encodes a Plus End-Localized Microtubule-Interacting Protein Involved in Directional Cell Expansion. *The Plant Cell*, 16(6), 1506–1520. <https://doi.org/10.1105/tpc.020644>
- Seleiman, M. F., Al-Suhaibani, N., Ali, N., Akmal, M., Alotaibi, M., Refay, Y., Dindaroglu, T., Abdul-Wajid, H. H., & Battaglia, M. L. (2021). Drought Stress Impacts on Plants and Different Approaches to Alleviate Its Adverse Effects. *Plants*, 10(2), 259. <https://doi.org/10.3390/plants10020259>
- Shapiro, L., McAdams, H. H., & Losick, R. (2002). Generating and Exploiting Polarity in Bacteria. *Science*, 298(5600), 1942–1946. <https://doi.org/10.1126/science.1072163>
- Shibata, M., & Sugimoto, K. (2019). A gene regulatory network for root hair development. *Journal of Plant Research*, 132(3), 301–309. <https://doi.org/10.1007/s10265-019-01100-2>
- Shoji, T., Narita, N. N., Hayashi, K., Asada, J., Hamada, T., Sonobe, S., Nakajima, K., & Hashimoto, T. (2004). Plant-Specific Microtubule-Associated Protein SPIRAL2 Is

- Required for Anisotropic Growth in Arabidopsis. *Plant Physiology*, 136(4), 3933–3944.
<https://doi.org/10.1104/pp.104.051748>
- Sichel, S. R., Bratton, B. P., & Salama, N. R. (2022). Distinct regions of *H. pylori*'s bactofilin CcmA regulate protein–protein interactions to control helical cell shape. *ELife*, 11, e80111. <https://doi.org/10.7554/eLife.80111>
- Simmons, C., Söll, D., & Migliaccio, F. (1995). Circumnutation and gravitropism cause root waving in *Arabidopsis thaliana*. *Journal of Experimental Botany*, 46(1), 143–150.
<https://doi.org/10.1093/jxb/46.1.143>
- Simon Mittman, A. (2019, July 10). *Balance, symmetry, and emphasis – Smarthistory*. Smarthistory. <https://smarthistory.org/balance-symmetry-and-emphasis/>
- Slovak, R., Göschl, C., Su, X., Shimotani, K., Shiina, T., & Busch, W. (2014). A Scalable Open-Source Pipeline for Large-Scale Root Phenotyping of Arabidopsis. *The Plant Cell*, 26(6), 2390–2403. <https://doi.org/10.1105/tpc.114.124032>
- Smallwood, M., Martin, H., & Knox, J. P. (1995). An epitope of rice threonine- and hydroxyproline-rich glycoprotein is common to cell wall and hydrophobic plasma-membrane glycoproteins. *Planta*, 196(3). <https://doi.org/10.1007/BF00203651>
- Smyth, D. R. (2016). Helical growth in plant organs: Mechanisms and significance. *Development*, 143(18), 3272–3282. <https://doi.org/10.1242/dev.134064>
- Spalding, E. P., & Miller, N. D. (2013). Image analysis is driving a renaissance in growth measurement. *Current Opinion in Plant Biology*, 16(1), 100–104.
<https://doi.org/10.1016/j.pbi.2013.01.001>

- Spéder, P., Ádám, G., & Noselli, S. (2006). Type II unconventional myosin controls left–right asymmetry in *Drosophila*. *Nature*, *440*(7085), 803–807.
<https://doi.org/10.1038/nature04623>
- Stan, G., & Solares, S. D. (2014). Frequency, amplitude, and phase measurements in contact resonance atomic force microscopies. *Beilstein Journal of Nanotechnology*, *5*, 278–288.
<https://doi.org/10.3762/bjnano.5.30>
- Sycuro, L. K., Pincus, Z., Gutierrez, K. D., Biboy, J., Stern, C. A., Vollmer, W., & Salama, N. R. (2010). Peptidoglycan Crosslinking Relaxation Promotes *Helicobacter pylori*'s Helical Shape and Stomach Colonization. *Cell*, *141*(5), 822–833.
<https://doi.org/10.1016/j.cell.2010.03.046>
- Taina, I. A., Heck, R. J., & Elliot, T. R. (2008). Application of X-ray computed tomography to soil science: A literature review. *Canadian Journal of Soil Science*, *88*(1), 1–19.
<https://doi.org/10.4141/CJSS06027>
- Takeda, S., Yonekawa, Y., Tanaka, Y., Okada, Y., Nonaka, S., & Hirokawa, N. (1999). Left-Right Asymmetry and Kinesin Superfamily Protein KIF3A: New Insights in Determination of Laterality and Mesoderm Induction by *kif3A*^{−/−} Mice Analysis. *The Journal of Cell Biology*, *145*(4), 825. <https://doi.org/10.1083/jcb.145.4.825>
- Takenaka, Y., Watanabe, Y., Schuetz, M., Unda, F., Hill, J. L., Phookaew, P., Yoneda, A., Mansfield, S. D., Samuels, L., Ohtani, M., & Demura, T. (2018). Patterned Deposition of Xylan and Lignin is Independent from that of the Secondary Wall Cellulose of *Arabidopsis* Xylem Vessels. *The Plant Cell*, *30*(11), 2663–2676.
<https://doi.org/10.1105/tpc.18.00292>

- Tanaka, H., Dhonukshe, P., Brewer, P. B., & Friml, J. (2006). Spatiotemporal asymmetric auxin distribution: A means to coordinate plant development. *Cellular and Molecular Life Sciences CMLS*, 63(23), 2738–2754. <https://doi.org/10.1007/s00018-006-6116-5>
- Taylor, H. M., Upchurch, D. R., Brown, J. M., & Rogers, H. H. (1991). Some Methods of Root Investigations. In *Developments in Agricultural and Managed Forest Ecology* (Vol. 24, pp. 553–564). Elsevier. <https://doi.org/10.1016/B978-0-444-89104-4.50075-X>
- Taylor, I., Lehner, K., McCaskey, E., Nirmal, N., Ozkan-Aydin, Y., Murray-Cooper, M., Jain, R., Hawkes, E. W., Ronald, P. C., Goldman, D. I., & Benfey, P. N. (2021). Mechanism and function of root circumnutation. *Proceedings of the National Academy of Sciences*, 118(8), e2018940118. <https://doi.org/10.1073/pnas.2018940118>
- Teramoto, S., Takayasu, S., Kitomi, Y., Arai-Sanoh, Y., Tanabata, T., & Uga, Y. (2020). High-throughput three-dimensional visualization of root system architecture of rice using X-ray computed tomography. *Plant Methods*, 16(1), 66. <https://doi.org/10.1186/s13007-020-00612-6>
- Tetard, L., Passian, A., Farahi, R. H., Davison, B. H., Jung, S., Ragauskas, A. J., Lereu, A. L., & Thundat, T. (2011). Nanometrology of delignified *Populus* using mode synthesizing atomic force microscopy. *Nanotechnology*, 22(46), 465702. <https://doi.org/10.1088/0957-4484/22/46/465702>
- Tetard, L., Passian, A., Farahi, R. H., Kalluri, U. C., Davison, B. H., & Thundat, T. (2010). Spectroscopy and atomic force microscopy of biomass. *Ultramicroscopy*, 110(6), 701–707. <https://doi.org/10.1016/j.ultramic.2010.02.035>

- Tetard, L., Passian, A., Farahi, R. H., Thundat, T., & Davison, B. H. (2015). Opto-nanomechanical spectroscopic material characterization. *Nature Nanotechnology*, 10(10), Article 10. <https://doi.org/10.1038/nnano.2015.168>
- Tetard, L., Passian, A., Jung, S., Ragauskas, A. J., & Davison, B. H. (2012). Development of New Methods in Scanning Probe Microscopy for Lignocellulosic Biomass Characterization. *Industrial Biotechnology*, 8(4), 245–249. <https://doi.org/10.1089/ind.2012.0017>
- Thitamadee, S., Tuchiara, K., & Hashimoto, T. (2002). Microtubule basis for left-handed helical growth in Arabidopsis. *Nature*, 417(6885), 193–196. <https://doi.org/10.1038/417193a>
- Thomas, J., Ingerfeld, M., Nair, H., Chauhan, S. S., & Collings, D. A. (2013). Pontamine fast scarlet 4B: A new fluorescent dye for visualising cell wall organisation in radiata pine tracheids. *Wood Science and Technology*, 47(1), 59–75. <https://doi.org/10.1007/s00226-012-0483-x>
- Thompson, M. V., & Holbrook, N. M. (2004). Root-Gel Interactions and the Root Waving Behavior of Arabidopsis. *Plant Physiology*, 135(3), 1822–1837. <https://doi.org/10.1104/pp.104.040881>
- Tollner, E. W., Ramseur, E. L., & Murphy, C. (1994). Techniques and Approaches for Documenting Plant Root Development with X-Ray Computed Tomography. In *Tomography of Soil-Water-Root Processes* (pp. 115–133). John Wiley & Sons, Ltd. <https://doi.org/10.2136/sssaspecpub36.c10>

- Topp, C. N., Bray, A. L., Ellis, N. A., & Liu, Z. (2016). How can we harness quantitative genetic variation in crop root systems for agricultural improvement? *Journal of Integrative Plant Biology*, 58(3), 213–225. <https://doi.org/10.1111/jipb.12470>
- Toyota, M., Furuichi, T., Tatsumi, H., & Sokabe, M. (2008). Cytoplasmic Calcium Increases in Response to Changes in the Gravity Vector in Hypocotyls and Petioles of Arabidopsis Seedlings. *Plant Physiology*, 146(2), 505–514. <https://doi.org/10.1104/pp.107.106450>
- Trachsel, S., Kaeppler, S. M., Brown, K. M., & Lynch, J. P. (2011). Shovelomics: High throughput phenotyping of maize (*Zea mays* L.) root architecture in the field. *Plant and Soil*, 341(1), 75–87. <https://doi.org/10.1007/s11104-010-0623-8>
- Tsai, Y.-C., Delk, N. A., Chowdhury, N. I., & Braam, J. (2007). Arabidopsis Potential Calcium Sensors Regulate Nitric Oxide Levels and the Transition to Flowering. *Plant Signaling & Behavior*, 2(6), 446–454.
- U.S. National Park Service. (2021, September 25). *The Largest Trees in the World—Sequoia & Kings Canyon National Parks* (U.S. National Park Service). <https://www.nps.gov/seki/learn/nature/largest-trees-in-world.htm>
- Vadillo-Rodríguez, V., Busscher, H. J., Norde, W., de Vries, J., Dijkstra, R. J. B., Stokroos, I., & van der Mei, H. C. (2004). Comparison of Atomic Force Microscopy Interaction Forces between Bacteria and Silicon Nitride Substrata for Three Commonly Used Immobilization Methods. *Applied and Environmental Microbiology*, 70(9), 5441–5446. <https://doi.org/10.1128/AEM.70.9.5441-5446.2004>
- van den Berg, C., Willemsen, V., Hendriks, G., Weisbeek, P., & Scheres, B. (1997). Short-range control of cell differentiation in the Arabidopsis root meristem. *Nature*, 390(6657), Article 6657. <https://doi.org/10.1038/36856>

- Varma, A., de Pedro, M. A., & Young, K. D. (2007). FtsZ Directs a Second Mode of Peptidoglycan Synthesis in *Escherichia coli*. *Journal of Bacteriology*, 189(15), 5692–5704. <https://doi.org/10.1128/JB.00455-07>
- Vaughn, L. M., & Masson, P. H. (2011). A QTL Study for Regions Contributing to *Arabidopsis thaliana* Root Skewing on Tilted Surfaces. *G3 & Genes/Genomes/Genetics*, 1(2), 105–115. <https://doi.org/10.1534/g3.111.000331>
- Verbelen, J.-P., De Cnodder, T., Le, J., Vissenberg, K., & Baluška, F. (2006). The Root Apex of *Arabidopsis thaliana* Consists of Four Distinct Zones of Growth Activities. *Plant Signaling & Behavior*, 1(6), 296–304.
- Verger, S., Liu, M., & Hamant, O. (2019). Mechanical Conflicts in Twisting Growth Revealed by Cell-Cell Adhesion Defects. *Frontiers in Plant Science*, 10. <https://doi.org/10.3389/fpls.2019.00173>
- Verger, S., Long, Y., Boudaoud, A., & Hamant, O. (2018). A tension-adhesion feedback loop in plant epidermis. *ELife*, 7. <https://doi.org/10.7554/eLife.34460>
- Verhertbruggen, Y., Walker, J. L., Guillon, F., & Scheller, H. V. (2017). A Comparative Study of Sample Preparation for Staining and Immunodetection of Plant Cell Walls by Light Microscopy. *Frontiers in Plant Science*, 8. <https://doi.org/10.3389/fpls.2017.01505>
- Verhey, K. J., Kaul, N., & Soppina, V. (2011). Kinesin Assembly and Movement in Cells. *Annual Review of Biophysics*, 40(1), 267–288. <https://doi.org/10.1146/annurev-biophys-042910-155310>
- Wang, B., Bailly, A., Zwiewka, M., Henrichs, S., Azzarello, E., Mancuso, S., Maeshima, M., Friml, J., Schulz, A., & Geisler, M. (2013). *Arabidopsis* TWISTED DWARF1 Functionally Interacts with Auxin Exporter ABCB1 on the Root Plasma

- Membrane[C][W]. *The Plant Cell*, 25(1), 202–214.
<https://doi.org/10.1105/tpc.112.105999>
- Wang, C., Li, J., & Yuan, M. (2007). Salt Tolerance Requires Cortical Microtubule Reorganization in Arabidopsis. *Plant and Cell Physiology*, 48(11), 1534–1547.
<https://doi.org/10.1093/pcp/pcm123>
- Wang, S., Furchtgott, L., Huang, K. C., & Shaevitz, J. W. (2012). Helical insertion of peptidoglycan produces chiral ordering of the bacterial cell wall. *Proceedings of the National Academy of Sciences*, 109(10), E595–E604.
- Wang, S., Kurepa, J., Hashimoto, T., & Smalle, J. A. (2011). Salt Stress–Induced Disassembly of Arabidopsis Cortical Microtubule Arrays Involves 26S Proteasome–Dependent Degradation of SPIRAL1[C][W]. *The Plant Cell*, 23(9), 3412–3427.
<https://doi.org/10.1105/tpc.111.089920>
- Wang, Y., Wang, B., Gilroy, S., Wassim Chehab, E., & Braam, J. (2011). CML24 is Involved in Root Mechanoresponses and Cortical Microtubule Orientation in Arabidopsis. *Journal of Plant Growth Regulation*, 30(4), 467–479. <https://doi.org/10.1007/s00344-011-9209-9>
- Wasteneys, G. O. (2000). The Cytoskeleton and Growth Polarity. *Current Opinion in Plant Biology*, 3(6), 503–511. [https://doi.org/10.1016/S1369-5266\(00\)00120-5](https://doi.org/10.1016/S1369-5266(00)00120-5)
- Weizbauer, R., Peters, W. S., & Schulz, B. (2011). Geometric Constraints and the Anatomical Interpretation of Twisted Plant Organ Phenotypes. *Frontiers in Plant Science*, 2.
<https://doi.org/10.3389/fpls.2011.00062>
- Went, F. W. (1974). Reflections and Speculations. *Annual Review of Plant Physiology*, 25(1), 1–27. <https://doi.org/10.1146/annurev.pp.25.060174.000245>

What's so special about the Higgs boson? (2023, January 20). CERN.

<https://home.cern/science/physics/higgs-boson/what>

Whittington, A. T., Vugrek, O., Wei, K. J., Hasenbein, N. G., Sugimoto, K., Rashbrooke, M. C., & Wasteneys, G. O. (2001). MOR1 is essential for organizing cortical microtubules in plants. *Nature*, *411*(6837), 610–613. <https://doi.org/10.1038/35079128>

Willats, W. G. T., McCartney, L., Mackie, W., & Knox, J. P. (2001). Pectin: Cell biology and prospects for functional analysis. *Plant Molecular Biology*, *47*(1), 9–27. <https://doi.org/10.1023/A:1010662911148>

Willemsen, V., Bauch, M., Bennett, T., Campilho, A., Wolkenfelt, H., Xu, J., Haseloff, J., & Scheres, B. (2008). The NAC Domain Transcription Factors FEZ and SOMBRERO Control the Orientation of Cell Division Plane in Arabidopsis Root Stem Cells. *Developmental Cell*, *15*(6), 913–922. <https://doi.org/10.1016/j.devcel.2008.09.019>

Wong, J. H., & Hashimoto, T. (2017). Novel Arabidopsis microtubule-associated proteins track growing microtubule plus ends. *BMC Plant Biology*, *17*(1), 33. <https://doi.org/10.1186/s12870-017-0987-5>

Wormit, A., & Usadel, B. (2018). The Multifaceted Role of Pectin Methylesterase Inhibitors (PMEIs). *International Journal of Molecular Sciences*, *19*(10). <https://doi.org/10.3390/ijms19102878>

Wu, S., Lee, C.-M., Hayashi, T., Price, S., Divol, F., Henry, S., Pauluzzi, G., Perin, C., & Gallagher, K. L. (2014). A plausible mechanism, based upon SHORT-ROOT movement, for regulating the number of cortex cell layers in roots. *Proceedings of the National Academy of Sciences*, *111*(45), 16184–16189. <https://doi.org/10.1073/pnas.1407371111>

- Xu, T., Niu, J., & Jiang, Z. (2022). Sensing Mechanisms: Calcium Signaling Mediated Abiotic Stress in Plants. *Frontiers in Plant Science*, 13. <https://doi.org/10.3389/fpls.2022.925863>
- Yasrab, R., Atkinson, J. A., Wells, D. M., French, A. P., Pridmore, T. P., & Pound, M. P. (2019). RootNav 2.0: Deep learning for automatic navigation of complex plant root architectures. *GigaScience*, 8(11), giz123. <https://doi.org/10.1093/gigascience/giz123>
- Ye, Z., & Zhao, X. (2010). Phase imaging atomic force microscopy in the characterization of biomaterials. *Journal of Microscopy*, 238(1), 27–35. <https://doi.org/10.1111/j.1365-2818.2009.03282.x>
- Yeats, T., Velloso, T., Sorek, N., Ibáñez, A., & Bauer, S. (2016). Rapid Determination of Cellulose, Neutral Sugars, and Uronic Acids from Plant Cell Walls by One-step Two-step Hydrolysis and HPAEC-PAD. *BIO-PROTOCOL*, 6(20). <https://doi.org/10.21769/BioProtoc.1978>
- Yu, B., Zheng, W., Xing, L., Zhu, J.-K., Persson, S., & Zhao, Y. (2022). Root twisting drives halotropism via stress-induced microtubule reorientation. *Developmental Cell*, 57(20), 2412–2425.e6. <https://doi.org/10.1016/j.devcel.2022.09.012>
- Yuen, C. Y. L., Pearlman, R. S., Silo-suh, L., Hilson, P., Carroll, K. L., & Masson, P. H. (2003). WVD2 and WDL1 Modulate Helical Organ Growth and Anisotropic Cell Expansion in Arabidopsis. *Plant Physiology*, 131(2), 493–506. <https://doi.org/10.1104/pp.015966>
- Zabackis, E., Huang, J., Müller, B., Darvill, A. G., & Albersheim, P. (1995). Characterization of the cell-wall polysaccharides of Arabidopsis thaliana leaves. *Plant Physiology*, 107(4), 1129–1138.
- Zamil, M. S., & Geitmann, A. (2017). The middle lamella—More than a glue. *Physical Biology*, 14(1), 015004. <https://doi.org/10.1088/1478-3975/aa5ba5>

- Zamil, M. S., Yi, H., & Puri, V. M. (2014). Mechanical characterization of outer epidermal middle lamella of onion under tensile loading. *American Journal of Botany*, 101(5), 778–787. <https://doi.org/10.3732/ajb.1300416>
- Zhang, T., He, T., Yan, C., Gao, X., Ma, J., & Li, H. (2018). In situ attenuated total reflection-Fourier transform infrared (ATR-FTIR) spectroscopy combined with non-negative matrix factorization for investigating the synthesis reaction mechanism of 3-amino-4- amino-oxime furazan. *Analytical Methods*, 10, 5817–5822.
- Zhang, T., Tang, H., Vavylonis, D., & Cosgrove, D. J. (2019). Disentangling loosening from softening: Insights into primary cell wall structure. *The Plant Journal*, 100(6), 1101–1117. <https://doi.org/10.1111/tpj.14519>
- Zhang, T., Vavylonis, D., Durachko, D. M., & Cosgrove, D. J. (2017). Nanoscale Movements of Cellulose Microfibrils in Primary Cell Walls. *Nature Plants*, 3, 17056. <https://doi.org/10.1038/nplants.2017.56>
- Zhang, T., Zheng, Y., & Cosgrove, D. J. (2016). Spatial organization of cellulose microfibrils and matrix polysaccharides in primary plant cell walls as imaged by multichannel atomic force microscopy. *The Plant Journal*, 85(2), 179–192. <https://doi.org/10.1111/tpj.13102>
- Zhang, Y., & Friml, J. (2020). Auxin guides roots to avoid obstacles during gravitropic growth. *New Phytologist*, 225(3), 1049–1052. <https://doi.org/10.1111/nph.16203>
- Zhang, Y., Mao, J., Peng, J., Tomsia, A. P., Jiang, L., & Cheng, Q. (2022). Ginkgo seed shell provides a unique model for bioinspired design. *Proceedings of the National Academy of Sciences*, 119(49), e2211458119. <https://doi.org/10.1073/pnas.2211458119>

- Zhang, Y., Yu, J., Wang, X., Durachko, D. M., Zhang, S., & Cosgrove, D. J. (2021). Molecular insights into the complex mechanics of plant epidermal cell walls. *Science*, 372(6543), 706–711. <https://doi.org/10.1126/science.abf2824>
- Zhang, Z., van Ophem, D., Chelakkot, R., Lazarovitch, N., & Regev, I. (2022). A mechano-sensing mechanism for waving in plant roots. *Scientific Reports*, 12(1), Article 1. <https://doi.org/10.1038/s41598-022-14093-1>
- Zheng, Y., Cosgrove, D., & Ning, G. (2017). High-resolution field emission scanning electron microscopy (FESEM) imaging of cellulose microfibril organization in plant primary cell walls. *Microscopy and Microanalysis*, 23(5), 1048–1054.
- Zhou, W., Li, D., Pšenička, J., Boyce, C. K., & Wang, J. (2019). A left-handed fern twiner in a Permian swamp forest. *Current Biology*, 29(22), R1172–R1173. <https://doi.org/10.1016/j.cub.2019.10.005>
- Zhu, C., Ganguly, A., Baskin, T. I., McClosky, D. D., Anderson, C. T., Foster, C., Meunier, K. A., Okamoto, R., Berg, H., & Dixit, R. (2015). The Fragile Fiber1 Kinesin Contributes to Cortical Microtubule-Mediated Trafficking of Cell Wall Components. *Plant Physiology*, 167(3), 780–792. <https://doi.org/10.1104/pp.114.251462>
- Zhu, X., Li, S., Pan, S., Xin, X., & Gu, Y. (2018). CSI1, PATROL1, and exocyst complex cooperate in delivery of cellulose synthase complexes to the plasma membrane. *Proceedings of the National Academy of Sciences*, 115(15), E3578–E3587. <https://doi.org/10.1073/pnas.1800182115>

Appendix I: Application of pan-sharpening algorithm for correlative multimodal imaging using AFM-IR²

6.1 Abstract

The coupling of atomic force microscopy with infrared spectroscopy (AFM-IR) offers the unique capability to the characterize local composition of a broad variety of materials with nanoscale resolution. In order to fully utilize the measurement capability of AFM-IR, a three-dimensional dataset (2D map with a spectroscopic dimension) needs to be acquired, which is prohibitively time-consuming at the same spatial resolution of regular AFM scan. In this paper, we provide a novel approach to process spectral AFM-IR data based on a multicomponent pan-sharpening algorithm. This approach requires one spectral map with low spatial resolution and a limited number of chemical maps at given wavenumbers. As a result, we are able to generate high-resolution maps of component distribution, produce chemical maps at any wavenumber available in the spectral range, and perform correlative analysis of the physical and chemical properties of the samples. We highlight our approach using plant cell walls as a model substrate and showcase the interplay between mechanical stiffness of the sample and its composition. We believe our pan-sharpening approach can enable deeper understanding of structure-property relationship of materials at nanoscale.

² This chapter has been adapted from Borodinov et al., 2019.

6.2 Introduction

In the last decade, improvements in instrumentation and data analytics have facilitated a paradigm-shift in scanning probe microscopy (SPM). SPM allows acquisition of localized chemical and/or physical properties for a wide range of materials, yielding unique insights into the structure-property relationship of functional materials (Cui et al., 2016; Floresyona et al., 2017), novel composites (Mikhalchan et al., 2018; Brown et al., 2016), and biological objects (Clede et al., 2013; Kochan et al., 2018; Pancani et al., 2018; Gourion-Arsiquaud et al., 2014). This approach involves datasets where spatial coordinates may be augmented with one or more spectroscopic dimensions. Such datasets are then analyzed and interpreted using multivariate statistics (Belianinov and Vasudevan et al., 2015; Somnath et al., 2018), spectral unmixing (Kannan et al., 2018), neural networks (Nikiforov et al., 2009; Kumar et al., 2011), and component analysis (Belianinov and Kalinin et al., 2015). As a result, it enables correlative multi-modal imaging (Ovchinnikova et al., 2015) which can highlight optomechanical (Dazzi et al., 2012), electromechanical (Gruverman et al., 1998; Kalinin et al., 2002; Thompson et al., 2012), and electrochemical (Li et al., 2015) interactions in materials. However, acquiring spectral datasets requires capture of a full spectrum at each spatial location. In some cases, it is possible to perform rapid spectroscopic imaging via full signal capture (G-mode) (Collins and Ahmadi et al., 2016; Collins and Belianinov et al., 2016; Somnath et al., 2015), however, this avenue is not yet available for all possible spectroscopic modes (such as AFM-IR). Therefore, the time required to acquire such datasets increases proportionally with the number of points, making direct acquisition of the high-resolution spectral maps difficult. Potential sample drift and degradation, as well as drastically decreased throughput of such analysis, prompt a search for

alternative approaches to spectral imaging which could reliably reconstruct full-resolution dataset using reduced number of measurements.

For example, atomic force microscope infrared-spectroscopy (AFM-IR) facilitates nanometer resolution (~ 15 nm) topological, chemical, and mechanical analysis. Unlike Fourier-transform infrared spectroscopy, AFM-IR can only measure the absorption at a given wavenumber. Therefore, reasonable AFM-IR acquisition times can only be obtained with a sparse spectral map (with respect to spatial and spectral dimensions) and/or an absorption map at a given wavenumber (Dazzi et al., 2016; Morsch et al., 2016). While both these types of AFM-IR analysis approaches provide sample chemical non-homogeneity, they still do not yield a full high-resolution dataset which would be useful for correlative analysis. One approach to the merging of spectral data contained in different channels is the use of sharpening algorithms such as data fusion (Van de Plas et al., 2015). They establish the relationship between known signals in the images and use it to provide context-aware interpolation for the low-resolution image. This approach is well-suited for the case when the functional relationship between two images (e.g. how change of one parameter is related to change of the second one) is not precisely known *a priori* and needs to be established during the analysis. However, correlations in this data fusion algorithm are built by individual spectral lines and do not account for the fact that intensities of the lines in spectrum are heavily constrained. Meanwhile, for the case of spectral datasets, this constraint is well-understood and can be used to generate high-resolution images with higher confidence in the final result using physically meaningful constraints. For example, if the available information channels generate partially overlapping subsets of a bigger dataset (that is impossible or impractical to measure), this fact should be actively used throughout the reconstruction of such dataset. To achieve this, a number of pan-sharpening algorithms have

been developed for the processing of satellite images to restore color images based on grayscale map (Vivone et al., 2015) and restore spectral datasets from multispectral maps (Loncan et al., 2015).

In this paper, we apply a coupled non-negative matrix factorization (CNMF) pan-sharpening (PS) algorithm for AFM-IR data. We demonstrate the restoration of the full spectral dataset at the resolution of a standard AFM scan with the added possibility of extracting spectral signatures of individual components as well as their abundance across the sample. Thus, we propose a multicomponent analysis-based approach to AFM-IR enabled by PS approach. We describe in detail factors influencing its results and discuss the applicability of quality metrics for the evaluation of the fusion product. Furthermore, we highlight the practical application of our method for the analysis of plant cell walls, providing a correlation between mechanical properties and chemical composition at nanoscale. We believe this PS algorithms can be readily adopted in other areas of spectral chemical imaging such as time-of-flight secondary ion mass spectrometry (ToF-SIMS), helium ion microscope secondary ion mass spectrometry (HIM-SIMS) and AFM mass spectrometry (AFM-MS).

6.3 Materials and Methods

6.3.1 AFM-IR

All experimental AFM-IR datasets were acquired using Anasys NanoIR2-s instrument with spectral ranges 917-1173, 1311-1409, 1505-1867 cm^{-1} . Commercially available NanoIR probes for contact mode with force constants 0.07 N/m were used.

6.3.2 Plant Sample Preparation

Arabidopsis thaliana Columbia-0 plants were grown on soil in a growth chamber at 24°C at a 16h/8h light/dark photoperiod (long-day) condition. The top-most internode of four-week-old plant stems were hand sectioned using a razor blade, without being embedded. The resulting section was spread and compressed onto a SiO₂/Si⁺ wafer substrate to obtain a sample for analysis.

6.3.3 Data Analysis

AFM-IR measurements and algorithm development were conducted at the Center for Nanophase Materials Sciences, which is a US DOE Office of Science User Facility supported under Contract DE-AC05-00OR22725, (N.B., A.V.I, A.B., S.V.K, O.S.O). A portion of algorithm development was a part of the AI Initiative, sponsored by the Laboratory Directed Research and Development Program of Oak Ridge National Laboratory (S.J., R.K.V), managed by UT-Battelle, LLC, for the U.S. Department of Energy (DOE). The plant sciences portion of this work was supported by the Center for Engineering MechanoBiology (CEMB), an NSF Science and Technology Center, under grant agreement CMMI: 15-48571 (N.B. and M.F.).

6.4 Results and Discussion

6.4.1 Algorithm Description

Pan-sharpening (PS) is a family of algorithms that are widely used for image processing. Fundamentally, PS relies on the fact that there is a clear and well-defined relationship between information captured by two or more channels with different spatial resolutions. For example, traditional algorithms for PS combine low resolution RGB and high-resolution grayscale maps. In this case one can easily find the grayscale value of a pixel based on the values of individual

color channels. The resulting grayscale image, however, will contain less information rendering the reverse calculation not possible as multiple color images can collide into the same grayscale map (meaning, multiple color images can generate the same grayscale image). However, if it is known that certain pixel i on a grayscale image has certain RGB values (r_i, g_i, b_i) and grayscale intensity (h_i) , it can be assumed that a neighboring pixel j with grayscale intensity (h_j) close to (h_i) has RGB values (r_j, g_j, b_j) that are also close to (r_i, g_i, b_i) . This assumed continuity of the image is generally considered feasible as RGB values of a pixel on a map corresponds to a specific object, landscape feature or a type of material which are similar within some local area. For example, if two pixels belong to a roof on a satellite image are red, it is reasonable to assume that the rest of the roof is red as well.

Same basic considerations can be applied to a more general case of spectral pan-sharpening. Here, each pixel in the image is characterized by a full spectral vector $(x_1, x_2, \dots, x_n)_i$. At the same time, this full spectrum can be unambiguously condensed into RGB values (r_i, g_i, b_i) or grayscale intensity (h_i) . Here, RGB images and a sparse spectral map are used to restore the full-resolution dataset where a distinct spectrum is assigned to each pixel. The prerequisites for the PS approach are essentially the same – some degree of feature continuity as well as functional dependence between spectral and single-frequency datasets. It is worth noticing that while traditionally RGB channels are used to build single-band maps (commonly referred to as multispectral), it is possible to generalize this approach and expand it for an arbitrary set of distinct maps as long as the mathematical method of their generation from the spectral dataset is known.

In the case of AFM-IR, the 3D spectral dataset with low-spatial resolution is formed by acquiring point spectra on a two-dimensional grid. AFM-IR images at a fixed wavenumber (FW)

play the role of multispectral maps which will be used for the full dataset estimation. It is evident that there are multiple choices for the wavenumber selection. Figure 6.4.1 displays the overall idea of PS applied for AFM-IR. In this paper, we will refer to the original full resolution dataset $\mathbf{X} = [x_1, \dots, x_n] \in \mathbb{R}^{m_\lambda \times n}$ with a total of n points and m_λ spectral bands as *ground truth* while the result of pan-sharpening algorithm will be *pan-sharpened* hyperspectral dataset $\tilde{\mathbf{Y}}_H$. H and M subscripts are designated for hyperspectral (full resolution spectral map) and multispectral data (a group of FW images). In this paper, $\mathbf{Y}_H \in \mathbb{R}^{m_\lambda \times m}$ denotes a hyperspectral dataset with low spatial resolution and a total of m points, and $\mathbf{Y}_M \in \mathbb{R}^{n_\lambda \times n}$ is a multispectral full resolution dataset with n_λ bands (each of them is a FW image). There are multiple methods of restoration the $\tilde{\mathbf{Y}}_H$ including, but not limited to, component substitution (CS), multiresolution analysis (MRA), Bayesian methods, neural networks (NN), and matrix factorization. Coupled non-negative matrix factorization (CNMF) was chosen due to its relatively low computational costs (lower than Bayesian and NN approaches but higher than CS and MRA) and high quality of the factorization product as indicated by relevant metrics. Another reason for such choice was the incorporated analysis of component distribution which allows the use of the entire spectral range for calculating the abundance maps. Since the final goal of IR chemical imaging is to pinpoint the spatial localization of individual species with distinct spectral signatures rather than investigation of isolated IR bands, this advantage will play a significant role in correlative comparison of registered images. This approach allows for the meaningful investigation of the interplay between chemical and physical properties measured by different methods, ultimately opening a pathway for better understanding the composition-structure-property relationship at nanoscale.

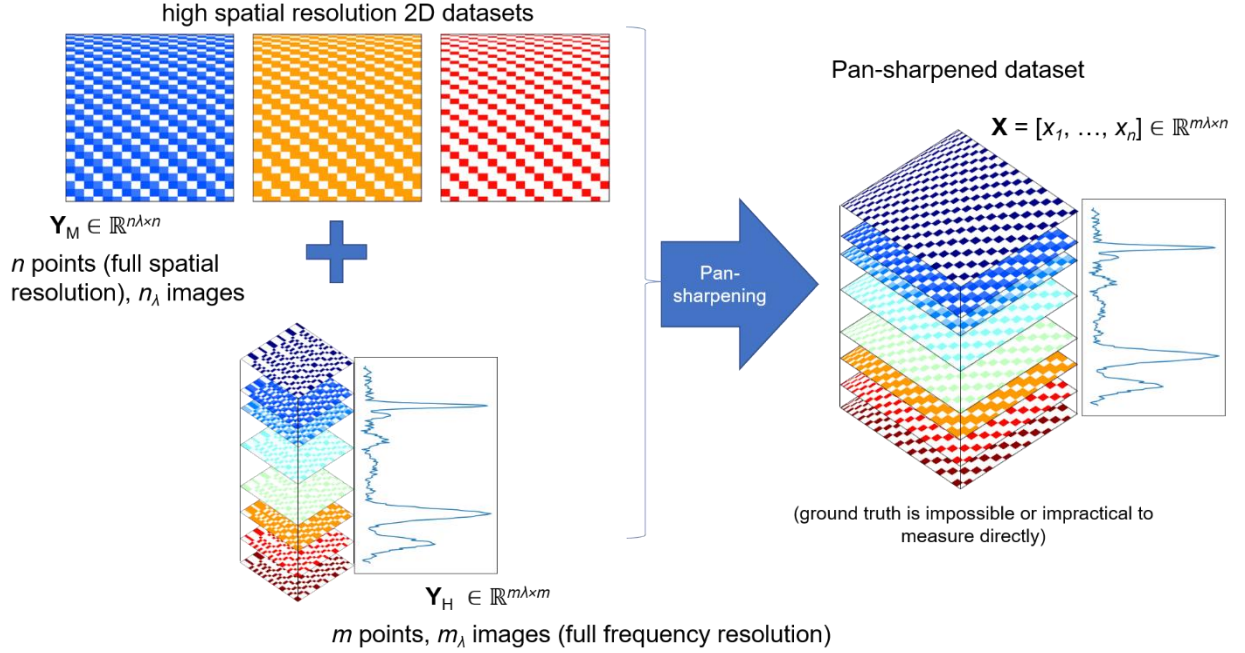


Figure 6.4.1. The general idea of the spectral pan-sharpening algorithm – create a dataset which is impossible or impractical to acquire directly by combining several fixed wavenumber images and an image with high spectral but low spatial resolution.

It is important to highlight that pan-sharpening approaches actively use the knowledge of how spectral imaging and FW maps are related. This acts as additional constraints on the algorithm output. This differentiates our method from the cases where the relationship between two channels is not known a priori and is being established during the analysis.²⁷ Thus, we incorporate our expertise in the AFM-IR technique to generate results using physically meaningful limitations. This allows to view spectral and spatial modes of AFM-IR operation as complimentary parts of the dataset that can be directly accessed. Specifically, a single wavenumber map is a slice of a 3D data cube (two physical and one spectroscopic dimension) while a low-resolution spectral map is a downsampled subset of the 3D data cube by its physical dimensions.

The details of CNMF are reviewed by Loncan et al. (Loncan et al., 2015). In brief, the assumptions behind this method are: a) there is a distinct number of endmembers with unique spectral characteristics, b) the spectral image in each point is a linear combination of endmember spectra (which may or may not be presented in pure form in the dataset). Both of these are reasonable for the case of AFM-IR where a given number of materials or regions (such as chemical interface) have intrinsic spectra with varying intensity across the image. Thus, one can represent \mathbf{X} as:

$$\mathbf{X} = \mathbf{H}\mathbf{U} \quad (1)$$

where $\mathbf{H} \in \mathbb{R}^{m_\lambda \times \rho}$ is a matrix representing spectra of ρ endmembers, and $\mathbf{U} \in \mathbb{R}^{\rho \times n}$ is the matrix containing the abundance maps of corresponding endmembers. For a low-resolution image, it can be stated that:

$$\mathbf{Y}_H \approx \mathbf{H}\mathbf{U}_H \text{ and } \mathbf{Y}_M \approx \mathbf{H}_M\mathbf{U} \quad (2)$$

where \mathbf{U}_H is the abundance map matrix of the low-resolution image and \mathbf{H}_M is the endmember matrix for the FW maps. Generally, these can be calculated from \mathbf{U} and \mathbf{H} if the spectral responses are known, however, directly accessing these matrices is not required. CNMF performs spectral unmixing of \mathbf{Y}_H and \mathbf{Y}_M and then assuming that NMF components of both decompositions are related, it combines \mathbf{H} estimated through the first decomposition and \mathbf{U} estimated through the second decomposition. Here we start with NMF unmixing of \mathbf{Y}_H by minimizing the Frobenius norm of the difference between \mathbf{Y}_H and $\mathbf{H}\mathbf{U}_H$ using random initial guess and multiplicate update solver. This yields the spectra of the endmembers contained in \mathbf{H} . The second decomposition is performed to calculate \mathbf{U} . Here, \mathbf{U}_H is spatially upsampled using bilinear interpolation and then used as an initial guess for \mathbf{U} . To generate the initial guess for \mathbf{H}_M ,

we sliced \mathbf{H} selecting only those wavenumbers that correspond to FW high resolution maps. Finally, to restore $\tilde{\mathbf{Y}}_H$ we multiply \mathbf{H} and \mathbf{U} . As a result of this operation, high-resolution abundance maps of each components are produced.

6.4.2 Simulated Dataset

To prove the feasibility of the PS via coupled NMF decomposition, we have applied it to four datasets. First, we have created a dataset that would simulate the real AFM-IR data. Three types of materials with distinct IR spectra (simulated as a series of Gaussian curves, Figure 6.5.1A) are spatially separated on a map. In addition, random noise is added (Figure 6.5.1B). A series of FW maps similar to the one displayed in Figure 6.5.1C and spectral low resolution map (a section is shown on Figure 6.5.1D) were used for the fusion. The results are showcased in Figure 6.4.2.

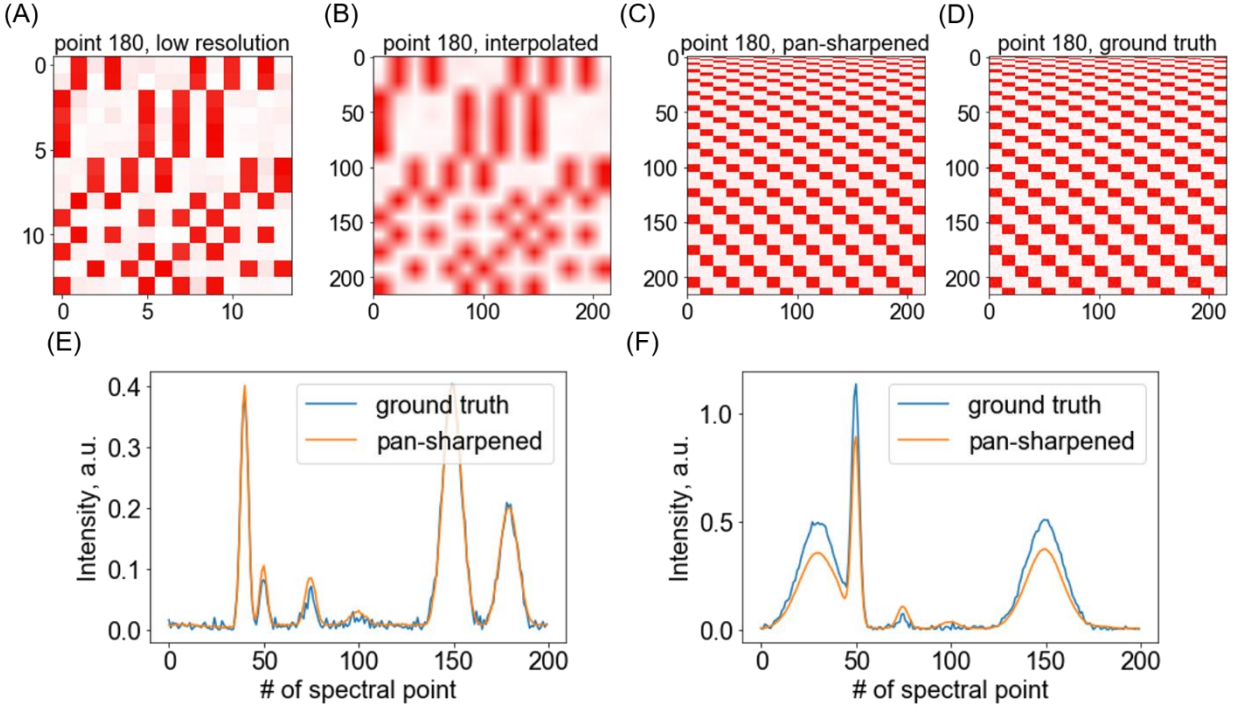


Figure 6.4.2. Pan-sharpening applied to the simulated dataset using three NMF components at a downsampling rate of 16. The FW images at spectral point 180 are shown. The FW slice of spectral dataset used for the PS (A) and its interpolation into the original image size (B) are very poor representations of the actual distribution of the band across the sample. However, the pan-sharpened image (C) is very close to the ground truth (D). The point spectra of the pan-sharpened dataset (E, F) are reasonably close to the ground truth, however, some distortions are evident. Notice that with small amounts of NMF components PS also performs denoising.

It is evident that the CNMF algorithm, with three spectral components, performs well at restoring the dataset. Visual examination of the maps at specific wavenumbers generated from \mathbf{X} and $\tilde{\mathbf{Y}}_H$ confirms the applicability of the pan-sharpening algorithm for this type of data.

Additionally, as CNMF operates by extracting individual components (Figure 6.5.2), the random noise can be removed from the data (Figure 6.4.2E,F). When the number of components increases past three, the effect of denoising is observed to a lesser degree. In order to quantitatively evaluate the quality of CNMF-based fusion, we used a number of metrics used in the pan-sharpening community. Specifically, we used three metrics: cross-correlation (CC), spectral angle mapper (SAM), and root-mean square error (RMSE). Geometric distortion of PS

result at a given wavenumber can be calculated using cross-correlation between two images. The resulting number is a measure of how similar the ground truth and the PS result are at that wavenumber. To get the global quality metric, values of CC for different wavenumbers are averaged. To estimate the spectral distortion, a spectral shape preservation is calculated in each point. This is achieved by dividing an inner product of two spectra in a given pixel (one from the ground truth and one from the PS product) by l^2 norms of those spectra. This value (spectral angle mapper) indicates the level of spectral distortion in a pixel. These pixelwise SAMs are averaged to generate an overall quality measure for a PS product. Finally, RMSE is used a third metric which is sensitive to all distortions in the data reconstruction. Overall, this set of measures allows to estimate both geometrical and spectral quality of the PS algorithm as CC describes the geometric distortion, SAM represents spectral distortion, and RMSE is a general measure of PS operation. The ideal values for CC is 1, while for SAM and RMSE the ideal value is 0 which would be attained if the PS achieved perfect dataset restoration.

We have investigated the influence of the number of NMF components as well as downsampling rate (defined here as downsampling by the same value for both axes, e.g. a 256 x 256 map turned into 16 x 16 would have a downsampling rate of 16) and number of FW maps used for the restoration on all three metrics (Figure 6.5.3). It is evident that when the number of NMF component falls below the number of distinctive spectral signatures (in this case 3), the quality of restoration is poor for all of the metrics used. At the same time, even when downsampling reaches 16 (meaning that the spectral map used for the reconstruction was only 16 x 16 pixels), the metrics are barely affected. Finally, increase of the number of FW maps used did improve the results of fusion. In the simulated dataset there are 7 characteristic peaks. While the selection of the maps does matter, it is clear that a more diverse FW input leads to a higher

quality PS result. When the number of FW maps falls below 5, the results are no longer accurate. This study highlights main rules for the CNMS-based PS: 1) number of NMF components should be at least equal to the number of distinctively dissimilar spectral signatures, 2) FW maps should be acquired for more than half of the relevant peaks, and 3) the downsampling rate can be increased significantly to speed up the measurement.

One may notice that even under the best conditions for the PS algorithm, the quality metrics are far from ideal reaching only $CC = 0.6$ and $SAM = 0.4$. This is an unexpected effect of the random noise found in the dataset. When investigated closely (Figure 6.5.4), it is clear that CNMF performs well for both noisy and clean datasets; however, the presence of random variations strongly affects metrics. CC and SAM are influenced the most while RMSE, as a metric, is more robust to noise. This is an important finding as it highlights the limited applicability of the traditional metrics used to evaluate the products of PS fusion for the case of a random noise in the dataset. Indeed, when the noise is removed, all three measures show much better results (Figure 6.5.5).

As first part of the CNMF algorithm is the endmember extraction, it is important to ensure that the sampling for the spectral mapping is representative. If there is a small object with unique spectra which did not make it to the spectral map, indeed, the PS product will not be representative. However, if the endmembers captured during the low spatial resolution scan are sufficient (meaning, any point spectrum in the dataset can be represented as a linear combination of these endmembers), then the feature of interest will be observed. For example, Figure 6.4.2A displays a slice of a very coarse spectral map. On this map the pattern is heavily distorted. However, as we use high-spatial channel to get the geometric information, we can effectively restore even smallest features.

6.4.3 Experimental AFM-IR Dataset

To confirm the assessment of CNMF-PS algorithm for AFM-IR, we acquired a high-resolution spectral map so the ground truth \mathbf{X} is known. At this stage we have used a test sample provided by Anasys which is a microtomed slide of poly(methyl methacrylate) (PMMA) and polystyrene embedded in epoxy matrix. The polystyrene and epoxy used for the preparation of a test sample have almost indistinguishable spectra because of the IR laser range, so NMF analysis uses only two components here (PMMA and epoxy/polystyrene). Figure 6.4.3 displays the NMF abundance maps after the low-resolution spectral image was decomposed (A). After interpolation, abundance maps obtain high spatial resolution (B), however, these maps do not contain new context-aware information. After a second round of NMF which uses FW images, the abundance maps converge to a detailed image (C, D). As a result, the restored maps restore $\tilde{\mathbf{Y}}_H$ with high visual quality as evident from Figure 6.4.3 (C, D, E, F) and Figure 6.5.6. Standard metrics of the PS fusion product evaluation also suggest that the algorithm is effective (Figure 6.5.7). For the analysis of the experimental data, we have also added an additional step of spectra normalization that adjusts mean and standard deviation of FW images and spectral map to match.

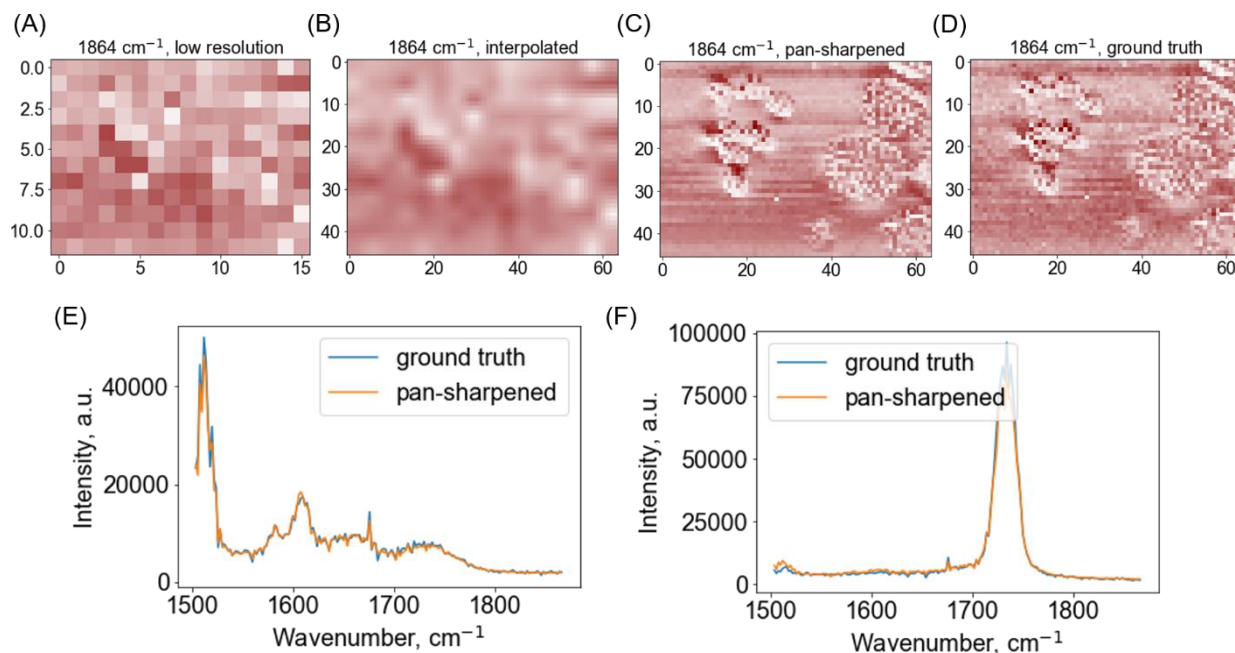


Figure 6.4.3. Pan-sharpening applied to AFM-IR dataset with known ground truth: spectral 12x16 image and 3 FW maps (1604, 1730 and 1800 cm⁻¹) were used to reconstruct the spectral 46 x 64 image with 2 NMF components. Low resolution map (A) cannot be efficiently interpolated (B), however, a product of pan-sharpening is very close to the ground truth both in terms of information about chemical distributions (C, D) and point spectra (D, E).

To further illustrate the applicability of CNMF-PS, we have performed a reconstruction of a full resolution dataset using FW maps at 1041, 1153, 1605, and 1733 cm⁻¹ and a 16 x 16 spectral map. The resulting restored dataset contains maps of IR absorption at every wavenumber available with 256 x 256 resolution. Figure 6.4.4 display the comparison of the maps in the \mathbf{X} and $\tilde{\mathbf{Y}}_H$. Maps used in the process of the fusion (1041 and 1733 cm⁻¹) as well as maps measured as control ones (such as 1363 cm⁻¹) highlight the efficiency of the approach used here to acquire multidimension datasets (see Figure 6.5.8 for NMF abundance maps).

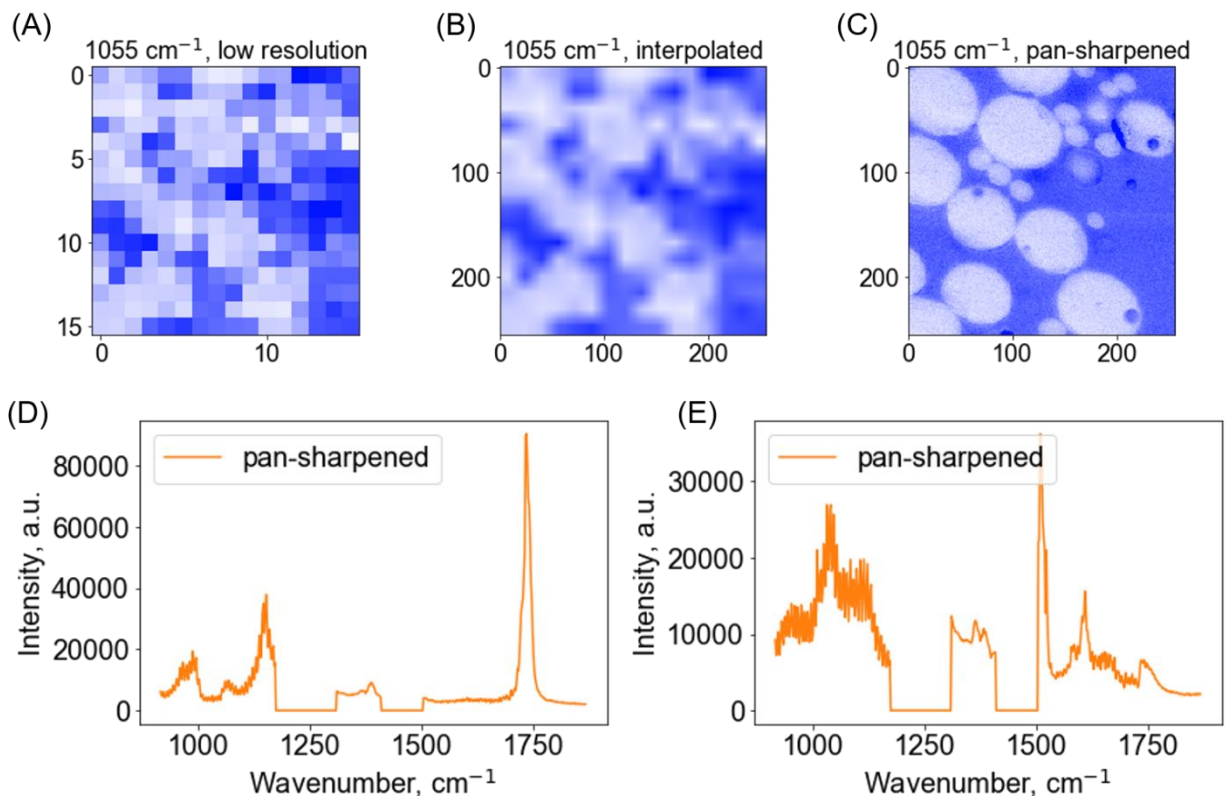


Figure 6.4.4. Pan-sharpening applied to AFM-IR dataset: spectral 16x16 image and 4 FW maps (1041, 1153, 1605 and 1733 cm^{-1}) were used to reconstruct the spectral 256 x 256 image with 2 NMF components. It is clear that PS restores dataset well after the histogram adjustment. Initial low resolution of spectral maps (A) cannot be efficiently interpolated (B), however, pan-sharpened image allows to gather detailed information about chemical distributions (C) and point spectra (D, E).

In order to capture the high-resolution spectral map of a similar quality it would take 16 x 16 = 256 times longer, which is substantial considering that acquiring a single spectrum takes about 30 seconds. Reconstructing from smaller maps allows reducing acquisition time and mitigating potential sample degradation and drift.

6.4.4 Correlative Analysis of Chemical and Mechanical Properties Using CNMF-PS

To further demonstrate the practical application of CNMF-PS algorithm, we have applied it for the analysis of plant cell walls. The primary plant cell wall is a composite material

composed of reinforcing cellulose microfibrils embedded in a mixture of other cell wall polymers, such as pectins, xyloglucans, and other non-cellulosic polysaccharides (Cosgrove, 2005; Burton et al., 2010). There is spatial and physiochemical heterogeneity in the composition and organization of polymers in the plant cell wall that is impossible to replicate in a synthetic composite material (Jochi et al., 2018; Cosgrove, 2018). This heterogeneity in the cell wall correlates with different mechanical properties across the cell, and this has bearing on whole-plant growth, cell morphogenesis, and development of tissues (Cosgrove, 2018; Gindl et al., 2004). The intrinsic complexity of the cell wall confers a plant cell the ability to provide mechanical support and strength, yet also allow for growth and flexibility in challenging environmental conditions. Advancing our understanding of the composition and organization of polymers in the plant cell wall has practical applications in biofuel energy initiatives. For instance, it may enable alterations of the cell wall chemical composition to modify wood properties and improve processes designed for biomass delignification (Tetard et al., 2012). Improved understanding of structure-property relationships that define the plant cell wall requires obtaining nanometer resolution of topological, chemical, and mechanical properties. In this work, we have prepared *Arabidopsis thaliana* plant stem for analysis with AFM-IR to obtain a correlated chemical and mechanical signature of the cell wall. This will provide insight as to how the chemical complexity and spatial variation within the cell wall contributes to its mechanical properties, such as adhesion, plasticity, and elasticity.

CNMF-based pan-sharpening was applied for an AFM-IR dataset acquired from plant cell wall placed on a Si substrate. A sparse spectral map with 256 points (16x16 grid) was fused with 8 FW maps acquired at 1071, 1131, 1319, 1403, 1533, 1591, 1653, 1740 cm^{-1} . It was found that there are two distinct spectral signatures which were identified during NMF decomposition

of the spectral dataset (Figure 6.4.5A). Strong peaks were observed in the endmember spectra of component 1 at 1591-1653 cm^{-1} likely corresponding to an Amide I band and component 2 at 1131 cm^{-1} likely corresponding to ether bond stretching. Based on these strong peak observations, component 1 was assigned as plant protein and component 2 as cell wall polysaccharides. Alonso-Simón et al. compiled a summary of wavenumbers obtained by Fourier Transform Infrared (FTIR) spectroscopy of cell walls and report that FTIR adsorption bands at 1120, 1140, and 1160 cm^{-1} correspond to xyloglucan, pectin, and cellulose, respectively (Alonso-Simon et al., 2011). The abundance maps corresponding to these NMF spectral components are presented in Figure 6.4.5B,C, which allows us to determine the distribution of the materials in the sample with respect to all peaks rather than by only one or two characteristic frequencies. Such an approach is more quantitative as it allows for efficient unmixing of overlapping IR signatures. In addition, it scales well with increasing number of the components. This is a very useful property of the CNMF-PS which makes the comparative analysis of complementary data well-grounded.

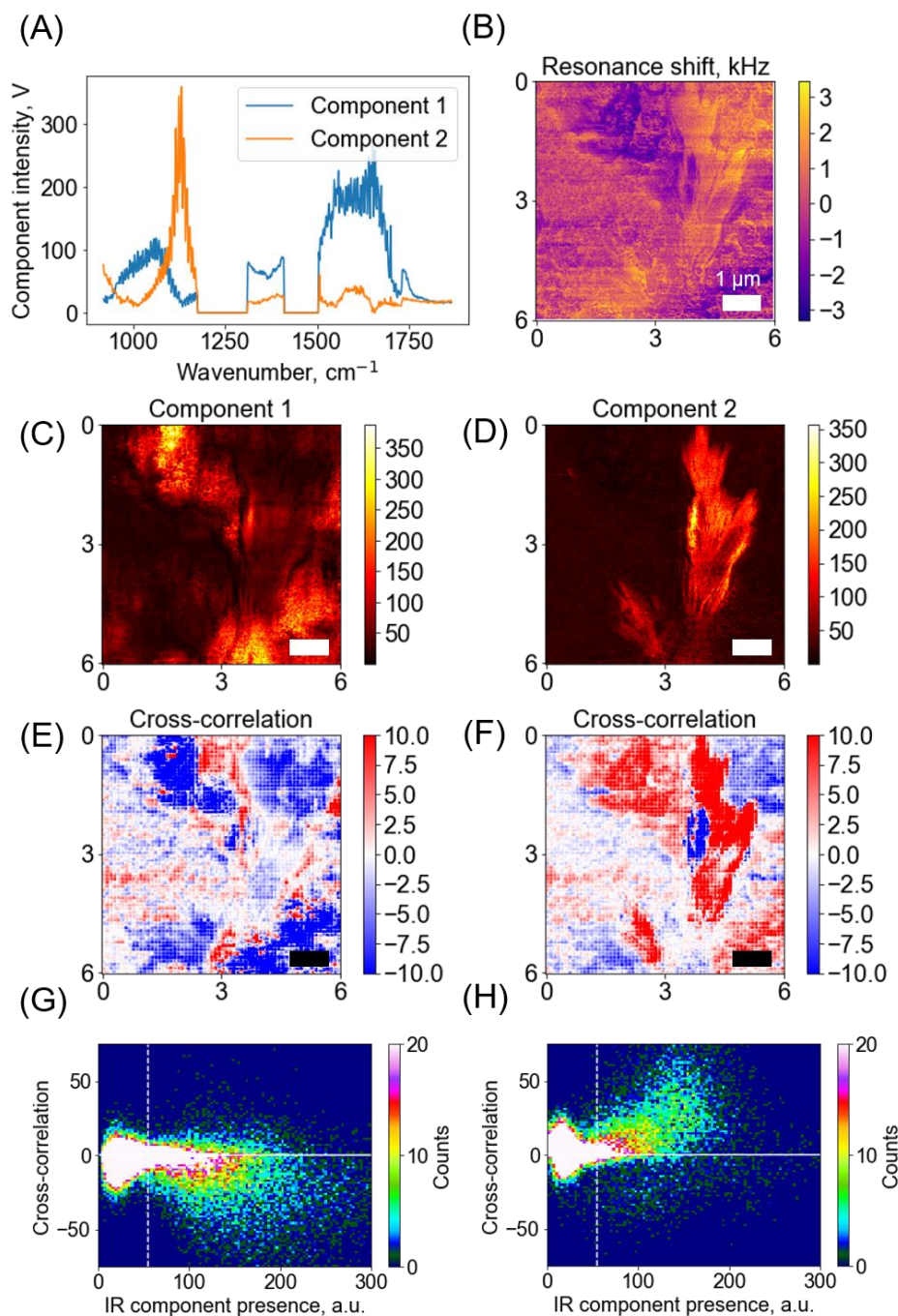


Figure 6.4.5. Pan-sharpening for data fusion: the restored IR dataset from a biological object was separated into two components (A) and correlated with the contact resonance (B). The abundance maps of the components (C,D) shows the primary localization of corresponding chemicals. Cross-correlation clearly indicates that component 1 is soft as increasing of this component loading leads to decrease in sample stiffness (E, G) while component 2 has the opposite effect (F, H). Spearman coefficient between IR component loadings and resonance shift were -0.28 and 0.28, correspondingly.

We collected a map of mechanical contact resonance over the sample. While the resonant frequency is heavily determined by the cantilever itself, the local properties of the surface which the tip is in contact with can shift the frequency up (for stiffer samples) or down (for less rigid ones). This is reflected on Figure 6.4.5B: the mechanical properties are not uniform across the sample. Visual comparison between Figures 6.4.5C,D and Figure 6.4.5B suggests that higher polysaccharide content in a given pixel increases contact resonance frequency while protein plays the opposite role, which is in good agreement from the known properties. While cell wall polysaccharides can have Young's moduli in the range of 2-140 GPa (Chanliaud et al., 2002; Gibson et al., 2012) proteins show stiffness in the ranges 0.03-0.3 MPa (Mauri et al., 2008). We have calculated a Spearman correlation which describes the correlated monotonicity of two datasets and does not imply the normal distribution of the values being compared. If a relationship between two datasets can be perfectly described as a monotonic function, Spearman's rank is equal to +1 or -1 depending on whether or not this monotonic function increases or decreases. This measure is convenient for the case of correlating dissimilar datasets as it does not require this relationship to be linear or even known in a closed form. As long as the relationship between physical and chemical parameters is monotonic, Spearman's rank would be suitable for highlighting it. Indeed, Spearman's rank for Figure 6.4.5C and Figure 6.4.5B (protein content and mechanical contact resonance) is -0.302 and for Figure 6.4.5D and Figure 6.4.5B (cell wall content and mechanical contact resonance) is +0.283 with p values being 0.0. To characterize the local similarity and highlight the regions with strongest correlation, we calculated cross-correlation within corresponding 4x4 kernels situated on respective images (Figure 6.4.5E,F). Plotting these values against the IR component intensity confirms the visual assessment and the results of Spearman's rank calculation.

The presence of a certain type of material with a distinct IR signature affects the local stiffness. Hence, in the areas where the abundance of a given component is high, we might expect strong correlation (or anticorrelation) with the resonance shift. In the areas where this component is absent the value of cross-correlation is expected to be close to zero as observed variations of the local stiffness are unrelated to the presence of a specific material. Indeed, below noise floor the IR signals and peak shift are not correlated (below white dashed line), however, if IR signal is strong enough (to the right of the white dashed line), the correlation becomes apparent. Overall, the increasing presence of component 1 leads to gradually decreasing contact resonance while component 2, on the contrary, positively contributes to the local stiffness. CNMF-PS procedure not only allows the restoration of large multidimensional datasets but also paves the way for correlative analysis (such as comparison of local mechanical properties with the distribution of specific components).

In this paper we have demonstrated the applicability of pan-sharpening algorithm to restore full spectral and full spatial resolution AFM-IR dataset. This method drastically decreases time required to acquire spectral images while simultaneously providing multicomponent analysis capability. We discuss the influence of the parameter affecting the result such as downsampling rate, number of components used for decomposition as well as number of fixed wavenumber maps involved in dataset restoration. Finally, we showcase the application of PS CNMF algorithm for correlative analysis of plant cell walls in identifying the relationship between local mechanical properties and chemical composition. Such approaches can be readily adopted for other spectral imaging techniques utilized in chemical imaging of complex materials.

6.5 Supplementary Information

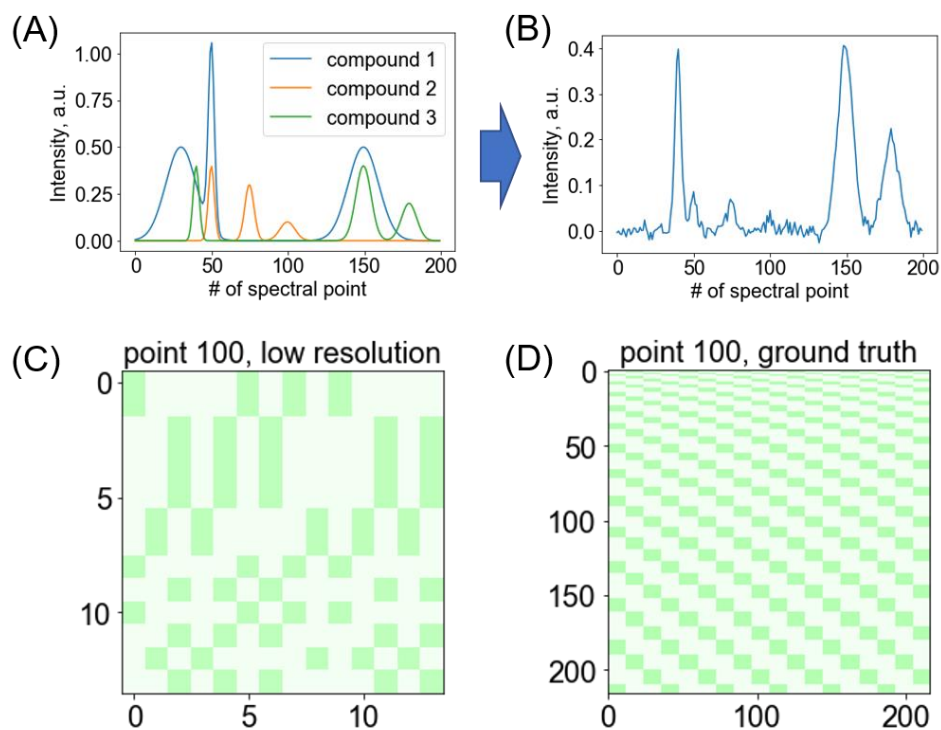


Figure 6.5.1. Simulated dataset which contains three distinct compounds with unique spectra (A). An example of a point spectrum is shown in panel (B). The FW maps (C) and spectral low resolution map (D) are the inputs of the PS algorithm.

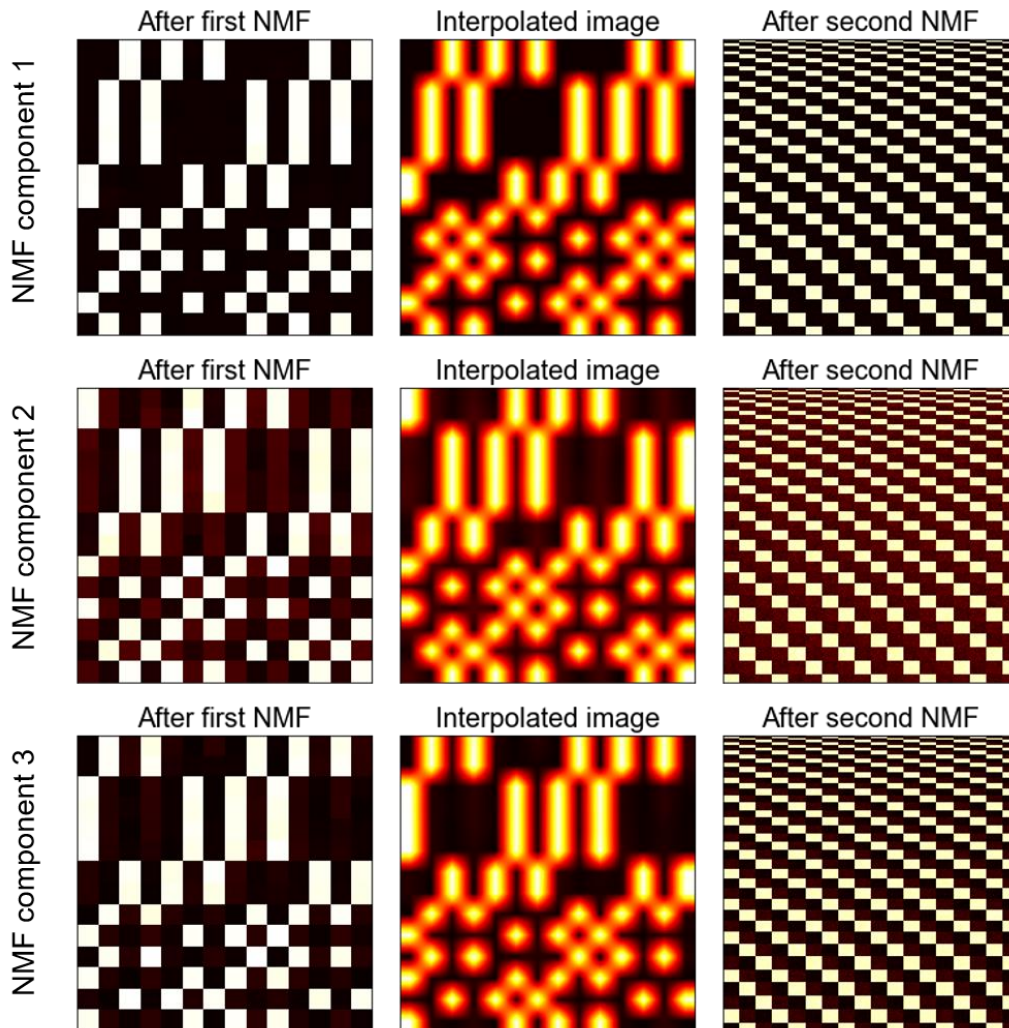


Figure 6.5.2. Component abundance maps after first NMF, interpolation and after second NMF for a simulated dataset.

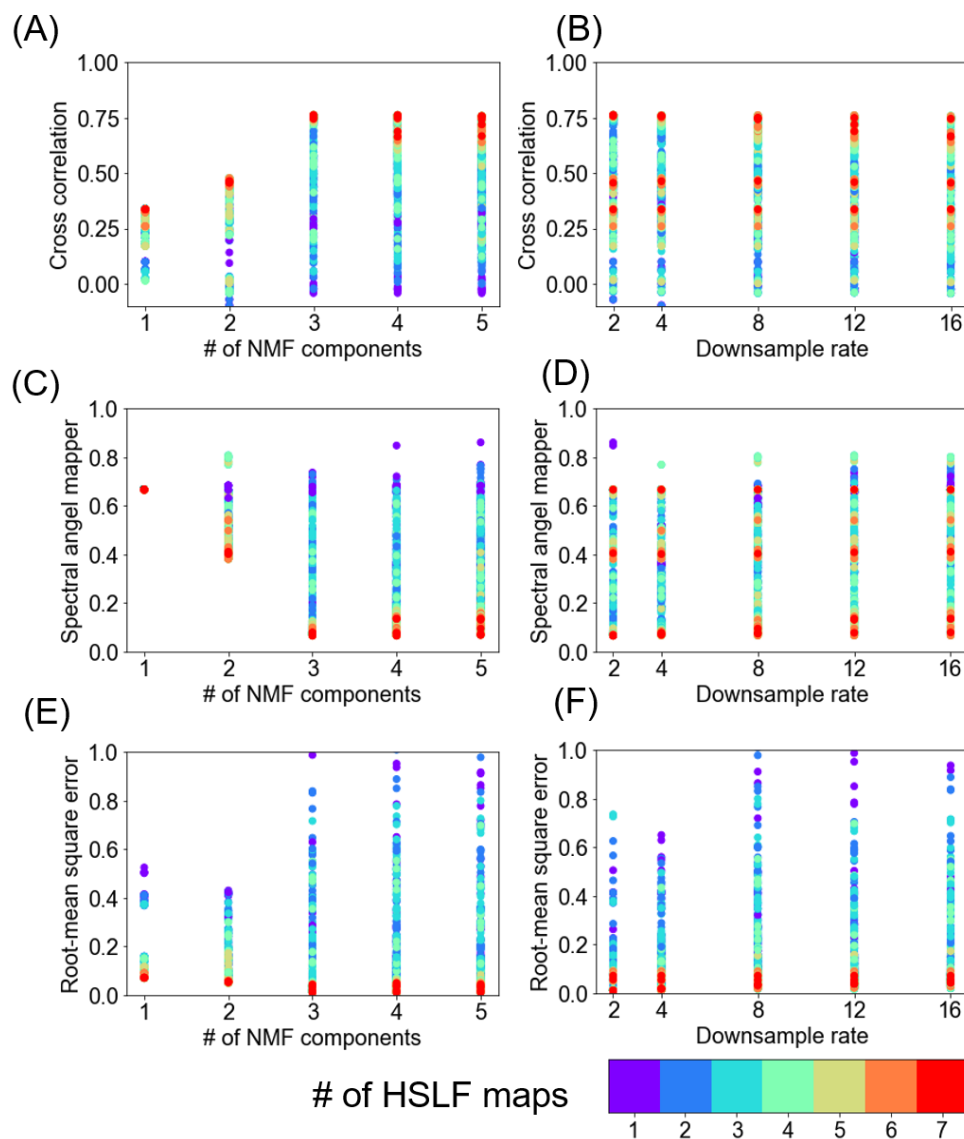


Figure 6.5.3. Cross correlation, SAM and RMSE as a function of the number of NMR components and downsample rate for a simulated dataset with noise. While downsample rate below 16 has almost no effect on the quality of fusion, it is clear that at least 3 NMF components are required for PS in this case.

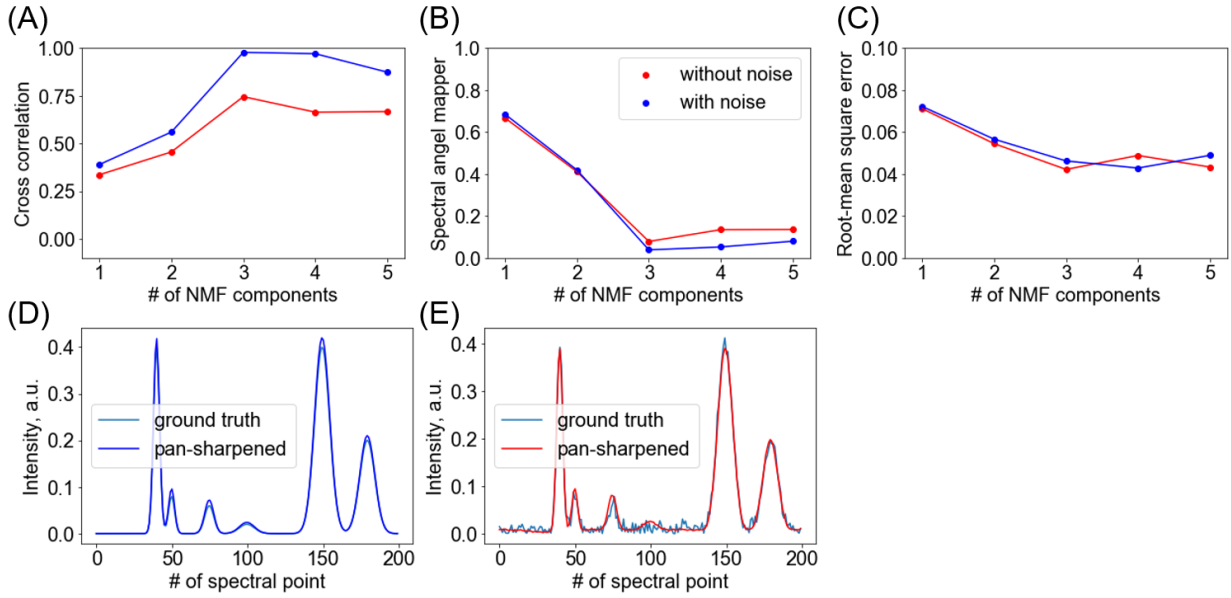


Figure 6.5.4. Quality assessment of the CNMF PS algorithm (downsample rate 16). Both cross correlation (A) and spectral angle mapper (B) show significantly different values suggesting drastic difference between quality of restoration while RMSE (C) values are similar. However, visual assessment of fusion product shows reasonable results for both clean (D) and noisy (E) data.

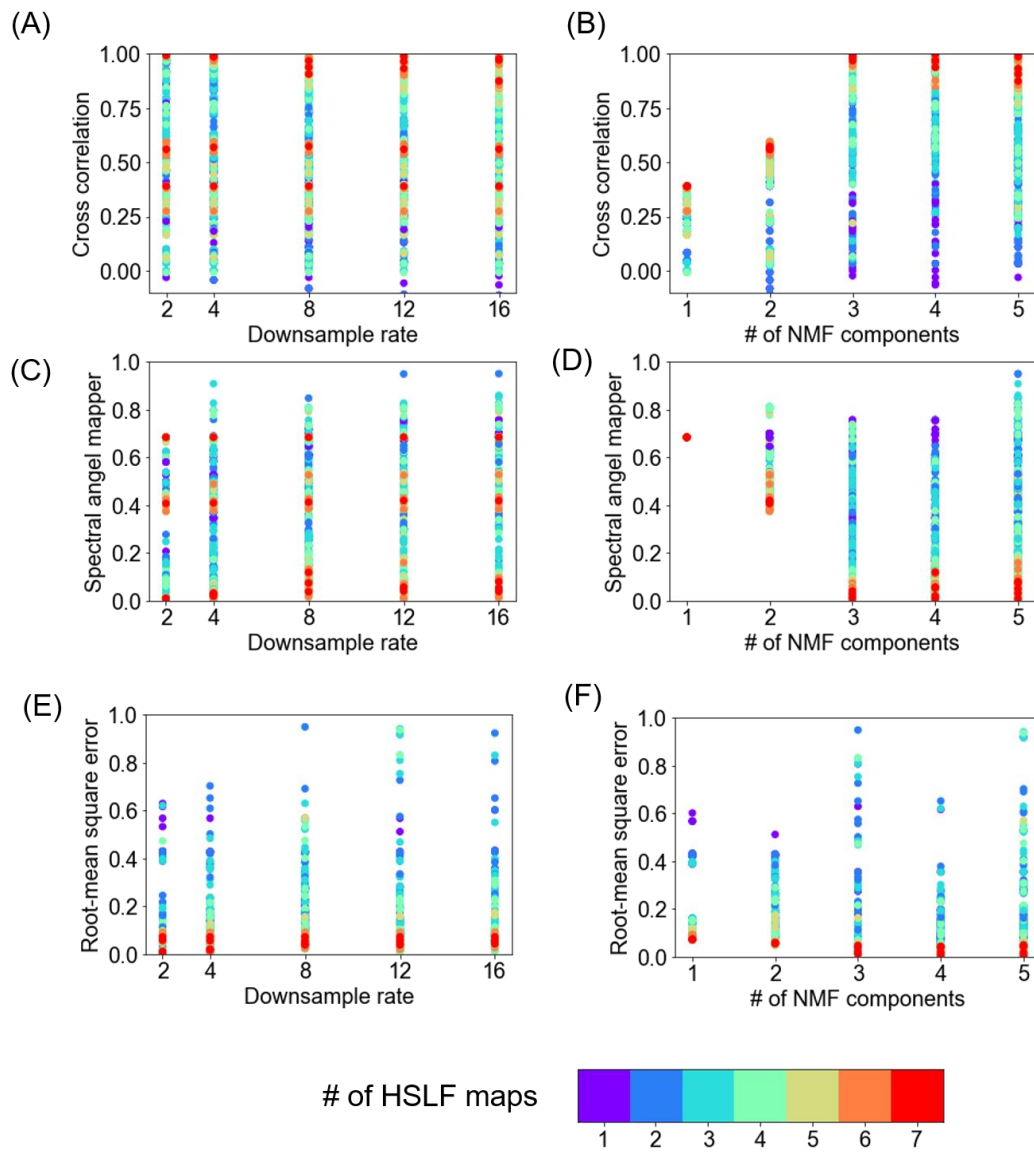


Figure 6.5.5. Cross correlation, SAM and RMSE as a function of the number of NMR components and downsample rate for a simulated dataset without noise. Again, at least 3 NMF components are required for high-quality PS in this case.

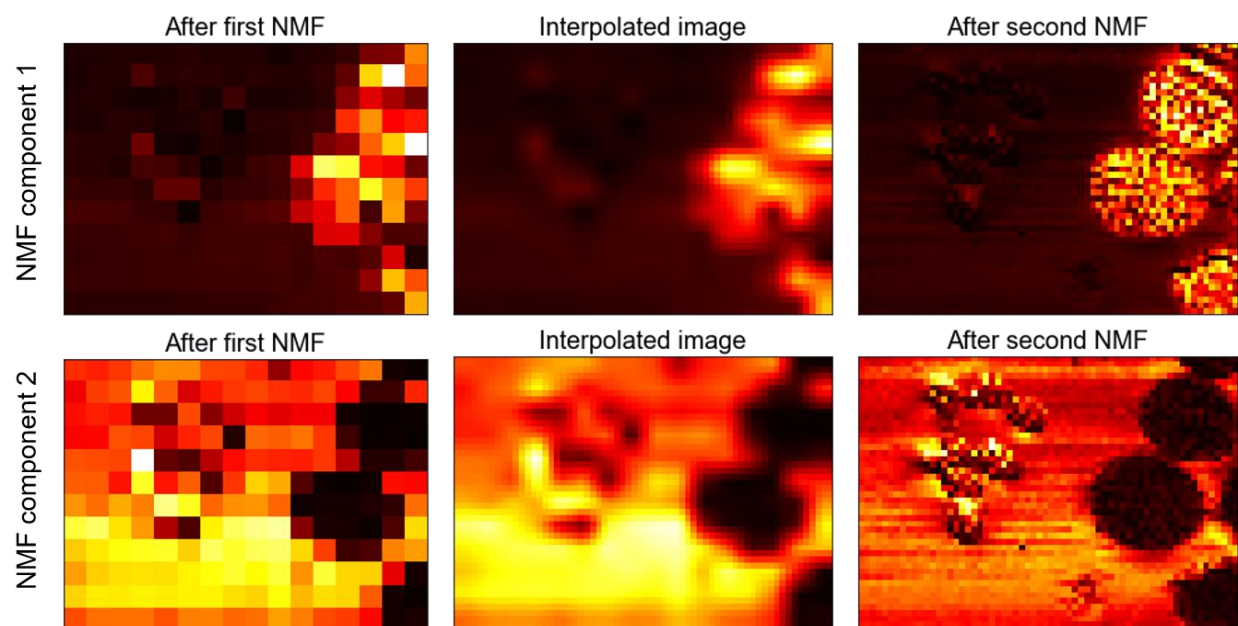


Figure 6.5.6. Component abundance maps after first NMF, interpolation and after second NMF for a spectral PMMA/polystyrene+epoxy dataset with known ground truth.

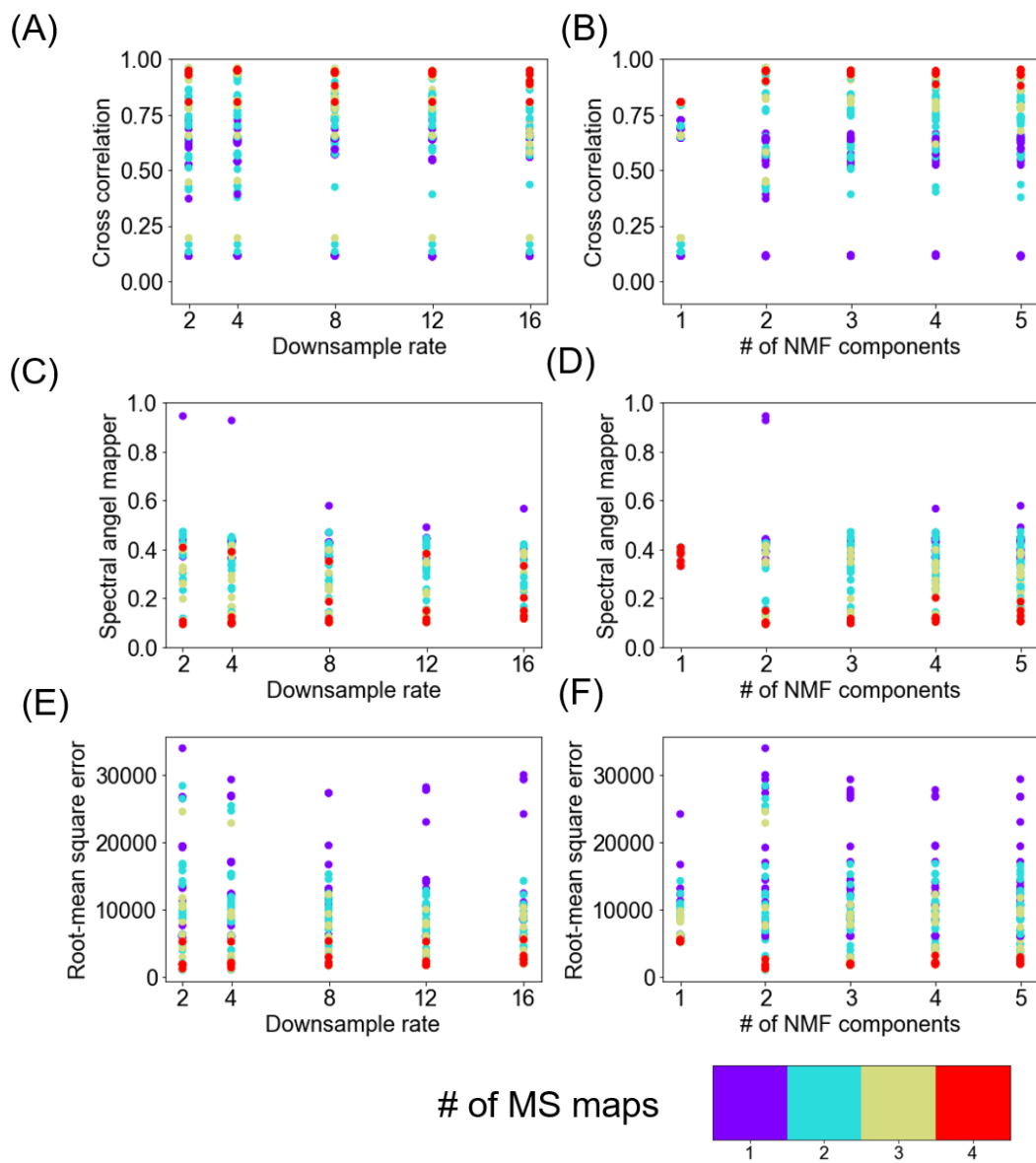


Figure 6.5.7. Cross correlation, SAM and RMSE as a function of the number of NMR components and downsample rate for a real AFM-IR dataset. 2 NMF components are required for high-quality PS in this case.

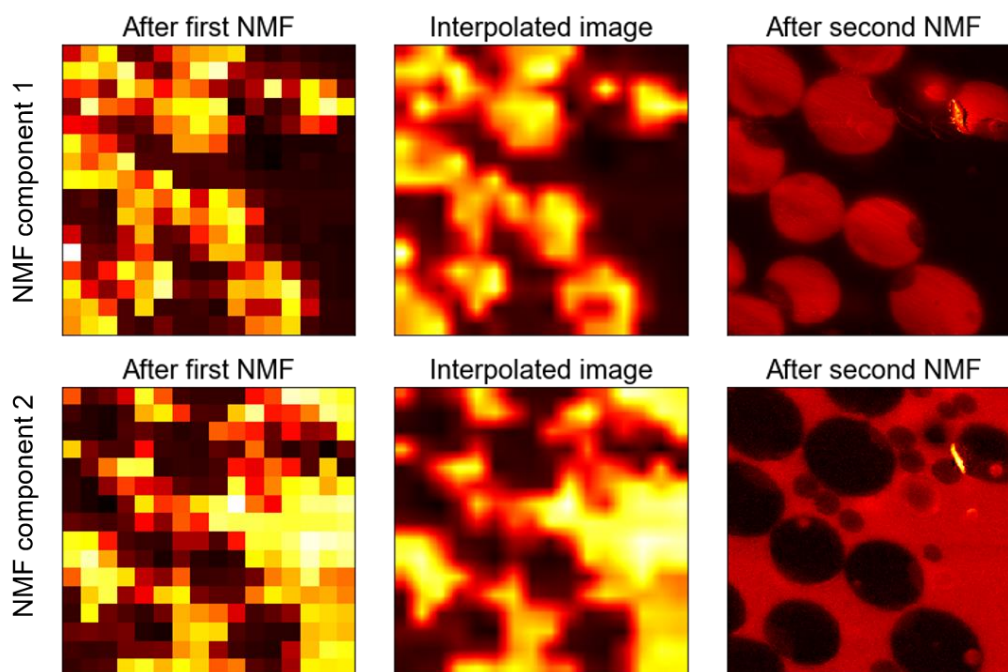


Figure 6.5.8. Component abundance maps after first NMF, interpolation and after second NMF for a use-case PMMA/polystyrene+epoxy dataset.

6.6 References

- Alonso-Simon, A.; Garcia-Angulo, P.; Melida, H.; Encina, A.; Alvarez, J. M.; Acebes, J. L., The use of FTIR spectroscopy to monitor modifications in plant cell wall architecture caused by cellulose biosynthesis inhibitors. *Plant Signal Behav* 2011, 6 (8), 1104-10.
- Belianinov, A.; Kalinin, S. V.; Jesse, S., Complete information acquisition in dynamic force microscopy. *Nat Commun* 2015, 6, 6550.
- Belianinov, A.; Vasudevan, R.; Strelcov, E.; Steed, C.; Yang, S. M.; Tselev, A.; Jesse, S.; Biegalski, M.; Shipman, G.; Symons, C.; Borisevich, A.; Archibald, R.; Kalinin, S., Big data and deep data in scanning and electron microscopies: deriving functionality from multidimensional data sets. *Adv Struct Chem Imaging* 2015, 1 (1), 6.
- Brown, P. S.; Bhushan, B., Durable, superoleophobic polymer-nanoparticle composite surfaces with re-entrant geometry via solvent-induced phase transformation. *Scientific Reports* 2016, 6.
- Burton, R. A.; Gidley, M. J.; Fincher, G. B., Heterogeneity in the chemistry, structure and function of plant cell walls. *Nat Chem Biol* 2010, 6 (10), 724-32.
- Chanliaud, E.; Burrows, K. M.; Jeronimidis, G.; Gidley, M. J., Mechanical properties of primary plant cell wall analogues. *Planta* 2002, 215 (6), 989-96.
- Clede, S.; Lambert, F.; Sandt, C.; Kascakova, S.; Unger, M.; Harte, E.; Plamont, M. A.; Saint-Fort, R.; Deniset-Besseau, A.; Gueroui, Z.; Hirschmugl, C.; Lecomte, S.; Dazzi, A.; Vessieres, A.; Policar, C., Detection of an estrogen derivative in two breast cancer cell lines using a single core multimodal probe for imaging (SCoMPI) imaged by a panel of luminescent and vibrational techniques. *Analyst* 2013, 138 (19), 5627-5638.

- Collins, L.; Ahmadi, M.; Wu, T.; Hu, B.; Kalinin, S. V.; Jesse, S., Breaking the Time Barrier in Kelvin Probe Force Microscopy: Fast Free Force Reconstruction Using the G-Mode Platform. *ACS Nano* 2017, *11* (9), 8717-8729.
- Collins, L.; Belianinov, A.; Somnath, S.; Rodriguez, B. J.; Balke, N.; Kalinin, S. V.; Jesse, S., Multifrequency spectrum analysis using fully digital G Mode-Kelvin probe force microscopy. *Nanotechnology* 2016, *27* (10), 105706.
- Cosgrove, D. J., Growth of the plant cell wall. *Nat Rev Mol Cell Biol* 2005, *6* (11), 850-61.
- Cosgrove, D. J., Nanoscale structure, mechanics and growth of epidermal cell walls. *Curr Opin Plant Biol* 2018, *46*, 77-86.
- Cui, Z.; Coletta, C.; Rebois, R.; Baiz, S.; Gervais, M.; Goubard, F.; Aubert, P.-H.; Dazzi, A.; Remita, S., Radiation-induced reduction–polymerization route for the synthesis of PEDOT conducting polymers. *Radiation Physics and Chemistry* 2016, *119*, 157-166.
- Dazzi, A.; Prater, C. B., AFM-IR: Technology and Applications in Nanoscale Infrared Spectroscopy and Chemical Imaging. *Chem Rev* 2016, *117* (7), 5146-5173.
- Dazzi, A.; Prater, C. B.; Hu, Q.; Chase, D. B.; Rabolt, J. F.; Marcott, C., AFM-IR: combining atomic force microscopy and infrared spectroscopy for nanoscale chemical characterization. *Appl Spectrosc* 2012, *66* (12), 1365-84.
- Floresyona, D.; Goubard, F.; Aubert, P. H.; Lampre, I.; Mathurin, J.; Dazzi, A.; Ghosh, S.; Beaunier, P.; Brisset, F.; Remita, S.; Ramos, L.; Remita, H., Highly active poly(3-hexylthiophene) nanostructures for photocatalysis under solar light. *Applied Catalysis B-Environmental* 2017, *209*, 23-32.
- Gibson, L. J., The hierarchical structure and mechanics of plant materials. *J R Soc Interface* 2012, *9* (76), 2749-66.

- Gindl, W.; Gupta, H. S.; Schoberl, T.; Lichtenegger, H. C.; Fratzl, P., Mechanical properties of spruce wood cell walls by nanoindentation. *Appl Phys a-Mater* 2004, 79 (8), 2069-2073.
- Gourion-Arsiquaud, S.; Marcott, C.; Hu, Q. C.; Boskey, A. L., Studying Variations in Bone Composition at Nano-Scale Resolution: A Preliminary Report. *Calcified Tissue International* 2014, 95 (5), 413-418.
- Gruverman, A.; Auciello, O.; Tokumoto, H., Imaging and control of domain structures in ferroelectric thin films via scanning force microscopy. *Annu. Rev. Mater. Sci.* 1998, 28, 101-123.
- Jesse, S.; Kalinin, S. V., Principal component and spatial correlation analysis of spectroscopic-imaging data in scanning probe microscopy. *Nanotechnology* 2009, 20 (8), 085714.
- Jochi, Y.; Seki, T.; Soejima, T.; Satoh, K.; Kamigaito, M.; Takeoka, Y., Spontaneous synthesis of a homogeneous thermoresponsive polymer network composed of polymers with a narrow molecular weight distribution. *Npg Asia Materials* 2018, 10, 840-848.
- Kalinin, S. V.; Bonnell, D. A., Imaging mechanism of piezoresponse force microscopy of ferroelectric surfaces. *Phys. Rev. B* 2002, 65 (12), 11.
- Kannan, R.; Ievlev, A. V.; Laanait, N.; Ziatdinov, M. A.; Vasudevan, R. K.; Jesse, S.; Kalinin, S. V., Deep data analysis via physically constrained linear unmixing: universal framework, domain examples, and a community-wide platform. *Adv Struct Chem Imaging* 2018, 4 (1), 6.
- Kochan, K.; Peng, H.; Wood, B. R.; Haritos, V. S., Single cell assessment of yeast metabolic engineering for enhanced lipid production using Raman and AFM-IR imaging. *Biotechnol Biofuels* 2018, 11 (1), 106.

- Kumar, A.; Ovchinnikov, O.; Guo, S.; Griggio, F.; Jesse, S.; Troler-McKinstry, S.; Kalinin, S. V., Spatially resolved mapping of disorder type and distribution in random systems using artificial neural network recognition. *Phys. Rev. B* 2011, *84* (2).
- Li, J. Y.; Li, J. F.; Yu, Q.; Chen, Q. N.; Xie, S. H., Strain-based scanning probe microscopies for functional materials, biological structures, and electrochemical systems. *Journal of Materiomics* 2015, *1* (1), 3-21.
- Loncan, L.; Almeida, L. B.; Bioucas-Dias, J. M.; Briottet, X.; Chanussot, J.; Dobigeon, N.; Fabre, S.; Liao, W. Z.; Licciardi, G. A.; Simoes, M.; Tourneret, J. Y.; Veganzones, M. A.; Vivone, G.; Wei, Q.; Yokoya, N., Hyperspectral Pansharpening: A Review. *IEEE Geosci. Remote Sens. Mag.* 2015, *3* (3), 27-46.
- Mauri, A. N.; Añón, M. C., Mechanical and Physical Properties of Soy Protein Films with pH-Modified Microstructures. *Food Science and Technology International* 2008, *14* (2), 119-125.
- Mikhalchan, A.; Banas, A. M.; Banas, K.; Borkowska, A. M.; Nowakowski, M.; Breese, M. B. H.; Kwiatek, W. M.; Paluszkiwicz, C.; Tay, T. E., Revealing Chemical Heterogeneity of CNT Fiber Nanocomposites via Nanoscale Chemical Imaging. *Chem. Mater.* 2018, *30* (6), 1856-1864.
- Morsch, S.; Liu, Y.; Lyon, S. B.; Gibbon, S. R., Insights into Epoxy Network Nanostructural Heterogeneity Using AFM-IR. *ACS Appl Mater Interfaces* 2016, *8* (1), 959-66.
- Nikiforov, M. P.; Reukov, V. V.; Thompson, G. L.; Vertegel, A. A.; Guo, S.; Kalinin, S. V.; Jesse, S., Functional recognition imaging using artificial neural networks: applications to rapid cellular identification via broadband electromechanical response. *Nanotechnology* 2009, *20* (40), 405708.

- Ovchinnikova, O. S.; Tai, T.; Bocharova, V.; Okatan, M. B.; Belianinov, A.; Kertesz, V.; Jesse, S.; Van Berkel, G. J., Co-registered Topographical, Band Excitation Nanomechanical, and Mass Spectral Imaging Using a Combined Atomic Force Microscopy/Mass Spectrometry Platform. *ACS Nano* 2015, 9 (4), 4260-9.
- Pancani, E.; Mathurin, J.; Bilent, S.; Bernet-Camard, M.-F.; Dazzi, A.; Deniset-Besseau, A.; Gref, R., High-Resolution Label-Free Detection of Biocompatible Polymeric Nanoparticles in Cells. *Particle & Particle Systems Characterization* 2018, 35 (3), 1700457.
- Somerville, C.; Bauer, S.; Brininstool, G.; Facette, M.; Hamann, T.; Milne, J.; Osborne, E.; Paredez, A.; Persson, S.; Raab, T.; Vorwerk, S.; Youngs, H., Toward a systems approach to understanding plant cell walls. *Science* 2004, 306 (5705), 2206-11.
- Somnath, S.; Belianinov, A.; Kalinin, S. V.; Jesse, S., Full information acquisition in piezoresponse force microscopy. *Applied Physics Letters* 2015, 107 (26).
- Somnath, S.; Law, K. J. H.; Morozovska, A. N.; Maksymovych, P.; Kim, Y.; Lu, X.; Alexe, M.; Archibald, R.; Kalinin, S. V.; Jesse, S.; Vasudevan, R. K., Ultrafast current imaging by Bayesian inversion. *Nat Commun* 2018, 9 (1), 513.
- Tetard, L.; Passian, A.; Jung, S.; Ragauskas, A. J.; Davison, B. H., Development of New Methods in Scanning Probe Microscopy for Lignocellulosic Biomass Characterization. *Industrial Biotechnology* 2012, 8 (4), 245-249.
- Thompson, G. L.; Reukov, V. V.; Nikiforov, M. P.; Jesse, S.; Kalinin, S. V.; Vertegel, A. A., Electromechanical and elastic probing of bacteria in a cell culture medium. *Nanotechnology* 2012, 23 (24), 245705.

Van de Plas, R.; Yang, J.; Spraggins, J.; Caprioli, R. M., Image fusion of mass spectrometry and microscopy: a multimodality paradigm for molecular tissue mapping. *Nat Methods* 2015, *12* (4), 366-72.

Vivone, G.; Alparone, L.; Chanussot, J.; Dalla Mura, M.; Garzelli, A.; Licciardi, G. A.; Restaino, R.; Wald, L., A Critical Comparison Among Pansharpening Algorithms. *Ieee Transactions on Geoscience and Remote Sensing* 2015, *53* (5), 2565-2586.

Appendix II: Structural insights into how the *Arabidopsis* SPIRAL2 protein targets and stabilizes microtubule minus ends³

7.1 Abstract

The acentrosomal cortical microtubules of higher plants dynamically assemble into specific array patterns that determine the axis of cell expansion. Recently, the *Arabidopsis* SPIRAL2 (SPR2) protein was shown to regulate cortical microtubule length and light-induced array reorientation by stabilizing microtubule minus ends. SPR2 autonomously localizes to both the microtubule lattice and minus ends and decreases the minus end depolymerization rate. Here, we used biochemical, structural, cell biological, and genetic experiments to identify the structural determinants required for SPR2 to target and stabilize microtubule minus ends. We present the crystal structure of the SPR2 N-terminal domain, which reveals a unique TOG domain architecture with seven HEAT repeats. We demonstrate that a coiled-coil domain mediates multimerization of SPR2 that provides avidity for microtubule binding and is essential to bind soluble tubulin. The TOG domain, a basic region, and coiled-coil domain are necessary and sufficient to target and stabilize microtubule minus ends both *in vitro* and in plants. These results reveal how a TOG domain, which is typically found in microtubule plus-end regulators, has been appropriated in plants to regulate microtubule minus ends.

³ This chapter has been adapted from Fan et al., 2023.

7.2 Introduction

Plant cortical microtubules (MTs) play an essential role in cell morphogenesis by guiding the deposition of cellulose (Paredez et al., 2006) and matrix polysaccharides (Zhu et al., 2015; Kong et al., 2015) into the cell wall. This function relies on the creation and maintenance of distinctive cortical MT arrays in different cell types as well as their dynamic rearrangement in response to various internal and external stimuli (Oda, 2015). Since the bulk of cortical MTs have free plus and minus ends, modulating the dynamics of both ends is important to array organization and remodeling.

The dynamics of both MT ends are controlled by a group of specialized proteins that recognize specific tubulin conformations at the MT plus end and minus end, respectively (Akhmanova and Steinmetz, 2015; Nogales and Zhang, 2016). MT plus-end tracking proteins (+TIPs) specifically decorate growing plus ends and serve to stabilize plus ends and link them to other cellular structures (Galjart, 2010). Likewise, MT minus-end targeting proteins (-TIPs) stabilize free MT minus ends and attach them to other cellular structures (Akhmanova and Steinmetz, 2019).

In animals, the calmodulin-regulated spectrin-associated protein (CAMSAP)/Patronin/Nezha family of -TIPs has been studied extensively. Different members of this protein family either track growing MT minus ends (Jiang et al., 2014), progressively accumulate on the MT lattice formed by growth at the minus end (Jiang et al., 2014), or bind to and inhibit the growth of minus ends (Hendershott and Vale, 2014). This protein family is distinguished by the presence of a C-terminal CAMSAP1, KIAA1078 and KIAA1543 (CKK) domain which confers MT minus-end targeting (Atherton et al., 2019, 2017).

Plants lack the CAMSAP/Patronin/Nezha protein family. Recently, the plant-specific TORTIFOLIA1/SPIRAL2 (SPR2) protein was found to autonomously localize to and stabilize MT minus ends (Fan et al., 2018; Leong et al., 2018; Nakamura et al., 2018). Loss of SPR2 greatly enhances the frequency and rate of MT minus end depolymerization and impairs the ability of the cortical MT array to dynamically reorient in response to blue light perception (Fan et al., 2018; Leong et al., 2018; Nakamura et al., 2018). Notably, the SPR2 protein differs from the CAMSAP/Patronin/Nezha protein family in both structure and dynamics. SPR2 lacks the CKK domain that is necessary for CAMSAP/Patronin/Nezha proteins to recognize MT minus ends. In addition, unlike the CAMSAP/Patronin/Nezha proteins, SPR2 tracks depolymerizing MT minus ends both *in vivo* and *in vitro*, localizes to the MT lattice, and to a lesser extent to growing MT plus ends (Fan et al., 2018; Nakamura et al., 2018).

The Arabidopsis SPR2 protein contains five predicted Huntington, elongation factor 3, phosphatase 2A, target of rapamycin 1 (HEAT) repeats at the amino terminus followed by a basic region and coiled-coil domain (Fan et al., 2018). A HEAT repeat domain followed by a basic region is reminiscent of the tumor overexpressed gene (TOG) domain-containing MT regulatory proteins XMAP215 and CLASP, which localize primarily to MT plus ends in both plants and animals (Brouhard et al., 2008; Kawamura and Wasteney, 2008; Mimori-Kiyosue et al., 2005; Ambrose et al., 2007). A TOG domain is characterized by the presence of six HEAT repeats that form a paddle-shaped structure, and in the case of the yeast XMAP215 member, Stu2, binds a tubulin dimer with high affinity (Al-Bassam et al., 2006, 2007; Slep and Vale, 2007; Ayaz et al., 2012). While TOG domains are best known for their ability to bind to free tubulin subunits (Ayaz et al., 2012, 2014), structural differences in some of the TOG domains of XMAP215 and CLASP proteins confer binding to MT lattice-incorporated tubulin (Fox et al.,

2014; Byrnes and Slep, 2017; Leano and Slep, 2019). Proteins that contain more than two TOG domains (e.g., human and plant XMAP215 homologs) function as monomers (Currie et al., 2011; Lechner et al., 2012; Widlund et al., 2011), whereas those that contain only one or two TOG domains (e.g., yeast XMAP215 homologs and Cep104) function either as dimers or oligomers (Al-Bassam et al., 2006; Gard et al., 2004; Rezabkova et al., 2016), with the possible exception for the mitogen-activated protein kinase activator MEKK1 (Filipčík et al., 2020). Thus, involvement of multiple TOG domains is an important characteristic of proteins that regulate MT dynamics.

Here, we report structural, biochemical, and cell biological data that together identify key structural features of SPR2 for targeting and stabilizing MT minus ends. We found that the N-terminus of SPR2 contains a single tubulin-binding TOG domain followed by a basic region that confers binding to the MT lattice. X-ray crystallography revealed that the TOG domain of SPR2 is structurally unique with seven HEAT repeats. In addition, we demonstrate that multimerization of SPR2 by the coiled-coil domain increases its MT-binding affinity and is essential for SPR2 to bind and recruit soluble tubulin dimers to a MT. When expressed in the *Arabidopsis thaliana spr2-2* mutant, the N-terminal and coiled-coil domains of SPR2 are necessary and sufficient to stably localize to the minus ends of cortical MTs and inhibit their depolymerization rate. Together, our results establish SPR2 as a distinct TOG domain-containing protein that has evolved to regulate the dynamics of MT minus ends.

7.3 Materials and Methods

7.3.1 Plant Growth

Arabidopsis thaliana (L.) Heynh. Columbia-0 (Col-0) plants were used for all experiments. For growth on plates, seeds were sterilized with 25% (v/v) bleach for 10 min, rinsed five times with sterile water, suspended in 0.1% (w/v) sterile agarose solution, and planted on plates containing 2.2 g/L MS salts with Gamborg's vitamins (Caisson Laboratories), 3 g/L Sucrose, pH 5.7. Seeds were stratified in the dark at 4°C for 2-3 days and then grown at 23°C under 16 h light for 4 days. When transferred to the soil, seedlings were grown under continuous light at 22°C.

7.3.2 Constructs

For live imaging, the *pSPR2::SPR2-mRuby* construct (Fan et al., 2018) was modified by replacing the full-length *SPR2* cDNA with the appropriate truncated *SPR2* cDNAs. These constructs were introduced into the *spr2-2* mutant expressing a GFP-TUB6 MT marker (Fan et al., 2018) using *Agrobacterium*-mediated floral dip transformation. Transgenic plants were selected using 100 mg/L gentamicin with 50 mg/L kanamycin, and homozygous lines containing a single copy of the transgene were used for further study.

For protein expression, the pGEX *SPR2-GFP* construct (Fan et al., 2018) was modified by inserting a PaeI restriction site between *SPR2* and *GFP*, and the PreScission protease site was replaced by a TEV protease site. *SPR2* fragments were generated using PCR, restriction digested by BamHI and PaeI enzymes, and used to replace the full-length *SPR2* in the modified pGEX *SPR2-GFP* construct. To generate His-tagged expression constructs, *SPR2* cDNA encoding residues 33-333 aa and 503-566 aa were obtained using PCR and individually sub-cloned into

pET28 (MilliporeSigma) using engineered NdeI and EcoRI restriction endonuclease sites to generate thrombin-cleavable His-tagged proteins. Primers used in this study are listed in Table 7.6.2.

7.3.3 Protein Purification

GST-tagged SPR2 proteins were expressed in *E. coli* Rosetta DE3 cells and purified using affinity chromatography with Glutathione Sepharose beads (GE Healthcare) in a cold room. Purified proteins were treated with His-tagged TEV protease (1.7 mg/ml) in cleavage buffer (50 mM Tris-HCl, 150 mM NaCl, 1 mM EDTA, 1 mM dithiothreitol, 1% Triton X-100, pH 7.0) for 20 hours to remove the GST tag, and free SPR2 proteins were separated from the beads by centrifugation. The TEV protease was removed from the digested proteins by incubation with Ni²⁺-NTA beads for 2.5 hours in a cold room. Isolated proteins were desalted using PD-10 columns (GE Healthcare) and exchanged into BRB80 buffer (80 mM piperazine-1,4-bis(2-ethanesulfonic acid), 1mM MgCl₂, and 1mM EGTA, pH 6.8) supplemented with 50 mM NaCl to prevent protein aggregation. Proteins were either flash-frozen in liquid nitrogen and kept at -80°C for long-term storage or kept on ice and used within 1 week.

His-tagged SPR2 proteins were expressed in *E. coli* BL21 DE3 pLysS cells and purified using Ni²⁺-NTA column (Qiagen). The N-terminal His₆ tag was cleaved with bovine α -thrombin (Haematologic Technologies). Cleaved proteins were filtered over a benzamidine-Sepharose (GE Healthcare) column to remove thrombin and a subsequent Ni²⁺-NTA column used to remove uncleaved His₆-tagged protein. Cleaved protein constructs were buffer exchanged into storage buffer (25 mM Tris pH 8.5, 500 mM NaCl, and 0.1% β -mercaptoethanol), concentrated using 3

kDa Amicon Ultra Spin Concentrators (MilliporeSigma), flash-frozen in liquid nitrogen, and stored at -80°C. Detailed protein purification procedures are provided in Supplemental Methods.

7.3.4 MT Cosedimentation

MTs were prepared using unlabeled porcine brain tubulin (Cytoskeleton Inc) reconstituted in ice-cold BRB80 buffer, polymerized in the presence of 1mM Mg-GTP for 1 hour at 37°C, and assembled MTs stabilized with 20 µM paclitaxel (Cytoskeleton Inc). Different concentrations of taxol-stabilized MTs were co-incubated with either 2 µM SPR2(1-500)-GFP or SPR2(1-570)-GFP, 0.1 mg/ml bovine serum albumin (BSA), and 20 µM paclitaxel for 20 min. MTs and bound proteins were sedimented by centrifugation at 100,000 g at 25°C for 20 min. Supernatant and pellet fractions were resuspended in equal volumes of loading buffer and analyzed using SDS-PAGE. The amount of SPR2 protein in the supernatant and pellet fractions was quantified using densitometry.

7.3.5 *In vitro* MT Dynamics Reconstitution Experiments

In vitro assays with dynamic MTs were conducted as described in (Fan et al., 2018). Briefly, 300 nM GMPCPP-stabilized MT seeds containing 1:12 biotin-labeled and 1:10 rhodamine-labeled porcine tubulins (Cytoskeleton Inc) bound to coverslips were used to initiate MT polymerization by flowing in 20 mM 1:25 rhodamine-labeled porcine tubulin in BRB80 buffer containing 1% methyl cellulose (4000 cP, MilliporeSigma), 50 mM DTT, 2 mM GTP, an oxygen-scavenging system, and 500 nM of either full-length or truncated SPR2-GFP proteins. Images were collected by a 100X (NA 1.45) objective and a back-illuminated electron-multiplying CCD camera (ImageEM; Hamamatsu) at 2 s intervals.

7.3.6 Live Imaging of Arabidopsis Seedlings

Variable-angle epifluorescence microscopy images were collected from hypocotyl epidermal cells of four-day-old, light-grown Arabidopsis seedlings as described in (Fan et al., 2018).

7.3.7 Soluble Tubulin Pulldown

Anti-GFP beads (MBL Life Science) were equilibrated in binding buffer (BRB80 buffer supplemented with 50 mM NaCl and 0.05% Tween-20) and incubated with 1 μ M full-length SPR2-GFP protein on a rotary shaker for 2.5 hours at room temperature. Beads were then blocked with 3 μ M BSA for 1 hour on a shaker in a cold room and 2 μ M unlabeled porcine tubulin (Cytoskeleton Inc) prepared in binding buffer containing 10 mM DTT and 0.2 mM PMSF was added and incubated overnight. Beads were centrifuged at 1000 g for 1 min, washed 3-times with binding buffer, transferred to a fresh tube and washed again for 5-times with binding buffer. Bound proteins were then analyzed with SDS-PAGE. As controls, 1 μ M of full-length SPR2-GFP and 2 μ M unlabeled porcine tubulin were incubated separately with the anti-GFP beads.

7.3.8 Imaging Soluble Tubulin Binding to MT-bound SPR2-GFP Proteins

GMPCPP-stabilized MTs were assembled using 50 μ M unlabeled porcine tubulin containing 1:12 biotin-labeled porcine tubulin (Cytoskeleton Inc.) and polymerized in the presence of 1mM GMPCPP (Jena Bioscience) at 37°C for 30 min. 300 nM GMPCPP-stabilized MTs were introduced into a flow chamber and allowed to bind to 20% anti-biotin antibody for 10 min. 100 nM of the specified SPR2-GFP proteins along with 2.5 μ M 1:9 rhodamine-labeled porcine tubulin were then introduced into the flow chamber in BRB80 buffer containing 1%

methyl cellulose (4000 cP, MilliporeSigma), 50 mM DTT and an oxygen-scavenging system (Fan et al., 2018). GFP and rhodamine were excited using 5 mW 488 nm and 561 nm diode-pumped solid-state lasers and images collected by a 100x (NA 1.45) objective and a back-illuminated electron-multiplying CCD camera (Image EM; Hamamatsu) at 2 s intervals.

7.3.9 Size Exclusion Chromatography Multi-Angle Light Scattering

Full-length and truncated SPR2 constructs were individually injected onto a Superdex 200 10/300 GL size exclusion column (GE Healthcare) pre-equilibrated and run in storage buffer supplemented with 0.2 g/L sodium azide. Samples were subsequently passed consecutively through a Wyatt DAWN HELEOS II light scattering instrument and a Wyatt Optilab rEX refractometer. The light scattering and refractive index values were used to calculate the weight-averaged molar mass (M_w) and the mass fraction in each peak using the Wyatt Astra V software program (Wyatt Technology Corp).

7.3.10 Crystallization, Data Collection, and Structure Determination

The SPR2 N-terminal domain construct (residues 33-333) was crystallized using the hanging drop method: 2 μ l of 15.7 mg/ml protein plus 2 μ l of a 1 ml well solution containing 27.5% (w/v) PEG 3350, 150 mM ammonium phosphate, and 280 mM sodium iodide at 18 °C. A SPR2 crystal was cryo-frozen in 27.5% (w/v) PEG 3350, 150 mM ammonium phosphate, and 30% (v/v) glycerol. Two native diffraction data sets were collected on single crystal (after a translation of the crystal along the axis of the goniometer) at the Advanced Photon Source 22-ID beamline at 100 K (each collection: 360 frames, 0.5° oscillations, 12398.420 eV; run 1 start = -119.00°, run 2 start = -28.00°). Data were processed and merged using HKL2000 (Otwinowski and Minor, 1997). AlphaFold was used to generate a model of the SPR2 N-terminal domain

(residues 33-333) (Jumper et al., 2021; Varadi et al., 2022), from which a truncated model (residues 43-323) was used in a molecular replacement search to phase the structure. The molecular replacement search yielded a refined log likelihood gain of 212 for one protomer in the asymmetric unit (57% solvent). Initial models were built using AutoBuild (PHENIX) followed by reiterative buildings in Coot (Emsley et al., 2010) and refinement runs using phenix.refine (PHENIX) (Adams et al., 2010). Refinement runs used real space and reciprocal space refinement protocols, including simulated annealing with torsion angle molecular dynamics (temperatures: 5,000 K start, 300 K final, 50 steps), initial secondary structure restraints, individual B-factor refinement, and atomic displacement parameters using a maximum-likelihood target. The final refinement run yielded a R_{free} value of 25.9%. The final model includes SPR2 residues 33-327, an N-terminal Gly-Ser-His-Met cloning artifact, a single iodine atom, and seven water molecules. Data collection and refinement statistics are summarized in Table 7.6.1. Structure images were generated using the PyMOL Molecular Graphics System, version 2.4.0 (Schrödinger, LLC), including use of the program's structure alignment protocol (except for the structure alignment of SPR2 and Stu2 TOG2 (pdb 4U3J) (Ayaz et al., 2014) which used the Dali server (Holm, 2020). Sequence similarity was based on the following amino acid grouping criteria: [N,Q,H], [T,S,C], [D,E], [R,K], [F,Y,W], [L,V,I,M], [A,G,S], [P].

7.3.11 Quantification and Statistical Analysis

All experiments were repeated at least three times using independent plants and protein preparations. Statistical significance of data was calculated using the Student's *t*-test. To quantify the dynamics of MTs *in vivo* and *in vitro*, kymographs of individual MTs were generated using

the Dynamic Kymograph plugin (Zhou et al., 2020) and analyzed using the MT Kymograph Analysis plugin (Zhou et al., 2020). Graphs and curve fitting was done using GraphPad Prism.

7.3.12 Data Deposition

Coordinates for the *Arabidopsis thaliana* SPIRAL2 TOG domain structure have been deposited in the Protein Data Bank under accession code: 8D00.

7.4 Results

7.4.1 The N-terminal region of SPR2 mediates MT lattice binding and minus-end localization

To identify the domains that enable SPR2 to bind and stabilize MT minus ends, we generated truncated versions of the SPR2 protein that were tagged with green fluorescent protein (GFP) at their C-terminus (Figure 7.4.1A). Full-length and truncated GFP-labeled SPR2 proteins were recombinantly expressed and purified (Figure 7.4.1B) and used to assess MT binding in functional reconstitution experiments. In these *in vitro* experiments, we used dynamic rhodamine-labeled MTs that polymerized from immobilized GMPCPP-stabilized MT fragments (called ‘seeds’). We found that the N-terminal fragment of SPR2 that lacks the basic region (1-276 aa) does not bind to MTs (Figure 7.4.1C). Inclusion of the basic region conferred uniform binding along the MT lattice, with the extent of MT binding correlating positively with the length of the basic region (compare the 1-340 aa and 1-400 aa fragments in Figure 7.4.1C). Notably, a larger N-terminal fragment which includes the complete basic region as well as an unstructured region preceding the coiled-coil domain (1-500 aa) showed punctate MT lattice binding and minus end localization (Figure 7.4.1C), similar to full-length SPR2 (Figure 7.4.1F). Furthermore, the 1-500 aa fragment bound more readily to the GMPCPP-stabilized MT seeds

than to the GTP/GDP-state dynamic polymer (Figure 7.4.1C), also similar to full-length SPR2 (Figure 7.4.1F).

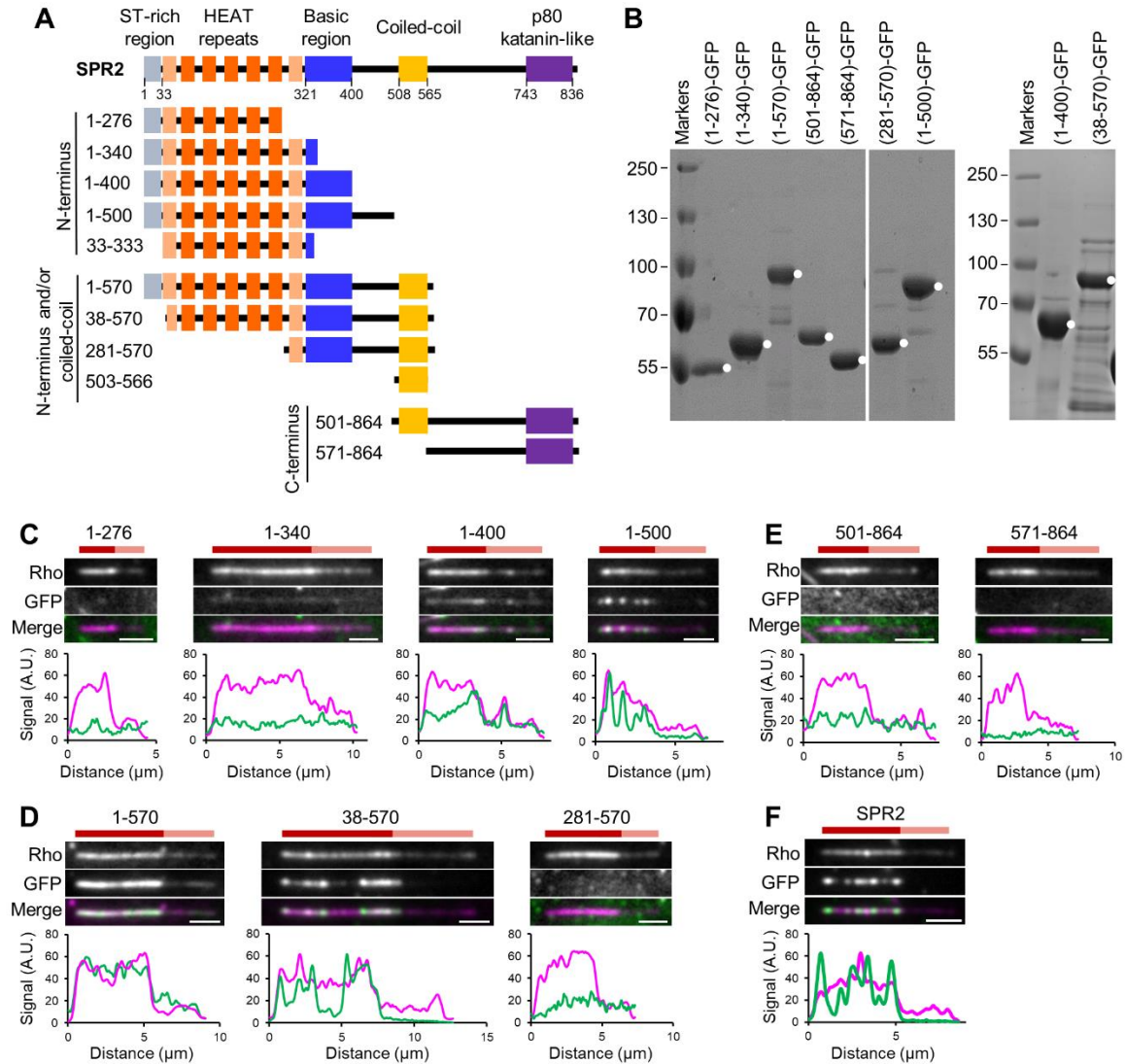


Figure 7.4.1. MT binding and minus-end localization of SPR2 fragments. (A) Schematic representation of the domain architecture of SPR2 protein and the various truncations used in this study. (B) Coomassie Blue-stained SDS-PAGE gels of recombinantly expressed and purified GFP-tagged SPR2 protein fragments. Dots indicate the expected size of each protein. (C-F) Representative images of the localization of 500 nM GFP-tagged N-terminal fragments (C), N-terminus and coiled-coil containing fragments (D), C-terminal fragments (E), and full-length SPR2 (F) along rhodamine-labeled microtubules (Rho). Fluorescence intensity profiles of microtubules (magenta) and SPR2 protein (green) are shown below each image set. A.U., arbitrary units. Scale bar = 2 μ m.

The coiled-coil domain dramatically increased MT binding of the N-terminal fragment of SPR2 (1-570 aa). The 1-570 aa fragment occasionally showed punctate MT binding, but more commonly showed continuous signal along the MT length with a strong preference for the GMPCPP-stabilized MT seeds over the GTP/GDP-state dynamic polymer (Figure 7.4.1D). Deletion of the Ser/Thr-rich region at the extreme N-terminus (38-570 aa) did not perturb MT lattice binding and minus end localization (Figure 7.4.1D). However, a larger deletion that encompasses the HEAT repeat region (281-570 aa) is unable to bind to MTs (Figure 7.4.1D).

The C-terminal region of the SPR2 protein, with or without the coiled-coil domain, does not bind to MTs (Figure 7.4.1E). Comparing the MT binding of the various SPR2 protein fragments to full-length SPR2 protein indicates that the 38-570 aa fragment most closely mimics the extent and pattern of MT binding of full-length SPR2.

7.4.2 Multimerization of SPR2 enhances microtubule binding

Given the striking difference in the extent of MT decoration between the 1-500 aa and 1-570 aa fragments of SPR2, we investigated whether the coiled-coil domain increases the MT binding affinity of SPR2. Using MT co-sedimentation assays, we found that the 1-500 aa fragment shows nonsaturating MT binding with an apparent K_D of 17.4 μM (Figures 7.4.2A and 7.4.2C). By contrast, the 1-570 aa fragment bound to MTs with an apparent K_D of 1.3 μM (Figures 7.4.2B and 7.4.2D). Therefore, the coiled-coil domain increases the MT binding affinity of SPR2 by at least one order of magnitude.

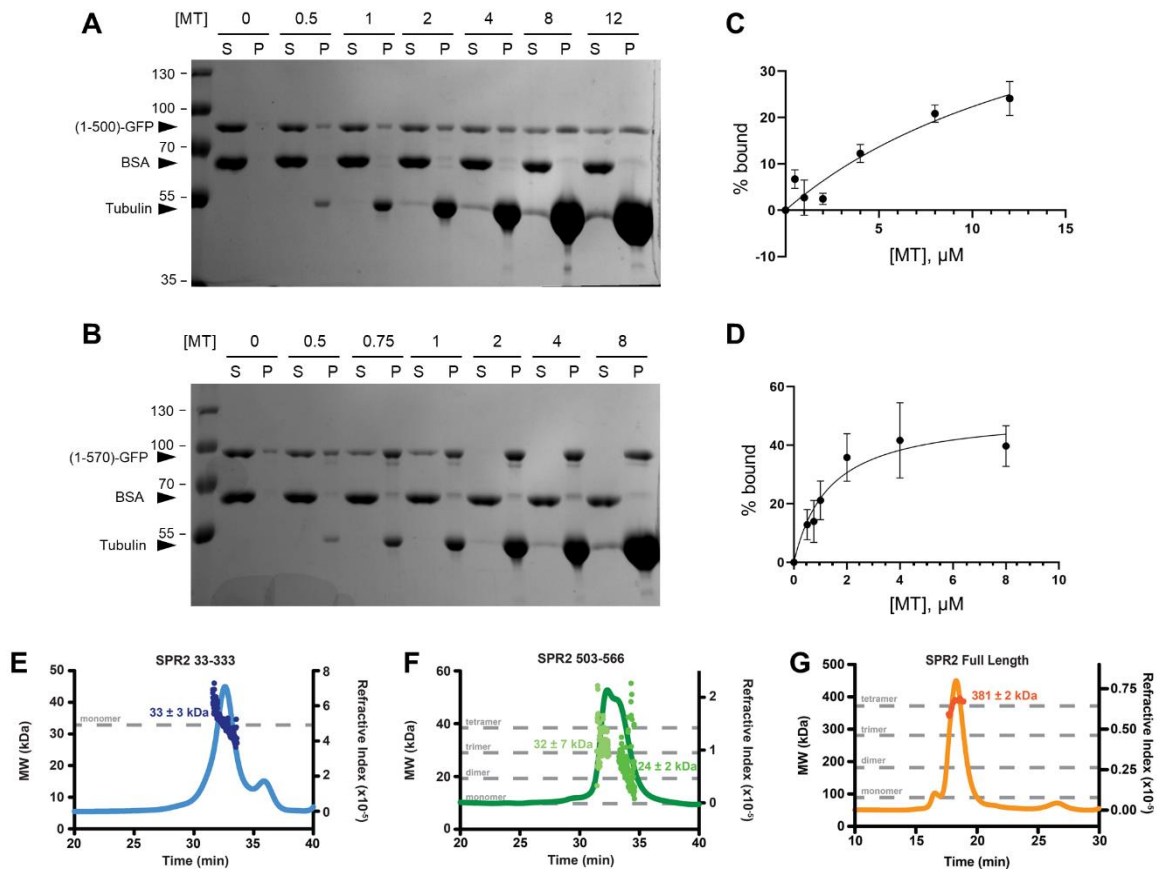


Figure 7.4.2. Multimerization state of SPR2. (A, B) Coomassie Blue-stained SDS-PAGE gels of microtubule cosedimentation assays. 2 μ M (1-500)-GFP (A) or (1-570)-GFP (B) were co-incubated with increasing concentrations of taxol-stabilized microtubules, 0.1 mg/ml BSA, and 20 μ M taxol for 20 min. S, supernatant; P, pellet. Arrowheads identify the different protein bands. (C, D) MT binding curves for (1-500)-GFP (C) or (1-570)-GFP (D), respectively. Each data point represents the mean \pm SD from three independent experiments. The data were fit to a model assuming single-site specific binding yielding apparent K_D values of 17.4 μ M and 1.3 μ M for (1-500)-GFP and (1-570)-GFP, respectively. (E-G) SEC-MALS analysis of SPR2 33-333 (E), SPR2 503-566 (F), and full-length SPR2 (G). Plots show the elution profile of each construct from a size exclusion column as measured using the refractive index (y-axis at right) over time. The experimentally determined mass is plotted in kDa (MW, y-axis at left) over time for each main peak. The average mass (\pm SD) is indicated. For each construct, dashed gray lines indicate the monomeric formula weight. For the traces of the SPR2 503-566 and the SPR2 1-864 constructs, additional dashed gray lines indicate the MW of theoretical dimer, trimer, and tetramer species. Plots shown are representative of experiments run in duplicate.

Yeast two-hybrid and bimolecular fluorescence complementation experiments have demonstrated that SPR2 interacts with itself (Fan et al., 2018; Haikonen et al., 2013). In addition, photobleaching analysis indicates that SPR2 exists primarily as multimers (Fan et al., 2018). To determine whether the coiled-coil domain is responsible for multimerization of SPR2, we

purified the SPR2 N-terminal domain (33-333 aa), central domain (503-566 aa), and full-length protein and analyzed each construct using size exclusion chromatography-multi angle light scattering (SEC-MALS). The SPR2 N-terminal domain (Figure 7.4.2E) eluted as one main peak with an experimentally determined mass (33 ± 3 kDa) similar to the monomeric formula weight (32.8 kDa). By contrast, the SPR2 central region containing the coiled-coil domain eluted as a bimodal peak (Figure 7.4.2F). Analysis of the experimental mass across the first portion of the bimodal peak yielded a mass of 32 ± 7 kDa while the later portion of the bimodal peak yielded a mass of 24 ± 2 kDa. The predicted masses of dimeric (19.2 kDa), trimeric (28.9 kDa), and tetrameric (38.5 kDa) species indicate that the SPR2 central domain forms a higher-order oligomer, potentially a tetramer formed as a dimer of dimers. The full-length SPR2 eluted as a single main peak with an experimental mass of 381 ± 2 kDa, aligned with a predicted tetramer mass of 376 kDa (Figure 7.4.2G). Prior SEC-MALS analysis of the SPR2 C-terminal domain from *P. patens* and *A. thaliana* (649-864 aa) revealed a monomeric domain (Ohno et al., 2023; Bolhuis et al.). These results indicate that the central coiled-coil domain mediates tetramerization and that regions flanking residues 503-566 contribute to tetramer stability.

7.4.3 The 1-500 aa, 1-570 aa and 38-570 aa fragments of SPR2 inhibit the dynamics of microtubule minus ends

Our *in vitro* reconstitution experiments showed that the 1-500 aa, 1-570 aa and 38-570 aa fragments of SPR2 localize to the minus ends of GMPCPP-stabilized MTs (Figures 7.4.1C and 7.4.1D). To determine whether these SPR2 fragments affect the dynamics of MT plus and minus ends, we conducted kymograph analysis (Figure 7.4.3A). We included the 1-400 aa fragment in this analysis to assess whether its binding along the lattice influences MT dynamics.

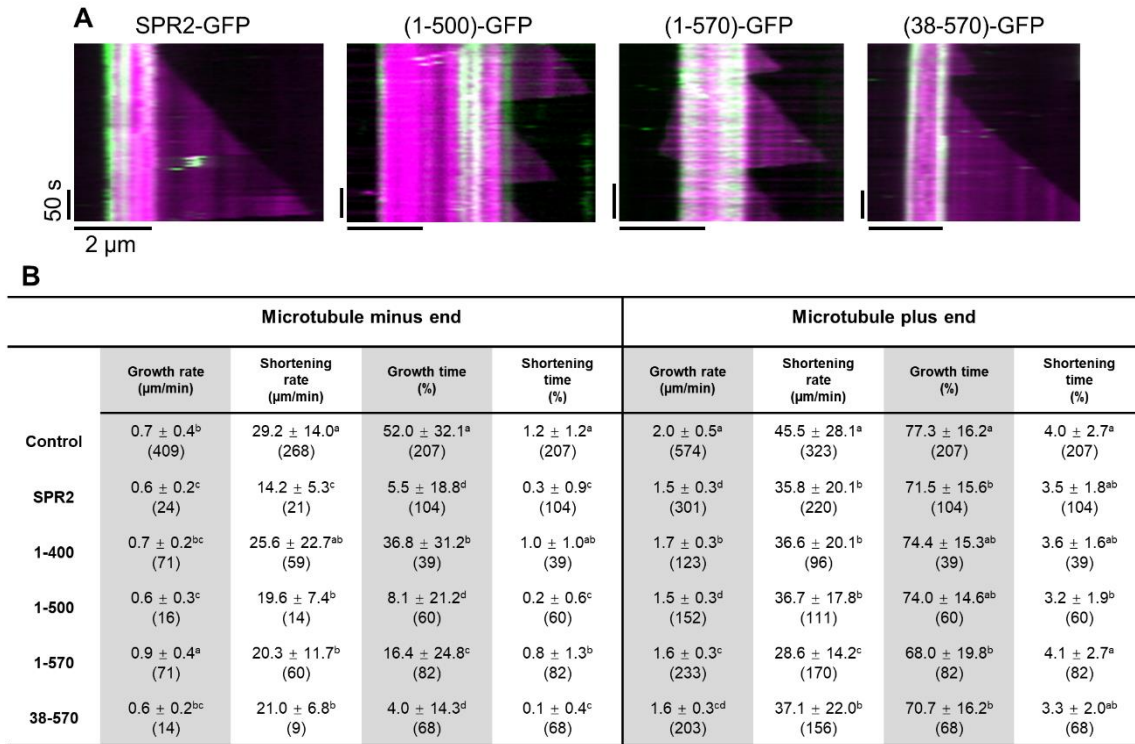


Figure 7.4.3. Effect of SPR2 fragments on MT dynamics in vitro. (A) Kymographs of MTs in the presence of 500 nM of indicated SPR2 proteins. (B) In vitro MT dynamics measurements for the experiments shown in (A). Only MTs that had continuous GFP signal at the minus end were analyzed. Values are means \pm SD (n = number of events for growth and shortening rates; n = total number of kymographs for percent growth and shortening times). The letters indicate statistically distinguishable groups as determined by the Student's t -test ($p < 0.05$).

MT minus ends that had a clearly detectable GFP signal from the 1-500 aa, 1-570 aa and 38-570 aa fragments spent significantly less time growing and shortening compared to the tubulin-alone control (Figure 7.4.3B). This effect is like that of the full-length SPR2 protein. Unexpectedly, the 1-570 aa fragment, which showed the highest MT binding, inhibited MT minus end dynamics to a lesser degree than the 1-500 aa and 38-570 aa fragments (Figure 7.4.3B).

The 1-400 aa fragment impacted MT minus end dynamics significantly less than the 1-500 aa, 1-570 aa and 38-570 aa SPR2 fragments (Figure 7.4.3B). All the SPR2 fragments used in this study altered the dynamics of MT plus ends to a small degree (Figure 7.4.3B). This is likely

an indirect effect of these proteins binding to the MT lattice, as previously reported for full-length SPR2 (Fan et al., 2018).

7.4.4 SPR2 binds to free tubulin dimers

The Arabidopsis SPR2 protein is predicted to contain five HEAT repeats near the N-terminus (Figure 7.4.1A), flanked by predicted, conserved pairs of helices. We wondered whether SPR2 has an additional, cryptic sixth HEAT repeat, which would collectively constitute a TOG domain. Since TOG domains are best known for their ability to bind to free tubulin dimers (Ayaz et al., 2012, 2014), we conducted pulldown experiments to test this possibility with full-length SPR2-GFP. These experiments revealed that SPR2-GFP can bind directly to soluble GDP-state tubulin (Figure 7.4.4A). To determine the structural elements required for SPR2 to bind to free tubulin and to investigate whether SPR2 can simultaneously bind to free tubulin and MT lattice, we used a total internal reflection fluorescence microscopy-based assay. In this assay, unlabeled GMPCPP-MTs were co-incubated with GFP-labeled SPR2 protein and GDP-state rhodamine-labeled tubulin (Figure 7.4.4B). In the absence of SPR2 protein, rhodamine-labeled tubulin did not localize to MTs (Figure 4C). However, in the presence of full-length SPR2-GFP protein, we observed punctate rhodamine-tubulin signal that coincides with SPR2-GFP puncta along the MT lattice (Figure 7.4.4C). Similarly, rhodamine-tubulin puncta consistently colocalized with 1-570 aa and 38-570 aa SPR2 puncta on the MT lattice (Figure 7.4.4C). However, 1-500 aa and 1-400 aa SPR2 fragments were unable to recruit rhodamine-tubulin to the MT lattice (Figure 7.4.4C). Therefore, we conclude that multimerization is required for SPR2 to bind and recruit tubulin dimers to the MT lattice.

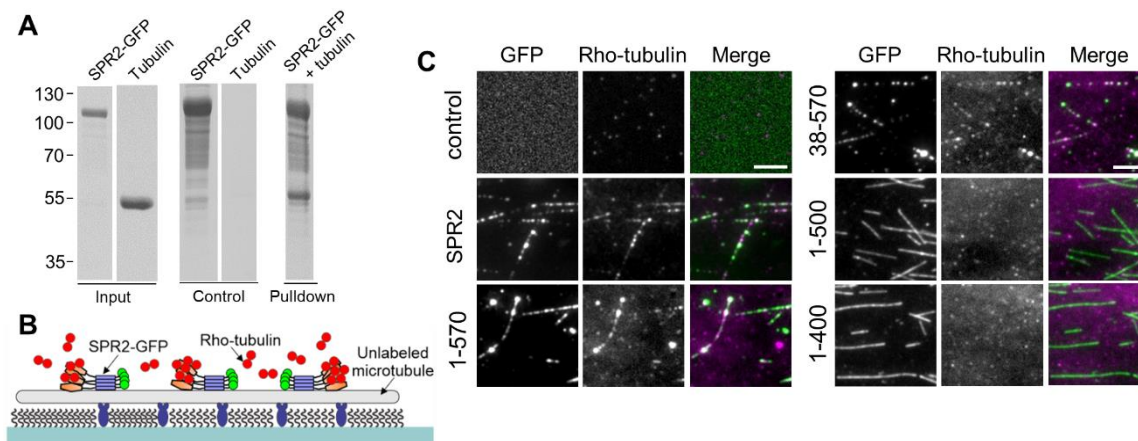


Figure 7.4.4. SPR2 binds soluble tubulin dimers. (A) Coomassie Blue-stained gel of an in vitro pulldown experiment with GFP-tagged full-length SPR2 incubated with soluble tubulin. (B) Schematic diagram of the in vitro assay to determine whether SPR2 and various fragments can bind simultaneously to MT lattice and tubulin subunits. (C) Micrographs of 100 nM of the indicated GFP-tagged SPR2 proteins incubated with unlabeled GMPCPP-stabilized MTs and soluble rhodamine-labeled tubulin. Scale bars = 5 μm.

7.4.5 The SPR2 N-terminal domain is an architecturally distinct TOG domain

To gain insight into the architecture of the SPR2 N-terminal domain, we determined the crystal structure of a construct spanning residues 33-333 aa to 2.5 Å resolution (for crystallographic statistics see Table 7.6.1). The structure was solved by molecular replacement using search model coordinates obtained from AlphaFold (Jumper et al., 2021; Varadi et al., 2022). The final, refined model ($R = 0.214$, $R_{\text{free}} = 0.259$, see final $2F_o - F_c$ electron density in (Figure 7.6.1A) encompasses residues 33-327, and consists of seven HEAT repeats (HR), designated HR A-G. Together, these HRs structurally resemble a TOG domain (Figure 7.4.5A), although its α -solenoid includes an additional HR relative to the six found in TOG structures determined to date. The refined model aligns well with the AlphaFold prediction model ($C\alpha$ RMSD = 1.1 Å), with differences localized to the HR C-D inter-HEAT loop, and the relative positioning of HR A and HR G (Figures 7.6.1B and 7.6.1C). Like tubulin-binding TOG domains, the SPR2 N-terminal domain has an extended paddle-like conformation due to an offset in the α -

solenoid structure between HR C and HR D that limits the twist common to HEAT repeat domains. Amino acid conservation maps primarily to the face of the domain formed by intra-HEAT loops, which has an overall basic charge that would complement the negatively charged MT exterior (Figure 7.4.5B, 7.6.2, and 7.6.3A-7.6.3C).

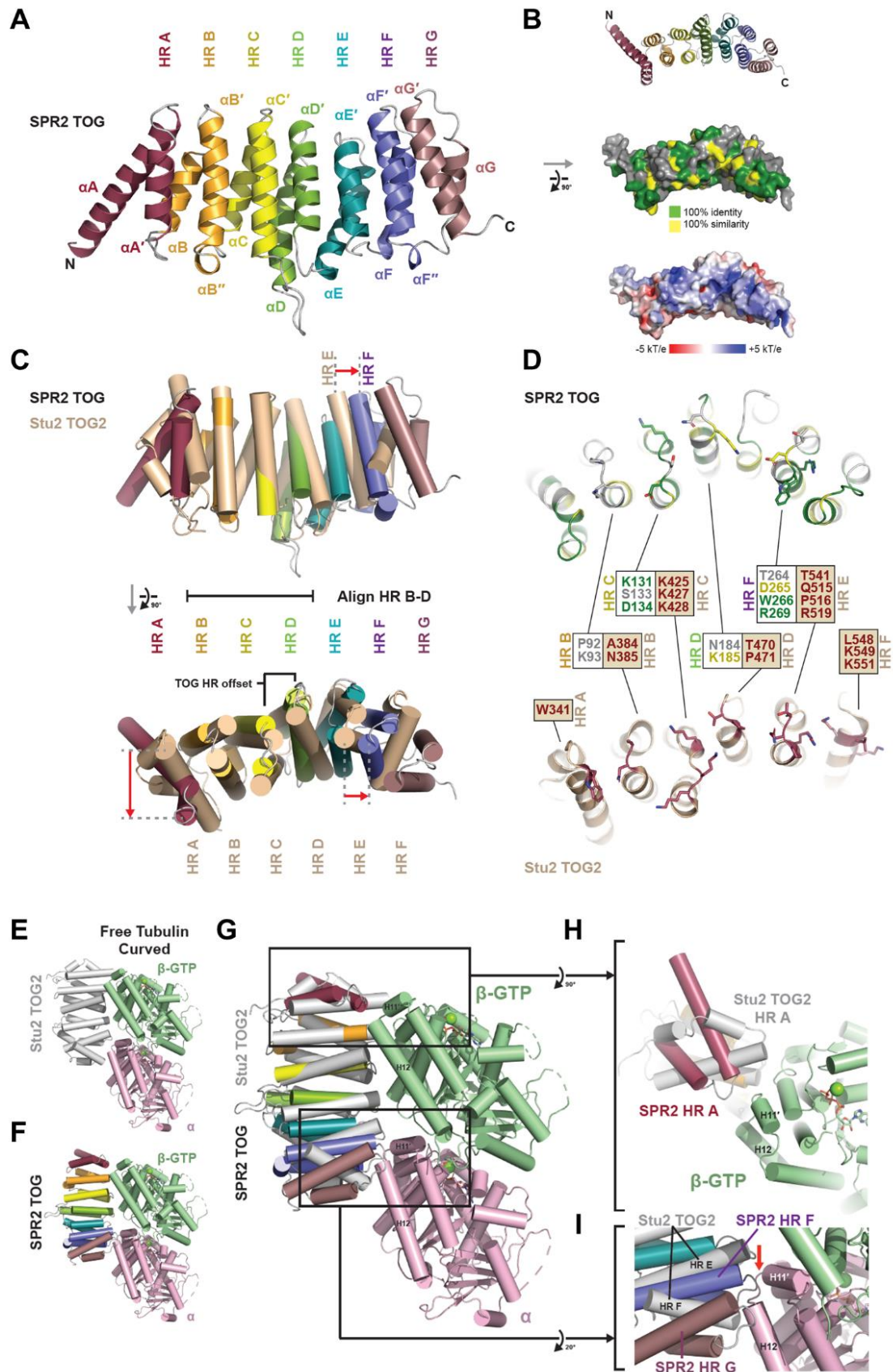


Figure 7.4.5. SPR2 contains a bona fide TOG domain with a unique architecture. (A) Cartoon diagram of the SPR2 TOG domain, containing HEAT repeats HR A-G. (B) SPR2 TOG domain as in (A) after a 90° rotation about the x-axis in cartoon (above), and surface (middle: mapping conservation; below: electrostatics) representation. (C) SPR2 (above: oriented as in (A); below: after a 90° rotation) aligned with Stu2 TOG2 (Ayaz et al., 2014) over HRs B-D. Key structural differences are indicated with red arrows. (D) Comparison of SPR2 (above, residues colored according to conservation as in (B)) and Stu2 TOG2 (below, showing key residues involved in tubulin binding) intra-HEAT repeat residues. (E-I) Comparison of Stu2 TOG2 bound to tubulin (E) (Ayaz et al., 2014), and SPR2 TOG modeled on tubulin after alignment to Stu2 TOG2 HR B-D without (F), and with Stu2 TOG2 shown (G-I).

We next compared the SPR2 N-terminal domain to the Stu2 TOG2 structure from the Stu2 TOG2:αβ-tubulin complex, since the tubulin-binding determinants observed in this complex are well defined (Ayaz et al., 2014). The SPR2 N-terminal domain aligned best to Stu2 TOG2 when the alignment was focused on HRs B-D (Dali Z score 2.1; Cα RMSD = 2.1 Å, 113 of 124 residues aligned). When superimposed, the tubulin-binding intra-HEAT loops of Stu2 TOG2 align well to those of SPR2, and Stu2 residues involved in tubulin-binding have homology to many of the SPR2 residues at equivalent positions (Figures 7.4.5C and 7.4.5D).

Significant structural differences are noted in the relative positioning of the flanking HRs (Figure 7.4.5C). SPR2 HR A is rotated around the α-solenoid axis relative to Stu2 TOG2 HR A while SPR2 HRs E-G are shifted along the α-solenoid axis relative to Stu2 TOG2 HRs E-F. The SPR2 HR E is shorter than the Stu2 TOG2 HR E, and its compaction into the α-solenoid effectively positions SPR2 HR F to structurally mimic Stu2 HR E, though positioned further along the α-solenoid axis (Figure 7.4.5C). Key Stu2 TOG2 HR E tubulin-binding residues have position-equivalent homologs in the SPR2 HR F intra-HEAT loop, suggesting that SPR2 may use its elongated TOG architecture to bind a structural state of tubulin that is distinct from the curved tubulin conformation engaged by Stu2 TOG2 (Figure 7.4.5D) (Ayaz et al., 2014). Given the structural homology to Stu2 TOG2, and the structural variation observed in TOG structures determined to date (Al-Bassam et al., 2007; Byrnes and Slep, 2017; Leano and Slep, 2019; Maki

et al., 2015) we designate the SPR2 N-terminal domain a bona fide TOG domain with distinct structural attributes.

7.4.6 Structural modeling suggests that the SPR2 TOG domain uses unique structural elements to bind to $\alpha\beta$ -tubulin

To explore how SPR2 might engage a tubulin dimer, we used the structural alignment of the SPR2 TOG domain on the Stu2 TOG2: $\alpha\beta$ -tubulin structure discussed above (Figure 7.4.5C). As the alignment was focused on the HR B-D region, which engages β -tubulin, we used the β -tubulin subunit to anchor structural alignments. Alignment of SPR2 TOG to the Stu2 TOG2: $\alpha\beta$ -tubulin structure highlighted unique features of the SPR2 TOG domain that may be used to engage tubulin (Figures 7.4.5E-5I). SPR2 TOG HRs A-D complement the surface of β -tubulin, but distinct from canonical TOG domains, the SPR2 HR A intra-HEAT loop is uniquely angled towards the β -tubulin H11'-H12 segment (Figure 7.4.5H). This explains why the SPR2 HR A intra-HEAT loop lacks a conserved tryptophan, found in canonical TOG domains, that engages determinants on β -tubulin H3. Instead, the SPR2 HR A loops positions a conserved arginine (R56) within hydrogen bonding distance of determinants on β -tubulin H11'. SPR2 HR E is recessed into the TOG structure and is not predicted to contact β - or α -tubulin. However, SPR2 HR F structurally mimics Stu2 TOG2 HR E and is similarly positioned to contact α -tubulin H11' (distance from H11 as modeled: 2 Å), although the SPR2 HR F intra-HEAT loop is positioned more towards the minus end of the tubulin subunit than Stu2 TOG2 HR E (Figure 7.4.5I). The additional SPR2 HEAT repeat, HR G, is uniquely positioned to engage α -tubulin H12 (Figure 7.4.5I). Collectively, the SPR2 TOG domain features distinct architectural determinants in HR A and HRs F-G that likely engage the H11'-H12 segments of β - and α -tubulin, respectively.

7.4.7 The 1-570 aa and 38-570 aa fragments of SPR2 rescue helical growth of the *spr2-2* mutant

To determine whether the SPR2 fragments that bind and stabilize MT minus ends *in vitro* are functional *in vivo*, we used genetic complementation of the *spr2-2* knockout mutant, which has a strong right-handed helical growth phenotype (Shoji et al., 2004). The coding sequence of full-length SPR2, 1-500 aa, 1-570 aa and 38-570 aa fragments fused to mRuby were expressed under the control of the *SPR2* promoter in the *spr2-2* mutant containing a GFP-TUB6 microtubule marker. Consistent with previous work (Fan et al., 2018), expression of full-length SPR2-mRuby in the *spr2-2* mutant rescues helical growth of cotyledons (Figure 7.4.6A), true leaves (Figure 7.4.6B), and petals (Figure 7.4.6C). For the 1-500 aa fragment, we analyzed six independent single-insertion homozygous lines. All these plants were morphologically indistinguishable from the *spr2-2* mutant and exhibited right-handed helical growth of cotyledons (Figure 7.4.6A), true leaves (Figure 7.4.6B), and petals (Figure 7.4.6C). For the 1-570 aa fragment, we analyzed eight independent single-insertion homozygous lines. Of these, two lines appeared like wild-type plants (e.g., line #2-4), indicating full complementation (Figures 7.4.6A-6C). The remaining six (1-570)-mRuby expressing plants showed partial complementation (e.g., line #23-3), such that cotyledons showed right-handed helical growth (Figure 7.4.6A), but true leaves and petals appeared like wild-type (Figures 7.4.6B and 7.4.6C).

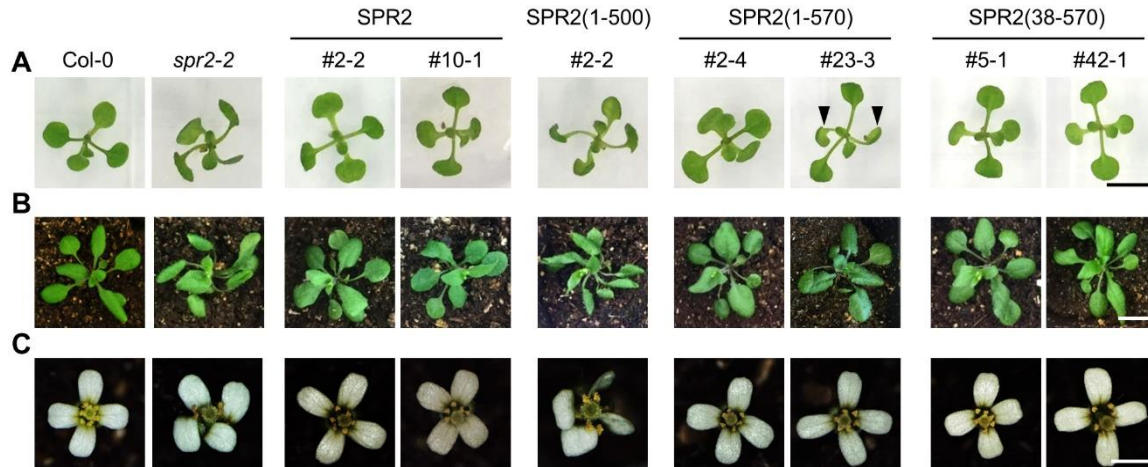


Figure 7.4.6. Phenotypes of *spr2-2* mutant expressing SPR2 fragments. Images of Col-0, *spr2-2* mutant, and *spr2-2* mutant complemented with either SPR2-mRuby, (1-500)-mRuby, (1-570)-mRuby, or (38-570)-mRuby fusion proteins. (A) Seedlings 10 days after germination. (B) 20-day-old plants grown in the soil. (C) Flowers from adult plants. Arrowheads in (A) point to the twisted cotyledons in the partially complemented (1-570)-mRuby #23-3 line. Scale bar = 0.5 cm for seedling and plants; scale bar = 1 mm for flowers.

For the 38-570 aa fragment, we analyzed five independent single-insertion homozygous lines. Three of these lines showed full complementation (e.g., lines #5-1 and #42-1), with cotyledons, true leaves, and petals showing wild-type-like morphology (Figures 7.4.6A-7.4.6C). The remaining two lines did not show any mRuby signal, probably because of gene silencing, and therefore were not analyzed further.

7.4.7 The 1-570 aa and 38-570 aa fragments of SPR2 stabilize microtubule minus ends *in vivo*

We next performed live imaging of hypocotyl epidermal cells to determine whether the complementation results of the different SPR2 fragments can be explained by their localization pattern and effect on cortical MT dynamics. Full-length SPR2-mRuby localizes continuously at free cortical MT minus ends (Fan et al., 2018) (Figures 7.4.7A and 7.4.7B), with an average dwell time of 106 s ($n = 130$). In striking contrast, the (1-500)-mRuby signal appeared only sporadically at cortical MT minus ends (Figure 7.4.7C), with an average dwell time of 7 s ($n =$

102). The cortical MT minus ends in these plants depolymerized rapidly (Figure 7.4.7D), like in the *spr2-2* mutant (Fan et al., 2018; Nakamura et al., 2018).

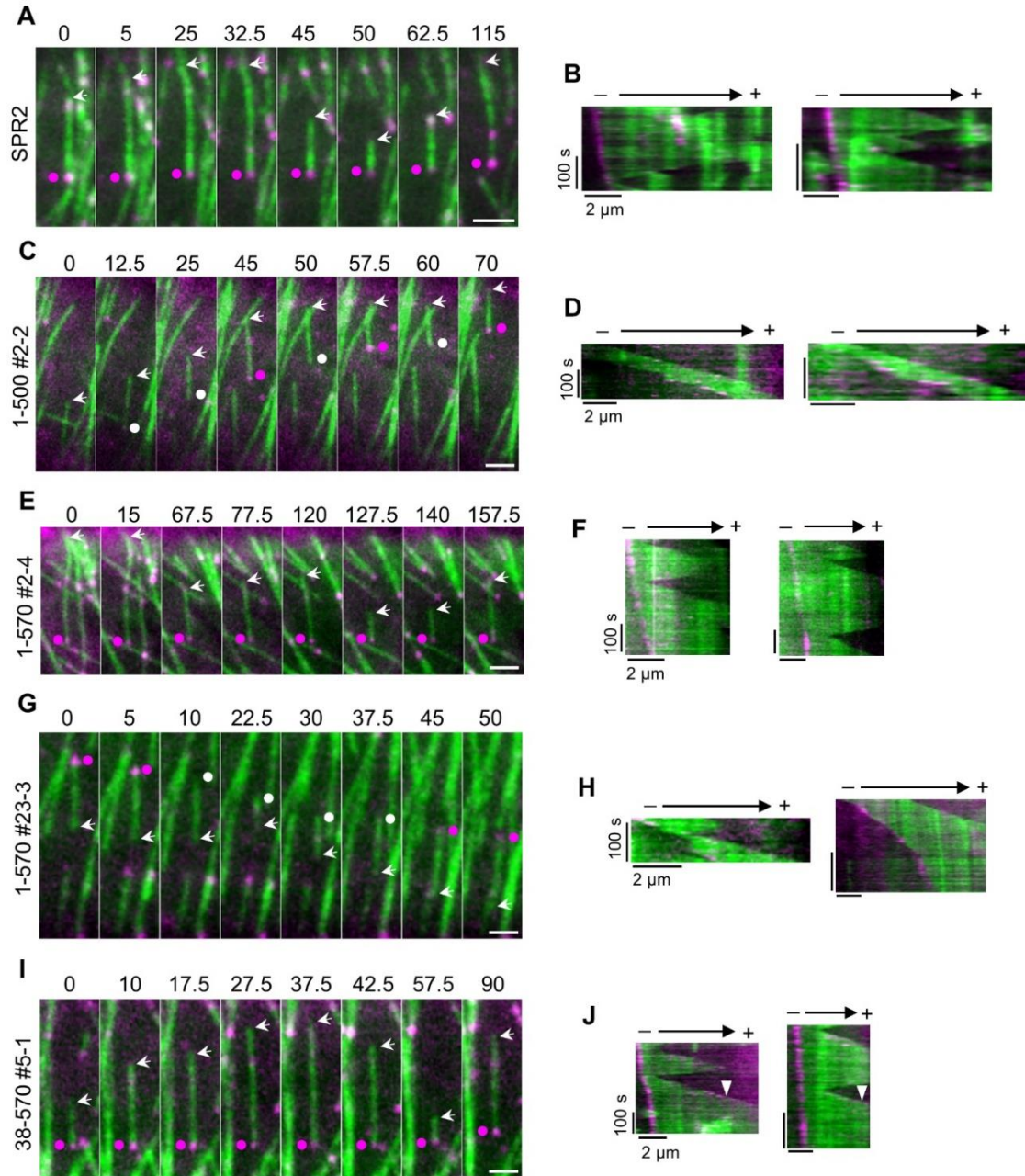


Figure 7.4.7. Cortical MT dynamics and minus end localization of SPR2 fragments in hypocotyl epidermal cells. Montage and kymograph showing the localization and cortical MT dynamics of full-length SPR2-mRuby (A, B), (1-500)-mRuby (C, D), (1-570)-mRuby line #2-4 that shows full complementation (E, F), (1-570)-mRuby line #23-3 that shows partial complementation (G, H), and (38-570)-mRuby line #5-1 (I, J). Numbers above each montage indicate time in seconds. Arrow and dot label the MT plus and minus end, respectively. A purple dot indicates when the

mRuby signal is present at the minus end. A white dot indicates when the mRuby signal is absent at the minus end. Arrowheads in (J) point to (38-570)-mRuby signal at growing plus-ends. Scale bar = 2 μ m.

In the 1-570 #2-4 line which shows full complementation, we observed continuous (1-570)-mRuby signal at minus ends with an average dwell time of 147 s ($n = 71$) (Figure 7.4.7E). In addition, the cortical MT minus ends in this plant depolymerized slowly like in wild-type plants (Figure 7.4.7F). By contrast, in the 1-570 #23-3 line in which embryonic tissues show right-handed twisting, the (1-570)-mRuby signal at cortical MT minus ends was sporadic (Figures 7.4.7G), with an average dwell time of 65 s ($n = 81$). The cortical MT minus ends in this plant depolymerized rapidly (Figures 7.4.7H), like in the *spr2-2* mutant. Lastly, in the 38-570 complementation lines, the (38-570)-mRuby signal is present continuously at cortical MT minus ends (Figures 7.4.7I), with an average dwell time of 105 s ($n = 110$) and the minus ends of these cortical MTs show wild-type-like dynamics (Figures 7.4.7J).

We used these data to quantify the growth and shortening rates as well as the time spent growing, shortening, and pausing for both the plus and minus ends of cortical MTs. The 1-500 aa, 1-570 aa and 38-570 aa fragments partially rescued the growth rate of the plus ends, except for the 1-570 aa line #23-3 in which the plus-end growth rate is statistically indistinguishable from control plants (Table 7.4.1). The MT plus-end shortening rate was statistically the same between all the lines (Table 7.4.1). For time spent by the plus ends in the various phases, the 1-500 aa lines failed to restore these parameters to control values; in fact, the deviation from control values was even more severe in these plants compared to the *spr2-2* mutant. By contrast, the 1-570 aa and 38-570 aa lines showed at least partial rescue of these parameters, with 38-570 aa line #5-1 being the most like control plants (Table 7.4.1).

With respect to the cortical MT minus ends, both the shortening rate and time spent shortening were more severely altered in the 1-500 aa lines compared to the *spr2-2* mutant (Table 7.4.1). However, in the 1-570 aa and 38-570 aa lines, these parameters were at least partially restored to control values (Table 7.4.1).

Table 7.4.1. Dynamics of cortical microtubule plus and minus ends

		Growth rate ($\mu\text{m}/\text{min}$)	Shortening rate ($\mu\text{m}/\text{min}$)	Growth time (%)	Shortening time (%)	Pause time (%)
Plus end	SPR2	4.8 ± 1.8^c (114)	20.1 ± 22.5^a (79)	88.7 ± 10.0^e (75)	11.3 ± 10.0^a (75)	0 (75)
	<i>spr2-2</i>	8.1 ± 5.1^a (59)	20.6 ± 12.4^a (9)	98.1 ± 6.0^b (53)	1.9 ± 6.0^{de} (53)	0 (53)
	1-500 #2-2	6.2 ± 2.3^b (62)	11.4 ± 5.3^a (2)	99.9 ± 1.2^a (61)	0.2 ± 1.2^e (61)	0 (61)
	1-570 #2-4	5.7 ± 1.7^b (63)	22.0 ± 13.6^a (26)	93.0 ± 11.9^{cd} (51)	7.0 ± 11.9^{bc} (51)	0 (51)
	1-570 #23-3	4.6 ± 1.5^c (57)	19.7 ± 15.9^a (22)	95.9 ± 7.4^{bc} (45)	4.1 ± 7.4^{cd} (45)	0 (45)
	38-570 #5-1	6.3 ± 3.4^b (101)	20.5 ± 26.2^a (66)	89.3 ± 9.8^d (65)	10.7 ± 9.8^{ab} (65)	0 (65)
	38-570 #42-1	6.0 ± 1.7^b (55)	25.8 ± 16.4^a (26)	94.3 ± 6.8^c (42)	5.8 ± 6.8^{bc} (42)	0 (42)
Minus end	SPR2	NA	1.5 ± 2.7^{ef} (111)	NA	61.0 ± 38.0^d (74)	39.0 ± 38.0^a (74)
	<i>spr2-2</i>	NA	7.8 ± 6.2^b (68)	NA	89.3 ± 20.0^b (52)	10.7 ± 20.0^c (52)
	1-500 #2-2	NA	8.6 ± 6.7^a (66)	NA	98.0 ± 7.3^a (61)	2.0 ± 7.2^d (61)
	1-570 #2-4	NA	2.8 ± 6.3^d (66)	NA	77.8 ± 33.3^c (59)	22.2 ± 33.2^b (59)
	1-570 #23-3	NA	4.8 ± 6.3^c (60)	NA	80.4 ± 27.5^{bc} (51)	19.7 ± 27.5^{bc} (51)
	38-570 #5-1	NA	1.2 ± 2.4^f (124)	NA	79.4 ± 28.4^c (68)	20.6 ± 28.4^b (68)

38-570 #42-1	NA	1.8 ± 2.2^e (64)	NA	84.2 ± 22.4^{bc} (38)	15.8 ± 22.4^{bc} (38)
-----------------	----	-------------------------	----	------------------------------	------------------------------

Values are means \pm SD (n = number of events). NA, not applicable. The letters indicate statistically distinguishable groups as determined by the Student's t-test, $p < 0.05$.

7.5 Discussion

The acentrosomal cortical MT cytoskeleton of higher plants consists of treadmilling polymers with abundant free minus ends (Shaw et al., 2003). The SPR2 protein has emerged as a plant-specific MT minus-end targeting protein which localizes to and tracks free minus ends and greatly reduces their depolymerization rate (Fan et al., 2018; Leong et al., 2018; Nakamura et al., 2018). However, the structural elements of SPR2 that confer minus end localization and protection against rapid depolymerization are unknown. In this study, we show that a unique TOG domain followed by a basic region and unstructured linker, and oligomerization via a central coiled-coil domain, are important for SPR2 to target and stabilize free MT minus ends.

We demonstrate that the N-terminal region of SPR2 contains a bona fide TOG domain. Importantly, we found that oligomerization is required for SPR2 to co-bind soluble tubulin and the MT polymer in our assay. Our SEC-MALS data indicates that SPR2 exists as a tetramer. A single tetramer of SPR2 is likely sufficient to protect a minus end from rapid depolymerization since four SPR2 molecules are typically found at stabilized minus ends *in vitro* (Fan et al., 2018). It remains to be determined whether all four TOG domains in a SPR2 tetramer are involved in binding soluble tubulin and whether SPR2's ability to bring free tubulin to a MT is required for minus end protection.

Our crystallographic structure revealed that the TOG domain of SPR2 has a distinctive architecture consisting of seven HEAT repeats, making it unique among TOG domain-containing proteins. Alignment of SPR2 TOG to the Stu2 TOG2: $\alpha\beta$ -tubulin structure indicates that unique

features in HR A and HRs F-G of the SPR2 TOG domain likely engage the H11'-H12 segments of β - and α -tubulin, respectively. Future work will test the importance of specific amino acids in the SPR2 TOG domain for tubulin binding, their contribution to the minus-end stabilizing function of SPR2, and the role of binding the H11'-H12 segments of β - and α -tubulin.

We found that a positively charged region following the TOG domain facilitates MT lattice binding by SPR2, probably by binding to the negatively charged MT surface. Oligomerization of SPR2 greatly enhances MT binding, likely through an avidity-based mechanism in which a SPR2 tetramer use its basic regions to engage multiple sites on the MT lattice. In the MT plus-end polymerase, XMAP215, a lattice-binding basic region is thought to be important for function at physiological concentrations by promoting accumulation of XMAP215 at the plus end (Widlund et al., 2011). The basic region of SPR2 might play a similar role. SPR2 molecules diffuse along the MT lattice both *in vitro* (Fan et al., 2018) and *in vivo* (Yao et al., 2008; Wightman et al., 2013). Upon arrival at a minus end, diffusive SPR2 molecules become immobilized and remain persistently at the minus end (Fan et al., 2018). Thus, the lattice-binding basic region likely enhances SPR2's localization to minus ends, especially at low concentrations. In addition, lattice binding might enable SPR2 to track depolymerizing minus ends.

In our *in vitro* experiments, the ~100 aa segment between the basic region and coiled-coil domain is necessary for minus end localization. This region is predicted to be disordered and it is possible that it mediates recognition of a specific tubulin face or conformation uniquely found at the minus end.

When expressed in the Arabidopsis *spr2-2* mutant, the 1-500 aa fragment of SPR2 is unable to complement the helical growth phenotype. While this fragment localizes to cortical MT minus ends, it does not prevent their rapid depolymerization. This inability correlates with a dramatically lower dwell time at cortical MT minus ends compared to full-length SPR2. Hence, stable association of SPR2 to minus ends is required for its function. The low MT binding affinity of the 1-500 aa fragment provides one possible explanation for its sporadic localization to cortical MT minus ends. Alternatively, this fragment might be non-functional due to its inability to recruit tubulin subunits to MTs.

The Arabidopsis *spr2-2* mutant expressing the 1-570 aa fragment of SPR2 showed either complete complementation or partial complementation wherein embryonic organs remained twisted but post-embryonic organs are wild-type-like. Full complementation was associated with stable localization of the 1-570 aa fragment to cortical MT minus ends and slow minus end depolymerization. By contrast, partial complementation was associated with sporadic localization at cortical MT minus ends and their rapid depolymerization in hypocotyl epidermal cells. Whether the difference in complementation strength between these plants is due to differences in expression level of this fragment remains to be determined.

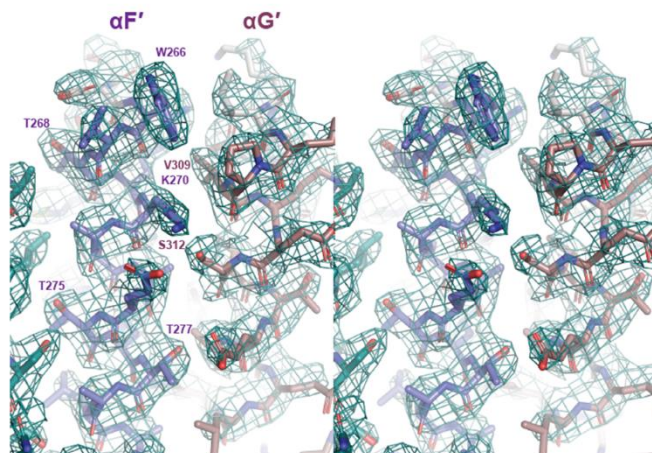
The 38-570 aa fragment of SPR2 showed complete complementation when expressed in the Arabidopsis *spr2-2* mutant. This fragment best recapitulates the MT binding and minus end stabilizing activity of full-length SPR2 *in vitro*. Further, it shows continuous tracking of depolymerizing cortical MT minus ends *in vivo*, similar to full-length SPR2. We intentionally generated this fragment to determine whether the Ser/Thr-rich region regulates SPR2's localization and function, potentially via phosphorylation. However, our data demonstrate that the N-terminal 37 aa are dispensable for the normal activity of SPR2.

We found that the C-terminal domain of SPR2 is not required for targeting and stabilizing MT minus ends. In addition, it does not contribute to the occasional localization of SPR2 to growing cortical MT plus ends (Fan et al., 2018), since the 38-570 aa fragment is able to do so. Recently, the SPR2 C-terminal domain was found to have structural homology to the C-terminal domain of the p80 katanin regulatory subunit (Ohno et al., 2023; Bolhuis et al.). While this raises the possibility that SPR2 might interact with katanin to regulate MT dynamics, it remains to be experimentally determined.

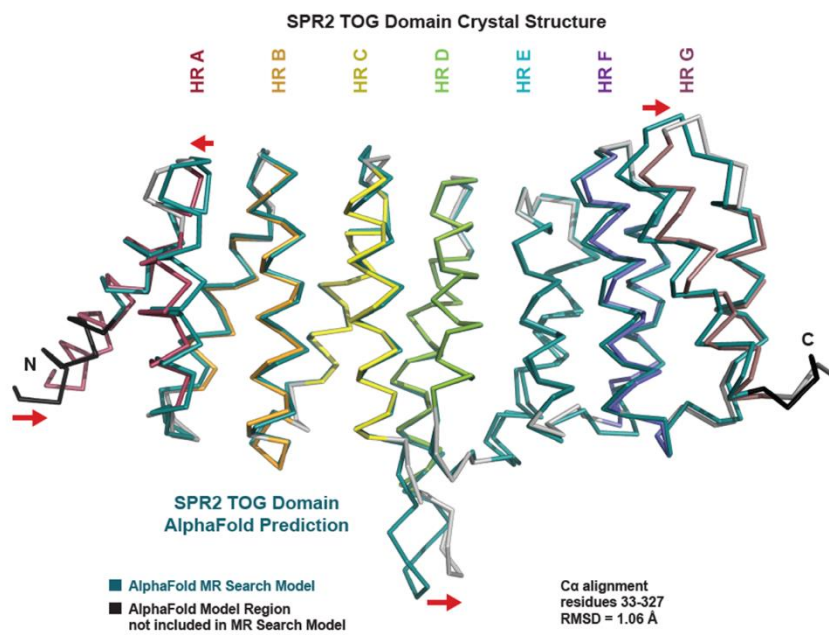
How might SPR2 reduce the depolymerization rate of the MT minus end? Based on our data, one possible mechanism is that SPR2 brings new tubulin subunits to minus ends, which would slow their depolymerization rate. Alternatively, SPR2 might stabilize the MT lattice conformation at the minus end to inhibit depolymerization. A third possibility is that a tetramer of SPR2 binds to multiple lattice sites, perhaps on different protofilaments, thus preventing the outward curling of protofilaments and consequently limiting minus end depolymerization. We note that these distinct mechanisms are not mutually exclusive. Regardless of the exact mechanism, our data establish SPR2 as a TOG domain-containing protein involved in regulating the dynamics of MT minus ends.

7.6 Supplementary Information

A



B



C

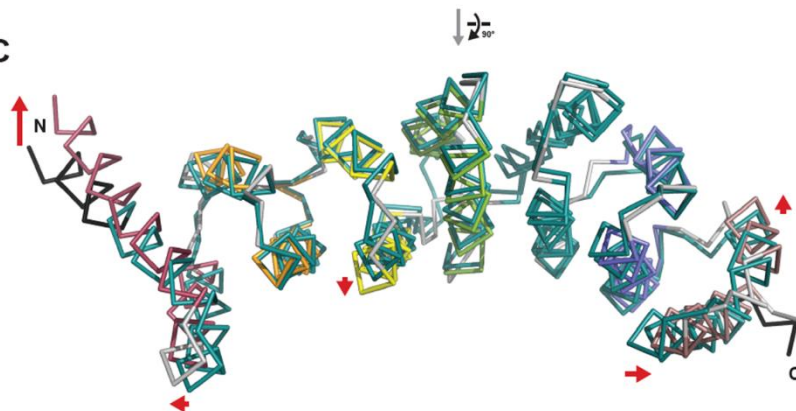


Figure 7.6.1. The SPR2 TOG domain structural core aligns well to the AlphaFold prediction model. (A) Stereodiagram of SPR2 TOG HR F α F' and HR G α G' helices, 2Fo-Fc electron density contoured at 1.0 σ . (B-C) SPR2 TOG domain crystal structure (multiple colors) aligned to the AlphaFold prediction model (teal region used in molecular replacement search model, black region excluded from the search model). Major differences between the refined crystal structure and the AlphaFold prediction are indicated with red arrows. (C) Alignment as in (B), rotated 90° about the x-axis.

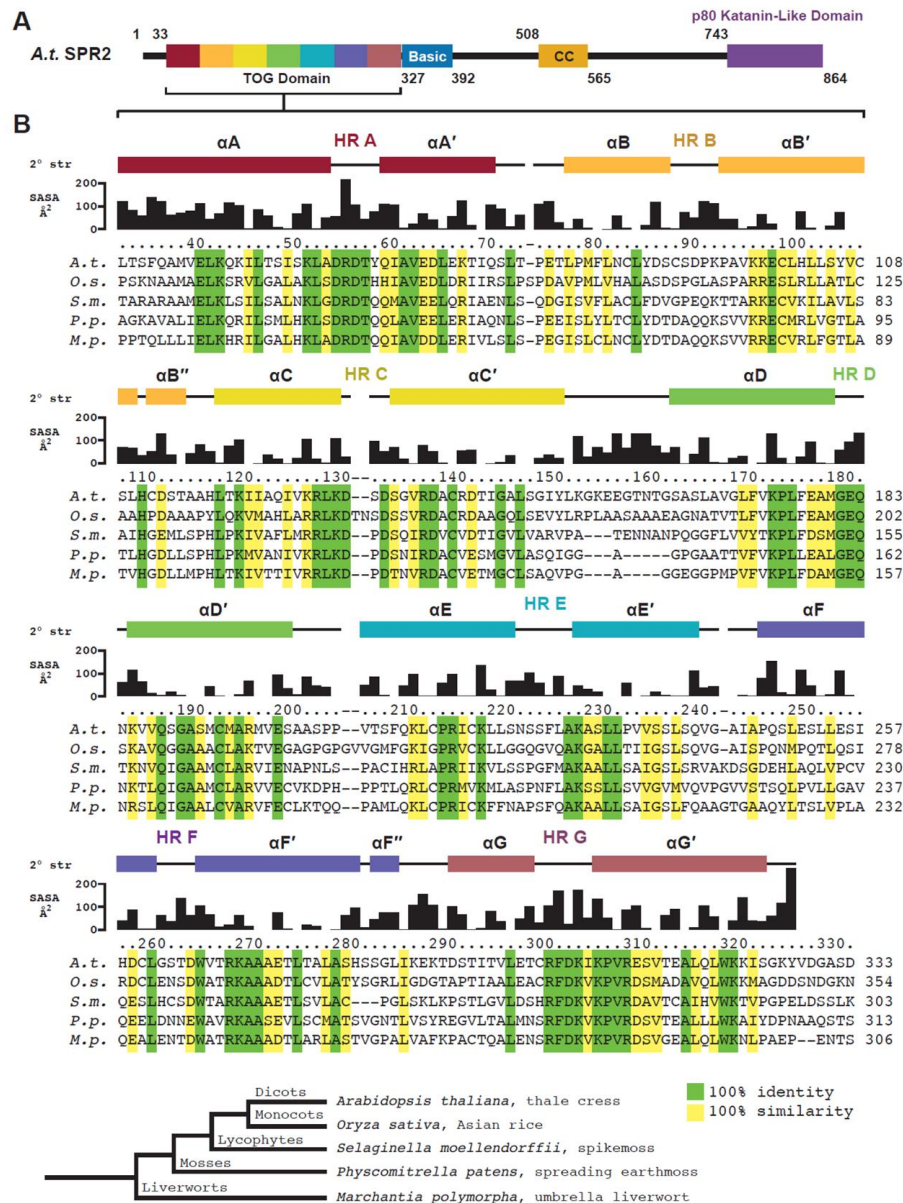


Figure 7.6.2. The SPR2 TOG domain is highly conserved across plants. (A) Domain architecture of *Arabidopsis thaliana* (A.t.) SPR2. (B) Sequence alignment of A.t. SPR2 and homologs from *Oryza sativa* (O.s.), *Selaginella moellendorffii* (S.m.), *Physcomitrella patens* (P.s.), and *Marchantia polymorpha* (M.p.). Identity (green) and similarity (yellow) is contoured at 100% across homologs. Secondary structure, solvent accessible surface area (SASA), and residue number for the A.t. SPR2 TOG structure is indicated above the alignment.

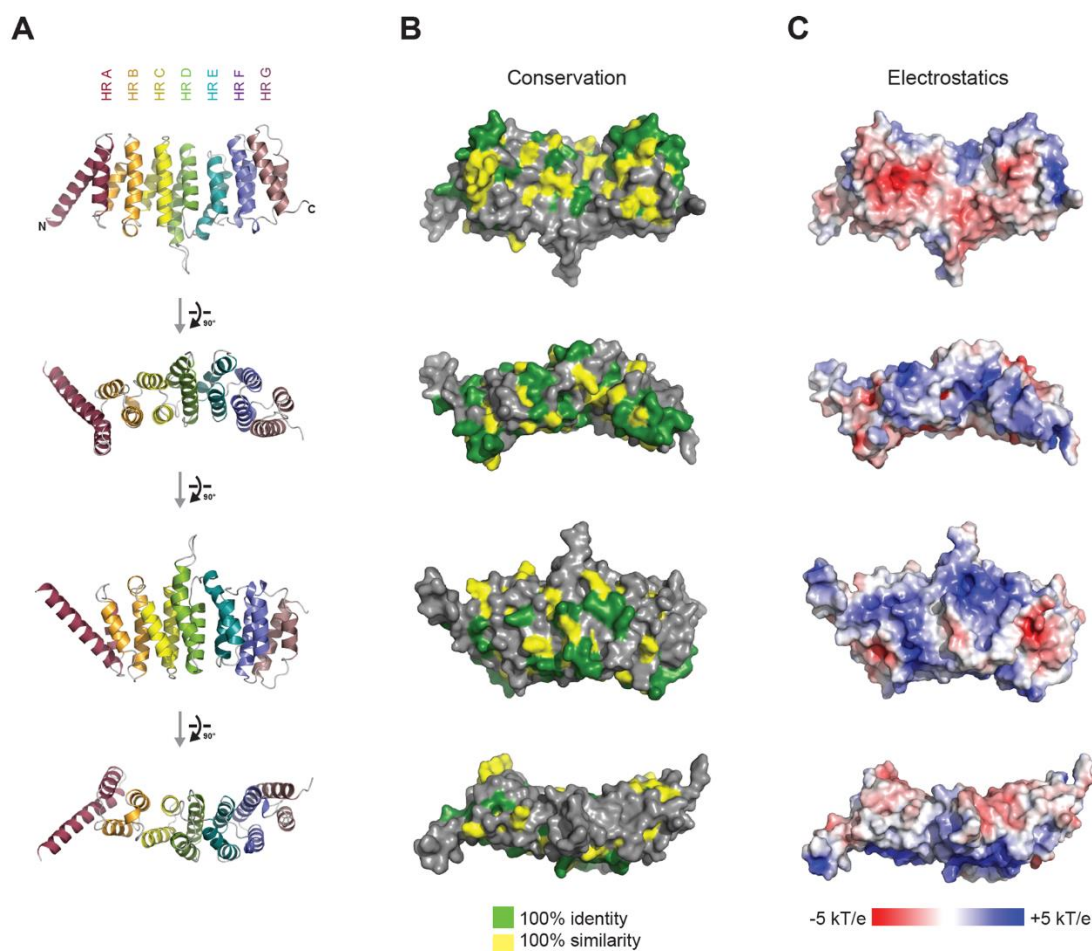


Figure 7.6.3. The SPR2 TOG domain face composed of intra-HEAT loops is highly conserved and basic. (A) SPR2 TOG domain shown in cartoon format, rotated in 90° increments along the x-axis. (B-C) SPR2 TOG domain shown in surface format with identity (green) and similarity (yellow) (delineated as in Figure 7.6.2) mapped on the surface (B), and showing electrostatics (C), oriented as in (A).

Table 7.6.1. Crystallographic data processing and refinement statistics.

Crystal	SPR2 residues 33-333
Data Collection	
Wavelength (Å)	1.000
Space group	I222
Cell dimensions: a, b, c (Å)	72.8, 78.5, 131.9

Resolution (Å)	50.00-2.80 (2.90-2.80)
# Reflections: Measured / Unique	108,812 (8496) / 9490 (944)
Completeness (%)	98.7 (99.8)
Mean redundancy	11.5 (9.0)
$\langle I/\sigma I \rangle$	19.7 (2.6)
R_{sym}	0.164 (0.842)
CC1/2	0.993 (0.872)
CC*	0.998 (0.965)
Refinement	
Resolution (Å)	38.36-2.80 (2.95-2.80)
R/ R_{free} (%)	21.4 (27.6) / 25.9 (34.5)
# Reflections, R/ R_{free}	8246 (917) / 1078 (113)
Total atoms: Protein / Water / Iodine	2256 / 7 / 1
Stereochemical ideality (rmsd): Bonds (Å) / Angles (°)	0.003 / 0.535
Ramachandran Analysis: Favored / Allowed (%)	97.6 / 2.3

Values in parentheses indicate statistics for the highest-resolution shell.

Table 7.6.2. Oligonucleotides used in Appendix II.

Primer name	Sequence (5'-3')
BamHI-SPR2 F	GCCCCTGGGATCCATGAGCACACCT
PaeI-SPR2 R	TTGCGGCGCATGCCTTGTCGAACTG
PaeI-GFP F	CGACAAGGCATGCGCCGAACAACCGGAGCCATGGTGAGC

NotI-GFP R	GTCACGGCGGCCGCTTACTTGTACAGCTCG
PaeI-SPR2 (1-276) R	TGTTGCGGCGCATGCCAGGGTCTCAGCCGC
PaeI-SPR2 (1-340) R	TGTTGCGGCGCATGCACTAGCTGAAAGCTT
PaeI-SPR2 (1-400) R	TTGTTGCGGCGCATGCATCTTTATCACTTAAGAC
PaeI-SPR2 (1-500) R	GTTGCGGCGCATGCGAAGGAGCCTTCAGATTGGTTATCA
PaeI-SPR2 (1-570) R	GTTGCGGCGCATGCGAGATTAGCCCTACGA
BamHI-SPR2 (38-570) F	CCAGGGCCATATGGGATCCGCAATGGTGGAGCTG
BamHI-SPR2 (281-570) F	GCCCCTGGGATCCTCACATTCAAGCGGTTTAATTAA
BamHI-SPR2 (501-864) F	GGCCCCTGGGATCCACAAGTAATAGAGGAA
BamHI-SPR2 (571-864) F	CCCCTGGGATCCACAGCTGGGTTTGGCAA
BstBI-GST F	CTGAAAATGTTCTGAAGATCGTTTATGTCATAAAAC
15A-TEV-BamHI R	GTGTGCTCATGGATCCGCCCTGGAAGTACAGGTTCTCATCCGATGCTG CTGCTGCTGCTGCTGCTGCTGCTGCTGCTGCT
SPR2 33 Nde F	GGCAGGACCCATATGCTCACTTCGTTCCAAGCAATGGTGGAG
SPR2 333 Eco R	GCCGAGCCTGAATTCTTAATCTGAAGCACCATCGACATATTTCCAG
SPR2 503 Nde F	GGCAGGACCCATATGAATAGAGGAAATTGGTCAGCCATCCAG
SPR2 566 Eco R	GCCGAGCCTGAATTCTTAACGACCTGATGATATCGAAAGATCTCTTG

7.7 References

- Adams, P.D. et al. (2010). PHENIX: a comprehensive Python-based system for macromolecular structure solution. *Acta Crystallogr D Biol Crystallogr* 66: 213–221.
- Akhmanova, A. and Steinmetz, M.O. (2015). Control of microtubule organization and dynamics: two ends in the limelight. *Nat Rev Mol Cell Biol* 16: 711–726.
- Akhmanova, A. and Steinmetz, M.O. (2019). Microtubule minus-end regulation at a glance. *Journal of Cell Science* 132: jcs227850.
- Al-Bassam, J., van Breugel, M., Harrison, S.C., and Hyman, A. (2006). Stu2p binds tubulin and undergoes an open-to-closed conformational change. *Journal of Cell Biology* 172: 1009–1022.
- Al-Bassam, J., Larsen, N.A., Hyman, A.A., and Harrison, S.C. (2007). Crystal structure of a TOG domain: conserved features of XMAP215/Dis1-family TOG domains and implications for tubulin binding. *Structure* 15: 355–362.
- Ambrose, J.C., Shoji, T., Kotzer, A.M., Pighin, J.A., and Wasteneys, G.O. (2007). The *Arabidopsis CLASP* Gene Encodes a Microtubule-Associated Protein Involved in Cell Expansion and Division. *The Plant Cell* 19: 2763–2775.
- Atherton, J. et al. (2017). A structural model for microtubule minus-end recognition and protection by CAMSAP proteins. *Nat Struct Mol Biol* 24: 931–943.
- Atherton, J. et al. (2019). Structural determinants of microtubule minus end preference in CAMSAP CKK domains. *Nat Commun* 10: 5236.
- Ayaz, P., Munyoki, S., Geyer, E.A., Piedra, F.-A., Vu, E.S., Bromberg, R., Otwinowski, Z., Grishin, N.V., Brautigam, C.A., and Rice, L.M. (2014). A tethered delivery mechanism explains the catalytic action of a microtubule polymerase. *Elife* 3: e03069.

- Ayaz, P., Ye, X., Huddleston, P., Brautigam, C.A., and Rice, L.M. (2012). A TOG: $\alpha\beta$ -tubulin complex structure reveals conformation-based mechanisms for a microtubule polymerase. *Science* 337: 857–860.
- Bolhuis, D.L., Dixit, R., and Slep, K.C. Crystal structure of the Arabidopsis SPIRAL2 C-terminal domain reveals a p80-Katanin-like domain. *bioRxiv* 2022.12.28.522140.
- Brouhard, G.J., Stear, J.H., Noetzel, T.L., Al-Bassam, J., Kinoshita, K., Harrison, S.C., Howard, J., and Hyman, A.A. (2008). XMAP215 Is a Processive Microtubule Polymerase. *Cell* 132: 79–88.
- Byrnes, A.E. and Slep, K.C. (2017). TOG–tubulin binding specificity promotes microtubule dynamics and mitotic spindle formation. *J Cell Biol* 216: 1641–1657.
- Currie, J.D., Stewman, S., Schimizzi, G., Slep, K.C., Ma, A., and Rogers, S.L. (2011). The microtubule lattice and plus-end association of *Drosophila* Mini spindles is spatially regulated to fine-tune microtubule dynamics. *Mol Biol Cell* 22: 4343–4361.
- Emsley, P., Lohkamp, B., Scott, W.G., and Cowtan, K. (2010). Features and development of Coot. *Acta Crystallogr D Biol Crystallogr* 66: 486–501.
- Fan, Y., Burkart, G.M., and Dixit, R. (2018). The Arabidopsis SPIRAL2 Protein Targets and Stabilizes Microtubule Minus Ends. *Curr Biol* 28: 987-994.e3.
- Filipčík, P., Latham, S.L., Cadell, A.L., Day, C.L., Croucher, D.R., and Mace, P.D. (2020). A cryptic tubulin-binding domain links MEKK1 to curved tubulin protomers. *Proc Natl Acad Sci U S A* 117: 21308–21318.
- Fox, J.C., Howard, A.E., Currie, J.D., Rogers, S.L., and Slep, K.C. (2014). The XMAP215 family drives microtubule polymerization using a structurally diverse TOG array. *Mol Biol Cell* 25: 2375–2392.

- Galjart, N. (2010). Plus-end-tracking proteins and their interactions at microtubule ends. *Curr Biol* 20: R528-537.
- Gard, D.L., Becker, B.E., and Josh Romney, S. (2004). MAPping the eukaryotic tree of life: structure, function, and evolution of the MAP215/Dis1 family of microtubule-associated proteins. *Int Rev Cytol* 239: 179–272.
- Haikonen, T., Rajamäki, M.-L., and Valkonen, J.P.T. (2013). Interaction of the microtubule-associated host protein HIP2 with viral helper component proteinase is important in infection with potato virus A. *Mol Plant Microbe Interact* 26: 734–744.
- Hendershott, M.C. and Vale, R.D. (2014). Regulation of microtubule minus-end dynamics by CAMSAPs and Patronin. *Proc Natl Acad Sci U S A* 111: 5860–5865.
- Holm, L. (2020). Using Dali for Protein Structure Comparison. *Methods Mol Biol* 2112: 29–42.
- Jiang, K., Hua, S., Mohan, R., Grigoriev, I., Yau, K.W., Liu, Q., Katrukha, E.A., Altelaar, A.F.M., Heck, A.J.R., Hoogenraad, C.C., and Akhmanova, A. (2014). Microtubule minus-end stabilization by polymerization-driven CAMSAP deposition. *Dev Cell* 28: 295–309.
- Jumper, J. et al. (2021). Highly accurate protein structure prediction with AlphaFold. *Nature* 596: 583–589.
- Kawamura, E. and Wasteneys, G.O. (2008). MOR1, the *Arabidopsis thaliana* homologue of *Xenopus* MAP215, promotes rapid growth and shrinkage, and suppresses the pausing of microtubules in vivo. *Journal of Cell Science* 121: 4114–4123.
- Kong, Z., Ioki, M., Braybrook, S., Li, S., Ye, Z.-H., Julie Lee, Y.-R., Hotta, T., Chang, A., Tian, J., Wang, G., and Liu, B. (2015). Kinesin-4 Functions in Vesicular Transport on Cortical

- Microtubules and Regulates Cell Wall Mechanics during Cell Elongation in Plants. *Mol Plant* 8: 1011–1023.
- Leano, J.B. and Slep, K.C. (2019). Structures of TOG1 and TOG2 from the human microtubule dynamics regulator CLASP1. *PLoS One* 14: e0219823.
- Lechner, B., Rashbrooke, M.C., Collings, D.A., Eng, R.C., Kawamura, E., Whittington, A.T., and Wasteneys, G.O. (2012). The N-terminal TOG domain of Arabidopsis MOR1 modulates affinity for microtubule polymers. *J Cell Sci* 125: 4812–4821.
- Leong, S.Y., Yamada, M., Yanagisawa, N., and Goshima, G. (2018). SPIRAL2 Stabilises Endoplasmic Microtubule Minus Ends in the Moss *Physcomitrella patens*. *Cell Struct Funct* 43: 53–60.
- Maki, T., Grimaldi, A.D., Fuchigami, S., Kaverina, I., and Hayashi, I. (2015). CLASP2 Has Two Distinct TOG Domains That Contribute Differently to Microtubule Dynamics. *J Mol Biol* 427: 2379–2395.
- Mimori-Kiyosue, Y., Grigoriev, I., Lansbergen, G., Sasaki, H., Matsui, C., Severin, F., Galjart, N., Grosveld, F., Vorobjev, I., Tsukita, S., and Akhmanova, A. (2005). CLASP1 and CLASP2 bind to EB1 and regulate microtubule plus-end dynamics at the cell cortex. *Journal of Cell Biology* 168: 141–153.
- Nakamura, M., Lindeboom, J.J., Saltini, M., Mulder, B.M., and Ehrhardt, D.W. (2018). SPR2 protects minus ends to promote severing and reorientation of plant cortical microtubule arrays. *J Cell Biol* 217: 915–927.
- Nogales, E. and Zhang, R. (2016). Visualizing microtubule structural transitions and interactions with associated proteins. *Curr Opin Struct Biol* 37: 90–96.

- Oda, Y. (2015). Cortical microtubule rearrangements and cell wall patterning. *Front Plant Sci* 6: 236.
- Ohno, M., Higuchi, Y., and Hayashi, I. (2023). Crystal structure of the C-terminal domain of the plant-specific microtubule-associated protein Spiral2. *Acta Crystallogr F Struct Biol Commun* 79: 17–22.
- Otwinowski, Z. and Minor, W. (1997). Processing of X-ray diffraction data collected in oscillation mode. *Methods Enzymol* 276: 307–326.
- Paredez, A.R., Somerville, C.R., and Ehrhardt, D.W. (2006). Visualization of cellulose synthase demonstrates functional association with microtubules. *Science* 312: 1491–1495.
- Rezabkova, L., Kraatz, S.H.W., Akhmanova, A., Steinmetz, M.O., and Kammerer, R.A. (2016). Biophysical and Structural Characterization of the Centriolar Protein Cep104 Interaction Network. *J Biol Chem* 291: 18496–18504.
- Shaw, S.L., Kamyar, R., and Ehrhardt, D.W. (2003). Sustained microtubule treadmilling in *Arabidopsis* cortical arrays. *Science* 300: 1715–1718.
- Shoji, T., Narita, N.N., Hayashi, K., Hayashi, K., Asada, J., Hamada, T., Sonobe, S., Nakajima, K., and Hashimoto, T. (2004). Plant-specific microtubule-associated protein SPIRAL2 is required for anisotropic growth in *Arabidopsis*. *Plant Physiol* 136: 3933–3944.
- Slep, K.C. and Vale, R.D. (2007). Structural basis of microtubule plus end tracking by XMAP215, CLIP-170, and EB1. *Mol Cell* 27: 976–991.
- Varadi, M. et al. (2022). AlphaFold Protein Structure Database: massively expanding the structural coverage of protein-sequence space with high-accuracy models. *Nucleic Acids Res* 50: D439–D444.

- Widlund, P.O., Stear, J.H., Pozniakovsky, A., Zanic, M., Reber, S., Brouhard, G.J., Hyman, A.A., and Howard, J. (2011). XMAP215 polymerase activity is built by combining multiple tubulin-binding TOG domains and a basic lattice-binding region. *Proc Natl Acad Sci U S A* 108: 2741–2746.
- Wightman, R., Chomicki, G., Kumar, M., Carr, P., and Turner, S.R. (2013). SPIRAL2 determines plant microtubule organization by modulating microtubule severing. *Curr Biol* 23: 1902–1907.
- Yao, M., Wakamatsu, Y., Itoh, T.J., Shoji, T., and Hashimoto, T. (2008). Arabidopsis SPIRAL2 promotes uninterrupted microtubule growth by suppressing the pause state of microtubule dynamics. *J Cell Sci* 121: 2372–2381.
- Zhou, R., Liu, H., Ju, T., and Dixit, R. (2020). Quantifying the polymerization dynamics of plant cortical microtubules using kymograph analysis. *Methods Cell Biol* 160: 281–293.
- Zhu, C., Ganguly, A., Baskin, T.I., McClosky, D.D., Anderson, C.T., Foster, C., Meunier, K.A., Okamoto, R., Berg, H., and Dixit, R. (2015). The fragile Fiber1 kinesin contributes to cortical microtubule-mediated trafficking of cell wall components. *Plant Physiol* 167: 780–792.